Statistical analysis of ionospheric total electron content

Katamzi, Zama

Award date:
2011

Awarding institution:
University of Bath

STATISTICAL ANALYSIS OF IONOSPHERIC TOTAL ELECTRON CONTENT

Zama Thobeka Katamzi

A thesis submitted for the degree of Doctor of Philosophy

University of Bath
Department of Electronic and Electrical Engineering

March 2011

COPYRIGHT

Zama T Katamzi

Abstract

Certain modern radio systems that rely on trans-ionospheric propagation require knowledge of changes in total electron content (TEC). Understanding rapidly changing, small amplitude perturbations in the ionosphere is important in order to quantify the accuracy of those systems. The main aim of this thesis is to collect statistical information on the perturbations and wave structures present in the ionosphere, for use in radio astronomy calibrations and future communication systems planning. To gain this information, TEC calculated from instruments measuring Faraday rotation on signals from geostationary satellites were used. These measurements were collected in Italy over the period of 1975-1982 and 1989-1991 at one minute intervals.

An important class of TEC fluctuations is travelling ionospheric disturbances (TIDs). Here, temporal variations of mid-latitude slant TEC measurements during two solar cycle phases, i.e solar minimum in 1975-1976 and solar maximum in 1989-1990, were studied. Direct inspection of Savitzky-Golay filtered TEC data was used to extract the amplitudes of TIDs. Fourier analysis was used to extract the most dominant periods of the TIDs. Discrete Meyer wavelet together with the ANOVA method to determine TID variation changes in different parts of the day. Another class of TEC fluctuations presented in this thesis is diurnal double maxima (DDM) structures. These structures were observed during mid-day in our TEC measurements between 1975 and 1991. Verification of the DDM observations was sought by using $foF2$ and $hmF2$ measurements from an ionosonde in Rome.

A combination of ionospheric 3-D tomographic imaging and ray propagation theory has been used for the first time to demonstrate a method that can show how the new European radio array LOFAR will be affected by the ionosphere. This was achieved from a case study of a geomagnetic quiet day ionosphere by simulating how ray propagations, at different elevations and frequencies, will behave as they traverse the ionosphere. The important result from this study was that continuous monitoring of the telescope will be important during operation of the array if the errors introduced by the ionosphere are to be accurately corrected for. The study of TEC changes over different short time windows demonstrated that the ionosphere vastly varies over short time scales, thus making the monitory non trivial. Statistical analysis of the TEC changes will also be useful to the new European GPS augmentation system EGNOS as an indicator on whether the ionospheric measurements from the system are realistic.

Contents

List of Figures

List of Abbreviations

AE Auroral Electrojet

ART Algebraic Reconstruction Technique

ANOVA ANalysis Of VAriance

ATS Application Technology Satellite

CMEs Coronal Mass Ejections

DDM Diurnal Double Maxima

DROTI Derivative of Rate Of change of Tec Index

EGNOS European Geostationary Navigational Overlay Service

EOFs Empirical Orthogonal Functions

ESA European Space Agency

EUV Extremely Ultra Violet

GLONASS GLObal NAvigation Satellite System

GNSS Global Navigation Satellite System

GPS Global Positioning System

HF High Frequency

IGS International GNSS Services

IMAGE International Monitor for Auroral Geomagnetic Effects

INGV Istituto Nazionale di Geofisica e Vulcanologia

INTERMAGNET International Real-time Magnetic Observatory Network

IRI International Reference Model

LEO Low Earth Orbit

LF Low Frequency

LOFAR LOw Frequency ARray

MART Multiplicative Algebraic Reconstruction Technique

METEOSAT METEOrological SATellites

MIDAS Multi-Instrument Data Analysis System

MINRES MINimum RESidue

NASA National Aeronautics and Space Administration

NOAA National Oceanic and Atmospheric Administration

OTS Orbital Test Satellite

RIMS Ranging and Integrity Monitory Stations

ROTI Rate of change of Tec Index

SIRIO Satellite Italiano Ricerca Industriale Orientata

SIRT Simultaneous Iterative Reconstruction Technique

SKA Square Kilometre Array

SPIDR Space Physics Interactive Data Resource

sTEC slant TEC

SVD Singular Value Decomposition

TEC Total Electron Content

TECU Total Electron Content Unit

TIDs Traveling Ionospheric Disturbances

UHF Ultra High Frequency

UT Universal Time

VHF Very High Frequency

WAAS Wide Area Augmentation System

WDC World Data Center

List of Symbols

$\mathbf{B}$	magnetic field
B	magnetic field strength
c	speed of light
Dst	Disturbed storm time index
$\mathbf{E}$	electric field
e	electron charge
ε_0	permittivity of free space
f	radio wave frequency
f_c	critical frequency
$foF2$	peak frequency of the F2 region
$hmF2$	peak height of the F2 region
Kp	planetary K index
m_e	mass of electron
μ	refractive index
$MUF(3000)F2$	most usable frequency reflected in the F2 region for a ground distance of 3000 km
$M(3000)F2$	maximum usable frequency factor
N_e	electron density
ω	angular frequency
ω_b	Brunt-Väisälä angular frequency
Ω	angle of polarisation
$\mathbf{v}$	plasma drift velocity

Acknowledgements

First and foremost I would like to thank God my Lord, who has blessed me with many gifts in my life. I would also like to especially thank my parents, siblings, aunts, uncles (especially Malume Ntsiki) and cousins for all their support and encouragement during my very long 'career' as a student.

I am very much indebted to my supervisor Prof Cathryn Mitchell, for seeing a potential in me and giving me this opportunity to pursue a PhD within the Invert group. With her support and guidance I was able to conduct this research, she really is a very great supervisor. I would like to thank Paolo Spalla from CNR-IFAC (Italy) for providing me with very high quality data that I have extensively used in this project. Many thanks to Christopher Coleman from the University of Adelaide (Australia) for his help and allowing me to use his ray tracing software as part of this project. I would also like to thank the following organisations for providing a wealth of data which have been used to produce this thesis: IGS for the use of GPS data; IMAGE, INTERMAGNET and WDC (Japan) for the use of magnetometer data; INGV (Rome) for ionosonde data, SPIDR for Kp and Dst indices, NOAA (USA) for sunrise/sunset data.

I owe gratitude to Nathan Smith, not only for proof reading my thesis but for tolerating my many questions that came in all hours of the day and his help in the analysis of the data. Also, thanks to all my friends (especially Vicky, Gemma, Ben, Irene, Jude, Phumi, Anele, Mpume, Zama and Nikiwe) and colleagues (especially Julian, Joe, Caspar, Jenna and Damien) for all their help and support during my thesis.

Chapter 1

Introduction

1.1 Background

The solar terrestrial environment can be defined as the region of space that is closest to the Earth; a region close enough to affect human activities and to be studied from Earth, but remote enough to be beyond everyday experience, (*Hargreaves*, 1992). This environment includes the upper part of the terrestrial atmosphere, the outer part of the geomagnetic field and the solar emissions that affect them.

The Earth's atmosphere is generally divided into four regions based on the variation of temperature with altitude, as shown in Figure 1.1. However there are other methods of dividing the atmospheric regions based on other criteria, for example the variation of molecule composition or state of mixing with altitude, which yield different numbers of regions. The four regions based on temperature variations with altitude are: the troposphere, which has a temperature gradient -10 K/km at altitudes from the ground up to 10-12 km approximately; the stratosphere is the region where the temperature increases with altitude and is located above the troposphere and which terminates at the altitude of roughly 45-50 km; the mesosphere is located above the stratosphere where the temperature trend decreases with altitude and is considered the coldest part of the atmosphere; the thermosphere starts at about 85 km and is heated by solar ultra-violet radiation such that the temperature gradient remains positive. The heating from solar radiation causes gases of different density to separate and, because the pressure is low above 100 km, the ionised species do not recombine quickly. Thus the net concentration of ions and free electrons is greatest at altitudes above a few hundred kilometres. The presence of these

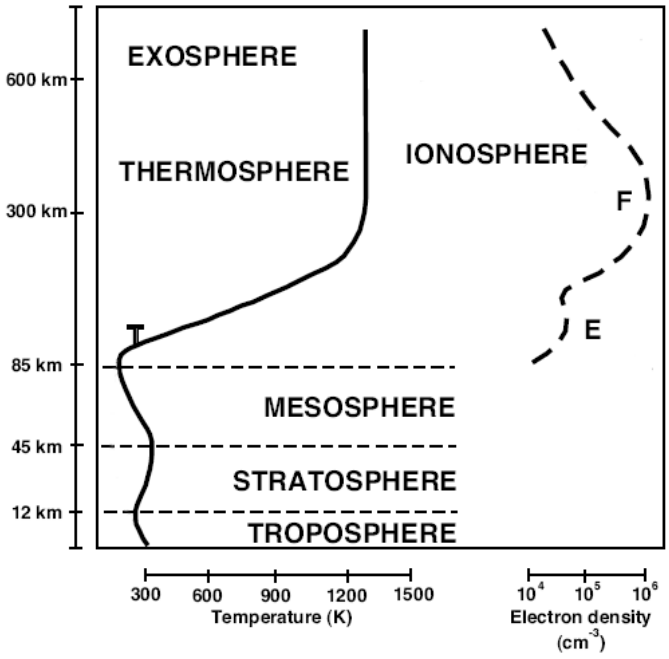

Figure 1.1: Atmospheric temperature profile with ionospheric density profile. Figure adapted from Hargreaves (1992).

electrons has an intense effect on the properties and behaviour of the medium. This part of the atmosphere, i.e the ionised part of the atmosphere, is known as the ionosphere and sits across the mesosphere and the thermosphere with the largest part of it in the thermospheric region. (*Hargreaves*, 1992)

The ionosphere is electrically conducting and can support strong electric currents. It also plays an important role in radio wave applications as it can affect radio propagation. This is especially important for the new generation of large radio astronomy arrays such as LOFAR (LOw Frequency ARray[1]). LOFAR is a new radio interferometric array that is currently under development in Europe. It consists of many antennas spread across several countries in Europe, but has a core of antennas in the Netherlands. The longest baseline of the array is about 1500 km. The array will operate at frequencies of 10-250 MHz. At these low frequencies, especially frequencies below 100 MHz, the ionosphere will have a strong effect on the radio signals, as will be demonstrated in Chapter 7. Also the ionosphere varies geographically and temporally, as will be discussed in detail in Section 2, and therefore the effect of the ionosphere on the radio signals across the array will differ and will need constant monitoring. LOFAR requires ionospheric calibration to 10^{-3} TECU, where

[1]http://www.lofar.org/

1 TECU = 10^{16} electrons per square meter, (*Gaussiran II et al.*, 2004). For an accuracy level this high, the calibration process will be sensitive to ionospheric wave structures as these can cause total electron content (TEC) perturbations as high as approximately 1 TECU, (*Tsugawa et al.*, 2007).

The total electron content (TEC) is one of the universal measures of the ionosphere. TEC is the measurement of the line integral of electron density along a path from a transmitter T, to a receiver R, represented by:

$$TEC = \int_R^T N_e(\theta, \phi, l, t)\mathrm{d}l, \tag{1.1}$$

where N_e is the variable electron density along the signal path l and $\mathrm{d}l$ is the path element. Electron density also varies with latitude θ, longitude ϕ, and time t. TEC corresponds to the total number of free electrons in a column with sectional area 1 m^2, and is measured in units of TEC unit (TECU), where 1 TECU = 10^{16} electrons per square meter. TEC measurements can be obtained from navigational systems such as Global Positioning Systems (GPS), geostationary satellites, or ionosondes. Chapter 3 will include discussions on how TEC is obtained from Faraday rotation measuring instruments, i.e polarimeters onboard geostationary satellites, and from GPS instruments.

The ionosphere as a plasma can support and generate a variety of waves, interactions and instabilities, (*Hargreaves*, 1992). The subject covered in this thesis is on the wave structures of the ionosphere; mainly the travelling ionospheric disturbances, the diurnal double maxima and lunar tides.

Travelling ionospheric disturbances (TIDs) are gravity wave signatures in the ionosphere. These were first observed by *Hines* (1960). Although many studies of TIDs have been made since, there are still lots of uncertainties regarding their generation and propagation mechanisms and so TIDs are still under investigation.

The diurnal double maxima (DDM) phenomenon manifests as twin peaks in the diurnal trend of the electron density or TEC during the day. It was first observed by *Kohl et al.* (1968) as a bite-out event, i.e a sudden depletion of peak electron density or TEC followed by a recovery. A few authors have studied this phenomenon, for example *Kohl et al.*

(1968), *Saryo et al.* (1989) and *Pi et al.* (1993). There is uncertainty on the driving forces of these structures, and this project hopes to clarify some of the confusions.

The gravitational force of the moon has been observed to produce tidal variations in the ionosphere, see *Bernhardt et al.* (1976) and *Pedatella and Forbes* (2010). The signature of the lunar tide in the ionosphere has been of interest because the mechanism behind it is known, and therefore the lunar tide is ideal for comparing models with observations.

The presence of wave perturbations in the ionosphere changes its dynamics. Studies of waves are therefore important in order to improve the accuracy of ionospheric models and forecast problems that may be encountered by radio systems when such perturbations occur.

1.2 Thesis Objectives

The main aim of this thesis is to collect statistical information of the wave structures present in the ionosphere, for use in radio astronomy calibrations' and future communication systems planning. To gain this information, TEC calculated from instruments measuring Faraday rotation on signals from geostationary satellites were used. These measurements were collected in Italy over the period of 1975-1982 and 1989-1991 at one minute intervals. These measurements are used in this project as they cover more than one solar cycle and will therefore allow for different solar activity comparison. The fast temporal sampling makes it possible to resolve small structures.

The main objective of this project is to quantify the changes in TEC from as many sources as possible in order to estimate the errors that might be experienced by new radio instruments. This main objective is then tackled by the following:

- find a suitable method of extracting TEC variations due to TIDs,
- study the diurnal double maxima (DDM) structures seen in TEC measurements and establish whether there is a single mechanism responsible for the DDM structures,
- extract information on ionospheric lunar tides,
- produce statistical information TEC, TIDs, DDMs, and tides e.g. time of occurrence,

amplitude and periods.

- investigate how modern radio instruments could be used in quantifying the effects of the ionosphere on the next generation of radio instruments.

1.3 Thesis Overview

A brief description of the ionosphere is given at the start of Chapter 2, which includes an overview of the morphology of the ionosphere. Features such as TIDs, DDM and tides are discussed. As ionospheric wave structures will be studied across different geomagnetic conditions, classification of storms and substorms are discussed in the final section of Chapter 2.

Chapter 3 will present the instruments and parameters used to observe and characterise the behaviour of the ionosphere. A definition of total electron content is given as this is the principal measure of the ionospheric waves used in this project. Starting from the Appleton equation, a derivation of TEC measurements from Faraday rotation measurements is given. Polarimeter systems onboard several geostationary satellites and details on the geostationary satellites are given. TEC measurements from GPS are used in tomographic imaging. Also, measurements of the maximum sounding frequency and the maximum height of the F2 layer from an ionosonde are used in the verification of the DDM structures. Therefore a brief overview of these systems is given. Finally Chapter 3 comes to an end with a brief description of magnetometers and the geomagnetic parameters that are derived from their observations. Kp, AE and X are parameters that are obtained from magnetometers and used in this project to categorise ionospheric events that occur during quiet and disturbed geomagnetic conditions.

Chapter 4 presents different methods for analysing different wave structures observed in TEC measurements. Case studies are given for each analysis method in order to evaluate the difference in the information obtained from each method. Section 4.1 presents a method of extracting tidal information from TEC measurements. The solar tide filter is basically a running mean of 29 days of TEC measurements. The design of the lunar filter is based on a cosine function that takes into account the lunar phase angle. This filter was used to compare the amplitude of the lunar component to the larger solar component and establish the importance of the lunar component in the daily variability of the

ionosphere. In Section 4.2 three different yet complementary methods are investigated and used in the analysis of TIDs: Savitzky-Golay filtering, Fourier analysis and wavelet analysis. Savitzky-Golay filtering was used to filter out the diurnal trend and study the amplitudes of the TIDs. The detrended signal was used in a windowed Fourier analysis to obtain wave periods of TIDs that occur in the day. A discrete wavelet transform, the discrete Meyer wavelet, was used to give an energy decomposition of the data. This was achieved by using the analysis of variance (ANOVA) method to divide the day into morning, mid-day and evening, and then investigate energy decomposition of TIDs in different parts of the day. Section 4.3 presents a method used to calculate relative amplitudes, the duration of the DDM features observed in TEC measurements, as well the probability of observing the features during different seasons and geomagnetic conditions.

A statistical study comparing TIDs during solar minimum (1975-1976) and solar maximum (1989-1990) is made in Chapter 5. Also a seasonal comparison within each solar cycle phase is done. This study is achieved by extracting TID information such as amplitudes, periods and variations due to TIDs in different parts of the day, using methods described in Chapter 4. Section 5.1 presents the questions that will be answered with this study, and Section 5.2 presents results used to answer these questions. The chapter is concluded with a summary of the results and conclusions.

DDM structures are explored in Chapter 6. These structures were identified by visually inspecting the slant TEC profiles and noting time of occurrence and magnitude of each peak, and time and magnitude of the trough. Duration and relative magnitude of each peak were then derived from these noted observations. Statistics by season and geomagnetic condition were obtained for the DDM structures. Previous studies have suggested a connection between substorm events and DDM structures and this connection was investigated. This involved categorising DDM structures into bite-out and enhancement structures and investigating if a substorm occurred before a bite-out or before each enhancement. The chapter is concluded with a summary of the results and conclusions.

Chapter 7 presents a brief discussion on ionospheric tomography with emphasis on the imaging method MIDAS (Multi-Instrument Data Analysis System) in Section 7.3. A ray tracing method is also presented in Section 7.4. Electron density maps from MIDAS are used in the ray tracing procedure to study ionospheric effects on low frequency ray propagations at different elevations; results are presented in Section 7.5. In Section 7.6 a study

of TEC changes over short time scales (less than about an hour) observed over many years (about 11 years) are presented. The intention is that this study will act as a guide to the radio science community on expected TEC fluctuations during different seasons, geomagnetic condition and solar activity. A summary of the results and conclusions are presented at the end of this chapter.

In Chapter 8 a summary of all the results and conclusions drawn are given. A brief discussion of possible future work is also presented in this chapter.

Chapter 2

The Ionosphere

In this chapter a description of the physics and morphology of the ionosphere is presented. Also brief descriptions of tides, traveling ionospheric disturbances, and diurnal double maxima are given. Section 2.1 will include ionospheric features and variations of these with solar and magnetic activities. In Section 2.2 the description of the travelling ionospheric disturbances (TIDs) will be presented with a brief review of the work already done on the mechanisms driving these structures. Section 2.3 presents the theory of the two mechanisms that are thought to drive the diurnal double maxima. Section 2.4 describes the lunar tides with regard to the ionosphere. Section 2.5 presents a brief outline of geomagnetic activity.

2.1 Structure of the Ionosphere

The ionosphere is the ionised plasma in the atmosphere which is created by photo-ionisation of the neutral atmosphere by extreme ultra-violet (EUV) radiation and high energy solar particles. The ionisation process is mainly due to solar photons interacting with the atoms and molecules in the ionosphere, which results in the electrons being stripped away from the parent atoms and molecules, and creating a number of free negatively charged electrons and positively charged ions. The morphology of the ionosphere depends on altitude, time, geographic/geomagnetic location, season and solar activity.

The ionosphere lies between the altitudes of approximately 50 to at least 1,000 km. This thick layer is generally divided into four regions: D, E, F regions and topside ionosphere.

The different regions are characterised by the variation of dominant molecules with altitude, see Figure 2.1:

- D-region: lies about 50-90 km, and is produced by hard X-ray radiation. Ionisation in this region is associated with NO, and at high solar activity with N_2 and O_2 to produce positive ions NO^+, O_2^+, and N_2^+, by the reaction $A + h\nu \rightarrow A^+ + e$ where A represents NO, N_2 and O_2.
- E-region: spans from approximately 90 to 120 km. This region is formed by soft X-ray radiation. In this region ionisation of mainly O_2 and N_2 results in the formation of O_2^+ and NO^+. The production of O_2^+ is through $O_2 + h\nu \rightarrow O_2^+ + e$. The production of NO^+ is a two-step process: 1) $N_2 + h\nu \rightarrow N_2^+ + e$; 2) $N_2^+ + O \rightarrow N + NO^+$.
- F-region: this region is located above 120 km and is produced by EUV radiation. The principal ionoisation of atomic O results in the formation of O^+, by the process $O + h\nu \rightarrow O^+ + e$. During the day this regions splits into two layers known as F1 and F2 regions. The highest density peak occurs in the F region or during the split, in the F2 region.
- topside ionosphere: lies above the F (or F2 during day time) region and may extend to 1000 km. The electron density decreases sharply in this region to reach a minimum at higher altitudes. This region is dominated by O^+ and H^+. The H^+ is obtained from the process $H + O^+ \rightarrow H^+ + O$.

The ionosphere has distinct features at some latitudes. At low latitudes, the ionosphere has regions of high electron concentration at approximately 20° above and below the magnetic equator and a trough, i.e region of lower electron concentration, at the magnetic equator. This is a characteristic of the fountain effect in which electrons experience a strong upwards drift due to the Earth's magnetic field. This drift, known as the $\mathbf{E}\times\mathbf{B}$ vertical plasma drift, is responsible for the redistribution of the electrons to higher latitudes in the equatorial region. This equatorial region of strong horizontal electron density gradients is known as the equatorial or Appleton anomaly region and is observed during the evening and quiet magnetic conditions. At midlatitudes, the ionosphere is largely controlled by solar EUV radiation and the neutral winds, and the electron density gradient is not as steep as at low and high latitudes. At high latitudes, the ionosphere exhibits very complex behaviour because of its connection to the magnetosphere and the interplanetary medium, through the Earth's magnetic field.

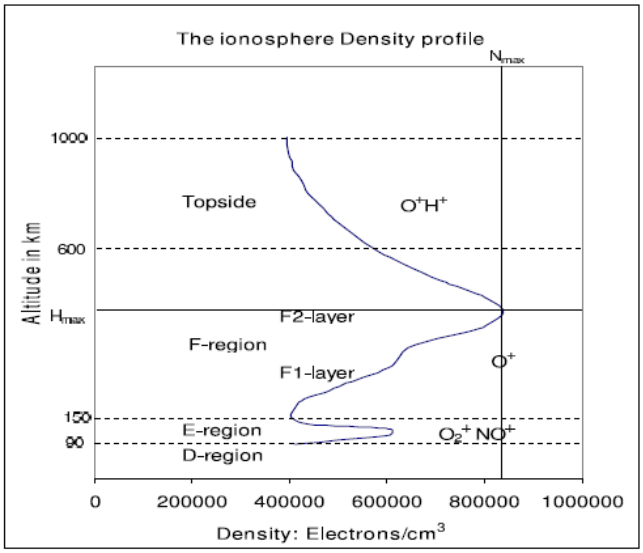

Figure 2.1: A typical ionospheric profile, with different regions and their dominant ions. Figure adapted from http://www.dcs.lancs.ac.uk/iono/ionosphere_intro/

The electron densities are generally greater during the day than at night time, as illustrated by Fig. 2.2. The D and F1 regions disappear at night, (*Hargreaves*, 1992). The E, and F2 regions persist at night. The E-region is much weaker and may sometimes disappear at night. The F2 region is always present but at night it has a lower electron concentration. The peak of the F2 region appears at high altitudes in the afternoon and evening and lowers to lower altitudes at night. The diurnal variation of the ionosphere is primarily due to the fact that as the Sun rises and moves across the sky, solar radiation produces ionised particles and the number of electron concentration increases. When the Sun sets recombination and other electron-loss processes are dominant, and thus the number of ionised particles decreases. Therefore to a rough approximation, the number of ionised electrons is greatest when the Sun is overhead, which is around noon. Another contributing factor to the diurnal variation in the polar regions is the $\mathbf{E}\times\mathbf{B}$ convection of ionisation from lower day lit latitudes towards the night-time. This is an important contribution for diurnal variation of the ionosphere during the long winter nights at high latitudes, (*Davies*, 1990).

The variation of the ionosphere with season is associated with revolution of the Earth around the Sun. The noon solar angle is higher in summer than winter. This should result in ionisation being greater in summer than in winter and is indeed observed to be the case for the D, E, and F1 region. However the F2 does not behave as expected. At

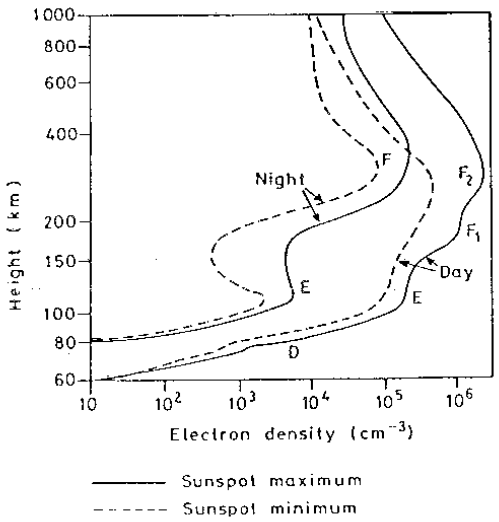

Figure 2.2: An example of daytime and night time ionospheric profiles. The dashed lines represent the same profiles but during different solar activities. Source Hargreaves (1991).

mid latitudes the noon F2 electron concentration peak is greater in winter than summer. This is known as the seasonal anomaly and is more pronounced in high mid latitudes than in low and high latitudes. The anomaly is caused by the seasonal changes in the relative concentrations of atomic and molecular species, (*McNamara*, 1991). More details are given in *Davies* (1990).

The solar activity variation is linked to the 11-year solar cycle. During the period of maximum sunspot number, which occurs when the solar cycle is at its peak, the ionisation is greater than at solar minimum because the solar radiation intensity is high thus enhancing the electron concentration in the ionosphere, as illustrated by Fig. 2.2. Geomagnetic storms are generally initiated by solar disturbances; solar flares and coronal mass ejections (CMEs). The solar disturbances are more frequent at solar maximum than solar minimum, (*Davies*, 1990). Highly energetic particles emitted from CMEs enter the ionosphere at high latitudes. During geomagnetic storms and substorms these particles produce auroras; which are the optical manifestation of solar particles interacting with atmospheric particles observed at high latitudes, (*Carlson and Egeland*, 1995). The night time E-region associated with auroras, known as the auroral E, has been observed to have high critical frequencies, almost as high at F region frequencies. At mid latitudes, the geomagnetic storms results in the critical frequency being reduced and the scale height increased in the F-region. The geomagnetic storms can have severe effects on satellites as

well as electronic instruments on Earth, such as power transformers. A further exploration of the subject is found in *Rishbeth and Garriott* (1969) and *Davies* (1990).

The ionosphere acts as a refractive medium to radio signals, and the index of refraction depends on the amount of ionisation. The ionosphere affects a wide range of frequencies, from extremely low frequencies (about 3 kHz) to super high frequencies (30 GHz), *Davies* (1990). In the 1920s, Appleton and others developed a mathematical theory of radio propagation in the ionosphere in the presence of the Earth's magnetic field; this will be discussed in greater detail in Chapter 3 of this thesis. The following paragraph briefly describes radio wave propagation in the ionosphere.

The D layer is responsible for high frequency radio wave absorption, while the E and F regions are responsible for the reflection of high frequency radio waves. The absorption is explained in *McNamara* (1991) as follows: when a radio wave traverse the ionosphere an electron absorbs the energy from this wave and it vibrates or oscillates at a frequency equal to that of the radio wave. The energy of the radio wave is thus transformed into kinetic energy or energy of motion. The oscillating electron re-radiates this energy in the form of radio waves so the energy of the radio wave is passed forward from one electron to the next. If, however, an oscillating electron collides with a heavy neutral atom, the energy is transferred to the atom. The atom does not vibrate at the radio wave frequency, because it is not a charged particle but uses its increased energy to increase it speed. The energy of the radio waves is therefore absorbed by the neutral atom. The absorption is strongest in the D region because at those heights there is a high abundance of the neutral atom. The F region can reflect vertical radio waves with frequencies less than about 10 MHz. This frequency is known as the critical frequency, and is obtained from the plasma frequency and electron density N_e relation, given by:

$$f_c = \sqrt{80.5 N_e} \tag{2.1}$$

The typical maximum electron density in the F region is around $12{\times}10^{11}$ electrons per cubic meter, which gives a critical frequency of approximately 10 MHz.

2.2 Travelling Ionospheric Disturbances (TIDs)

The atmosphere has a natural buoyancy, so that a 'parcel of air' displaced from its mean position will oscillate about that position at a rate known as the Brunt-Väisälä angular frequency, ω_b. For a wave with an angular frequency $\omega > \omega_b$, pressure is the primary restoring force and the wave is acoustic; for a wave with angular frequency $\omega < \omega_b$, gravity is the primary restoring force, (*Evans*, 1978). Traveling ionospheric disturbances (TIDs) are quasi-periodic perturbations observed at ionospheric altitudes but caused by the passage of gravity waves in the lower atmospheric regions. The first full description of gravity waves at atmospheric heights was presented by*Hines* (1960).

The following description is taken from *Evans* (1978). The waves transport energy away from the source that generate them and distribute this energy throughout the atmosphere. The energy distribution is an important property of the gravity waves. For an ideal atmosphere which is isothermal and dissipationless, a plane acoustic-gravity wave propagating at an angle θ with respect to the vertical will have its wave energy propagated in a direction given by:

$$\tan\theta_g = \left(1 - \frac{\omega_b^2}{\omega^2}\right)\tan\theta \tag{2.2}$$

where θ_g is the angle between the direction of the energy propagation and the vertical. For $\omega \gg \omega_b$, $\theta_g = \theta$ and the energy propagates in the same direction as the wave. As ω becomes smaller than ω_b, $\tan\theta_g$ differs in sign from $\tan\theta$ and energy propagates in the opposite direction to the direction of the wave propagation. Thus for any frequency the direction of propagation of the energy given off by the waves can be obtained from Equation (2.2) and a dispersion relation. Of course for the real atmosphere there will be dissipation of energy as the wave travels further from its source. At neutral atmospheric heights, the waves are dampened by processes such as viscous damping, thermal conductivity and background winds. At ionospheric heights, the energy of the wave is dissipitated by the frictional force imposed by the presence of ions which cannot be easily driven across magnetic field lines. This effect, known as the ion-drag effect, is more pronounced during day time when the ionisation is high.

Different mechanisms cause gravity wave perturbations in the atmosphere and result in TIDs, for example geomagnetic storms (see *Titheridge and Buonsanto* (1988), *Afraimovich*

et al. (2001), and *Afraimovich et al.* (2006)), solar eclipses (see *Chimonas and Hines* (1971), *Liu et al.* (1998), and *Sauli et al.* (2007)), and passing of the solar terminator (see *Cot and Teitelbaum* (1980), *Somsikov* (1987), *Somsikov* (1995), *Somsikov and Gangulay* (1995), *Galushko et al.* (1998), *Boska et al.* (2003) and *Afraimovich et al.* (2009)). In general, TIDs are associated with sudden local changes resulting in abrupt energy and momentum transfer to the plasma.

It is common to classify TIDs into large scale and medium scale structures as these generally have different sources and propagation properties. Large scale TIDs have horizontal wavelengths of more than a thousand kilometers, periods longer than an hour, and horizontal phase velocities between 400 and 1000 m/s. They can travel for many thousands of kilometers without much attenuation and largely originate from the polar region, moving equatorward. Large scale TIDs are thought to be caused by geomagnetic storms at high latitudes, through heating during energetic particle precipitation or heating by auroral electrojets, or motion of electrojets or motions of the auroral arc, (*Hargreaves*, 1992). Auroral heating can change global wind patterns in the thermosphere; large equatorward winds are established on the night side which can generate large amplitude gravity waves, (*Davies*, 1990). Medium scale TIDs have horizontal wavelengths of several hundred kilometers, periods between 15 minutes and an hour, and horizontal velocities between 100 and 250 m/s. The sources of the medium scale TIDs are largely uncertain as they have been observed from severe weather patterns, shears in the jet stream, seismic events and tsunamis, and wind updrafts over mountains, (*Lee et al.*, 2008).

2.3 Diurnal Double Maxima (DDM)

It has been noticed by *Rastogi and Sanatani* (1968), *Huang and Jeng* (1978) and others that the diurnal trend of the ionosphere tends to have two peaks around noon. This trend has been observed in the peak height of the F2 region (hmF2), the peak frequency of the F2 region (foF2), and the total electron content (TEC). Initially observations showed this to be a brief depletion period of ionisation during the peak followed by a recovery, thus the phenomenon was called a bite-out. However recent observation has shown that in addition to the bite-out, the double peak also occurs where there is an additional plasma enhancement prior to or after the midday peak. In order to incorporate the different types of the double peak structures, *Pi et al.* (1993) referred to them as diurnal double maxima (DDM). This term is adopted in this thesis. Figure 2.3 presents examples of the DDM

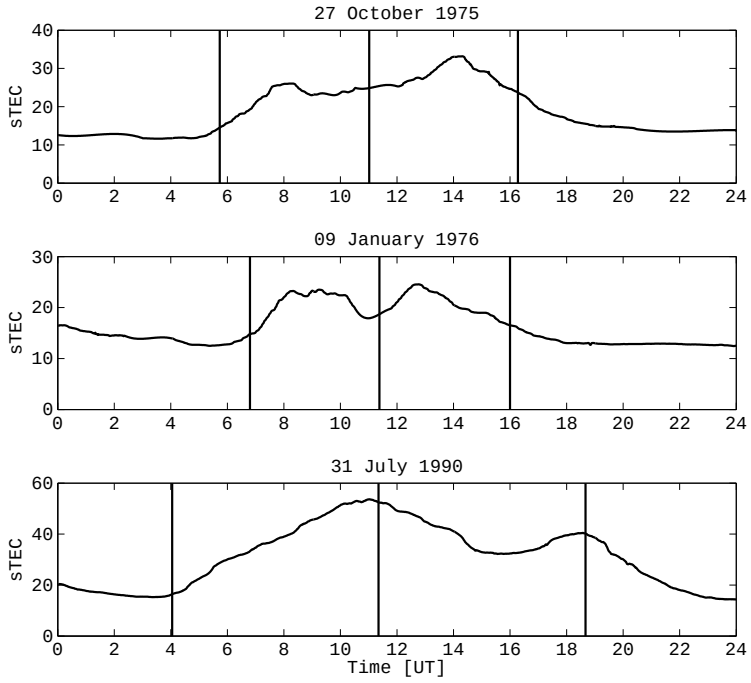

Figure 2.3: Examples of slant TEC (measured in TECU) profiles with diurnal double maxima. These illustrate that there are at least three categories: pre-noon enhancement, noon depletion and post-noon enhancement. The vertical lines mark local sunrise, noon, and sunset times in UT.

structures observed in TEC measurements. The DDM structures are observed during both magnetically quiet and disturbed days, although *Pi et al.* (1993), and *Huang and Jeng* (1978) found them to be more common during disturbed days. *Rastogi and Sanatani* (1968) observed the bite-out structures to be more prominent during solstitial months and during solar minimum than during solar maximum.

The DDM structures have been observed in the low and middle latitudes. The equatorial bite-out is thought to be linked to the $\mathbf{E}\times\mathbf{B}$ drift, see *Huang and Jeng* (1978). In the equatorial region the electric field is quite strong, and the ionospheric plasma drift responds to the orientation of the electric field relative to the magnetic field. The plasma drift velocity in this region is given by:

$$\mathbf{v} = \frac{\mathbf{E}\times\mathbf{B}}{|\mathbf{B}|^2}. \tag{2.3}$$

It is obvious that the plasma is lifted or pushed down when the electric field is perpendic-

ular to the magnetic field. When the plasma is pushed down, there is loss of free electrons resulting in the depletion of ionisation and a bite-out is observed.

In the mid-latutudes the bite-out events can be linked to neutral winds, *Kohl et al.* (1968). The neutral winds are mainly driven by pressure gradients due to daily temperature variations. The meridional winds generally attempt to drag the ionosphere along the magnetic field such that if the wind is blowing poleward, then the resultant motion of the vertical ionospheric drift velocity will be downwards. This means that the plasma will be pushed down to regions of higher recombination rates which results in the depletion of free electrons. Conversely if the wind is blowing towards the equator then there will be an upward plasma vertical drift which results in the enhancement of ionisation. There are arguments for and against these two mechanisms (see *Saryo et al.* (1989), *Pi et al.* (1993) and *Pi et al.* (1995)), which suggest that the cause of the midday bite-out or enhancements is not fully understood.

2.4 Tides

The following description is obtained from *Chapman and Lindzen* (1970) and *Hagan et al.* (2003). Tidal waves in the atmosphere are produced by the gravitational forces of the Sun and Moon and by solar heating. The tides by gravitational forces are a result of the balancing effort of the Earth's centrifugal force and the total gravitational attraction of the Sun/Moon. At the Earth's hemisphere nearer to the Sun/Moon the gravitational force is greater than the centrifugal force such that there is a distribution of unbalanced forces directed towards the Sun/Moon acting against the Earth's own gravitation force. At the opposite hemisphere, the Sun's/Moon's gravitation is less and the centrifugal force is greater so that there is also a distribution of unbalanced force obliquely upward there. The particles in the atmosphere therefore move under the action of these unbalanced forces. The thermal tide is generated by absorption of solar radiation. The absorption is periodic in time, because of the rotation of the Earth, and this gives rise to tidal oscillations.

The solar tides have many modes that are excited and have periods relating to the solar day (24 hours). The most observed modes are the diurnal, semidiurnal and terduirnal oscillations. The lunar modes excited have periods related to the lunar day (24.8 hours), and the second mode is the dominant mode in the contribution to the ionospheric effect

generated by the lunar tide. The lunar tides is modulated by the solar tide and since the lunar modes are very close to the solar modes, it is very difficult to separate them from the solar harmonics, (*Evans et al.*, 1983).

The following description is obtained from *Chapman and Lindzen* (1970). The solar and lunar daily variations are usually donoted by S and L respectively, and are the combination of all their harmonics such that $S = \sum_n S_n$ and $L = \sum_n L_n$ where,

$$S_n = s_n \sin(nt + \sigma_n) = A_n \cos nt + B_n \sin nt \tag{2.4}$$

$$L_n = l_n \sin(n\tau + \lambda_n) = a_n \cos n\tau + b_n \sin n\tau \tag{2.5}$$

$$A_n = s_n \sin\sigma_n,\ B_n = s_n \cos\sigma_n,\ a_n = l_n \sin\lambda_n,\ b_n = l_n \cos\lambda_n$$

where A_n, and B_n are the solar harmonic coefficients, a_n, and b_n are the lunar harmonic coefficients, s_n and l_n are the amplitudes of the solar and lunar harmonic respectively, n is an integer representing the solar or lunar tide modes, t and τ are the mean solar and lunar times respectively, and σ_n and λ_n are the solar and lunar phase angles respectively. The mean times are expressed as angular measures, where the angles are measured eastward from vernal equinox meridian to the meridian of the observer. Note that the units for S and L depend on the type of measurements used, for the case of TEC the units are TECU.

2.5 Geomagnetic Storms and Substorms

A storm or substorm is a disturbance lasting from a day to several days, in the case of the storm, or from minutes to several hours in the case of the substorm. The storm or substorm is a severe departure from normal behaviour of the magnetosphere and the ionosphere, and results in enhanced electric and magnetic fields, energetic particle precipitation, and intense increase or decrease of the electron density and electron content.

A principal defining property of a magnetic storm is the creation of an enhanced ring current, formed by ions and electrons in the 10-300 keV energy range, located usually between 2 and 7 Earth radii and producing a magnetic field disturbance, (*Gonzalez et al.*, 1994). The storm is initiated by an influx of highly energetic solar particles carried by a strong so-

lar wind that interacts with the Earth's magnetic field and filters down to the ionosphere. A geomagnetic storm has three distinct phases: the initial phase, the main phase and the recovery phase. The initial phase is characterised by an increase in the magnetic field, which is caused by the compression of the magnetosphere when the increased solar wind arrives, and lasts for a few hours. The main phase is characterised by a sustained southward interplanetary field and can last several hours. The main phase is followed by a slow return to normal conditions that is the recovery phase which can last over a few days. In *Mendillo* (2006) there is a comprehensive review of past TEC studies on storm phenomena.

A substorm is an event or series of events where energy from solar wind-magnetosphere interaction is suddenly dissipated in the auroral ionosphere and magnetosphere. The event is initiated on the night side of the Earth and can last for a short period of time, e.g an hour. A common substorm index is the auroral electrojet (AE) index calculated from AE = AU − AL. The AU index (known as the upper envelope) is proportional to the eastward electrojet while the AL index (known as the lower envelope) is proportional to the westward electrojet (*McPherron*, 1997).

A substorm event has 3 phases.

- The growth phase is a phase in which the energy extracted from the solar wind is primarily stored in the magnetotail while smaller amounts are dissipated in the ring current and ionosphere, in the form of ring current enhancement, Joule heating, and auroral particle precipitation. This phase is indicated by an increase in the strength of the auroral electrojets (*McPherron*, 1997).
- The expansion phase is a phase of explosive energy release followed by an increase in the flux of energetic particles deposited into the ionosphere. During this phase the auroral electrojets build up.
- The recovery phase is a phase where the disturbed region returns towards its pre-disturbed configuration.

Ionospheric processes are more intense and abrupt during a storm and/or a substorm. To investigate if the characteristics of the wave structures of interest change significantly under storm/substorm conditions, the analysis of the waves will be studied under both quiet and disturbed storm conditions. A link between the occurrence of DDM structures and substorms will also be tested.

2.6 Summary

In this chapter a brief morphology of the ionosphere was described, where the vertical structure of the ionosphere was seen to be characterised by geographic or geomagnetic location, time, season and solar activity. A brief overview of storms and substorms was also given. Three different wave structures that have been observed in the ionosphere, i.e traveling ionospheric disturbances (TIDs), diurnal double maxima (DDM) and tides, were described in this chapter as well. Understanding the different mechanisms and conditions that drive the ionosphere and its waves is important as it will allow accurate quantification of the error introduced by the ionosphere to radio signals that traverse it. The following chapter will discuss the different instruments used to measure the ionosphere and the parameters obtained from them.

Chapter 3

Instrumentation and Measurements

In this chapter the instruments and parameters used to observe and characterise the behaviour of the ionosphere are presented. Section 3.1 gives a brief description of geostationary satellites. How TEC measurements are obtained from Faraday rotation observations onboard geostationary satellites is outlined in Section 3.1.1. Section 3.2 presents a brief overview of the Global Positioning System (GPS) and Section 3.2.1 describes how TEC measurements are obtained from this system. The ionosonde is used as an instrument for independent verification of the DDM structures (see Section 2.3), and therefore it is described in Section 3.3. The geomagnetic activity plays an important role in the occurrence of most of the waves presented in Chapter 2, as the ionosphere behaves differently in low and high geomagnetic activity. The Kp and AE indices are used as indicators of geomagnetic and auroral activities and are presented in Sections 3.4.1 and 3.4.2 respectively. These indices are measured using ground based magnetometers which are described in Section 3.4.

3.1 Geostationary Satellites

A geostationary satellite orbits the earth at the same speed as the Earth's rotation speed, so effectively it is at a stationary position above a certain point on Earth. The orbital height of the satellites is about 36 000 km above ground. Geostationary satellites sometimes carry a radio beacon for ionospheric studies. A polarimeter is used to measure the angle of rotation caused by the ionosphere when a radio signal traverses through it.

Four geostationary satellites were used in this study in the period of 1975-1982 and 1989-1991: ATS-6, SIRIO 1, OTS-2 and METEOSAT-5. These satellites operated in the VHF (30-300 MHz) and UHF (300-3000 MHz) frequency bands. ATS (Application Technology Satellite) was a United States' NASA (National Aeronautics and Space Administration) program that consisted of six satellites with scientific experiments in addition to a variety of other technology. ATS-6, the last satellite in the ATS program, was launched on 30 May 1974 and operated until August 1979. TEC measurements available for this project from ATS-6 were collected from October 1975 - September 1976 and during this period ATS-6 was located at 35° E. SIRIO (Satellite Italiano Ricerca Industriale Orientata) was a joint project between NASA and the Italian's CNR-ISC (National Research Council - Italian Space Commission) for communications and space physics research. The mission consisted of two satellites launched in 1977 and 1982. SIRIO 1 was launched on 25 August 1977 and was located at 15° W. Measurements from this satellites were taken from September 1977 until September 1982 after which the satellite stopped operating. OTS (Orbital Test Satellite) is a series of ESA (European Space Agency) communication satellites that consist of 20 satellites launched between 1977 and 2001. OTS-2 was the second satellite in the series launched on 11 May 1978. Data available for this project from OTS-2 was collected between 1989 and January 1991 after which the satellite ceased to be operational. During this period the satellite was at location 5° E. The METEOSAT first generation program is a series of seven meteorological satellites that were launched between 1977 and 1997, and were operated by ESA. MEOSAT-5, the fifth satellite of the series, was launched in 1991 and stopped operations in April 2007. Data from this satellite was collected during February 1991 - December 1991 for this project, during which the satellite was located at 10° W. Onboard these satellites the polarimeter system was used for Faraday rotation measurements. The Faraday rotation measurements are then converted to slant TEC measurements as described in the following section.

3.1.1 Slant TEC Measurements from Faraday Rotation

When a linearly polarised wave enters the ionosphere it splits into two characteristic waves, ordinary and extra-ordinary, and each has its own polarisation. The two wave modes have different phase velocities so that their phase difference changes as they travel. At any point along their path the resultant signal is found by adding the fields of the two waves, but because of the phase difference the resulting polarisation is not the original linear

polarisation. The derivation of slant TEC from Faraday rotation presented in this section is obtained from *Budden* (1988).

The propagation of radio waves in the ionosphere, in the Earth's magnetic field, is described by the Appleton-Lassen equation. This equation describes the refractive index μ as:

$$\mu^2 = 1 - \frac{X(1-X)}{1 - X - \frac{1}{2}Y^2\sin^2\theta \pm [\frac{1}{4}Y^4\sin^4\theta + (1-X)^2Y^2\cos^2\theta]^{\frac{1}{2}}} \tag{3.1}$$

where

$$\omega_p^2 = \frac{N_e e^2}{m_e \varepsilon_0} \tag{3.2}$$

$$X = \frac{\omega_p^2}{\omega^2} = \frac{N_e e^2}{\varepsilon_0 m_e f^2} \tag{3.3}$$

$$Y = \frac{\omega_{ce}}{\omega} = \frac{Be}{2\pi m_e f}, \tag{3.4}$$

and θ is the angle between the direction of propagation of the radio waves and the Earth's magnetic field, B is the geomagnetic field strength, N_e is the electron density, e is the electron charge, ε_0 is the permittivity of free space, m is the mass of the electron, and f is the frequency of the wave. The plus sign refers to the ordinary wave and the minus sign refers to the extra-ordinary wave.

For VHF waves, the frequencies are much larger than plasma frequency (f_p) and the gyrofrequency (f_{ce}), i.e. $X \ll 1$, $Y \ll 1$. This means that:

$$\frac{1}{4}Y^4\sin^4\theta \ll (1-X)^2Y^2\cos^2\theta. \tag{3.5}$$

Therefore a quasi-longitudinal approximation can be used and the equation is reduced to:

$$\mu^2 \;=\; 1 - \frac{X(1-X)}{1 - X \pm [(1-X)^2Y^2\cos^2\theta]^{\frac{1}{2}}} \tag{3.6}$$

$$= 1 - \frac{X(1-X)}{1-X \pm (1-X)Y\cos\theta} \tag{3.7}$$

$$= 1 - \frac{X}{1 \pm Y\cos\theta} \tag{3.8}$$

Taking the square root of Equation (3.8), solving by Taylor expansion and ignoring the higher powers:

$$\mu_+ = 1 - \frac{1}{2}\frac{X}{1+Y\cos\theta} \quad \text{and} \quad \mu_- = 1 - \frac{1}{2}\frac{X}{1-Y\cos\theta}\,. \tag{3.9}$$

For the linearly polarised wave travelling in an magnetic field, the plane of polarisation makes an angle:

$$\partial\Omega = \frac{1}{2}k(\mu_+ - \mu_-)\partial s \tag{3.10}$$

$$= \frac{1}{2}k\left[1 - \frac{1}{2}\frac{X}{(1+Y\cos\theta)} - 1 + \frac{1}{2}\frac{X}{(1-Y\cos\theta)}\right]\partial s \tag{3.11}$$

$$= \frac{1}{2}k\left[\frac{X}{2}\frac{-(1-Y\cos\theta)+(1+Y\cos\theta)}{(1+Y\cos\theta)(1-Y\cos\theta)}\right]\partial s \tag{3.12}$$

$$= \frac{1}{2}k\left[\frac{X}{2}\frac{2Y\cos\theta}{1-Y^2\cos^2\theta}\right]\partial s \tag{3.13}$$

Then using $Y \ll 1$,

$$\partial\Omega = \frac{1}{2}kXY\cos\theta\partial s. \tag{3.14}$$

Then integrating to obtain the total phase change of the waves along path s:

$$\Omega = \frac{1}{2}k\int XY\cos\theta\partial s \tag{3.15}$$

.

Substituting in k, where $k = 2\pi f/c$, X and Y:

$$\Omega = \frac{e^3}{\varepsilon_0 cm^2 f^2}\int N_e B\cos\theta \mathrm{d}s \tag{3.16}$$

Equation (3.16) presents the relationship between slant TEC (sTEC) and total Faraday

rotation. Although geostationary satellites carrying Faraday rotation measuring instruments orbit at approximately 36000 km, sTEC can be derived quite accurately by only considering altitudes up to 2000 km. This is because the geomagnetic field is very weak at altitudes above 2000 km, so electrons at these altitudes and higher contribute very little to Faraday rotation. Conversely, electrons above 2000 km are not detected by the Faraday rotation technique and therefore sTEC derived from Faraday rotation measurements is a line integration of electron content up to about 2000 km. It is useful to note that only the first order term and the geomagnetic field term are taken into account in the derivation of Equation3.9 which is normal for most applications, see for example *Davies* (1990) and *Budden* (1988). However, for LOFAR frequencies (between approximately 10 and 250 MHz), the higher order terms are will not be negligible, especially for the milli-TECU (10^{-3} TECU) accuracy that LOFAR will require. Further details on this are discussed in Chapter 7.

The sTEC data were collected from Italy: Mortelliccio (42.95° N, 10.68° E) during 1975-1982, and Florence (43.48° N, 11.13° E) during 1989-1991, using 40 and 136 MHz frequencies. The mean ionospheric points, assuming an ionospheric height of 400 km, are: 1975-1976 (39.1° N, 14.1° E), 1977-1982 (39.0° N, 7.2° E), 1989-1991(January) (39.8° N, 10.5° E) and the rest of 1991 (40.2° N, 8.5° E). The sTEC profiles were recorded at one minute intervals. Methods to eliminate the phase ambiguity were based on the correlation of different frequencies, when available (e.g. ATS-6), or on the comparison with nearby ionosonde foF2 data (in Gibilmanna, Sicily, Italy) for all the other data when only one frequency was transmitted. Relative error of sTEC measurements was determined to be approximately 0.01 TECU. *Checcacci et al.* (1976), *Checcacci et al.* (1978), and *Ciraolo and Spalla* (1988) provide more details on the experiments and error analysis. In Appendix C, some examples of the TEC profiles obtained from these experiments are presented.

3.2 Global Positioning System

The Global Positioning System (GPS) was developed by the United States Department of Defence for instantaneous determination of position and velocity based on the time travel of the GPS signal. This system forms part of the Global Navigation Satellite System (GNSS) and is open for use to the general public. It has proven to be very useful in navigation, scientific studies and land surveying.

The space segment of GPS consists of a constellation of at least 24 operational satellites orbiting the earth at an altitude of about 20 200 km above ground. Six groups of four satellites occupy six evenly spaced circular orbital planes centered on the Earth. The orbits are inclined at 55° to the equatorial plane and separated by 60° right ascension of the ascending node. The orbital speed of the satellites is about 14 000 km/hour resulting in an orbital period of approximately 12 hours. This orbital arrangement ensures that at least four satellites are always visible from any point on Earth.

The GPS satellites broadcast radio signals continuously on two separate L-band frequencies, known as L1 and L2 respectively. The L1 and L2 have frequencies of 1575.42 MHz and 1227.60 MHz respectively. There is a new L-band frequency, L5, which broadcasts at 1176.45 MHz and is only available on the newer satellites. The L band frequencies are derived from a fundamental frequency of 10.23 MHz. In addition to the L band frequencies the system transmits a precision code (P-code). The P code is modulated on both the L1 and L2 frequencies and is used in the calculations of TEC, as will be discussed in Section 3.2.1.

The L1/L2 frequencies are received by GPS receivers located either on Earth or onboard a low Earth orbit (LEO) satellite. There are two types of receivers: a single frequency receiver and a dual frequency receiver. The single frequency receivers can only receive the L1 signal and therefore are not able to eliminate the error induced by the ionosphere in the signal. The dual frequency receivers receive both the L1 and L2 signals simultaneously and can mostly eliminate the effects of the ionosphere on the signal. The dual frequency receivers are therefore more accurate in their measurements than the single frequency receivers.

3.2.1 Slant TEC from Global Positioning System

In *Mannucci et al.* (1999) it is shown that TEC is calculated from GPS measurements by a linear combination of the carrier phase of the signal and the pseudo-range measurements:

$$L1 = \rho + \Delta\rho_{ph,1} + \lambda_1 n_1 + \varepsilon_1^r + \varepsilon_1^s \tag{3.17}$$

$$L2 = \rho + \Delta\rho_{ph,2} + \lambda_2 n_2 + \varepsilon_2^r + \varepsilon_2^s \tag{3.18}$$

$$P1 = \rho + \Delta\rho_{gr,1} + \tau_1^r + \tau_1^s \tag{3.19}$$

$$P2 = \rho + \Delta\rho_{gr,2} + \tau_2^r + \tau_2^s \tag{3.20}$$

where $L1$, $L2$, $P1$ and $P2$ are extracted from the C/A-code and P-code respectively, ρ is the non-dispersive delay term which combines together the geometric distance, tropospheric delay, clock errors and non-dispersive delays associated with hardware error; $\Delta\rho_{ph,1}$ and $\Delta\rho_{ph,2}$ are the range errors induced by the effects of the ionosphere on the phase velocities of the L1 and L2 frequencies respectively and are given by Equation (3.29) below; $\Delta\rho_{gr,1}$ and $\Delta\rho_{gr,2}$ are the range errors induced by the effects of the ionosphere on the group velocities of the L1 and L2 frequencies respectively and are given by Equation (3.30) below; $\lambda_1 n_1$ and $\lambda_2 n_2$ are the unknown integer cycle ambiguities associated with the carrier phase terms; and ε and τ terms are the dispersive delay terms associated with the receiver (denoted by r) and satellite (denoted by s) hardware errors.

The range errors are calculated from the refractive index as follows: starting with Equation (3.1) in Section 3.1.1, but assuming the magnetic field is negligible, i.e $Y = 0$, the refractive index is reduced to:

$$\mu^2 = 1 - \frac{X(1-X)}{1-X} = 1 - X. \tag{3.21}$$

Solving Equation (3.21) by expansion and ignoring the higher order powers as their contributions are generally much smaller than the first order term at UHF or higher frequencies in the terrestrial ionosphere, for example see *Strangeways et al.* (2007). Substituting for all the variables, the phase refractive index is obtained as:

$$\mu_{ph} = 1 - \frac{1}{2}X = 1 - \frac{40.3N_e}{f^2}. \tag{3.22}$$

Since the ionosphere is a dispersive medium, the group and phase velocities are different. For a group of waves, the refractive index is given by:

$$\mu_{gr} = \mu_{ph} + f\frac{\mathrm{d}\mu_{ph}}{\mathrm{d}f} \tag{3.23}$$

where:

$$\frac{\mathrm{d}\mu_{ph}}{\mathrm{d}f} = \frac{80.6N_e}{f^3}. \tag{3.24}$$

Therefore the group refractive index is:

$$\mu_{gr} = 1 - \frac{40.3N_e}{f^2} + f\frac{80.6N_e}{f^3} = 1 + \frac{40.3N_e}{f^2}. \tag{3.25}$$

The geometric range R from a receiver $\boldsymbol{r}$ to a satellite $\boldsymbol{s}$ along the line of sight, adopted from Fermat's principle, as presented in *Hofmann-Wellenhof et al.* (2001), is given by:

$$R = \int_r^s 1\mathrm{d}l, \tag{3.26}$$

and the pseudo-range ρ is given by:

$$\rho = \int_r^s \mu\mathrm{d}\rho. \tag{3.27}$$

The path length difference is:

$$\Delta\rho = \rho - R = \int_r^s \mu\mathrm{d}\rho - \int_r^s 1\mathrm{d}l = \int_r^s (\mu - 1)\mathrm{d}l \tag{3.28}$$

The last equality is valid because the integral is along the geometric path and thus $\mathrm{d}\rho$ can be changed to $\mathrm{d}l$. Substituting the phase refractive index given in Equation (3.22) into Equation (3.28), the phase delay is:

$$\Delta\rho_{ph} = -\int_r^s \frac{40.3N_e}{f^2}\mathrm{d}l = -\frac{40.3}{f^2}\int_r^s N_e\mathrm{d}l = -\frac{40.3}{f^2}TEC_{ph}. \tag{3.29}$$

It is important to note that the additional path due to refraction, results in larger TEC, and therefore an increase in the phase advance, more discussion in *Belcher and Strangeways* (2009). Similarly substituting for the group refractive index presented in Equation (3.25) into Equation (3.28) and simplifying, the group delay is given by:

$$\Delta\rho_{gr} = \frac{40.3}{f^2}TEC_{gr}. \tag{3.30}$$

The phase based TEC is calculated from the difference between the two observed carrier

phase measurements:

$$L = L1 - L2 = (\Delta\rho_{ph,1} - \Delta\rho_{ph,2}) + (\lambda_1 n_1 - \lambda_2 n_2) + b_r + b_s, \tag{3.31}$$

where b_r and b_s are the receiver and satellite hardware error between the L1 and L2 frequencies.

Similarly, the code based TEC is obtained from:

$$P = P2 - P1 = (\Delta\rho_{gr,2} - \Delta\rho_{gr,1}) + b'_r + b'_s, \tag{3.32}$$

where b'_r and b'_s are the receiver and satellite hardware error between P1 and P2.

The phase and group delays obtained in Equations (3.29) and (3.30) are substituted into Equations (3.31) and (3.32) respectively, to relate TEC with the carrier phase observables and also to relate TEC with pseudorange measurements as follows:

$$L = 40.3\left[\frac{1}{f_2^2} - \frac{1}{f_1^2}\right] TEC_{ph} + (\lambda_1 n_1 - \lambda_2 n_2) + b_r + b_s \tag{3.33}$$

$$P = 40.3\left[\frac{1}{f_2^2} - \frac{1}{f_1^2}\right] TEC_{gr} + b'_r + b'_s. \tag{3.34}$$

Using P measurements determines absolute TEC measurements with large random errors. However with the use of L measurements, precise relative TEC measurements with unknown integer ambiguity are obtained.

3.3 Ionosonde

An ionosonde is a vertical sounding high frequency radar, operating at the frequency range of 0.1 MHz - 30 MHz. The device operates by sending short pulses of radio energy into the atmosphere at set time intervals and measures the time delay required for a reflection of the signal by the ionosphere at each frequency. This procedure enables the determination of the height and the electron density of each ionisation layer. The time delay recorded by

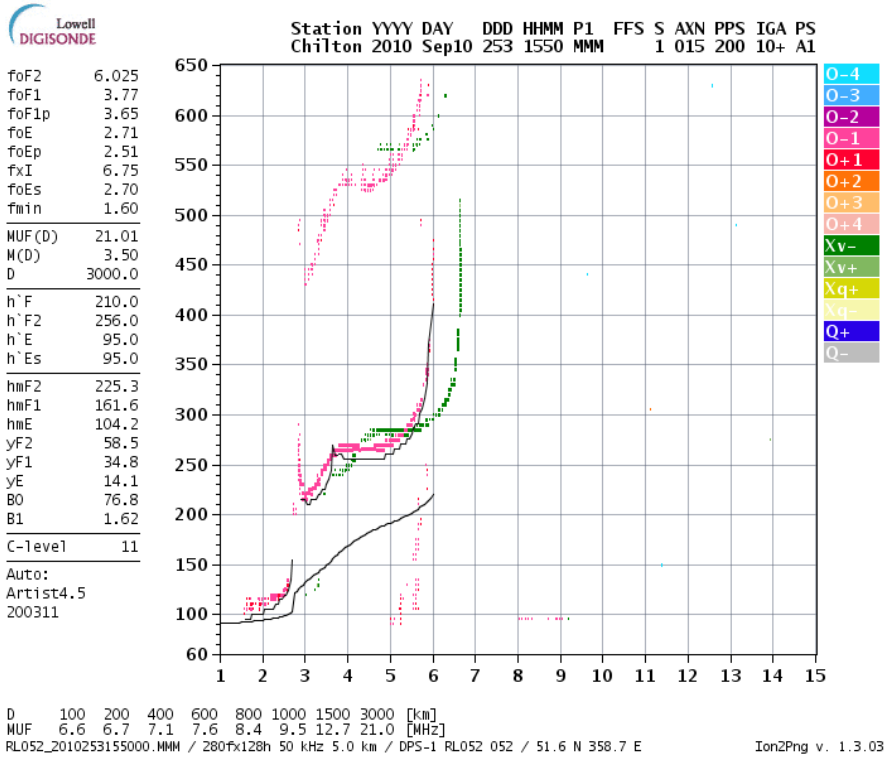

Figure 3.1: A typical daytime ionogram. Source http://www.wdc.rl.ac.uk/

the ionosonde is converted to height by assuming the signal travels at the speed of light according to:

$$h' = \frac{c\tau}{2} \tag{3.35}$$

where c is the speed of light, τ is the time delay and h' is virtual height of reflection. Equation (3.35) records virtual height because the signal does not really travel at the speed of light but at group velocity which is less than the speed of light; therefore the virtual height is always greater than the true height of reflection. The real height can be obtained by performing some scaling procedure. A figure of virtual height versus frequency is called an ionogram. An example given in Figure 3.1.

At low frequencies the signal propagates upwards with gradually decreasing speed until it reaches the level where the group velocity is zero, where it is reflected. A radio wave of higher frequency will penetrate to higher levels in the ionosphere until a level is reached where the plasma frequency is sufficient for reflection to occur. Eventually a frequency is reached where the signal can traverse the ionosphere without being reflected back, which

occurs when the ray is still not reflected to the horizontal at the F region electron density maximum. The ionosonde therefore measures the bottomside ionosphere, i.e. measures up to the maximum height of the F2 layer which corresponds to the maximum height at which the signal is reflected back to Earth. The sounding frequency can be converted to plasma frequency which in turn is converted to electron density by using Equation (3.2), which is then rewritten as:

$$N_e = 1.24 \times 10^{10} f^2 \tag{3.36}$$

where sounding frequency f is measured in units of MHz and N_e is in electrons per cubic meter.

A variety of ionospheric parameters are derived from ionosonde measurements, such as $foF2$, the maximum sounding frequency of the F2 region, and $MUF(3000)F2$, the maximum usable frequency reflected in the F2 region for a ground distance of 3000 km. $hmF2$ is the maximum reflection heights of the F2 region and can be calculated using Equations 1(a) from *Rishbeth et al.* (2000):

$$hmF2 = \frac{1490}{M(3000)F2} - 176, \tag{3.37}$$

where $M(3000)F2 = MUF(3000)F2/foF2$, and $hmF2$ is measured in kilometers (km) and the frequencies are measured in MHz. $foF2$ and $hmF2$ obtained from an ionosonde in Rome (41.8° N,12.5° E), will be used to verify the DDM structures (see Section 2.3). More details about the ionosonde and its measurements are provided in *Romano et al.* (2008).

3.4 Magnetometer

Geomagnetic storm and substorm indices are obtained from geomagnetic stations located all over the globe. A magnetometer measures Earth's magnetic field strength and fluctuations. There are mainly three kinds of magnetometer: fluxgate, liquid (proton) and vapor. These magnetometers measure the magnitude and direction of the magnetic field by using different field mechanisms. The parameters measured by the magnetometers and which describe the magnetic field are:

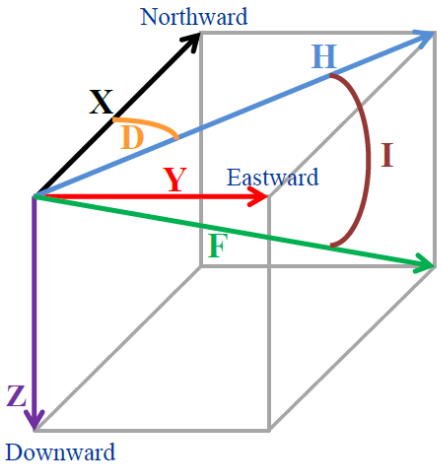

Figure 3.2: Schematic of the Earth's magnetic field components. Figure adapted from http://wdc.kugi.kyoto-u.ac.jp/element/eleexp.html

- declination (D) which is the angle between magnetic North and true North, measured in degrees; this is positive when the measured angle is East of true North and negative otherwise,
- inclination (I) which is the angle between the horizontal plane and the total field vector, measured in degrees,
- total magnetic field intensity (F), measured in nT,
- vertical component (Z) which is obtained from $Z = F \sin I$, and measured in nT,
- horizontal component (H) calculated from $H = F \cos I$, and measured in nT,
- North-South component (X) of the horizontal component (H) which is derived according to $X = H \cos D$, and measured in nT, and
- East-West component (Y) of the horizontal component (H) which is calculated from $Y = H \sin D$, and measured in nT.

Figure 3.2 shows a schematic of the field components while Figure 3.3 shows an example of the magnetogram.

(a) XYZF components

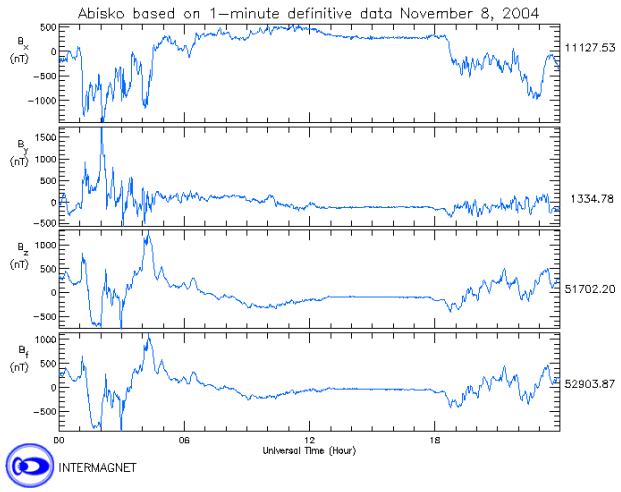

(b) HDZF components

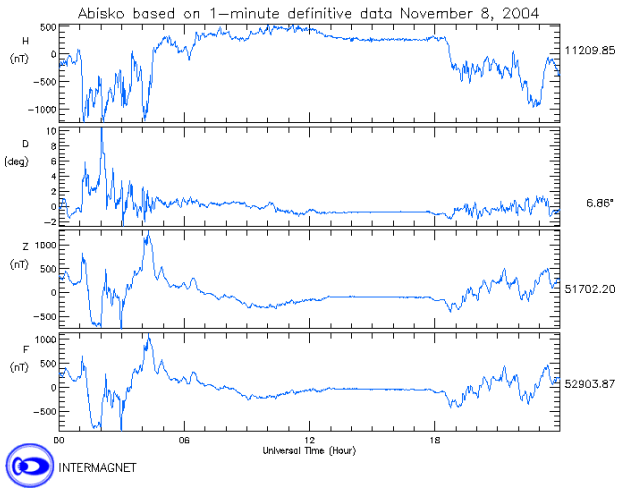

Figure 3.3: Examples of magnetograms. Source http://www.intermagnet.org

3.4.1 Kp Index

The Kp index indicates the level of disturbance of the magnetic field caused by a geomagnetic storm. The indices are measured in a 3-hour window by a network of magnetic observatories around the world. The Kp index varies between 0 and 9, 9 being the most disturbed geomagnetic condition. The Kp index is usually used to measure the strength of a geomagnetic storm and can be scaled as follows:

- 0-3: quiet magnetic condition,
- 3-6: moderate magnetic storm,
- 6-9: disturbed magnetic condition.

In this project the Kp index is used as an indicator of the strength of a geomagnetic storm, where $Kp < 3$ indicates a quiet geomagnetic conditions, $3 \leq Kp < 6$ indicates a moderate storm and $Kp \geq 6$ indicates a severe storm.

3.4.2 AE Index

Substorms are generally monitored by the auroral electrojet index AE which is defined by $AE = AU - AL$, where AU and AL are eastward and westward electrojet indices respectively, and are measured in nT. The AU and AL indices are calculated from the upper and lower envelopes of the H component respectively. The auroral electrojet indices are produced every minute by a chain of magnetic observatories in the auroral zone.

The AE index is customarily used to determine onset (when AE increases) and recovery phases (when AE decreases) of substorm activities, but does not define the magnitude of a substorm event. In fact *Rostoker et al.* (1980) express caution against using the AE index alone to identify substorm activity or the magnitude of the substorm event. Therefore in this project the AE index and the geomagnetic X component will both be used to identify substorm events.

3.5 Summary

GPS, geostationary satellites and ionosondes are not only useful for navigation and HF communications but they are also useful for studying the ionosphere. The ionospheric parameters that are obtained from such instruments, such as TEC, $foF2$ and $hmF2$ among others, can be used in the characterisation of the ionosphere. Magnetic indices like Kp and AE are used to indicate geomagnetic activity since the ionosphere is linked to the Earth's magnetic field.

Chapter 4

Analysis Techniques

The objective of this project is to study different wave structures that can be observed in the slant TEC measurements obtained from beacon satellites, as described in the previous chapter. The slant TEC, henceforth called TEC, was measured every minute from midnight to midnight and time is measured in UT (Universal Time). This chapter presents the different methods of analysis that were implemented to extract tidal, TID and DDM information. Section 4.1 presents an optimised finite duration impulse response filter that is used to decompose the data into tidal components and high frequency components that are not related to tides. This filter is useful in the study of tides because the solar and lunar frequency components are known and therefore making it is easier to define the narrow stop and pass bands for accepting harmonic components of the tides in the data. This filtering method is tested on a case study to investigate its suitability for use with our data. The high frequency components are used to extract TID information like periodicity, amplitudes and contribution to diurnal TEC variability. Section 4.2 presents background information on all the methods that will be used to study TIDs. These methods are the Savitzky-Golay filter, discrete Fourier analysis and discrete wavelet analysis. Each method is evaluated using a case study to determine its suitability in the study of TIDs. Section 4.3 describes the method that was used to identify the DDM structures in TEC measurements. This section includes methods used to calculate the magnitude of the peaks, time of occurrence, duration of the structure, and the probability of observing the structure during different geomagnetic conditions and seasons.

4.1 Tides Analysis

The lunar tides modulate effects produced by the solar tide. Since the lunar modes are very close to the solar modes, it is very difficult to separate them from the solar harmonics, (*Evans*, 1978). The solar and lunar tide filters described below are taken from a paper by *Bernhardt et al.* (1976). The *Bernhardt et al.* (1976) filtering method is chosen for this case because it has been shown to work for a data set similar to the one being used in this case, and is expected to be relatively easy to implement.

4.1.1 Tides Analysis Method

The solar tides filter was designed as follows: for every minute of a day, the mean of N days TEC was calculated. The resulting average diurnal variation of the TEC was taken as the solar tide contribution to the measured TEC, i.e TEC_{sol}. This mean diurnal TEC variation was then subtracted from every measurement for the N days. The mathematical representation of this filter is given by:

$$TEC_{sol}(t) = \frac{1}{N} \sum_{i=k-m}^{k+m} TEC_i(t) \tag{4.1}$$

where k is the day index such that k runs from 1 to N, $m = \frac{N-1}{2}$, and TEC_i is the original slant TEC measurements. This solar component was then subtracted from original measurements to give solar free measurements TEC_{sol_free}:

$$TEC_{sol\_free}(t) = TEC(t) - TEC_{sol}(t). \tag{4.2}$$

The lunar semi-diurnal tide component M_2 influences electron content variations. The tidal component has frequency (f_{M_2}) of 1.93227 cycles per day. This lunar tidal component is very close to the solar semi-diurnal frequency components, which is 2 cycles per day, and is much weaker than the neighbouring solar semi-diurnal sideband. The lower sideband of these components denoted L_1 has a frequency of $f_{M_2} - 1 = 0.93227$ cycles per day and the upper sideband, denoted L_3 has a frequency of $f_{M_2} + 1 = 2.93227$ cycles per day. The solar filter removes most of the solar harmonics but the sidebands remain. The lunar filter therefore must also filter out these sidebands. The lunar tide filter was designed as follows. First construct the weights of the lunar tide contribution from:

$$a_m = 2\cos(2\pi\Delta f m T), \tag{4.3}$$

where $T = 1$ day, $\Delta f = 2 - f_{M_2} = 0.0677262$ cycles per day, $m = [m_l; m_u] = \left[-\frac{N-1}{2}; \frac{N-1}{2}\right]$. The inclusion of the cosine function in the weights eliminates the necessity of additional filtering of the solar side bands. These weights were then applied to the remaining TEC measuremets, i.e the TEC measurements without the solar influence which is given by the TEC_{sol_free} measurements, summed and averaged to obtain the lunar-solar variations in the TEC measurements, as shown by the following equation:

$$TEC_{lun}(t) = \frac{1}{N}\sum_{i=m_l}^{m_u} a_m TEC_{sol\_free,i}(t), \tag{4.4}$$

where i is the day index, and $TEC_{sol\_free,i}(t)$ is the ith TEC diurnal variation without the solar component.

The lunar TEC diurnal variation was then removed from the TEC without the solar component (i.e TEC_{sol_free} measurements), and the residual diurnal TEC variation remains as shown by the following equation:

$$TEC_{res}(t) = TEC_{sol\_free}(t) - TEC_{lun}(t). \tag{4.5}$$

The residual diurnal TEC variation will then be examined for TIDs and other wave structures.

4.1.2 Assessment of the Tides Filter

The filter is basically a delay filter; it needs at least 29 central days and 59 days on either side to work, i.e 147 continuous days in total. This specification should smooth out the day to day variability in the data and reveal basic tidal components. This filtering method was first tested using data sets of length 156, taken from 02 July to 04 December 1991. This data block had the least data gaps in between and the longest continuous data. Where there were data gaps in the data, these were filled as follows:

- for a missing TEC data point in a day, the missing TEC value was filled in by the TEC value at the same time on the previous day,

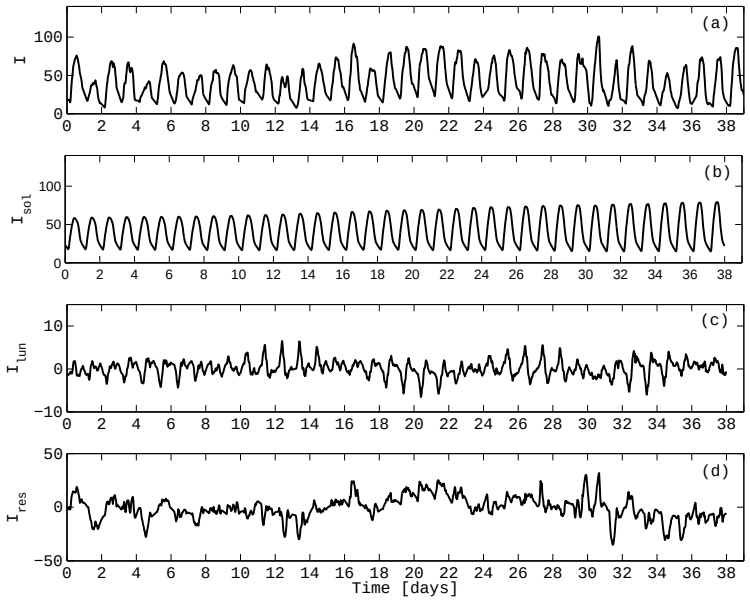

Figure 4.1: (a) Temporal TEC variation, (b) temporal TEC variation of the solar component, (c) temporal TEC variation of the lunar component and (d) temporal residual TEC variation of the high frequency component from 31 August to 06 October 1991. The unit for the vertical axis is TECU.

- for a day or two data gap, the gap was filled by a copy of the previous day's TEC values,
- for 3-4 consecutive missing days, the first 2 days were filled in by the previous day TEC values and the last 1-2 missing days were filled in by the following days' TEC measurements.

The data sampling was originally 1 minute but for this filter test a median TEC value every 30 minutes was taken, such that the sample rate for this filtered data was 30 minutes. Figure 4.1 below shows the TEC variation of the solar, lunar and residue components obtained during 31 August - 06 October 1991. Figure 4.1 (a) shows that the TEC signal varied between 7 and 101 TECU, (b) the solar component varied between approximately 15 and 79 TECU, (c) the lunar component varied between -7 and 7 TECU and (d) residual TEC varied between -35 and 32 TECU. It is interesting to note that the magnitude of the lunar component is much smaller than the magnitude of the high frequency components, i.e residual TEC variation.

To further investigate the frequencies and amplitudes of each component, fast Fourier transforms (FFT) of the unfiltered data, i.e 31 August - 6 October 1991 data presented in Figure 4.1(a) results in Figure 4.2(a). Figure 4.2(b) and 4.2(c) are obtained from the FFT of Figure 4.1(b) and 4.1(c) respectively. In short, Figure 4.2 presents the amplitude spectrum of the different components, where the amplitudes are calculated from the magnitude of the Fourier coefficients. Figure 4.2(a) shows the strongest component is centered at a period of roughly 1.001 cycles per day. This period corresponds roughly to 24 hours and therefore represents the diurnal modes of the solar tide. The semi-diurnal mode (period of 12 hours, frequency of 2 cycles per day in Figure 4.2(a)) is hardly above noise level. Figure 4.2(b) presents the dominant modes of the solar tide at 1.001 cycles per day. The observed periods of the solar tides from Figure 4.2(b) show that the dominant tidal mode in the original data, see Figure 4.2(a), are the solar tides. The lunar signature is not clearly identifiable from the spectra of the original TEC data, represented by Figure 4.2(a). Figure 4.2(c) is the frequency spectrum of the lunar component recovered from the use of the lunar filter. This amplitude spectrum show that the dominant modes of the lunar tides are 0.922 and 1.923 cycles per day. These frequencies are close to the L1 and M_2 frequencies. It is worth noting that the strongest mode of the lunar tide is found to be the L1 mode. This is interesting because in literature it is reported that M2 is the most dominant mode, see for example *Rishbeth and Garriott* (1969), and *Bernhardt et al.* (1976). It is worth noting that the amplitudes of L1 and M2 are below noise level, as illustrated by Figure 4.2(d). Also, the amplitude of the solar diurnal mode is slightly greater than the amplitude of the wave component with the same frequency from the original data. This means that the filter introduces extra energy to the solar component. Tidal modes at higher frequencies (i.e periods of 2 cycles per day or higher) are hard to isolate as they are not more significant than the noise. Because of the design of the filter it is not certain that the tidal modes extracted from the data are real or coincidental noise that had the same frequency.

Due to the uncertainties of the previous test, another was performed on slightly less data, a data set length of 147 days, but it is the only other continuous data block available. This data block covers the timeline of 04 October 1989 to 27 February 1990. Figure 4.3 below shows the TEC variation of the solar, lunar and residue components obtained during 02 - 30 November 1989. From Figure 4.3(a) it is found that the TEC signal varies between 3 and 100 TECU, Figure 4.3(b) shows that the solar component varies between approximately 9 and 84 TECU, from Figure 4.3(c) it is found that the lunar component varies between -7 and 9 TECU and in Figure 4.3(d) the residual TEC varies between -22

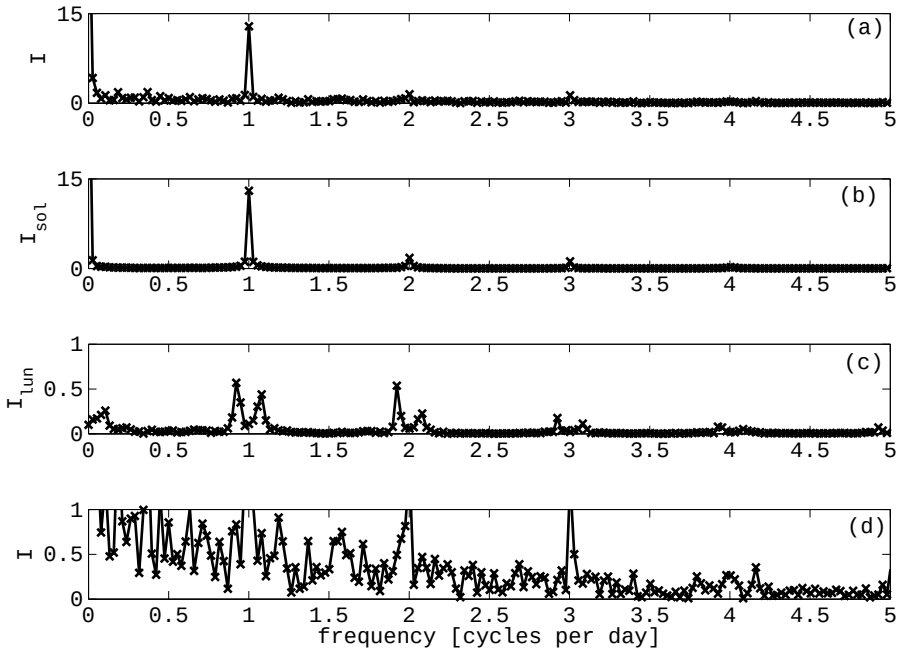

Figure 4.2: Amplitude spectrum of (a) original TEC measurements, (b) the solar component, (c) the lunar component and (d) original TEC measurement with same axis as the lunar component, from 31 August to 6 October 1991. The unit for the vertical axis is TECU.

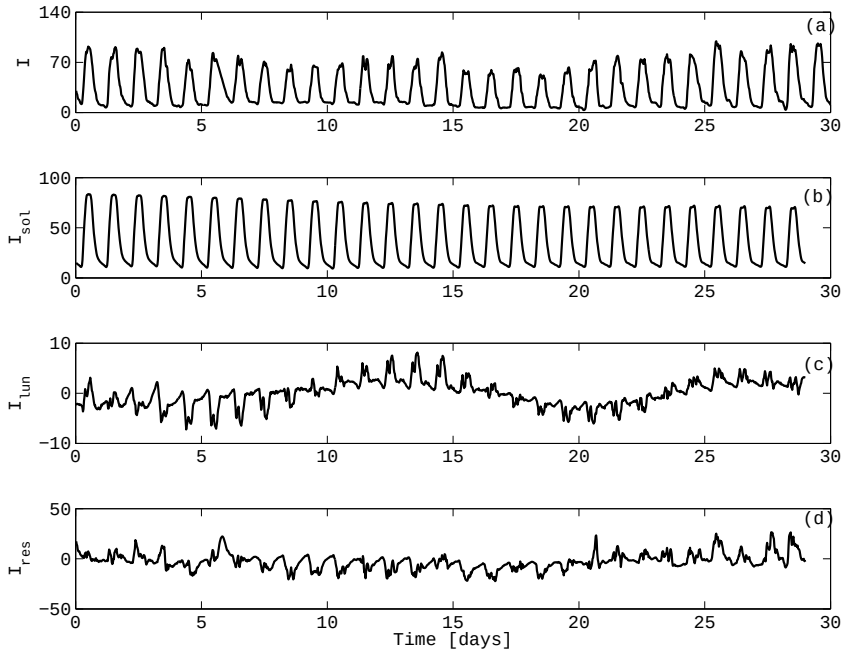

Figure 4.3: (a) Temporal TEC variation, (b) temporal TEC variation of the solar component, (c) temporal TEC variation of the lunar component and (d) temporal residual TEC variation of the high frequency component from 02 to 30 November 1989. The unit for the vertical axis is TECU.

and 27 TECU. A closer look at Figure 4.3 reveals a sinusoidal trend in the I_{lun} magnitude which has a period of roughly 18 days. This trend is not as pronounced in Figure 4.1. This indicates either another contribution to the ionospheric variation that is not filtered by either the solar or the lunar filter, or the filtering method introduces an artificial component. The 18-day wave could be a signature of a planetary wave, but further analysis is needed to confirm this.

Again an FFT was performed on the original TEC signal as well as the tidal components. The spectra of the original data, solar and lunar components are shown in Figure 4.4(a), 4.4(b) and 4.4(c) respectively. The spectrum of the original signal again does not reveal the lunar components, as can be seen from comparison of Figure 4.4(c) with Figure 4.4(d). However the diurnal mode, measured to be 1.001 cycles per day in both Figure 4.4(a) and (b), of the solar tide is clearly seen and the semi-diurnal mode, measured to be 2.003 cycles per day in both Figures 4.4 (a) and (b), is much smaller but still above noise level. Even though the L1 and M2 modes of the lunar tide are identifiable from Fig 4.4(c), they are

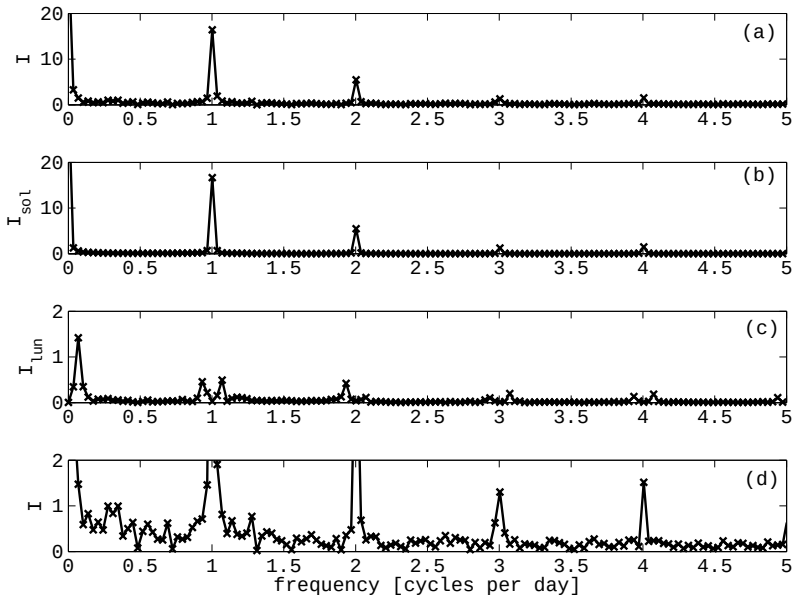

Figure 4.4: Amplitude spectrum of (a) original TEC measurements, (b) the solar component, (c) the lunar component and (d) original TEC measurement with same axis as the lunar component from 02 - 30 November 1989. The unit for the vertical axis is TECU.

unreliable because their amplitudes fall below noise level as is seen from Figure 4.4(d).

Even though the filter has been able to extract the tidal components from the data, it is difficult to verify the authenticity of the results of the lunar tide as the amplitudes of its' components were found to be below noise level and were not identifiable from the original data. This is probably because of the limitation of the data set, i.e data series had a lot of data gaps which had to be filled artificially and thus might have compromised the data, which resulted in not enough resolution to separate the lunar components from the solar component in the original TEC signal. Therefore the auntheticity of the tidal components is uncertain. Also, the semi-diurnal lunar tide component has been observed by many authors to be the strongest mode of the lunar tide and this is not the case in this study. It is therefore concluded that the filter presented here is not adequate for our data or that the M2 signal is not strong enough to detect.

(a) 21 February 1981

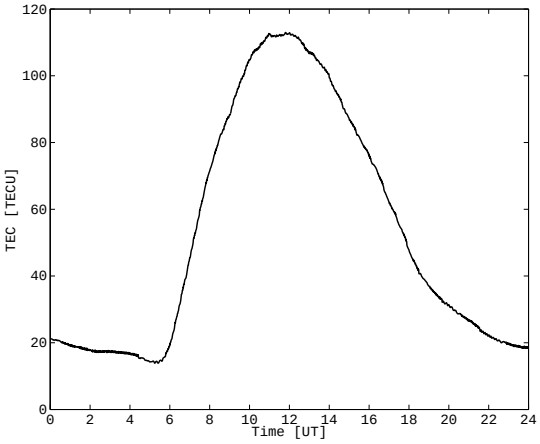

(b) 09 December 1990

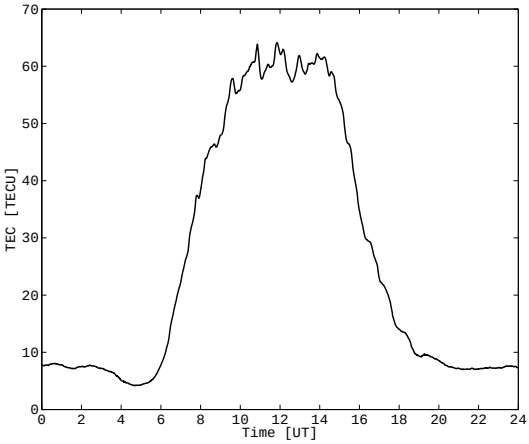

Figure 4.5: The TEC profile presented in (a) is fairly smooth and therefore represents an unperturbed day, while the TEC profile shown in (b) represents a perturbed day as there are wave structures present in the profile.

4.2 TID Analysis Methods

The main aim is to find another method that will allow an effective removal of low frequency components so that TID related information can be obtained. This is especially difficult since the TIDs are a relatively small component of the signal. However they will be much easier to identify in a spectrum because their frequencies are much higher than the solar component. Inspection of the raw time series data is a direct method of obtaining amplitude and period information of the wave structures present in the data, and is suitable when the structures vary in a simple manner within the data. However a more quantitative traditional method of extracting frequency and amplitude information of TIDs is Fourier analysis. Wavelet analysis is a complementary method which also gives temporal information on the signal. The next sections contain discussions on the use of all three methods and their respective limitations. In order to do this, a case study is done for two TEC profiles, see Figure 4.5, one fairly quiet profile and the other profile exhibiting TIDs. The smooth profile in Figure 4.5(a) is essentially due to the variation in the Sun's incident radiation as the Earth rotates. The small-scale variability in the second profile in Fig. 4.5(b) is the effect of sudden, irregular agents such as TIDs.

In order to extract information on medium and large scale TIDs, for example their statistical variation with seasons or solar activity, quantitative measurements of variation,

period and amplitude are required. Hence the following steps were performed:

- filter the discrete TEC time series using the Savitzky-Golay filter to obtain TID amplitude information, discussed in Section 4.2.1,
- use the filtered TEC data in Fourier analysis to obtain an energy density spectrum and statistical analysis of TID periods, discussed in Section 4.2.3,
- take the discrete TEC time series data, subtract its mean (this process will allow for the computation of variance as expressed in Equation (4.8) presented in Section 4.2.2) and use discrete wavelet analysis to obtain scalogram and variation information, explained in Section 4.2.2 and Section 4.2.4.

4.2.1 Savitzky-Golay Filter

The aim here is to subtract a low-pass filtered version of the signal from the TEC data in order to calculate amplitudes of the TIDs. The ideal solution would be to filter these waves by first learning how to recognise the TID signature in the signal and deciding on a suitable method to filter out the waves. For instance, if a TID was a pure time invariant sinusoidal wave it would be fairly trivial to remove it using a notch filter. However, filtering the waves present in the ionosphere is very difficult due to the non-stationarity in the TEC data, and to the unpredictability of medium scale waves (see *Reiger et al.* (2006)).

In order to calculate amplitudes of the TIDs, a filter was implemented to remove the slow varying waves and keep high frequency waves. A general moving average filtering function is:

$$g(t) = \sum_{n=-n_L}^{n_R} a_n f(t+n) \tag{4.6}$$

where n_L is the number of points prior to the data point t, n_R is the number of points following the data point t, and a_n are the filter coefficients. For non-linear varying functions the Savitzky-Golay filtering method seems a good choice because the a_n are given by a high order polynomial function. This means that for each point of the function, a polynomial is fitted by a least-squares criterion to all $(n_L + n_R + 1)$ points in the moving window, and the function g at t is set to the value of the polynomial at t. Filtering the function f using the Savitzky-Golay method results in a function f_D:

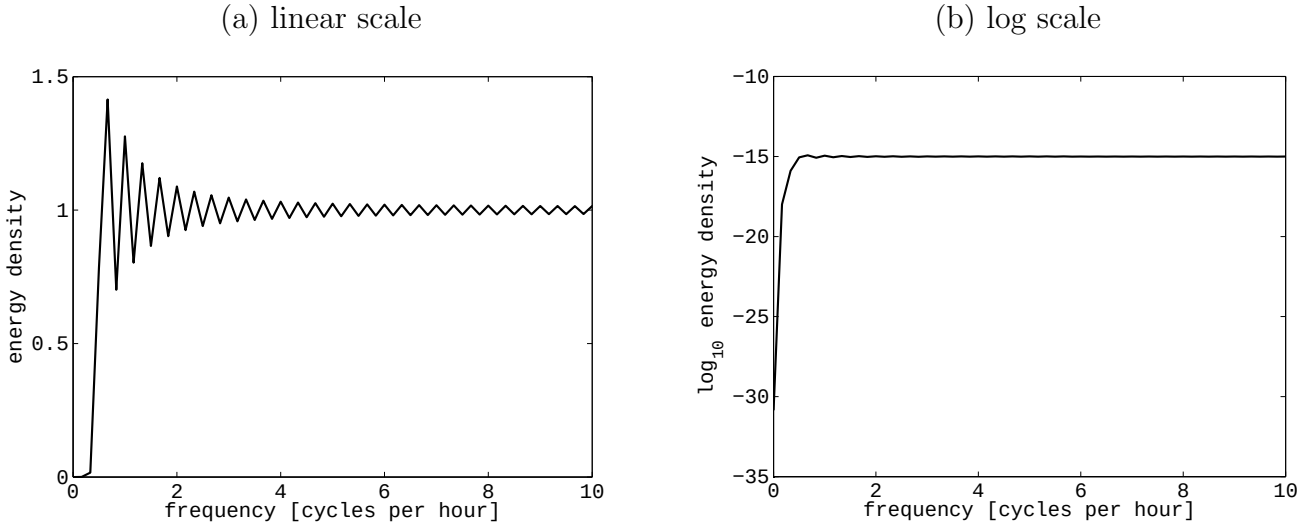

Figure 4.6: Energy density spectrum, in linear (a) and log (b) scales, of the Savitzky-Golay filter.

$$f_D(t) = f(t) - g_{SG}(t) \tag{4.7}$$

where the function $g_{SG}(t)$ is a special case of the function $g(t)$ but with a_n given by the Savitzky-Golay coefficients. The Savitzky-Golay filter is discussed in more detail by *Press et al.* (1992). The Savitzky-Golay was chosen because it is adaptive and comparatively gives good performance. This filter has also been used for similar purposes in time series data by many authors such as *Jonsson and Eklundh* (2004) and *Zhao and Reynolds* (2009).

To recover the high frequency structures present in the data, it is important to choose an appropriate order of the polynomial and length of the moving window. In this report, a_n was given by a sixth order polynomial, where $n_L = n_R = 180$. These were optimised empirically. However, it is important to recognise that in practice filtering will distort the high pass signal. For example, figure 4.6 presents the energy density spectrum of the filter, which reveals that the filter modifies the remaining high frequency structures especially those frequencies of interest to us; the filter amplifies some frequencies and attenuates others. This is not ideal as the objective of this study is to investigate the high frequency structures (frequencies between about 0.33-4 cycles per hour); such structures should remain relatively undistorted. However this disadvantage is tolerated because it is well understood, convenient and performs reasonably well.

(a) 21 February 1981 (b) 09 December 1990

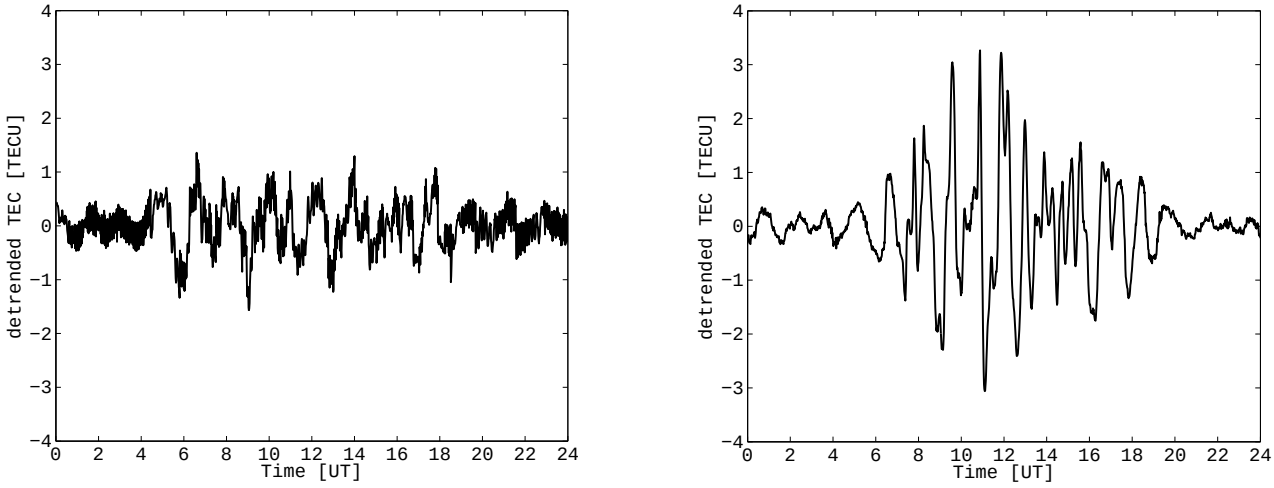

Figure 4.7: TEC profile presented in (a) is noisy but represents an unperturbed profile, while the TEC profile shown in (b) represents a perturbed day.

Figure 4.7 shows the filtered profiles from implementing the Savitzky-Golay filter on the profiles shown in Figure 4.6. It should be noted that the diurnal trend has been successfully removed but the noise has also been amplified, as especially seen in Figure 4.7(a) where there is high frequency jitter between time 0-4 and 18-24 UT hours at around the 0.5 TECU level.

4.2.2 Analysis of Variance

In order to quantify how the TID variation changes throughout the day using time series data, a measure of variability in terms of variance is going to be used. Hence a method to decompose the time series data in terms of variance, commonly called ANOVA (analysis of variance) (see *Percival and Walden* (2000) for details), is needed. One example of ANOVA is the energy density spectrum from Fourier analysis. However there are alternative energy decompositions, as explained below. Ideally the method used should avoid significant distortion of the data and also accommodate non-stationarity in the signal.

The following paragraph presents how ANOVA can be used for time series data. Let S_1, S_2, S_3,..., S_N represent a time series of N real valued variables. Total variation in the time series is defined as $N\sigma_S^2$ where:

$$\sigma_S^2 = \frac{1}{N}\sum_{i=1}^{N}(S_i - \mu_S)^2, \tag{4.8}$$

$$\mu_S = \frac{1}{N}\sum_{i=1}^{N} S_i. \tag{4.9}$$

For simplicity, each element in the time series can be regarded as a component in an N-dimension vector $\boldsymbol{S}$ where $\boldsymbol{S} \in \mathbb{R}^N \subset \mathbb{C}^N$ and $\mathbb{R}^N$ and $\mathbb{C}^N$ are the N-dimension spaces of real and complex numbers respectively.

Next, define an orthonormal basis $\{\boldsymbol{\psi}_1, \boldsymbol{\psi}_2, \boldsymbol{\psi}_3, \ldots, \boldsymbol{\psi}_N\}$ where $\boldsymbol{\psi}_i \in \mathbb{C}^N$. The signal with its mean removed can be decomposed into the sum of these basis vectors scaled by their corresponding coefficients:

$$\boldsymbol{S} = \sum_{i=1}^{N} c_i \boldsymbol{\psi}_i + \boldsymbol{\mu}_S, \tag{4.10}$$

where:

$$c_i = \boldsymbol{\psi}_i^H (\boldsymbol{S} - \boldsymbol{\mu}_S), \tag{4.11}$$

given $\boldsymbol{\mu}_S = \mu_S \boldsymbol{u}$ and $\boldsymbol{u}$ is a N-dimensional unit column vector. Then the total variation in the new basis can be expressed as:

$$N\sigma_S^2 = \sum_{i=1}^{N} \bar{c}_i c_i = \sum_{i=1}^{N} |c_i|^2, \tag{4.12}$$

where the bar notation denotes the complex conjugate. Thus $\{|c_1|^2, |c_2|^2, |c_3|^2, \ldots, |c_N|^2\}$ represents the contributions given by the 1^{st}, 2^{nd}, 3^{rd}, ... , N^{th} components, sometimes known as "modes", to the total variation in $\boldsymbol{S} - \boldsymbol{\mu}_S$.

For the Fourier transform the basis $\{\boldsymbol{\psi}_i\}$ in Eq (4.10) is a set of sinusoids of varying frequency where i is the frequency index, and $\{|c_1|^2, |c_2|^2, |c_3|^2, \ldots, |c_N|^2\}$ is commonly known as the "energy density spectrum". For the discrete wavelet transform $\{\boldsymbol{\psi}_i\}$ in

Equation (4.10) is a set of wavelets localised in time and scale such that $\{\boldsymbol{\psi}_i\} \equiv \{\boldsymbol{\psi}_{j,k}\}$ where j is the scale index and k is the time index, and $\{|c_1|^2, |c_2|^2, |c_3|^2, \ldots, |c_N|^2\}$ is a scalogram. Both the energy density spectrum and the scalogram have N coefficients; the energy density spectrum has no time resolution, whereas the scalogram sacrifices resolution in scale (frequency) for a limited resolution in time. It is useful to note that frequency is inversely proportional to scale, but the term "frequency" is strictly only applicable to sinusoidal components. The use and suitability of the Fourier and wavelet analysis methods will be discussed in the subsequent sections.

4.2.3 Fourier Analysis

One of the most popular methods for ANOVA is the discrete Fourier transform. For consistency and convention all the Fourier transforms plotted in this paper are the conventional MATLAB transforms[1]:

$$c'_k = \frac{1}{\sqrt{N}} \sum_{i=1}^{N} S_i \exp\left(-\frac{j2\pi(k-1)(i-1)}{N}\right) \qquad 1 \leq k \leq N. \tag{4.13}$$

Note that if an ANOVA decomposition is required as detailed in Section 4.2.2, the coefficients would need to be rescaled. In addition, for all the Fourier spectra the mean of TEC is not subtracted (however this only affects the zero frequency or "DC" component). Hence rather then use coefficients of the form c_i defined in Equation (4.11), the scaled coefficients c'_i will be used which will now refer to the "whole" time series, instead of the difference between it and its mean value. Hence $c_1 = 0$ and

$$c_k = \frac{1}{\sqrt{N}} c'_k \qquad 2 \leq k \leq N. \tag{4.14}$$

Figures 4.8 and 4.9 are $\log_{10}$ scaled energy density spectra of the quiet (21 February 1981) and wave-perturbed (09 December 1990) days respectively obtained after performing Fourier analysis. The Fourier transform method represents the time series by sinusoidal waves. Even if the source is non-stationary, the Fourier method determines the frequency spectrum over the entire region within the analysed window. Here the TEC signal is non-stationary and the wave structures within the signal do not necessarily exist throughout the whole day. Therefore the spectra in Figures 4.8 and 4.9 are obviously not in general

[1] http://www.mathworks.com/help/techdoc/ref/fft.html

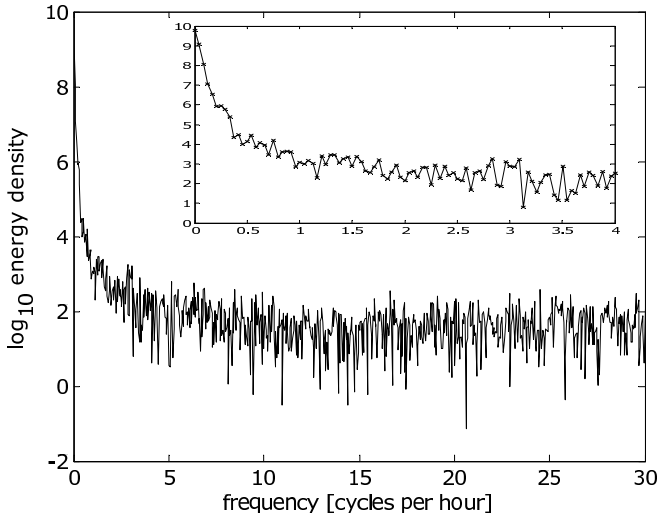

Figure 4.8: Energy density spectrum of TEC on 21 February 1981. The insert is a magnified spectrum showing the frequency range of interest (0-4 cycles per hour).

a true representation of the data at any particular instant in each day. The inserted figures in Figures 4.8 and 4.9 are the spectra magnified to see clearly the frequency range of TIDs reported in literature such as *Galushko et al.* (1998), and *Afraimovich et al.* (2009).

To overcome the "swamping" of DC and low frequency components, a potential solution is to filter the data before the Fourier analysis, i.e. apply a low pass filter to remove the low frequency structures. The Savitzky-Golay filter as discussed in Section 4.2.1 is a convenient method that effectively removes the low frequency structures. Subtracting the low pass output from the original signal yields a high pass filter. Here a high pass filter with cut-off frequency of about 0.3 cycles per hour (i.e. cut-off period of approximately 3 hours) is used. Denoting the energy density spectrum of a filtered signal by $\{|\tilde{c}_i|^2,\ i \in [1, N]\}$ then:

$$|\tilde{c}_i|^2 = |c'_i|^2 |h_i|^2, \tag{4.15}$$

where $|h_i|^2$ and $|c'_i|^2$ are coefficients drawn from the energy density spectrum of the high pass filter's impulse response and the energy density spectrum of the pre-filtered TEC data.

Figures 4.10 and 4.11 present energy density spectra of the filtered profiles shown in Figure 4.7. The spectra in Figures 4.10 and 4.11 may be compared to Figures 4.8 and 4.9, but are plotted on a linear rather than a log scale for clarity. The DC component and most of

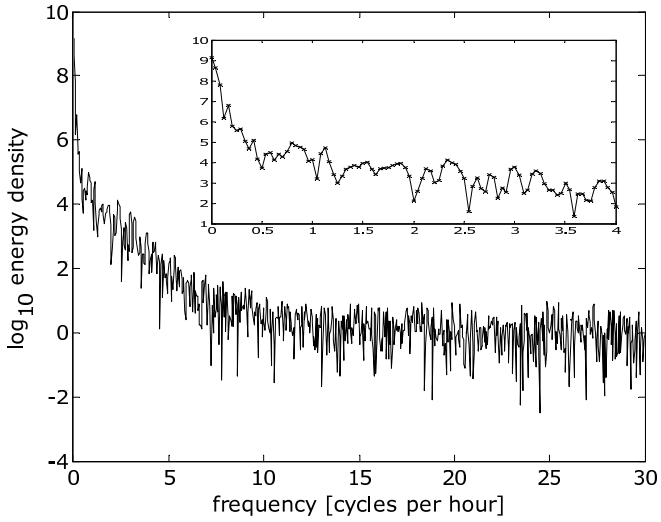

Figure 4.9: Energy density spectrum of TEC on 09 December 1990. The insert is a magnified spectrum showing the frequency range of interest (0-4 cycles per hour).

the low frequency structures have been filtered. The peaks in Figures 4.10 and 4.11 in the spectra give an indication of the strong components present within each day. For example the energy density spectrum of the insert of Figure 4.10 indicates that there is a wave structure at frequencies 0.3-1 cycles per hour (corresponding to a period of 1-3 hours). However care is required in interpreting the Fourier transforms when the underlying signal is non-stationary. As demonstrated by Figure 4.12, an intermittent pure sinusoidal signal has a wideband Fourier transform; this could be wrongly interpreted by a casual observer as being produced by a mixture of sinusoidal sources.

A potential method to deal with non-stationarity is via a windowed Fourier transform. The shape of the window function is important as it should ideally be a compromise between minimising distortion to the signal within the relevant time window and minimising distortion in the Fourier domain. The length of the window should be chosen such that the violation of the non-stationarity assumption within each window is not as severe as in the Fourier analysis over the whole day. A simple window function is the Gaussian function; it doesn't have large sidelobes when viewed in the frequency domain, so mitigates high frequency distortions. The Gaussian window is defined by:

$$w(t) = exp(-A(t - t_w)^2), \tag{4.16}$$

where $A = 1/(2\alpha^2)$, α is the standard deviation of the Gaussian, and t_w is the location of

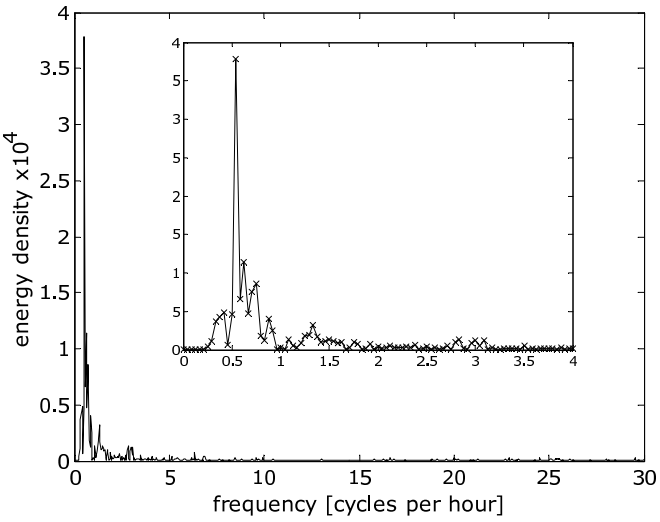

Figure 4.10: Energy density spectrum obtained from filtered TEC data on 21 February 1981.

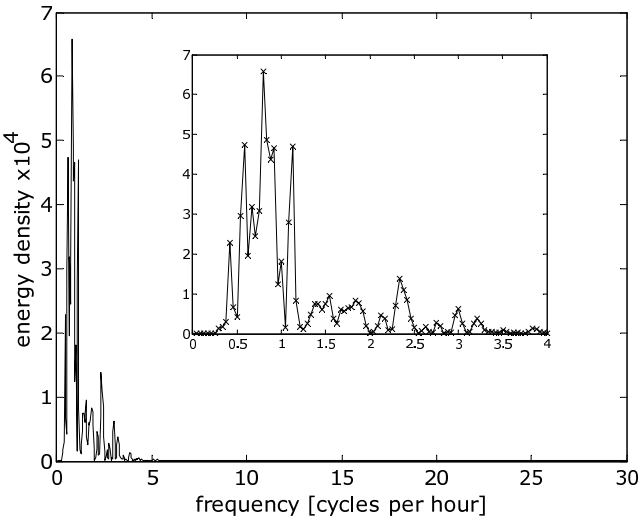

Figure 4.11: Energy density spectrum obtained from filtered TEC data on 09 December 1990.

(a) Intermittent sinusoidal function

(b) Corresponding energy density spectrum

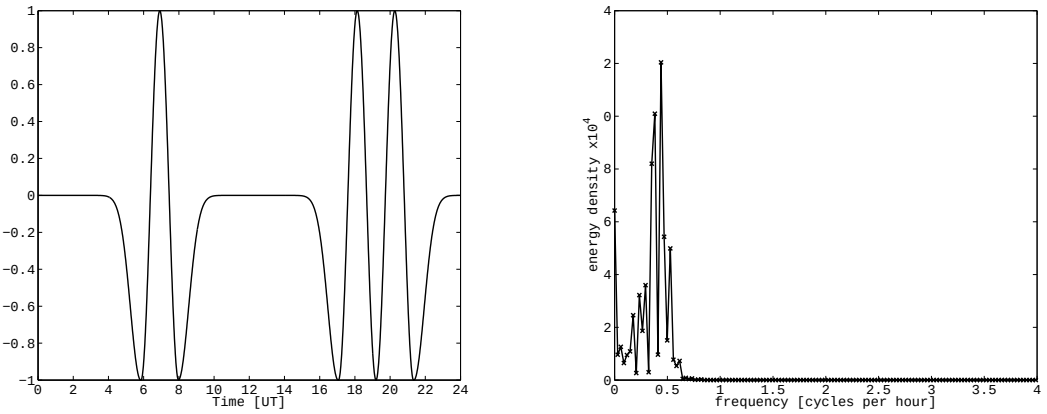

Figure 4.12: (a) Sine wave with a period of 2.13 hours and (b) its Fourier transform.

the centre of the window.

Figures 4.13 and 4.14 are the energy density spectra for the quiet and wave-perturbed days respectively, obtained when the Gaussian window is centred at midday (Time = 12 hours UT) and $\alpha^2 = 41.67$ hours^2. Figures 4.15 and 4.16 are the energy density spectra for the quiet and perturbed days respectively, obtained when the Gaussian window in time is centred on midday and $\alpha^2 = 10.17$ hours^2. A comparison across Figures 4.13 - 4.16 illustrates that for medium and large scale structures (frequencies between 1 and 2 cycles per hour) the width of the peaks broaden as the window narrows. This is because the standard deviation of the Gaussian window in time is inversely proportional to the standard deviation of the Gaussian function used for convolution in the frequency domain; see similarity theorem, for example in *Bracewell* (2000). This means that as the window size is reduced in the time domain, the underlying frequency resolution becomes poorer as more frequency components are smoothed. In particular, the DC component is large and swamps the frequency components near to it. In this paper a combination of a rectangular window with Gaussian tails was used in the statistical study presented in Section 5.2.2, because the rectangular window minimises the distortion of the data within the central part of the window whereas the Gaussian tails mitigate discontinuity artefacts. This "combination window" is expressed as:

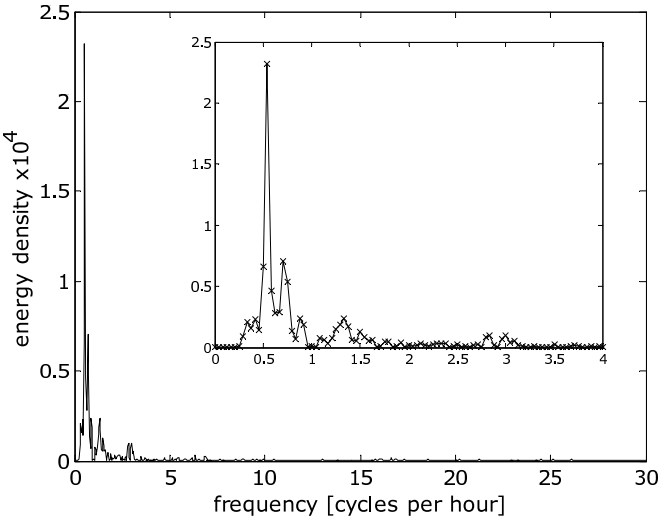

Figure 4.13: Energy density spectrum of 21 February 1981 after application of a window; window centred at midday (i.e 12 hours) and window length, $\alpha = 6.45$ hours. The insert is a magnified spectrum showing the frequency range of interest.

$$w(t) = \begin{cases} e^{-A(t-t_1)^2} & t < t_1 \\ 1 & t_1 \leq t \leq t_2 \\ e^{-A(t-t_2)^2} & t > t_2 \end{cases} \tag{4.17}$$

where t_1 and t_2 define the beginning and end of the rectangular window respectively.

In summary, the windowed Fourier analysis is useful because it gives a description of the wave structures in terms of frequency content. However as explained above, it has its limitations and complementary tools will be helpful. In particular, when the windowed Fourier transform is used to analyse portions of the day, the basis for the whole day is not orthonormal and an ANOVA decomposition for the whole day is not possible.

4.2.4 Wavelet Analysis

The wavelet transform permits the analysis of signals in the frequency and time domain, see *Daubechies* (1992), and is particularly suitable for non-stationary waves. For analysis of waves of a geophysical nature many authors use the Morlet wavelet, for example *Materassi and Mitchell* (2007), *Sauli et al.* (2007), and *Torrence and Compo* (1998), because its features are similar in shape to those of geophysical events. In this paper a discrete Meyer wavelet, see Figure 4.17 and *Misiti et al.* (2006), is used instead because it is similar

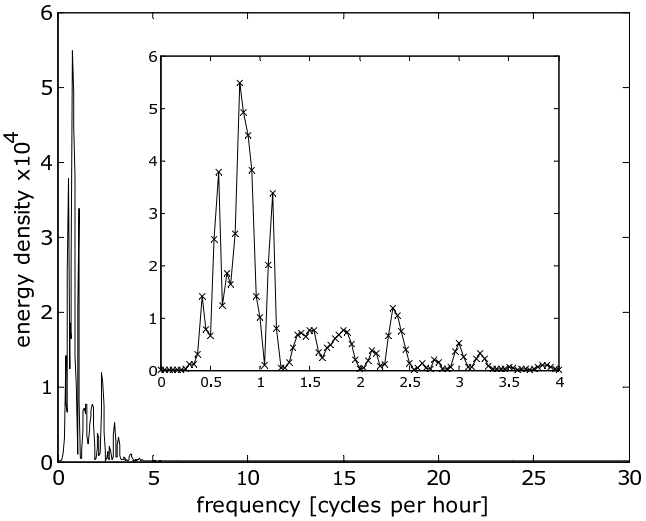

Figure 4.14: Energy density spectrum of 09 December 1990 after application of a window; window centred at midday (i.e 12 hours) and window length, $\alpha = 6.45$ hours. The insert is a magnified spectrum showing the frequency range of interest.

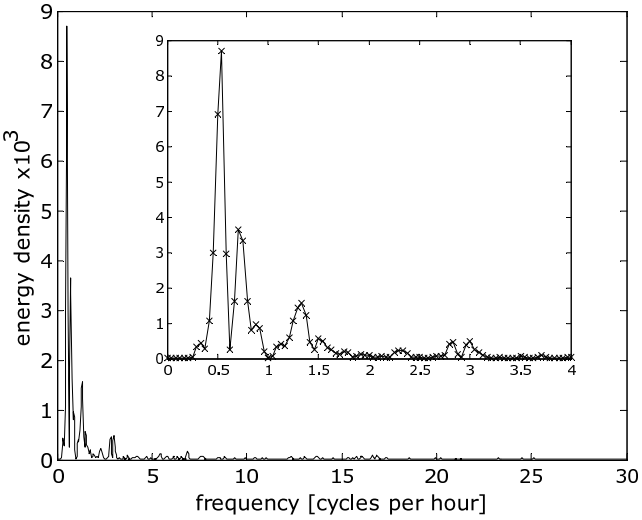

Figure 4.15: Energy density spectrum of 21 February 1981 after application of a window; window centred at midday (i.e 12 hours) and window length, $\alpha = 3.19$ hours. The insert is a magnified spectrum showing the frequency range of interest.

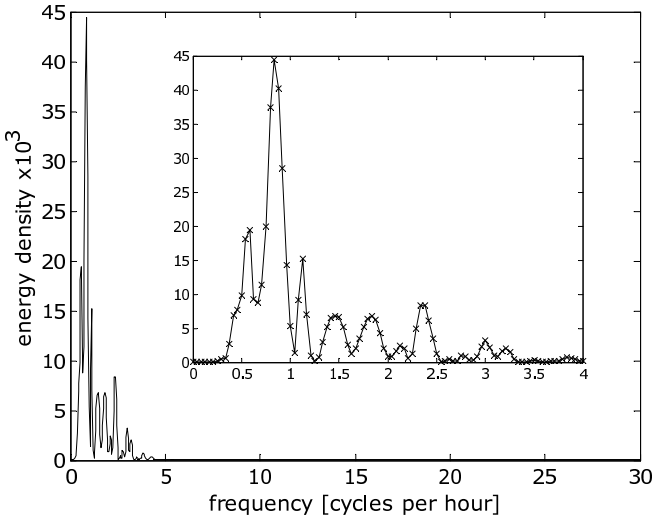

Figure 4.16: Energy density spectrum of 09 December 1990 after application of a window; window centred at midday (i.e 12 hours) and window length, $\alpha = 63.19$ hours. The insert is a magnified spectrum showing the frequency range of interest.

in shape to the Morlet wavelet but more importantly it can form an orthonormal basis (see *Daubechies* (1992)) which facilitates the application of the ANOVA method, presented in Section 4.2.2, for the decomposition of the total variation across different times and scales. The Meyer wavelet seems appropriate since wave-like perturbations in the ionosphere are finite in length and appear to oscillate quasi-periodically. The wavelet is used in a hierarchy, so the energy density spectrum in Figure 4.17 typically operates on the high pass output from a smaller scale format; at each scale there is effectively a bandpass filter, as discussed in detail by *Percival and Walden* (2000). The energy density spectrum has a low pass value of approximately 2 rather than 1 as expected; this is simply to accommodate the subsampling of the wavelet transform. The total variation in the signal is preserved since the wavelet basis is orthonormal, but only when zero padding is used at the boundaries. However there is some distortion due to the wavelet filter, i.e. some ripple in the energy density spectrum of the wavelet in Figure 4.17.

The use of the discrete Meyer wavelet, in the discrete wavelet transform, allows for the decomposition of TEC variation due to TIDs at each scale because the basis is orthonormal and therefore the squared magnitude of the coefficients of the wavelet transform can be summed along each scale size. This means it is possible to break down the TEC variability at each scale and compute the variability of TEC due to waves present at that scale, and having support centred in different parts of the day. For example, if N is the length of the time series and N is a power of 2 then the set of coefficients of the discrete wavelet

(a) Discrete Meyer wavelet function (b) Corresponding energy density spectrum

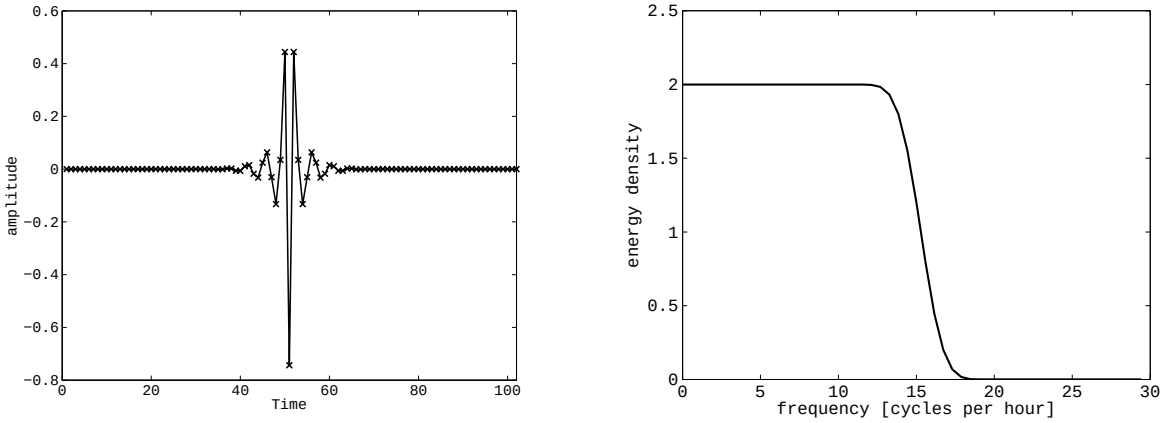

Figure 4.17: Discrete Meyer wavelet function (a) and its energy density spectrum (b).

transform are $\{c_{j,m(j)} | \, j \in [1, \log_2 N],\, m(j) \in [1, N/2^j]\}$, where $c_{j,m(j)}$ is the coefficient for a wavelet at spatial scale 2^j attributed to the time interval $\in [2^j(m(j)-1)+1, 2^j m(j)]$. The scaling by a factor of 2 is commonly called dyadic scaling and Fig. A.1 is a visual example where the blue dots and red crosses are the locations of the coefficients $c_{j,m(j)}$ at each scale and time. Furthermore, it is useful to note that the total variation of the original data is not modified during the wavelet analysis when zero padding is used for data outside the period analysed. However there are edge effects at the beginning and end of each day; these are discussed in more detail in Appendix A. While it would be useful to convert scale to period, this is not strictly possible because the Meyer wavelet is not sinusoidal. However an approximate method is described by *Misiti et al.* (2006) as follows: the conversion from scale to period is approximated by fitting a sinusoid wave to the wavelet function after subtracting its mean, i.e. through finding the period at which the magnitude of the Fourier transform of the wavelet function is maximised.

Since the scaling is on a dyadic scale, the frequency resolution is still poor at large scales but better at small scales. The scalogram of the discrete wavelet transform is difficult to interpret because its coefficients can be viewed as a coarse sample on the dyadic scale, as shown in Figure A.1. Thus for visualisation the scalograms are produced using an oversampled discrete wavelet transform, i.e. rather than calculate coefficients according to dyadic scaling, they are calculated and plotted at every time and scale. To illustrate how to interpret the scalogram, Figure 4.18 plots an intermittent sine wave and its scalogram. The sine function has a period of 128 minutes which corresponds to a scale size of about 85. Even though the energy is spread out across scales between 50 and 200, very little energy

(a) Intermittent sinusoidal function (b) Corresponding scalogram

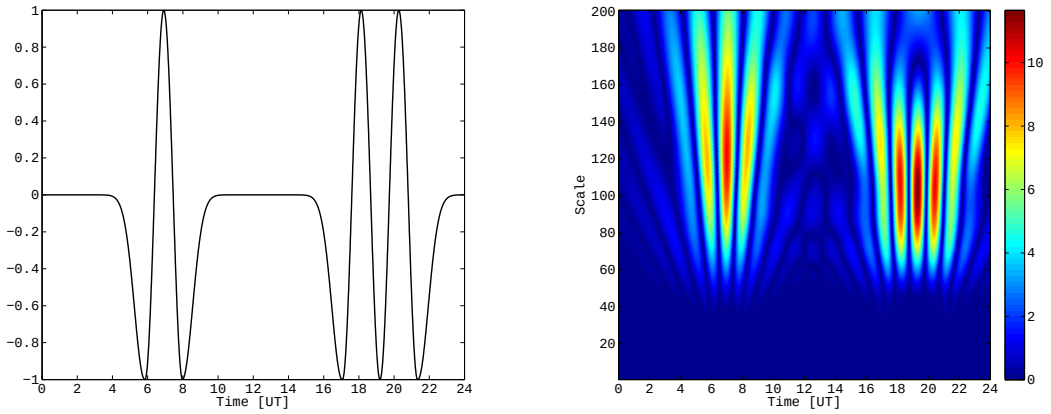

Figure 4.18: The scalogram (b) of the the intermittent sine function (a) with a period of 128 minutes (scale size 85) illustrates the frequency and time resolution of the discrete Meyer wavelet.

actually leaks to the nearest dyadic scales (i.e 42 and 170); however there is leakage across time due to the non-zero length of the filter. Figure 4.17 illustrates that the scalogram is useful in localising frequency content in time, which is not possible with the un-windowed Fourier transform applied to the whole day. Note that the coefficients of the scalogram are high when the peak of the sine function is either in phase or anti-phase with the wavelet peak, but the coefficients are low when the peak of the sine function is out of phase by 1/4 or 3/4 cycle. This gives a distinctive ripple pattern. It is very important to underline that although the frequency resolution of this wavelet is poor, it nevertheless gives limited time resolution: this kind of discrete based scalogram will be used only to single out the time at which the waves occur. Figure 4.19 presents the results of the wavelet analysis on the quiet and perturbed day. The quiet day scalogram in Figure 4.19 shows no signs of small and medium scale structures while large scale structures are present in the morning and evening. The perturbed day scalogram in Figure 4.19 shows that the wave signatures at medium scales occur around midday while the large scale structures are spread across the day. As in Fourier analysis, the "energy" of the wave structures in Figure 4.19 is spread across scales (periods). Also an individual wavelet suffers the same weakness as the sinusoid in the Fourier transform in that there is still averaging over the duration of the wavelet.

(a) 21 February 1981 (b) 09 December 1990

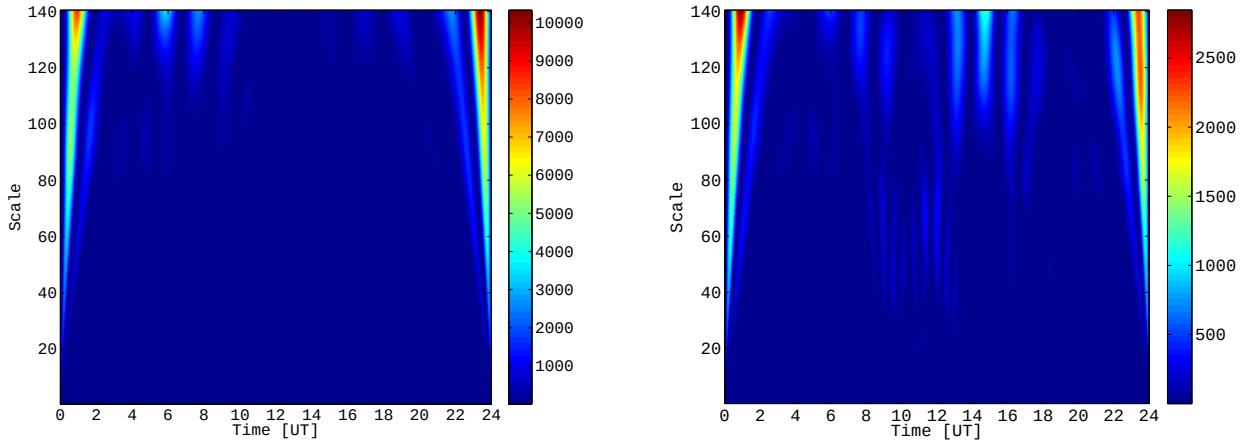

Figure 4.19: Scalograms of TEC on 21 February 1981 (a) and 09 December 1990 (b).

4.2.5 Limitations of the Amplitude and Variation Analyses

It is important to note that there are caveats to the interpretation of the results. The TEC data used in this study are measured from relatively low-elevation satellites, from a single location. The measured amplitude is dependent on the satellite elevation and also on the propagation direction and horizontal wavelength of the TID structures.

Hooke (1968) showed that spatially a TID is a sequence of enhancements and depletions in the horizontal direction. Note that the depletion is relative to the average electron density of the wave and will contain electron densities higher than the background. If the wavelength of the wave is larger than $2l$, i.e. $\lambda > 2l$ (see (a) in Figure 4.20), then the amplitude of the TID structure determined from our measurement would not be distorted; it would only be enlarged from the equivalent vertical TEC observations due to the slant ray path. If the wavelength of the wave is much smaller than $2l$, i.e. $\lambda << 2l$ (see (b) in Figure 4.20), then the amplitude of the TID structure determined from our analysis will probably be artificially smaller. For example, a TID structure traveling along the line of sight, will have an amplitude of zero as the contributions of the enhancements and depletion parts of the wave will cancel out.

Given the geometry of observation shown in Figure 4.21, it is possible to estimate the length, l, at which the TID wavelength will affect the accuracy of the observed amplitude of TIDs. This length l is defined as:

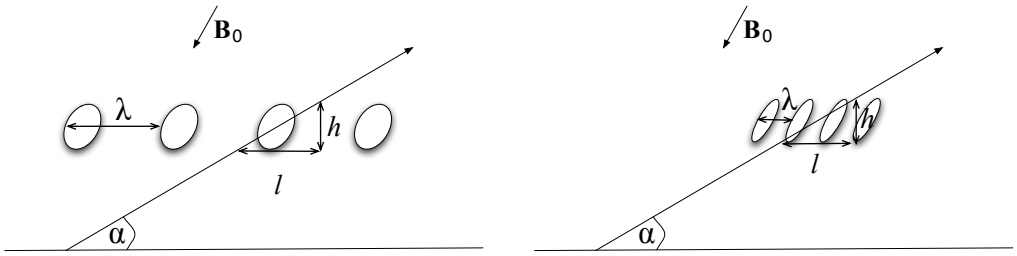

Figure 4.20: Sketch where each "blob" represents represent sequential enhancement maxima of the TID. (a) represents a TID structure whose wavelength $\lambda > 2l$, and (b) represents a TID structure whose wavelength $\lambda << 2l$. Note that the TID structures in each figure occur at the same height (d) in the ionosphere and have the same vertical extent. α is the elevation angle. The TIDs are aligned to the magnetic field ($\mathbf{B}_0$) as illustrated by *Hooke* (1968).

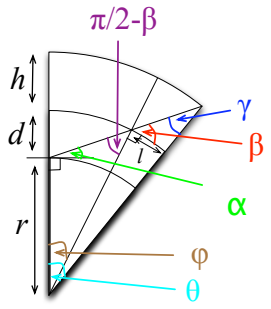

Figure 4.21: Illustration of the geometry of observation, where r is the Earth's radius, d is the height of the ionosphere, h is the thickness of the ionospheric layer in which the TIDs travel, and α is the elevation angle of the satellites.

$$l = (\theta - \varphi)(r + d) \tag{4.18}$$

where r is the radius of the Earth, d is the height of the ionosphere, and φ and θ are:

$$\varphi = \pi - (\pi/2 + \alpha) - (\pi/2 - \beta) = \beta - \alpha \tag{4.19}$$

$$\theta = \pi - (\pi/2 + \alpha) - \gamma = \pi/2 - \alpha - \gamma \tag{4.20}$$

Using the sine rule, it is possible to obtain φ from obtaining β:

$$\frac{sin(\pi/2 + \alpha)}{r + d} = \frac{sin(\pi/2 - \beta)}{r} \tag{4.21}$$

$$\frac{cos\alpha}{r + d} = \frac{cos\beta}{r} \tag{4.22}$$

$$\beta = cos^{-1}\left(\frac{r}{r + d} cos\alpha\right), \tag{4.23}$$

and θ from determining γ as follows:

$$\frac{sin(\pi/2 + \alpha)}{r + d + h} = \frac{sin\gamma}{r} \tag{4.24}$$

$$\frac{cos\alpha}{r + d + h} = \frac{sin\gamma}{r} \tag{4.25}$$

$$\gamma = sin^{-1}\left(\frac{r}{r + d + h} cos\alpha\right). \tag{4.26}$$

Substituting for β and γ from Equations 4.23 and 4.26 into Equations 4.19 and 4.20, l can be determined as:

$$l = (r + d)\left[-\cos^{-1}\left(\frac{r}{r + d}\cos\alpha\right) - \sin^{-1}\left(\frac{r}{r + d + h}\cos\alpha\right) + \frac{\pi}{2}\right] \tag{4.27}$$

where α is the elevation angle of the satellite and h is the thickness of the ionospheric layer. Using $r = 6365 \times 10^3$ km, $d = 100$ km, $h = 300$ km, and using the elevations of satellites $\alpha = 35°$ and $\alpha = 39°$, l can be estimated to be around 330 - 380 km.

This means that for our geometry the medium scale TIDs, which have horizontal scales of several hundred kilometers (*Hargreaves*, 1992), the amplitudes calculated are probably slightly underestimated; they are probably overestimated for large scale TIDs, which have horizontal scales over a thousand kilometers (*Hargreaves*, 1992). However, this cannot be compensated for because only the periods are measured and no velocity information is available, and hence horizontal wavelengths are not known. This is a limitation of the amplitude analysis and the analysis of variance, but not the analysis of the period/scale.

4.2.6 Summary

In summary, both Fourier analysis and wavelet analysis can be used to implement the ANOVA method but with different bases. The Fourier transform gives an energy density spectrum across frequency while the discrete wavelet transform gives an "energy density spectrum" across spatial scales and temporal location. Both give the same number of components/values, but the discrete wavelet transform sacrifices resolution in scale to give an improved resolution in time. This is not required if the signal is stationary, but when it is non-stationary as in this application then temporal resolution is useful. For example the Fourier transform over the full day cannot separate TIDs in the morning and afternoon, and while the windowed Fourier transform can be used, the window must be large enough to identify structures with periods of about 1-3 hours. This would still make the time localisation an issue. Furthermore, the window smoothes frequency components across scales, i.e it is difficult to attribute Fourier coefficients to a particular frequency with confidence (but this is also an issue with the discrete wavelet transform). Also one must be careful in comparing the variance of waves when windows overlap. On the other hand, the frequency localisation of the wavelet analysis is poor in comparison to Fourier analysis over a whole day, simply due to the dyadic restrictions of the discrete wavelet transform. Thus implementing both Fourier and wavelet analysis allows for extraction of complementary information and better analysis of TID statistics. In short, direct analysis of filtered data will be used to produce statistical information on TID amplitudes, the Fourier analysis to yield information abut dominant frequency components of TIDs, and wavelet analysis to implement ANOVA. However due to the nature of our data there is some limitation regarding the accuracy of the amplitudes and the variation analysis.

4.3 DDM Analysis Method

Through visual inspection of all the available TEC profiles, the days with a DDM structure were noted. The time and amplitude of the first peak, the depletion and the second peak of each DDM structure were also recorded. From these recordings, the duration of the structure was calculated using the following equation:

$$\text{Duration} = \text{Time}(\text{peak}_2) - \text{Time}(\text{peak}_1), \tag{4.28}$$

and the relative magnitude of each peak, i.e peak_n where $n \in [1, 2]$, was calculated using:

$$\text{Rel. magnitude of peak}_n = \frac{\text{TEC}(\text{peak}_n) - \text{TEC}(\text{depletion})}{\text{TEC}(\text{peak}_n)} \times 100. \tag{4.29}$$

The first peak was selected to occur after local sunrise and the second peak within 30 minutes after local sunset, to eliminate other phenomenon such as night-time enhancements. The magnitude of each peak relative to the depletion was selected to be greater than or equal to 6% to minimise the inclusion of small wave type fluctuations. Based on the number of days with a DDM structure recorded, the probability that a day with a DDM structure occurred during a particular season or geomagnetic condition was calculated using the following equation:

$$P(DDM|\text{season or condition } i) = \frac{N_{DDM,i}}{N_i} \times 100, \tag{4.30}$$

where $N_{DDM,i}$ is the number of days with a DDM structure in season or geomagnetic condition i, N_i is the total number of days in season or geomagnetic condition i, and i denotes winter, spring, summer and autumn for season and quiet, moderate and disturbed for geomagnetic condition. Also calculated was the probability of getting a DDM structure in a particular month:

$$P(DDM|\text{month } k) = \frac{N_{DDM,k}}{N_k} \times 100, \tag{4.31}$$

where $N_{DDM,k}$ is the number of days with DDM structure in month k, N_k is the total number days in month k and k represents months from January to December.

4.4 Summary

An optimised finite duration impulse response filter used to extract tidal information from TEC measurements was presented in Section 4.1. This filtering method was found to be unsuccessful because the authenticity of the results could not be verified, because the lunar modes extracted by the filter were below noise level and couldn't be identified in the energy spectrum of the original data.

Three different methods that can be used to extract information of TIDs, i.e Savitzky-Golay, Fourier and wavelet analyses. These methods were evaluated in Section 4.2. Each methods was found to give complementary information on TIDs; Savitzky-Golay was used to remove high frequency components in TEC measurement and to obtain amplitudes of the TIDs, Fourier analysis was used on the filtered TEC measurements to extract periods of the dominant TIDs, and wavelet analysis was used to give decomposition of the "energy" of the TEC data through the implementation of the ANOVA method. These methods were implemented and the results are presented in Chapter 5.

Equations to calculate the duration, relative magnitude of each peak, and probability of occurrence of a DDM structure were presented in Section 4.3. This analysis was performed on the TEC measurements and results are presented in Chapter 6.

Chapter 5

Travelling Ionospheric Disturbances (TIDs) Results

5.1 Introduction

TIDs are the ionospheric manifestation of gravity waves in the neutral atmosphere. In this chapter a statistical study comparing TIDs amplitudes, periods, and variations due to TIDs in different parts of the day during solar minimum in 1975-1976 and solar maximum in 1989-1990 is presented. In addition to the solar cycle comparison, a seasonal comparison within each solar cycle is presented. The study was conducted using TEC measurements from geostationary satellites described in Section 3.1. Geostationary satellites measurements are suitable for this type of study because measurements of TIDs are difficult to interpret from observations that move across the field of view with time, such as GPS ray paths. In fact GPS is particularly challenging because the ray path velocities through the ionosphere are comparable to the actual TID velocities (hundreds of meters per second). Since the TIDs themselves are moving, the observing instrument will impose a shift to the apparent period that is dependent on the direction. It then becomes necessary to account for the movement of both the instrument and the waves being observed without creating artificial shifts in the measured and inferred wave period and amplitude. This is challenging without prior knowledge of the wave direction. Thus the use of ionospheric measurements from geostationary satellites, which eliminates the motion problem and allows for a more direct study of temporal variation of the waves is advantageous to the study of TIDs. Figure 5.1 presents an example of waves observed in TEC measurements obtained from Faraday rotation measuring instruments on board geostationary satellites.

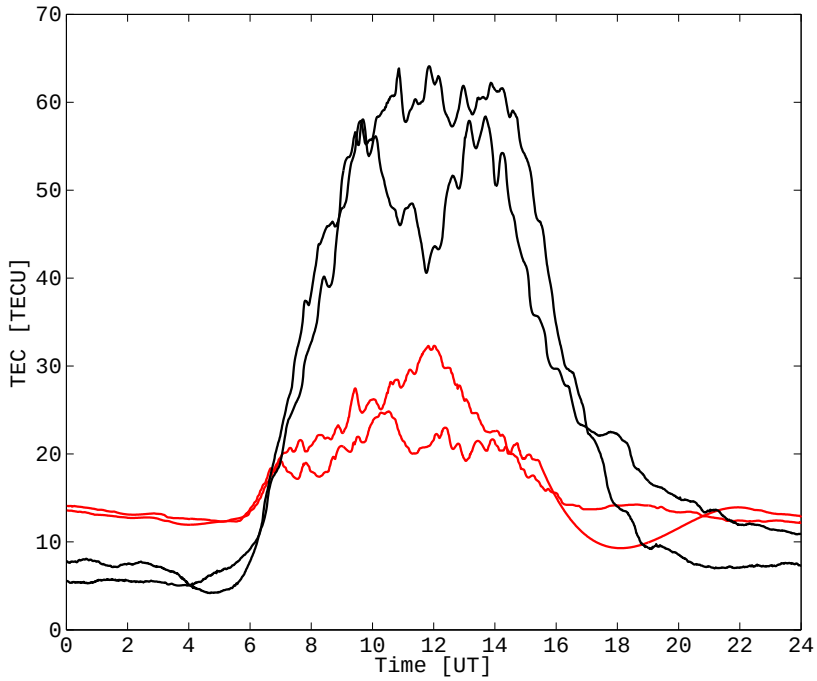

Figure 5.1: TEC daily profiles from Faraday rotation measurements. Black profiles recorded during solar maximum phase and red profiles recorded during solar minimum phase.

Different techniques have been used to obtain information on the spatial and temporal variation of gravity waves at different altitudes; for example *Dieminger et al.* (1970) have used geostationary satellites which measures ionospheric parameters up to about 2 000 km, *Kelley* (1997) has used rockets which measured under 360 km, *Zhang et al.* (2005) have used GPS which measures up to 20 200 km, and *Clemesha et al.* (2009) have used meteor radar measuring between 80-100 km.

The focus of this chapter is on the ionospheric signature of medium and large scale waves, i.e TIDs with periods defined here as ranging from 15 to 60 minutes and from 1 to 3 hours respectively. Geostationary TEC time series data have been used to extract information on the time variability of TIDs. The purpose of this study is to answer the following questions:

1. What is the range in amplitude of the TIDs?
2. What are the most common periods of the most dominant TIDs?

3. How does the TID variation change throughout the day?

4. How does the amplitude and period of TIDs compare across different seasons and different solar activity?

Questions 1, 2 and 3 will be answered by studying the direct detrended time series, Fourier analysis and wavelet analysis respectively. Direct inspection and Fourier analysis will be used to answer question 4. The answers to these questions will be useful in bounding the error introduced by TIDs in navigation systems and radio astronomy instruments, as they are or will be sensitive to the structure of the ionosphere. For example *Skone et al.* (2004), and *Yousuf and Skone* (2005) discuss the performance and accuracy of WAAS (Wide Area Augmentation System) under different ionospheric conditions and *Boonstra et al.* (2005), and *van der Tol and van der Veen* (2007) discuss the need for new methods of ionospheric calibration for new radio instruments such as LOFAR (Low Frequency Array[1]) and EGNOS (European Geostationary Navigational Overlay Service[2]).

For the analysis, the solar minimum period is represented by data from October 1975 to September 1976, and the solar maximum period from December 1989 to December 1990. There were data gaps due to technical difficulties such that the solar minimum period only has 124 whole days and the solar maximum has 276 whole days, where a whole day is taken as 24 UT hours midnight to midnight. Data was sampled at 1 minute intervals. As an example, the ionospheric TEC time series data for several days is overlaid in Figure 5.1 to illustrate the variability that is present in the data. In addition to the normal diurnal trend, the profiles also exhibit small scale perturbations which will be studied later in the chapter using direct inspection of the time series, Fourier transform, and wavelet transform methods. It is worth noting from Figure 5.1 that even though the TEC profiles at solar maximum have much larger absolute values and thus their perturbations are more prominent, the perturbations at solar minimum, especially between about 8-16 hours of a day, are quite visible in the original data.

[1]http://www.lofar.org/

[2]http://www.esa.int/esaNA/GGG63950NDC_egnos_0.html

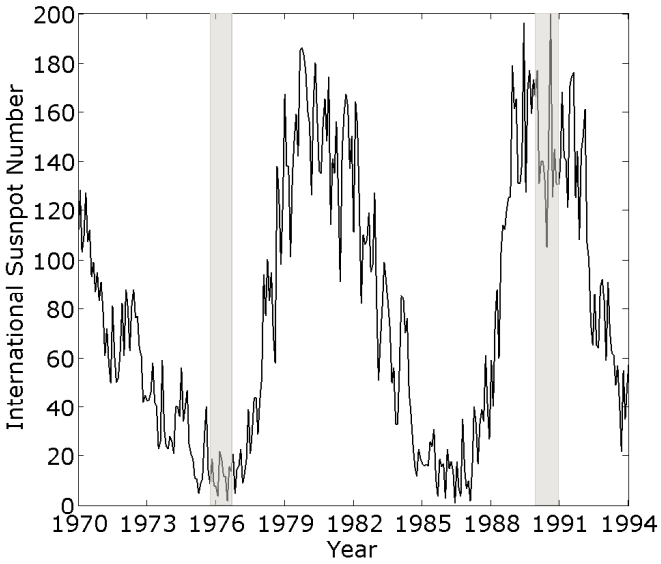

Figure 5.2: Long term variation of the monthly mean international sunspot number. The shaded regions indicate data coverage for solar minimum and solar maximum phases.

5.2 Results and Discussion

The days analysed were taken from the 1975-1976 solar minimum and the 1989-1990 solar maximum, as seen in in Figure 5.2. At solar minimum the days with complete data are spread across each season as follows: winter has 53 days, spring has 13 days, summer has 25 days and autumn has 33 days. At solar maximum the days with complete data are spread across each season as follows: winter has 96 days, spring has 27 days, summer has 79 days and autumn has 74 days. In each solar cycle, each day is denoted by the standard day of year, which is referred to as "day number" from hereforth.

Before discussion of the results, it must be noted that the comparison between different seasons has to be done carefully because distribution of the data across each season is very different and the amount of data available during the solar minimum phase is much smaller than the during solar maximum phase.

5.2.1 Direct Analysis of Filtered Time Series Data to Show TID Amplitudes

First it will be useful to gather statistics by direct inspection of the filtered data, effectively replicating what could be done by eye. Examples of filtered profiles for both solar minimum and solar maximum periods are presented in Appendix C. To analyse information on the size of the wave, the peaks and troughs due to TIDs present in the detrended data were collected. These were then used to calculate the "amplitudes" from consecutive peak-to-trough TEC values. To eliminate false peaks and troughs from noise or very short-term changes, the TEC value of the peak (trough) had to be greater (smaller) than 10 previous and 10 following TEC values, that is 20 minutes in total. Figures 5.3 (a) and (b) present the mean and maximum amplitudes for each day during solar minimum and solar maximum periods. Figures 5.3 (c) and (d) present the mean and maximum wave amplitudes expressed as a fraction of the maximum TEC for that day. The results presented in Fig. 5.3 show that amplitudes are greater during solar maximum than solar minimum, as also observed by *Soicher* (1988), but that the maximum amplitudes relative to the diurnal maximum TEC (i.e maximum TEC in relevant day) are similar in both solar minimum and solar maximum. This suggests that the TIDs in solar minimum are as important in percentage terms as the TIDs in solar maximum. Also, the amplitudes quoted in Figure 5.3(c) and (d) are much higher than those reported by *Tsugawa et al.* (2007); in that paper the relative amplitudes reported were in the range of 0-4% where as in Figure 5.3(c) and (d) they are in the range of 0-18%. However *Tsugawa et al.* (2007) used a slightly different method than the one used here to obtain the results. A tentative seasonal trend during solar maximum can be seen in Figure 5.3(b) and (d) where the maximum amplitudes are greatest during the winter season. During solar minimum Figure 5.3(a) and (c) show that autumn and winter amplitudes are typically greater than spring and summer amplitudes. A similar trend was observed for the mean amplitudes, although the trend is less pronounced. Similarly, *Tsugawa et al.* (2007) observed that the day time medium scale TID (MSTID) activity is greatest in winter, but the night time MSTID activity is greater in both winter and summer.

A seasonal analysis of the average maximum relative amplitudes during both phases of the solar cycle is presented in Table 5.1. During solar minimum, autumn and winter have on average TIDs with larger relative maximum amplitudes (8.4% and 9.9% respectively). During solar maximum, winter has on average the largest relative maximum amplitude (8.3%), contradictory to the solar maximum F-region (altitude of 160-250 km) study of

(a) Amplitude at solar minimum

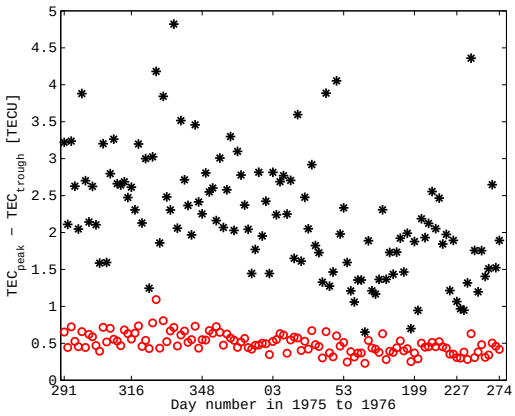

(b) Amplitude at solar maximum

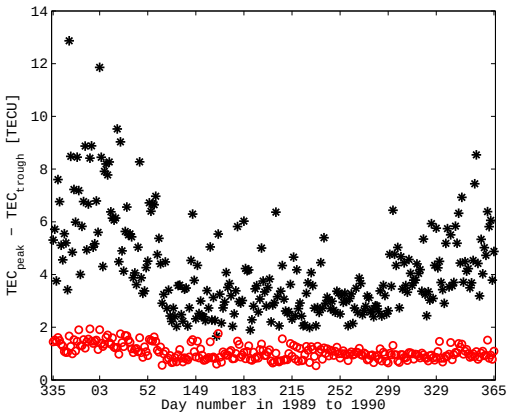

(c) Amplitude % at solar minimum

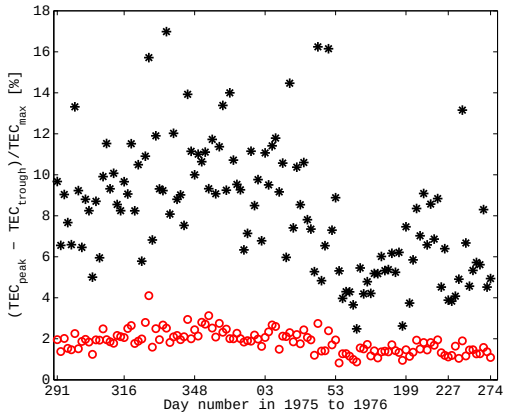

(d) Amplitude % at solar maximum

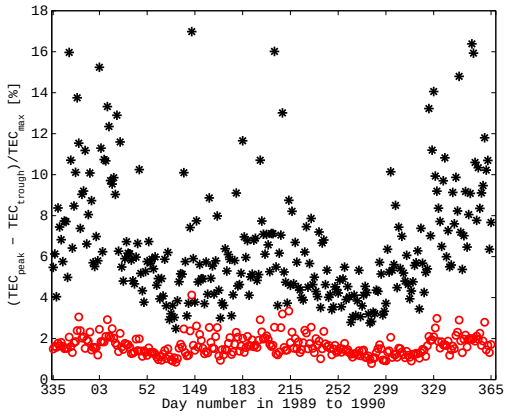

Figure 5.3: Wave "amplitudes" obtained from using direct time series analysis, with black "*" marking maximum values for each day and red "o" marking mean values for each day. (a) presents amplitudes during solar minimum and (b) during solar maximum. Relative amplitudes of the TIDs (scaled by the maximum TEC value for that day) during solar minimum and solar maximum are presented in (c) and (d) respectively. Note the uneven seasonal sampling of days along the abscissa axis.

Table 5.1: Season and solar cycle statistical analysis of the periods of the most dominant waves and mean maximum relative amplitudes of TIDs (quoted with their standard deviation). Figures are quoted to 1 decimal place. The number of data points within each season is also given.

	Solar minimum				Solar maximum			
	Autumn	Winter	Spring	Summer	Autumn	Winter	Spring	Summer
Period [hours]	1.6-1.9	1.1-1.3	1.3-1.5	1.7-2.0	1.4-1.5	1.3-1.4	2.0	1.4-1.5
Relative Magnitude of TIDs [%]	8.4 ± 2.5	9.9 ± 2.7	4.5 ± 0.9	6.2 ± 2.2	5.3 ± 0.9	8.3 ± 2.9	5.2 ± 1.2	6.0 ± 1.0
Magnitude of TIDs [TECU]	2.5 ± 0.7	2.5 ± 0.7	1.4 ± 0.4	1.8 ± 0.7	3.5 ± 0.9	5.8 ± 1.9	3.4 ± 1.1	3.2 ± 1.0
Number of days	33	25	13	53	74	96	27	79

Boskova and Lastovicka (2001) where they reported no detectable seasonal variation of maximum TID amplitudes at solar maximum. Winter TIDs at solar minimum are relatively larger than winter TIDs at higher solar activity, which is in agreement with the winter lower atmospheric TID results presented in the review paper by *Lastovicka* (2006).

It is important to note that one must be careful in relating these amplitudes to the original TEC signal as the analysis was performed on the high pass filtered TEC. In addition, note that the amplitude analysis is sensitive to the propagation direction and horizontal wavelength of the TIDs, which cannot be determined from our data.

5.2.2 TID Periods from Fourier Analysis

Next, to obtain information on the frequency components of the structures present in the data, the Fourier analysis method will be used. Through visual inspection of the data (and the wavelet analysis discussed later, see Figure 5.5) it was noticed that the wave structures with large amplitudes predominantly occur during the middle of the day, between about 08H00 and 16H00. Therefore it is sensible to use a windowed Fourier analysis over a window that encompasses most of this time interval to improve confidence in the interpretation of the Fourier method. The window of interest covers 8 hours during mid

day, and is centred at noon. A rectangular window spanning 7 hours with a Gaussian tail spanning 30 minutes at both the beginning and end of the window, as described in Equation 4.17 where $\alpha = 0.17$ hours, was chosen. The windowed Fourier transform was applied to TEC data that was detrended using the Savitzky-Golay filter with a cut-off period of 3 hours. The highest valued coefficients of the energy density spectrum from the windowed Fourier analysis of each detrended profile were located and their corresponding frequencies recorded. The frequencies were then converted to periods. The highest valued energy density coefficients were determined as the maximum energy density coefficient in the spectrum and any energy density coefficient higher than 30% of this maximum. This criterion allows us to determine if there is more than one dominant frequency (period) mode of the TIDs present within a day. Figure 5.4 presents the results of this analysis in a histogram format describing the most commonly occurring periods of the dominant wave structures at solar minimum and maximum. Note that the bin width in Figure 5.4(a) is approximately 0.043 cycles per hour and in Figure 5.4(b) it is approximately 0.044 cycles per hour. The bin widths are greater than the frequency resolution of the Fourier spectrum, which is 0.042 cycles per hour.

The histogram of the dominant waves presented in Figure 5.4(a) indicates that the most commonly occurring mode of the dominant waves during solar minimum has period of approximately 1.7-1.8 hours. During solar maximum the most commonly occurring modes of the dominant waves have periods of approximately 1.7-1.8 and 1.8-2.0 hours, as seen from Figure 5.4(b). During the solar minimum phase the minimum period of the dominant TIDs obtained from this Fourier analysis is roughly 23 minutes and the maximum period is roughly 3 hours. During the solar maximum phase the minimum period of the dominant TIDs obtained from Fourier analysis is roughly 26 minutes and the maximum period is roughly 3 hours. Hence we report that the periods of the most dominant TIDs are similar in both solar cycle phases but with marginally longer periods during solar maximum. It is worth noting that the cut-off period of the filter is the upper limit of the periods of the dominant TIDs that can be observed in this analysis.

Table 5.1 presents seasonal and solar cycle analysis of the period of the most dominant wave structures. The most dominant waves are longest (in period) in summer during solar minimum, but longest (in period) in spring during solar maximum. From the statistics presented in Table 5.1 it can be inferred that the waves that are most dominant are large scale TIDs.

(a) Periods at solar minimum

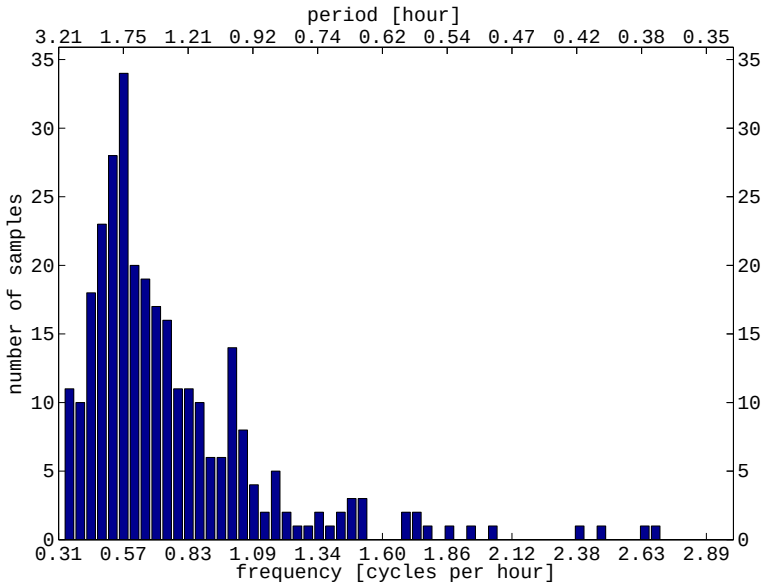

(b) Periods at solar maximum

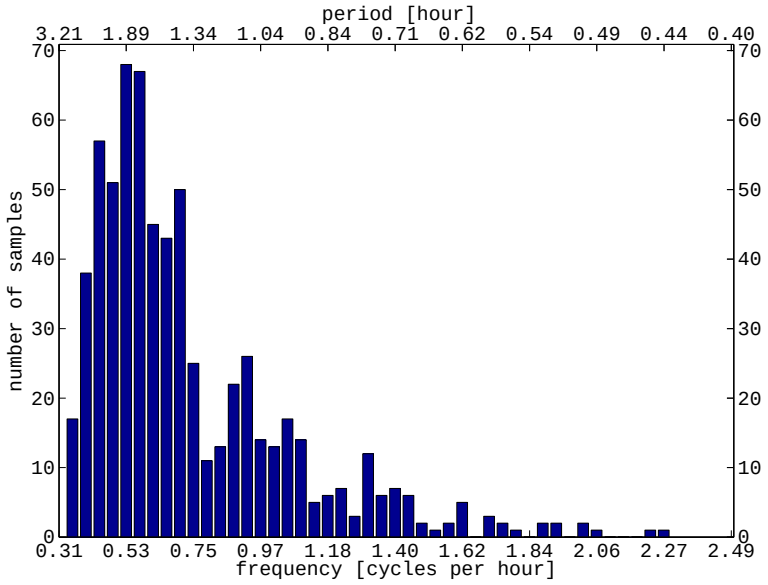

Figure 5.4: Histograms of the dominant TIDs occurring during (a) solar minimum and (b) solar maximum.

5.2.3 Analysing the Total Variation Using Wavelets

Next the discrete wavelet transform will be used to analyse the contribution of TIDs in various parts of the day. For each day a discrete Meyer wavelet transform of the TEC profiles was computed and the scalograms examined for wave signatures. The analysis in this section is based on the discrete Meyer wavelet with scale size 1 representing a wave period of about 1.5 minutes. Further examples of the oversampled wavelet transform using a discrete Meyer wavelet are presented in Appendix C, besides those already presented in Figure 4.19. The scales analysed are 32 and 64, corresponding to periods of approximately 48 minutes and 1.6 hours. These scales were chosen because scales higher than 64 fall outside our cutoff period of 3 hours; the next scale is 128 which corresponds to a period of roughly 3.2 hours. Scales below 32 had very small wavelet coefficients and were regarded as being difficult to distinguish from noise.

A convenient way of dividing up a day, which may allow us to determine in which part of the day there is the most significant variation (and for example where it is sensible to centre a windowed Fourier transform) is the following: morning 05H00 - 08H00, mid day 08H01 - 15H59, evening 16H00 - 21H00, and night 00H00 - 04H59 and 21H01 - 23H59; where the time is in UT and local time is approximately UT+1 hour. The time bounds of these categories were not strictly applied at all scales due to different temporal resolution at different scales. For example at scale 64 the coefficients belonging to the boundary of the morning category were calculated as 4.7 and 7.5, so coefficients 5 to 8 were used. However each coefficient was only attributed to a single category. To study the waves present at different times of the day, ANOVA was implemented and its output examined for local morning, mid-day and evening TIDs. A rough indication of the errors expected with this kind of analysis is discussed in Appendix A. Figure 5.5 shows TEC variation over different parts of the day across scales 32 and 64 for each day analysed (see Equation (A.2) for a description of how the variation of TEC within each window was obtained). Note that each plot in Figure 5.5 has different scaled axes.

A detailed look at the full set of scalograms reveals that the wave structures with a period of about 0.8 hours (48 minutes) typically occur during the day rather than in the evening or night. Some of the structures seen in the scalograms suggest that there is some inter-

ference between structures of different scales, where some structures combine to produce bigger structures or dampen each other. This may be due to natural physical mechanisms or/and a limitation in the wavelet analysis, and to be certain a wavelet with sharper frequency localisation would be required.

The comparison in Figure 5.5 shows that generally there is more TEC variation due to the observed medium scale waves (period of 48 minutes) during mid-day than during the morning or evening. This trend is not quite as clear for TIDs with longer periods, as can be seen in Figure 5.5, but is still detectable. It should be noted that the periods presented are those selected by the coarse, dyadic, sampling of the discrete wavelet transform. The following was observed:

- for both solar cycle phases the variation of mid-day waves was generally greater than those in the morning or evening,
- morning waves were larger than evening waves across both scales during the solar minimum phase, while no trend was detectable during the solar maximum phase,
- for the medium scale TIDs, i.e. period P = 0.8 hours, comparatively little activity in the summer was recorded during both solar cycle phases. This trend is similar to the TID amplitude trend reported in Section 5.2.1 and tentatively agrees with results reported by *Soicher* (1988) and *Klausner et al.* (2009). No seasonal trend could be detected for the large scale TIDs, i.e. period P = 1.6 hours.

5.2.4 Summary

Results from direct inspection of the detrended data showed that daily absolute maximum amplitudes range from 0.65 to 4.8 TECU during solar minimum and from 1.7 to 12.9 TECU during solar maximum. The observed maximum amplitudes of the waves are largest at solar maximum. The mean amplitudes are largest in autumn and winter with both seasons having a mean of 2.5 TECU during solar minimum. At solar maximum the mean amplitudes are largest in winter, where the mean wave amplitude is 5.8 TECU. From Fourier analysis it was observed that the periods of the waves vary between 0.44 and 3.0 hours during solar maximum and between 0.37 and 3.0 hours during solar minimum. The most commonly occurring period lies between approximately 1.7-1.8 hours during solar minimum and between approximately 1.7-2.0 hours during solar maximum. During solar minimum, the periods of the most dominant TIDs are longer in autumn and summer,

(a) P=0.8 hours, solar minimum

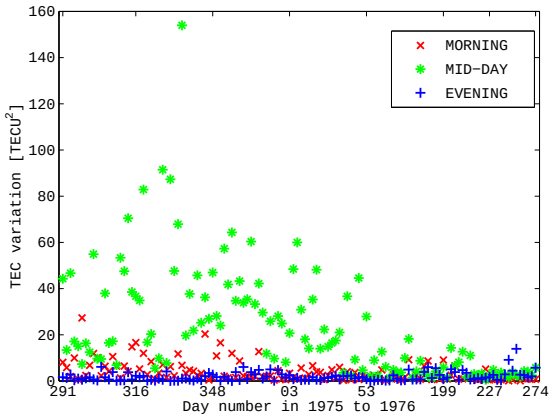

(b) P = 0.8 hours, solar maximum

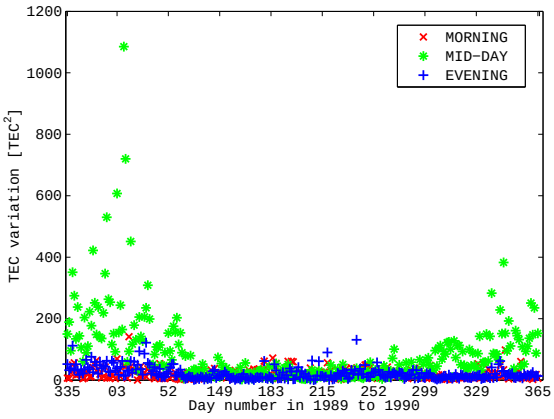

(c) P=1.6 hours, solar minimum

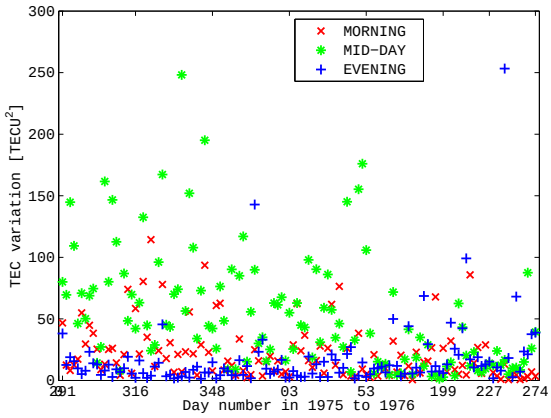

(d) P=1.6 hours, solar maximum

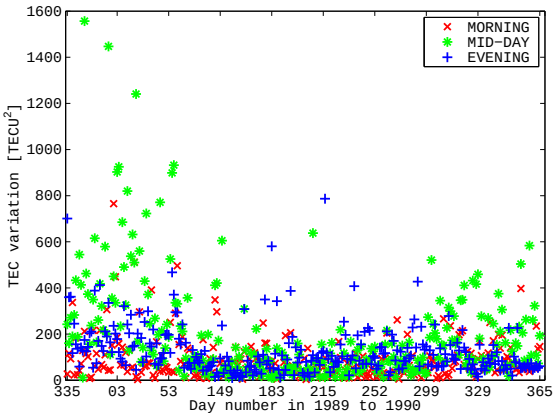

Figure 5.5: TEC variation due to TIDs with a period (P) of 0.8 hours (48 minutes) in (a) and (b) for solar minimum and maximum respectively; (c) and (d) present the TEC variation due to TIDs with a period of 1.6 hours for solar minimum and maximum respectively. Red "$\times$" marks the TIDs occurring in the morning, green "$*$" marks the TIDs occurring during mid-day, and blue "$+$" marks the TIDs occurring in the evening. Note the uneven seasonal sampling of days along the abscissa axis.

where such periods are in the range of 1.6-1.9 hours in autumn and 1.7-2.0 hours in summer. During solar maximum, the longest most common periods are found in summer, with a period of approximately 2.0 hours. Results from the discrete wavelet analysis show that TIDs contributed more significantly to the TEC variability during mid-day than during the morning and evening at the scales analysed. It is recognised that for the medium scale TIDs with shorter periods and shorter wavelengths, their amplitudes will have been underestimated due to the effects described in Section 4.2.5.

It should be noted that the analysis methods presented in this paper give complementary information and the statistics gathered from them generally agree. For example both direct inspection and wavelet analysis methods agree that the solar maximum TIDs are larger (amplitude and variation) than the solar minimum TIDs. Also, both direct inspection and wavelet analysis show that the winter TIDs are larger (in amplitude and variation) than summer waves during both solar cycle phases. Direct inspection also shows that the amplitudes are comparable in percentage terms during both solar cycle phases.

5.3 Conclusion

TEC time series data was obtained from geostationary satellites at an elevation of 35° during the solar minimum phase of 1975-1976 and at 39° during the solar maximum phase of 1989-1990. The data was studied using direct inspection of the time series data, discrete Fourier analysis and discrete wavelet analysis. The direct inspection was used to extract the amplitudes of TIDs, the Fourier analysis was used to extract the periods of the most dominant waves, while the wavelet method was used to give a decomposition of variation of the TEC data.

These methods were used to help answer the questions posed in Section 5.1.

1. What is the range in amplitude of the TIDs? The daily maximum amplitude of TIDs during solar minimum was found to vary between approximately 0.65 and 4.8 TECU and the daily mean amplitudes varied between 0.2 and 1.1 TECU. For each day during solar maximum the daily maximum amplitude of TIDs varied between approximately 1.7 and 12.9 TECU, and the daily mean amplitude varied between 0.54 and 1.9 TECU. As a fraction of the daily maximum TEC, the maximum amplitude was obtained at 17%, and the maximum of the mean amplitude was 4.1%

during both solar cycle phases.

2. What are the most common periods of the most dominant TIDs? The most commonly occurring period of the most dominant TIDs was 1.7-1.8 hours during solar minimum and 1.7-2.0 hours during solar maximum. However there were significant waves at all periods from roughly 20 minutes to 3 hours.

3. How does the TID variation change throughout the day? Results from discrete wavelet analysis suggest that the mid-day TIDs, with periods around 48 minutes and 1.6 hours, were predominantly larger in terms of energy than early morning or evening TIDs during both solar minimum and maximum. The morning waves were larger than the evening TIDs during solar minimum but a similar trend was not observed during solar maximum. No seasonal trend was observed for the large scale TIDs, i.e. period of 1.6 hours. However for the medium scale TIDs, i.e. period of 48 minutes, comparatively little activity was observed during summer during both phases of the solar cycle.

4. How does the amplitude and period of TIDs compare across different seasons and different solar activity? Direct inspection of detrended TEC data shows that the average and maximum amplitudes were greatest in winter during both solar cycle phases. However a secondary peak in TID activity in summer is seen during solar maximum. Analysing the periods of the most dominant components obtained from Fourier analysis, it was observed that during solar minimum the periods of such components were longer in autumn and summer than in winter and spring, while during solar maximum the longest periods of such components occurred in spring.

It is important to note that the statistics presented here are restricted to the field of view. Therefore they might not accurately reflect global statistics at any particular instant in time.

Large scale TIDs are commonly linked to auroral and geomagnetic activity at high latitudes. Sources of medium scale TIDs vary from those which are predictable and in-situ (e.g. solar eclipse and solar terminator) to those which are unpredictable and originate from the troposphere below (e.g. earthquakes). In order to trace the source(s) of the observed TIDs, data from other measuring stations would be needed and then correlated together to obtain measurements such as TID speed and direction. With our data from a single location, this is not possible.

TIDs of various scales are commonly observed throughout the day and across different seasons and solar activity. This means that the error introduced by TIDs in single frequency satellite navigational systems occurs persistently. For example *de Souza and Monico* (2007), *Allain and Mitchell* (2009), and *Rose et al.* (2009) studied errors introduced by the ionosphere on single frequency GPS signals. Therefore adequate modelling of TIDs should be included in such ionospheric models to reduce the TID effects and improve measurement accuracy. It is also important to tell astronomers when best to calibrate telescopes that are sensitive to ionospheric conditions, such as LOFAR, or what are the likely bounds on their errors, see for example *Boonstra et al.* (2005) and *van der Tol and van der Veen* (2007). The statistical analysis in this study is intended to supplement and stimulate further research into the physical mechanisms responsible for TIDs and thereby encourage the development of more accurate ionospheric models. Such models will be important for systems such as EGNOS, which are designed to correct GPS signals, allowing greater navigational and positional accuracy, see for example *Jakowski et al.* (2004).

Chapter 6

Diurnal Double Maxima (DDM)

DDM structures observed on 302 TEC profiles between 1975-1991 in the European midlatitude region have been studied. These profiles are presented in Appendix D. This chapter presents a statistical analysis on the occurrence of the DDM structures; their duration and relative magnitudes for different seasons, geomagnetic conditions and auroral activities, in order to understand the nature of these structures and establish whether there is a single mechanism responsible for these structures. The DDM structures are verified by ionosonde data from Rome. The results are presented and discussed in Section 6.1. Section 6.2 presents the conclusions and summary of the chapter.

6.1 Results and Discussion

A structure was classified as a DDM if: 1) the first peak was selected to occur after local sunrise and the second peak within 30 minutes of local sunset, to eliminate other phenomenon such as night time enhancements; 2) the relative magnitude of each peak was selected to be greater than or equal to 6% to minimise the inclusion of small wave type fluctuations. TEC profiles with DDM structures presented in Appendix B illustrates that the DDM structures can be divided into roughly three categories depending on the time of day they appear: pre-noon, noon and post noon. The statistical analysis was performed based the methods presented in Section 4.3 of Chapter 4. The data were grouped by season and geomagnetic activity. The geomagnetic activity was defined by one of the standard geomagnetic indices, the 3-hourly Kp index.

Figure 6.1 presents a statistical analysis of the relative magnitude of the peaks, the time of occurrence of each peak and the duration of the DDM structure for the entire data set. From the observations it is noted that for most of the TEC profiles with this structure, the magnitude of the first peak is usually larger than the magnitude of the second peak; out of 302 profiles with a DDM structure, 184 profiles (61%) have the first peak larger than the second peak. Comparing Figure 6.1(a) with Figure 6.1(b) it is observed that the most common relative magnitudes of the peaks are similar, at between 10-15% for both the first and second peaks. The relative magnitude of the first peak varies between 6% and 50%, while the relative magnitude of the second peak varies between 6% and 65%. Figure 6.1(c) shows that the first peak occurs between 5 and 15 UT and is most likely to occur between the hours of 10 and 11 UT. Figure 6.1(d) shows that the second peak occurs between 8 and 20 UT. The histogram for the second peak is a little more interesting as the distribution is bimodal suggesting that the second peak is most likely to occur between the hours of either 13-14 or 18-19 UT. The second peak rarely occurs before local midday while it is common for the first peak to appear around and after local noon. The duration of the DDM structures varies between 1 and 10 hours, but most of these structures occur over about 3-4 hours as seen from Figure 6.1(e). It should be noted that a data point at the boundary of the bin is counted in the preceding bin.

To produce statistical analysis on the diurnal double peak based on season and geomagnetic activity, the data was grouped into the following seasons: winter (December, January and February), spring (March, April and May), summer (June, July and August), and autumn (September, October and November). It was grouped into the following geomagnetic conditions, where the geomagnetic index Kp, computed every 3 hours, was used to determine the geomagnetic storm activity: quiet ($Kp < 3$), moderate ($3 \leq Kp < 6$) and disturbed ($Kp \geq 6$). A day with a DDM structure was classified as belonging to a moderate or disturbed category if a moderate or disturbed storm occurred on the same day but prior, to the first peak of the DDM structure.

Table 6.1 presents the probability of occurrence of the double peak according to season and geomagnetic activity, calculated using Equation 4.30. Given that a double peak was observed, the most likely season that the day belonged to is winter or summer which have conditional probabilities of 29% and 27% respectively. Figure 6.1 presents monthly probabilities, calculated using Equation 4.31, which demonstrate that January has the highest probability of having a DDM structure. The probability of having a DDM structure is

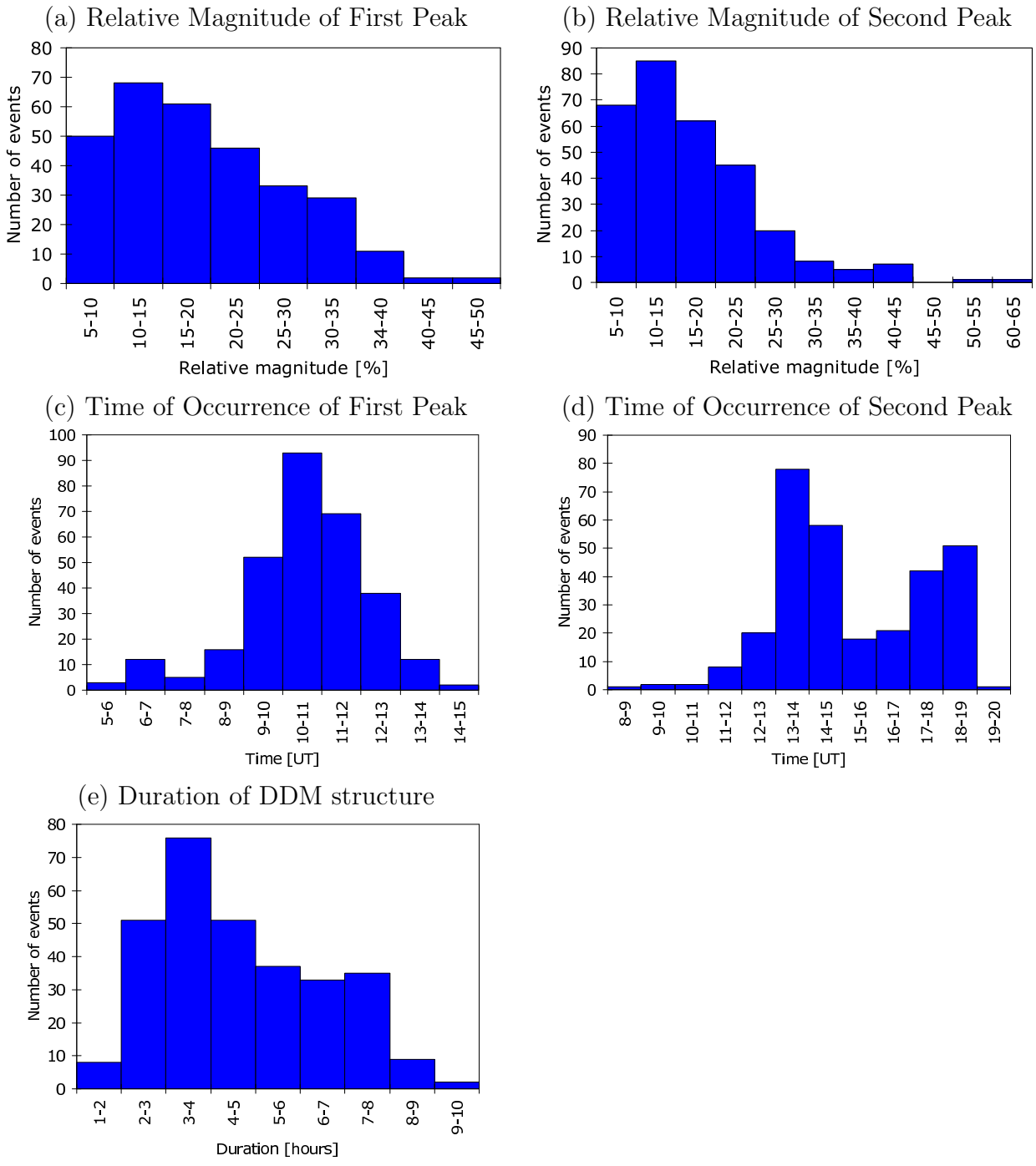

Figure 6.1: Histograms showing the distribution of relative magnitude, time of occurrence of each peak and the duration of the DDM structures.

Table 6.1: Summary of the occurrence of DDM structures during different seasons and geomagnetic conditions

	Total number of days	Number of days with a DDM structure	% probability of DDM in season/geomagnetic condition
winter	401	116	29
spring	225	37	16
summer	379	102	27
autumn	361	47	13
quiet	395	96	24
moderate	844	181	21
disturbed	127	25	20

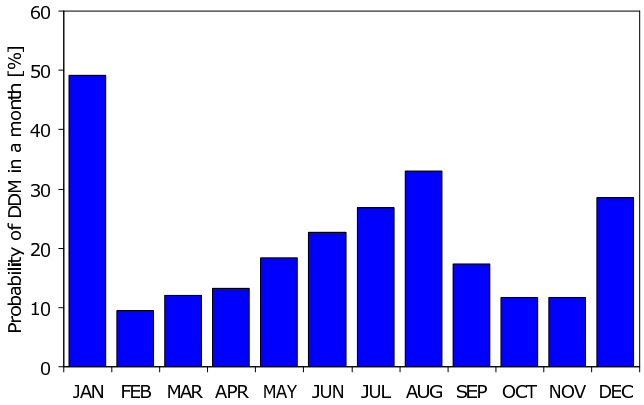

Figure 6.2: Probability of observing a DDM structure in a given month.

also higher in August than in neighbouring months. January falls in the winter season and August falls in the summer season in the Northern Hemisphere. Therefore the observed trend in Figure 6.1 is consistent with the seasonal bimodal peak noted in Table 6.1. These two observations are also not in disagreement with results from *Rastogi and Sanatani* (1968), who found that the bite-out structures are more prominent in solstitial months. It is also observed, in Table 6.1, that the probability of having a TEC profile with a DDM structure is similar across all the different geomagnetic conditions.

Table 6.2 and Table 6.3 present the seasonal and geomagnetic activity variations of the average relative magnitude of each peak, the average time of each peak and the average duration of the DDM structures. In terms of seasonal trend, Table 6.2 shows that the average relative magnitude of the first peak is smallest during autumn and greatest in summer, while the average relative magnitude of the second peak is similar throughout the seasons. The magnetic activity analysis in Table 6.3 reveals that the average relative magnitude of

Table 6.2: Seasonal analysis of relative magnitudes, time of occurrence, and duration of the DDM structures.

Season	Relative magnitude of 1st peak [%]		Relative magnitude of 2nd peak [%]		1st peak occurrence time [hour]		2nd peak occurrence time [hour]		Duration [hour]	
	Mean	Std dev	Mean	Std dev	Mean	Std dev	Mean	Std dev	Mean	Std dev
Winter	18	8	16	7	10.30	0.75	13.69	0.72	3.39	0.78
Spring	19	9	18	10	10.52	2.24	16.15	2.12	5.64	1.69
Summer	23	10	17	9	10.80	1.96	16.96	2.34	6.16	1.53
Autumn	14	7	15	10	10.97	1.41	14.73	1.53	3.75	1.39

the first and second peaks are largest during disturbed magnetic conditions. However if the standard deviations are taken into account in the average statistical analysis, then it is observed that the distributions in different seasons and magnetic conditions overlap and a trend cannot be determined accurately; this is also illustrated in Figure 6.3(a) and (b). Therefore calculations of confidence levels in the observed seasonal and geomagnetic trends on average relative magnitudes, times of occurrence and duration of DDM structures will be useful. The method of calculating confidence level is described in Appendix B. Results from confidence level calculations showed that there is a 58% confidence that the relative magnitude of the first peak is greater in summer than in spring, 56% confidence level that the first peak is greater during disturbed geomagnetic conditions than during quiet geomagnetic conditions, and 54% confidence level that the second peak is also greater during disturbed geomagnetic conditions than during quiet geomagnetic conditions. As the confidence levels in the comparison by seasonal and geomagnetic conditions are low for both peaks, there is little support for a dependency on seasonal or geomagnetic conditions.

From Table 6.2 it is observed that the time of occurrence of the first peak is similar in all the seasons, while the second peak occurs later in spring and summer. The confidence level was calculated at 71% for the second peak appearring later in spring than autumn. There was no clear trend with geomagnetic condition in the time of occurrence of either peak.

Figure 6.3(a) presents the relative magnitude of the peaks during different seasons, while Figure 6.3(b) presents the same data but during different geomagnetic conditions. It should be noted that the relative magnitude values are above 6% as this was the cut-off applied in the selection of these structures. A close inspection of Figures 6.3(a) and (b)

Table 6.3: Magnetic conditions analysis of time of occurrence, duration and relative magnitude of the DDM structures.

Magnetic condition	Relative magnitude of 1st peak [%]		Relative magnitude of 2nd peak [%]		1st peak occurrence time [hour]		2nd peak occurrence time [hour]		Duration [hour]	
	Mean	Std dev	Mean	Std dev	Mean	Std dev	Mean	Std dev	Mean	Std dev
Quiet	20	8	16	8	10.46	1.58	15.25	2.29	4.79	1.78
Moderate	18	9	16	8	10.65	1.53	15.17	2.21	4.52	1.80
Disturbed	23	12	20	13	10.78	1.90	15.91	2.13	5.13	1.97

reveals no clear season or geomagnetic trend; the relative magnitudes of the peaks are scattered widely for each season and geomagnetic activity. This is confirmed by the statistical analysis in Tables 6.2 and 6.3.

Figure 6.3(c) presents the seasonal statistical analysis for the time of occurrence of each peak. From Table 6.2 we can observe that on average the first peak occurred around the same hour but the time of occurrence of the second peak varies, with the summer having the latest second peak occurrence and winter having the earliest second peak occurrence. This then leads to the duration of the peak being minimal in winter and maximal in summer. This summer/winter trend is also noticeable in Figure 6.3(b), and is the reason for the bimodal shape of Figure 6.1(d). This trend might be due to the fact that the summer months have the longest sunlit period and therefore more chance of the second peak occurring before sunset. Figure 6.3(d) presents the time of occurrence of the first peak against the second peak, for all days, grouped according to geomagnetic condition. From Figure 6.3(d) it is observed that there is no detectable trend of the DDM structures with geomagnetic condition. The average time of occurrence of both peaks and the duration of the peak are similar in all geomagnetic conditions. These observations lead to the conclusion that although the time of occurrence of the double peak phenomenon has a seasonal trend, no clear geomagnetic trend can be observed.

An attempt was made to verify whether the DDM structures seen in sTEC measurements were also observed in $foF2$ measurements from an ionosonde in Rome (41.8° N,12.5° E); this instrument is closest in location to where the sTEC measurements were taken. However, since the ionosonde measurements and sTEC measurements were not co-located, there is a possibility that localised structures may not be recorded in both data sets. Details about the ionosonde and its measurements can be found in *Romano et al.* (2008). Out

(a) Seasonal variation of relative magnitudes

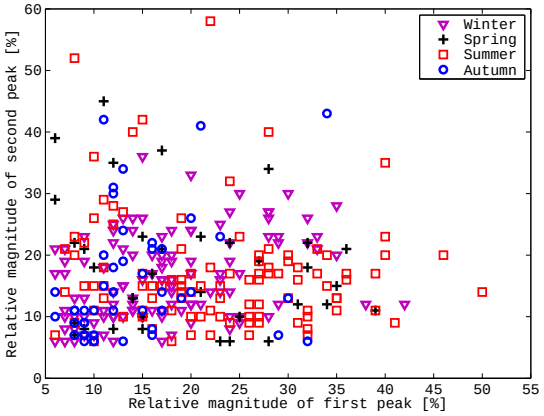

(b) Magnetic activity variation of relative magnitudes

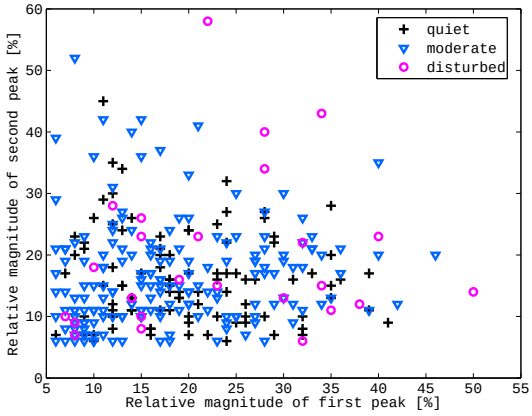

(c) Seasonal variation of time of occurrence of peaks

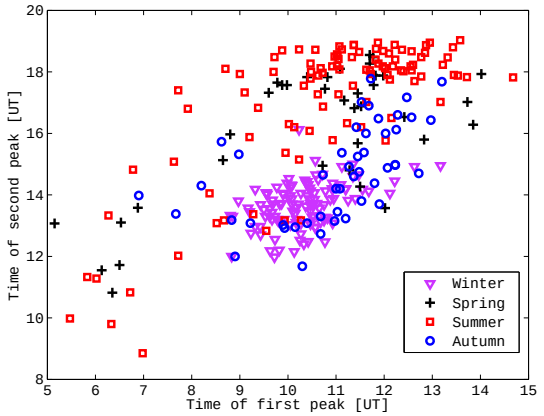

(d) Magnetic activity variation of time of occurrence of peaks

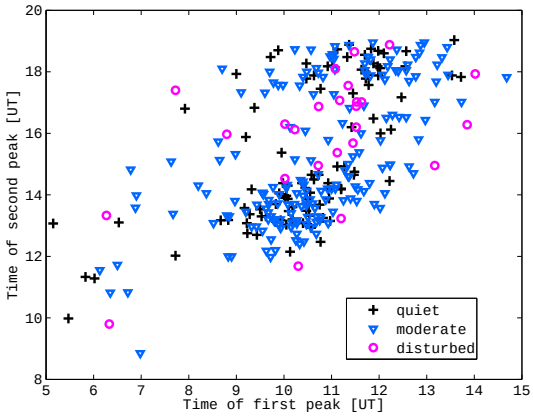

Figure 6.3: Variation of the times and relative magnitudes of the peaks by season and geomagnetic activity.

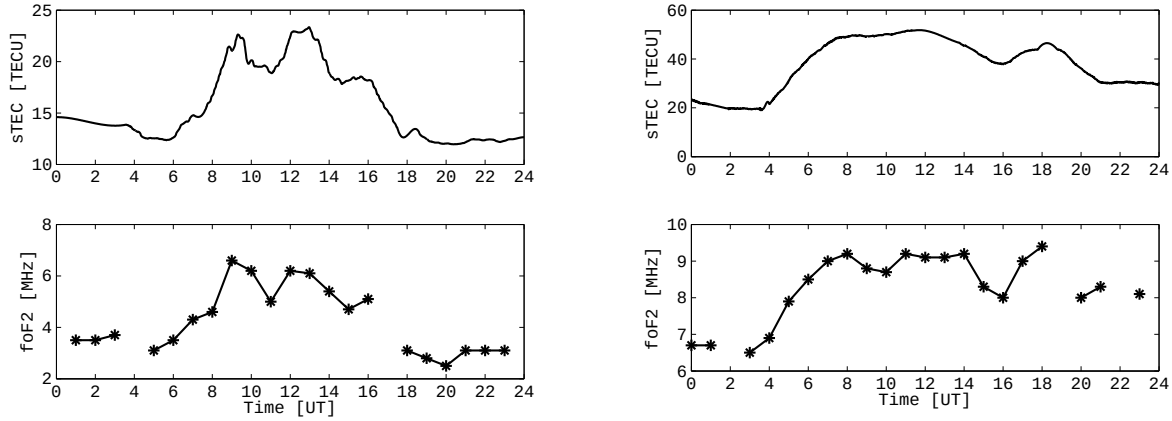

Figure 6.4: Daily variation of TEC and $foF2$.

of 302 days with DDM structures on their sTEC profiles, only 240 days could be compared with ionosonde data because of the poorer ionosonde data coverage. From these only 119 DDM structures could be verified from the $foF2$ measurements, the other 121 days of $foF2$ profiles did not have a definitive DDM structure. Figure 6.4 presents a couple of examples; in Figure 6.4(a) it is clear a DDM structure is seen in both TEC and $foF2$ measurements, while this structure is not so clear in the ionosonde measurements shown in Figure 6.4(b). It is worth noting that there are fundamental differences between the measurements: 1) ionosonde data has courser sampling, measurements taken every hour rather than every minute, and 2) the ionosonde only measures the bottomside ionosphere. Furthermore, the ionosonde only measures to the maximum height of the F2 region, $hmF2$, which is usually in the range of 200-400 km, whereas sTEC here is measured up to 2000 km. Therefore if the DDM structures occur in the altitudes above $hmF2$, they would not be visible in the ionosonde data.

Ionosonde measurements of $hmF2$ also from Rome were used to determine if this height parameter had the same double peak structures as the sTEC and $foF2$ measurements and if so, whether the structures occur at roughly the same time. If this is the case, the increase (decrease) of $hmF2$ may indicate that the DDM structures are due to plasma being lifted (depressed) to higher (lower) altitudes, due to either thermospheric winds or vertical $\mathbf{E} \times \mathbf{B}$ drifts, where the recombination rate is less (higher) if the structures are enhancements (depletions). A few cases were found where $hmF2$ had double peak structures and these occurred an hour or more before the structures observed in sTEC measurements. For illustration purposes Figure 6.5(a) is an example of supporting evidence and with the

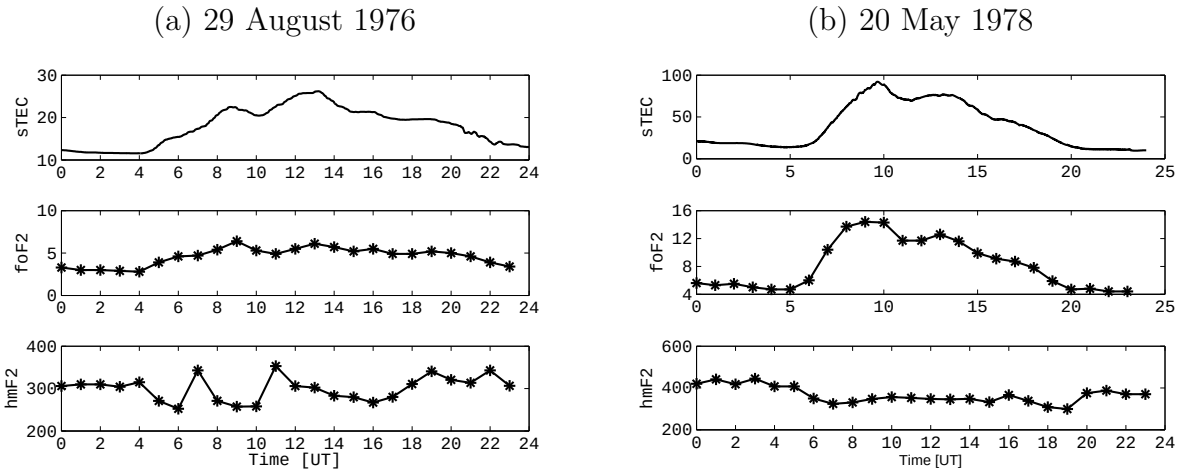

Figure 6.5: Daily variation of TEC, $foF2$ and $hmF2$. TEC is measured in TECU, $foF2$ in MHz and $hmF2$ in km.

uplifts in $hmF2$ at least 2 hours prior to double peaks being observed in the sTEC and $foF2$ measurements. Figure 6.5(b) is a counter example where double peaks are observed in sTEC and $foF2$ measurements but no corresponding peaks are seen in the $hmF2$ measurements. However, overall $hmF2$ observations either showed no double peak structure or showed a lot of wave structures characteristic of large scale TIDs. This analysis suggests that the DDM structures are not mainly caused by vertical plasma motions.

Pi et al. (1995) suggested that when a diurnal double peak occurs during substorm events, the double peak is a response to two substorm events. In particular, the first substorm occurs during post-sunrise and pre-noon, and the second occurs post-noon and pre-sunset. Hence a trend between the observation of a DDM structure and the occurrence of the substorms is next investigated. To detect this trend, a study of the double peak structures which occurred during the geomagnetically quiet days was done so that the results would be purely dependent on substorm events rather than geomagnetic storms. Here a substorm event was defined by an AE index above 300 nT; this threshold was chosen based on previously published substorm events (see for example *Kamide and Akasofu* (1983)). In Table 6.1 there were 96 days where a DDM structure was observed and it was geomagnetically quiet. Out of these 96 days, there were only 72 days with a double peak structure where AE data was available; no AE data were found for 1976, 1977 and 1989. The following observations can be made. There were:

- 9 days with DDM structures where a substorm occurred prior to each peak,

- 17 days with DDM structures where a substorm occurred prior to the first peak but none prior to the second peak,
- 14 days with DDM structures where a substorm occurred post the first peak but prior to the second peak and none prior to the first peak,
- 32 days with DDM structures, but with no substorm association.

Since there were only 9 days with a double peak structure where a substorm was observed prior to each peak, these results don't support the *Pi et al.* (1995) hypothesis. If this criterion is relaxed so a single substorm may cause either a bite-out or a TEC enhancement forming the second peak (in addition to the normal diurnal peak), then it is reasonable to expect that the substorm would occur before or during (but not after) the second peak of the DDM structure. Here, 40 (i.e. 56%) days with a DDM structure were found where a substorm might have caused this structure and 32 (i.e. 44%) days with a double peak structure were observed with no relation to a substorm event during that day. This leads us to believe that the DDM structures are not solely driven by substorm events. However, the data used in this analysis is limited to one location, whereas *Pi et al.* (1993) and *Pi et al.* (1995) have studied DDM structures occurring at different latitudes.

Rostoker et al. (1980) have warned against using only the electrojet indices in the study of substorm time evolution and advise that researchers should include original magnetogram observations in their study. To heed this suggestion, the magnetic field X component from a chain of Scandinavian magnetograms known as IMAGE[1] were then used together with the AE indices to identify substorm events related to DDM structures. Based on past substorm studies, it was observed that during a substorm the X component changes by about 100 nT or more (see for example *Amm et al.* (2006), *Blagoveshchensky et al.* (2009), and *Kamide and Akasofu* (1983)). Therefore this threshold was used in the characterisation of substorm activity. The IMAGE X component data are available from October 1982 onwards. Between 1980 and August 1982, X component measurement were used from magnetometers located in Sodankyla (located 67.37°N 26.65°E; data from January 1980 - August 1982) and Abisko (located 68.36°N 18.82°E; data from January 1981 - August 1982). It should be noted that for the next section only 60 days were available where DDM structures were observed and it was geomagnetically quiet. Thus, using an AE index of 300 nT and a perturbation of 100 nT or greater for the X component to identify an active

[1] http://www.ava.fmi.fi/image

substorm event, the following were observed:

- 4 days with DDM structures where a substorm occurred prior to each peak,
- 12 days with DDM structures where a substorm occurred prior to the first peak but none prior to the second peak,
- 3 days with DDM structures where a substorm occurred post the first peak but prior to the second peak and none prior to the first peak,
- 41 days with DDM structures, but with no substorm association.

These results are similar to the results presented previously in that most days with a DDM structure are not associated with substorm activity occurring prior to or during the occurrence of a DDM structure. However a looser definition of a substorm based on lower AE and X component thresholds may alternatively be used. For example, an AE threshold of 100 nT was used to differentiate between non-active periods in the electrojet index, as used by *Zhang et al.* (2008) and *Tanskanen* (2009), and a change of more than 10 nT in the X component of the magnetic fields. With this new criterion the following were observed:

- 33 days with DDM structures where a substorm occurred prior to each peak,
- 12 days with DDM structures where a substorm occurred prior to the first peak but none prior to the second peak,
- 7 days with DDM structures where a substorm occurred post the first peak but prior to the second peak and none prior to the first peak,
- 8 days with DDM structures with no substorm association.

With the looser definition, it is observed that if the suggestion of *Pi et al.* (1995) is considered, about 55% (33 out of 60) of the days with a DDM structure agree with *Pi et al.* (1995) and the other 45% do not. On the other hand there are 52 days with a DDM structure (87%) where at least one substorm occurred before or during the double peak, resulting in the conclusion that most of the DDM structures are associated with substorm activity if the thresholds are low enough.

Continuing the analysis, monthly mean sTEC profiles were constructed using those days without double peaks in each month. The monthly mean sTEC profiles were then com-

pared with the double peaks in order to categorise the double peak structures into enhancements (if the peaks of the DDM structure are greater than the monthly mean) and bite-outs/depletions (if the peaks of the DDM structure are less than the monthly mean). For the monthly mean to be calculated each month was chosen only if it had at least 20 days of data without DDM structures in order to give a meaningful representation of data for that month. This criterion meant that only 20 monthly mean profiles could be calculated for the data between 1975 and 1991. Therefore out of 304 days with a DDM structure only 53 days could be used for depletion or enhancement classification. Although there is some subjectivity in the classification, 22 days with a double peak were classified as peak enhancements and 21 days were classified as depletions/bite-outs, and 10 days did not exclusively belong to either category. Figure 6.6 presents examples of an enhancement double peak structure and a depletion double peak structure. If it is considered that the DDM structures are a response to some substorm driven phenomenon, then for the enhancement structures a substorm has to occur prior to each peak, and for the bite-out structures only one substorm is needed to occur prior to the bite-out. In this analysis, assuming an AE threshold of 100 nT for substorm activity, 19 from 22 enhancement structures were found where a substorm occurred prior to each peak (for example see Figure 6.6(a)), and 16 from 21 bite-out structures were found where a substorm occurred prior to the depletion (for example see Figure 6.6(b)).

Although substorm events have been observed prior to a double peak in our analysis, counter examples were also found where substorm events occurred during post-sunrise but pre-noon, and post-noon but pre-sunset, but no DDM structures. However no DDM structures were observed in association with these substorm events (see Figure 6.7(a)). In fact of the 779 days where sTEC profiles showed no double peak structure and AE indices could be obtained, 773 (96%) days were found where a substorm occurred before 12 UT, if AE $\geq$ 100 nT, 609 (76%) days if AE $\geq$ 300 nT. This shows that substorm events are fairly common, and if the DDM structures are an ionospheric response to some substorm driven phenomenon, then one would expect more DDM structures to be observed. Furthermore, there are also examples where a double peak structure was observed but a substorm event only occurred after the double peak phenomenon, see for example Figure 6.7(b).

Saryo et al. (1989) have suggested, based on their case study, that the cause of the DDM structures may be related to delayed storm effects on the neutral winds. Preliminary results do not support this as we have found several examples where on a day with a

(a) 06 December 1975

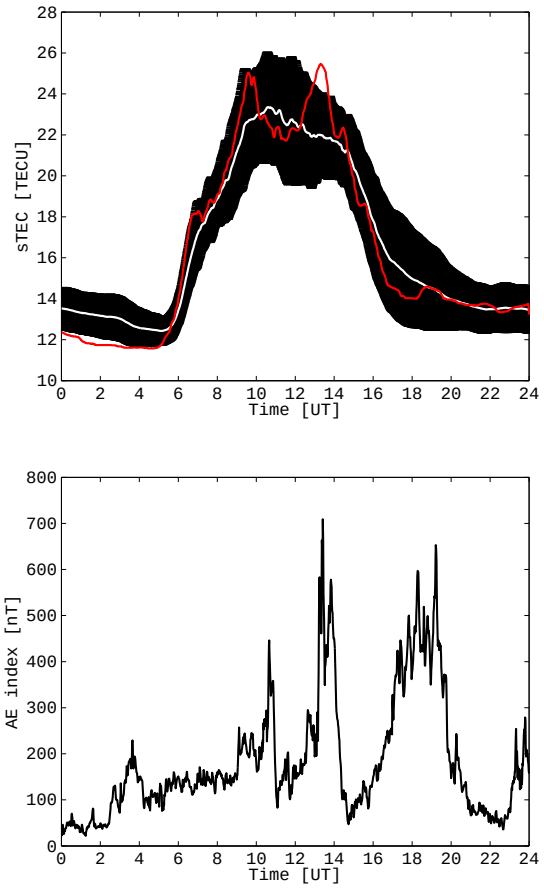

(b) 23 December 1990

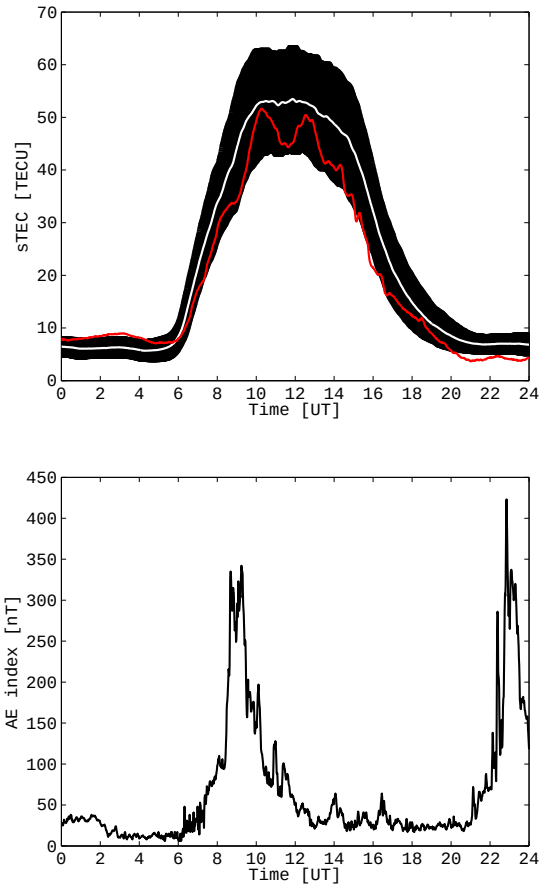

Figure 6.6: sTEC profiles showing DDM structures (red curves) plotted together with their respective monthly mean profiles (white curve). The black shaded curve indicates ± 1 standard deviation. Plotted below these are the AE indices for the same days.

(a) 04 September 1974 (b) 24 December 1980

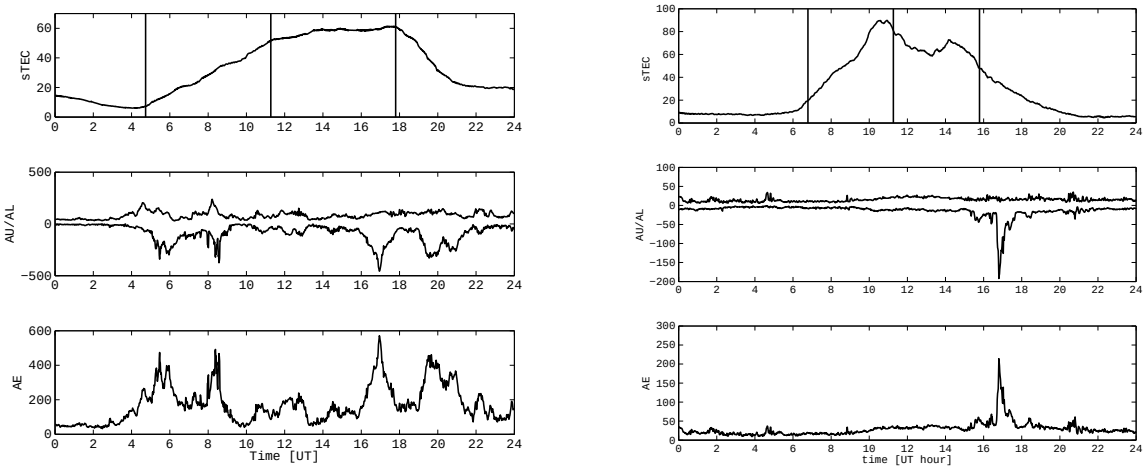

Figure 6.7: TEC profiles with and without a double peak plotted with the auroral electrojet indices AU, AL and AE. The measurement unit for TEC is TECU and for the auroral electrojet indices is nT. The vertical lines mark local sunrise, noon and sunset.

DDM structure, and up to 4 days prior to that day, there were no geomagnetic storms classified using Kp index greater than 3. However a more extensive analysis would be required to investigate such a dependency.

6.2 Conclusions

A study of the diurnal double maxima (DDM) structures at mid-latitudes has been presented in this paper. From the statistical analysis it was observed that the probabilities of occurrence of the DDM structure were similar during different geomagnetic conditions. Also, the rate of occurrence of a DDM structure was higher during winter and summer compared to autumn and spring.

The second peak appeared on average earliest in winter and latest in summer, while the time of occurrence of the first peak showed no seasonal trend. The average relative magnitude of the first peak was found to be largest in summer while the average relative magnitude of the second peak showed no seasonal trend. The average relative magnitudes of the peak were observed to be slightly higher during disturbed magnetic conditions. Confidence in seasonal and geomagnetic trends of the average relative magnitude of the peaks were determined to be low, and thus there was little support that the relative magnitudes

vary distinctively with season or geomagnetic condition. The average time of occurrence of the peaks showed no dependency on geomagnetic condition.

Some of the DDM structures observed in sTEC measurements were verified by $foF2$ ionosonde measurements from Rome. However although a similar diurnal trend was observed in both sTEC and $foF2$ measurements, the structures observed in the ionosonde data were more complicated. Comparison between sTEC and $hmF2$ measurements indicated that the DDM structures could not be mainly linked to vertical plasma movements in the bottomside ionosphere. However the ionosonde and sTEC measurements were not co-located and conclusions are limited. In addition, an enhancement can result in a broader ionosphere but with the peak parameters (i.e. foF2 and hmF2) remaining the same, which will result in the DDM structure not being visible in the ionosonde data but visible in TEC data.

A study of the relationship between the occurrence of a DDM structure and substorm activity was inconclusive, as the results were subjective depending on the threshold one used in defining substorm activity based on the AE index and/or the X component of the magnetic field. The subjectivity arises because, to the authors' best knowledge, no coherent AE index or X component threshold defining substorm activity can be found in the literature. However from the results of our analysis there was no clear indication that either substorms or storms were the main cause of the DDM structures, as the DDM structures occurred both with the presence and absence of the storms and substorms.

To conclude, while other studies have suggested that DDM structures are caused by either thermospheric winds or vertical $\mathbf{E}\times\mathbf{B}$ drift driven by geomagnetic storms and/or substorms, this study suggests that the DDM structures are not solely storm or substorm driven, but rather that there are multiple drivers. However, it should be noted that the results presented here are limited to only one location. It would be useful to confirm these observations using data from different locations. In addition wind patterns from global thermospheric wind models would be helpful, requiring accurate neutral wind observations in the thermosphere.

Chapter 7

Application to Radio Systems

In this chapter two different sources of ionospheric measurements are translated into a form that is useful for radio systems. In the first case, ionospheric tomographic maps of electron density are used to demonstrate a method to measure the refractive distortion on a new European radio telescope, LOFAR (LOw Frequency ARray). In the second, data from Section 3.1 are used to characterise the temporal TEC gradients that can be useful for EGNOS (European Geostationary Navigation Overlay Service). Both LOFAR and EGNOS require ionospheric information and it is intended that the results and ideas in this chapter can serve as a resource for them.

Sections 7.1 and 7.2 present brief descriptions of LOFAR and EGNOS. Section 7.3 gives an overview of tomographic imaging which is a method of continuously imaging the ionosphere, locally as well as globally. This imaging method was used in the subsequent ray tracing simulations. Section 7.4 presents a method that was used to simulate ray propagation in the ionosphere to illustrate how the low frequency signals will behave as they traverse the ionosphere. The results of the simulation are presented and discussed in Section 7.5. The TEC data from 1975-1982 and 1989-1991 described earlier, was used to produce statistics on the short-term TEC gradients as a guide to users of LOFAR and EGNOS on the variability of the ionosphere during different phases of the day, season, geomagnetic condition and solar cycle. This study is presented in Section 7.6. The chapter is concluded with a summary of the results.

7.1 LOw Frequency ARray (LOFAR)

LOFAR is a new radio interferometric array located in Europe that operates between roughly 10 and 250 MHz. In radio interferometry many radio telescopes/antennas separated by some distance are used collectively to observe the same celestial body. This method improves the resolution of the instrument, as it is not dependent on the size of the individual telescopes/antennas but on the maximum distance between the telescopes/antennas. Although LOFAR is already being used for radio astronomy projects (operational since October 2010), some LOFAR stations are still under construction.

LOFAR has two distinct types of antennas, the Low Band Antenna (LBA) that will operate between 10 and 90 MHz and the High Band Antenna (HBA) that will operate between 110 and 250 MHz. The frequencies between 90 and 110 MHz are not used to avoid frequency interference from commercial radio broadcasters (FM stations). The low frequencies and long baseline of LOFAR make it possible for radio astronomers to explore more deeply the nature and history of our universe. In addition to radio astronomy projects, LOFAR will be used in the geoscience and agricultural field [1].

When completed LOFAR will consists of roughly 44 low-cost antennas spread across 5 countries in Europe:

- 36 stations in the Netherlands,
- 5 stations in Germany - Effelsberg (50.5° N, 6.9° E), Garching bei Muenchen (48.2° N, 11.6° E), Tautenburg (51.0° N, 11.7° E), Potsdam (52.4° N, 13.1° E), and Jülich (50.9° N, 6.4° E),
- 1 station in Sweden - Onsala (57.4° N, 11.9° E),
- 1 station in the UK - Chilbolton (51.1° N, 1.4° W), and
- 1 station France - Nançay (47.4° N, 2.2° E).

The Netherlands stations are distributed over an area of about 100 kilometer in diameter. Half of the Netherlands stations, i.e 18 stations, are spread over a core area that is 2×3 kilometers wide and located between Exloo, Buinen and Buinerveen, while the other 18

[1] http://www.lofar.org/about-lofar/general-information/introduction

stations are distributed around this core area at distances of up to 50 kilometers. This core of LOFAR is located roughly at (52.9° N, 6.9°E). The longest baseline of the array is about 1500 km. More information about LOFAR is accessible at `http://www.lofar.org`.

7.2 European Geostationary Navigation Overlay Service (EGNOS)

EGNOS is an augmentation system similar to the US WAAS (Wide Area Augmentation System). It augments GPS (US system) and GLONASS (GLobal NAvigation Satellite System, Russian system) constellations and is mainly used to improve the accuracy of these constellations for safety critical services like aviation and rail. An augmentation system uses known position measurements of several reference points in order to determine the error in position from GPS measurements. EGNOS is a joint effort by the European Commission, European Space Agency (ESA), and Eurocontrol, which is the European Organisation for the Safety of Air Navigation.

EGNOS consists of three geostationary satellites, and a network of 34 ground stations called RIMS (Ranging and Integrity Monitoring Stations). The geostationary satellites of EGNOS are:

- 2 Inmarsat satellites (PRN 120 and PRN 126), one located 15.5° west and the other 25° east, and
- 1 ESA's Artemis satellite (PRN 124), located 21.5° east.

The signals from EGNOS cover most of Europe but the satellites are visible simultaneously from Europe, Africa and the Middle East. The satellites broadcast the same GPS L1 frequency (L1 = 1575.42 MHz) and ranging codes but have a different data format. EGNOS signals include accurate information on the position of each GPS satellite, the accuracy of the atomic clock on board each GPS satellite and disturbances within the ionosphere that might affect the accuracy of positioning measurements. These ionospheric measurements are obtained from a single layer ionospheric model for the L1 signal (*Perrin*, 2003). More information on EGNOS can be found at `http://www.esa.int/esaNA/egnos.html`.

7.3 Ionospheric Tomography: Multi-Instrument Data Analysis System (MIDAS)

LOFAR will operate at very low frequencies, between 10-250 MHz, and will be spread over a wide area in Europe. At these low frequencies the ionosphere will contribute significant errors to the signal. The ionosphere varies greatly with time and space, see Chapter 2, therefore the ionospheric errors across the array will be different. A global method of monitoring the ionosphere continuously and in real or near-real time, such as ionospheric tomography, will be useful in order to carefully assess the errors that might be experienced by LOFAR.

Ionospheric tomography is the reconstruction of the electron density distribution from TEC measurements (from navigation satellites) along the line of sight. The principle of tomography has been used in many different areas of science such as geology, biology and the best known application is in medicine where computerised tomography is used to take X-ray images of a human body. *Austen et al.* (1988) were the first to suggest the use of satellite measurement to reconstruct the electron density distribution from TEC measurements along a set of rays. *Raymund et al.* (1990) successfully tested the method in their simulated high latitude ionosphere work. Since then many authors, such as *Hajj et al.* (1994), *Mitchell et al.* (1997), *Bhuyan et al.* (2004) and *Yin and Mitchell* (2005) have used satellite TEC measurements to reconstruct electron density maps using different inversion methods.

For computational purposes Equation (1.1), see Chapter 3, is usually redefined in a matrix format as:

$$\boldsymbol{b} = \boldsymbol{A}\boldsymbol{x} + \boldsymbol{e}, \tag{7.1}$$

where $\boldsymbol{b}$ is the measured TEC, $\boldsymbol{A}$ the ray path lengths, $\boldsymbol{x}$ denotes the unknown electron density and $\boldsymbol{e}$ is the unknown offset. There are a number of techniques for solving Equation 7.1, collectively known as reconstruction techniques. *Bust and Mitchell* (2008) give a review of all techniques including the iterative method called ART (algebraic reconstruction technique), and its derative MART (multiplicative ART). Another ART derivative SIRT (simultaneous iterative reconstruction technique) is discussed in *Leitinger* (1999). Non-iterative techniques include the singular value decomposition (SVD), modified trun-

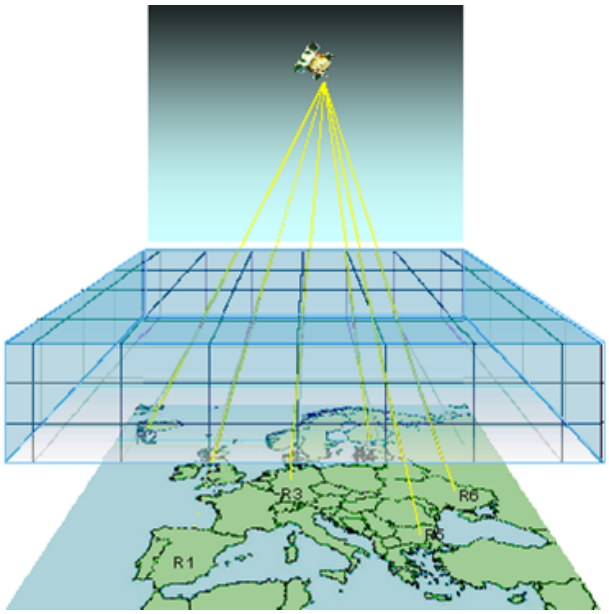

Figure 7.1: Illustration of the voxel geometry.

cated SVD discussed in *Raymund et al.* (1994), *Mitchell and Spencer* (2003), and *Bust and Mitchell* (2008), and stochastic inversion techniques, for example see *Fremouw et al.* (1992).

The reconstruction technique used in this project is called MIDAS, which stands for Multi-Instrument Data Analysis System. MIDAS was developed by the Invert group at the University of Bath to produce three dimensional time varying ionospheric maps. The software uses different instruments, such as GPS and low Earth orbit (LEO) satellites, to derive slant TEC and compute four dimensional maps of electron density. The slant TEC values are calculated from geometry free L1/L2 phase measurements as described in Equation (3.33), see Chapter 3.

In MIDAS, the ionospheric region of interest is divided into a three dimensional grid with each grid volume (also known as a voxel) bounded in latitude, longitude and altitude as illustrated by Figure 7.1. Assuming that the radio signal travels in a straight line (essentially true for the high end spectrum of high frequency signals like L1/L2), the length of each ray path element through each intersected voxel is calculated from the known positions of the satellites and receivers. The unknown electron densities are assumed to be constant within each voxel and contained in the column vector $\boldsymbol{x}$. The inversion problem can be expressed by the same equation given in Equation (7.1), but with the matrix $\boldsymbol{b}$

containing measured slant TEC and $\boldsymbol{A}$ containing the path lengths of a satellite-to-receiver signal propagating through each voxel. It is not possible to directly invert the matrix $\boldsymbol{A}$ and solve for $\boldsymbol{x}$, because $\boldsymbol{A}$ is typically singular and the inverse system is underdetermined. To overcome this, prior information is added to the algorithm to obtain a physically plausible solution. The approach used by MIDAS is to introduce a mapping function that transforms the problem into a set of empirical orthogonal basis functions (EOFs) with unknown coefficients. The time, geographic location and geophyiscal conditions can be used to specify the EOFs. In MIDAS, the EOFs are described by either the empirical model IRI (international reference model[2]) or by the Chapman function, which is described in *Davies* (1990). The EOFs provide the constraint to the vertical profile. Equation (7.1) now becomes:

$$\boldsymbol{b} = \boldsymbol{AMy} + \boldsymbol{e}, \tag{7.2}$$

where $\boldsymbol{y}$ represents the basis functions, and $\boldsymbol{M}$ represents the unknown coefficients representing the relative contribution of the basis functions, such that $\boldsymbol{My}$ defines a basis expansion of TEC. To eliminate $\boldsymbol{e}$, the differences between pairs of rows belonging to the same satellite-receiver pair are calculated. The resulting solution is then solved using MATLAB's MINRES (minimum residue[3]) or quadprog (quadratic programming[4]). Applying the coefficients back to the basis functions, the solution of electron density is given by:

$$\boldsymbol{x} = \boldsymbol{My}. \tag{7.3}$$

The algorithm is extended into a time-dependent inversion system by integrating the solution at discrete temporal steps of usually 10 minutes.

7.4 Ray Tracing

As previously mentioned, in Chapter 1 and later chapters, the ionosphere is a refractive medium and the propagation of radio waves deviates from linearity for the low end spectrum of high frequency waves. This means that a radio signal will experience both a signal

[2]http://modelweb.gsfc.nasa.gov/ionos/iri.html
[3]http://www.mathworks.com/help/techdoc/ref/minres.html
[4]http://www.mathworks.com/help/toolbox/optim/ug/quadprog.html

delay and a phase shift as it propagates through the ionosphere. Importantly here for LOFAR, the signals will refract and this is greater the lower the frequency. To investigate ray propagation under different ionospheric conditions, ray theory is used. The equations describing ray propagation, developed from *Coleman* (1993), used in this project are based on *Haselgrove* (1954). *Coleman* (2008) gives a detailed derivation of the Haselgrove equations from Maxwell's equations and equation of motion for ionospheric applications. The Haselgrove differential equations in *Coleman* (2008) are presented as follows:

$$\frac{dx_i}{dt} = -4p_i(1 - X - Y^2)(q^2 + 1) - 2p_iY^2 - 2p_i(\boldsymbol{p} \bullet \boldsymbol{Y})^2 \\ -2Y_i(p^2 - 1)(\boldsymbol{p} \bullet \boldsymbol{Y}) \tag{7.4}$$

$$\frac{dp_i}{dt} = \left\{[-(p^2 - 1) + (\boldsymbol{p} \bullet \boldsymbol{Y})^2 + 2(1 - 2X) - Y^2]q + 2 - 3X\right\}\frac{\partial X}{\partial x_i} + \\ \sum_{j=1}^{3}(p^2 - 1)[2(\boldsymbol{p} \bullet \boldsymbol{Y})p_j - 2(q + 1)Y_j]\frac{\partial Y_j}{\partial x_i}, \tag{7.5}$$

where $q = (p^2 - 1)/X$, $X = \omega_p^2/\omega^2$, $\boldsymbol{Y} = -e\boldsymbol{B}_0/m\omega$. In these equations $\boldsymbol{x}$ is the position vector of the ray, $\boldsymbol{p}$ is the normal to the surface of constant phase at that position, ω_p is the plasma angular frequency, ω is the signal angular frequency, $\boldsymbol{B}_0$ is the magnetic field of the Earth represented by a tilted dipole. It should be noted that q satisfies the quadratic equation $q^2(1 - X - Y^2) + q[(\boldsymbol{Y} \bullet \boldsymbol{p})^2 + 2(1 - X) - Y^2] + 1 - X = 0$. Electron density from MIDAS are converted to plasma frequency, using Equation (3.2) presented in Chapter 3, then substituted into Equations (7.4) and (7.5). Equations (7.4) and (7.5) are then solved using Runge-Kutta-Fehlberg adaptive techniques (*Coleman*, 1993). The use of this ray-tracing method with ionospheric maps from MIDAS will provide a near real time monitoring system for LOFAR frequency management.

The ray propagation paths will be plotted superimposed on electron density maps, showing how the ray path curves as it travels through the ionosphere. The ground distances are traveled by the ray given the position and bearing of the receiver, the elevation angle and the launch range (altitude of 5000 km); this geometry is illustrated by Figure 7.2.

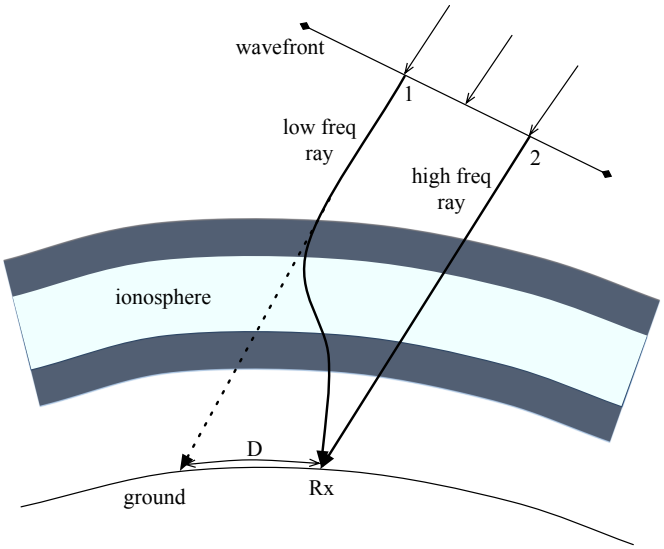

Figure 7.2: Sketch of the geometry of ray racing, where D is the ground range calculated for the ray launched from 5000 km, and given inital elevation angle and bearing of the receiver R_x

Also important for the LOFAR community is the distortion of wavefronts caused by the ionosphere. If a wavefront from an astronomical source arrives at a given point on the ground, such as a LOFAR array element, the element will receive energy from different points of the wavefront at different frequencies (see Figure 7.2). While the distortion is negligible at extremely high frequencies, it can be quite considerable at lower frequencies. The increased phase path length could potentially cause the lengthening of the geometrical path. However this is counterbalanced by the reduction in phase refractive index at lower frequencies. The distortion in phase in this thesis is described through the change in phase path, at a given point on the ground when the frequency changes from extremely high down to the desired LOFAR frequency. Phase path is defined as $P = \int \boldsymbol{k} \bullet d\boldsymbol{s}$ where $\boldsymbol{k}$ is the propagation vector and $d\boldsymbol{s}$ is the element of the ray path at a given point (see *Davies* (1990)). Note that the initial wavefront is taken to be a plane well above the ionosphere and that the start point on this plane will change with frequency.

7.5 Ray propagation results

In this section results for ray propagation for the ionospheric conditions on 24 March 2004 are presented as a case study for illustration purposes. This illustration was performed for the lower frequencies (10-50 MHz) that will be used by LOFAR, and over the European

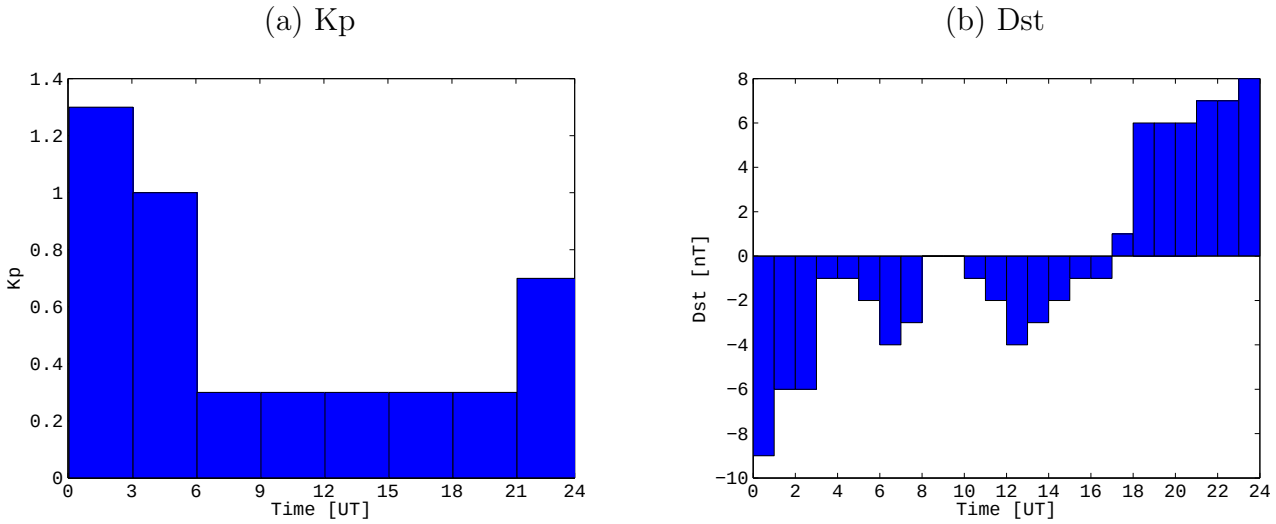

Figure 7.3: Kp and Dst indices on 24 March 2004

Table 7.1: LOFAR stations selected.

City/Town	Country	Latitude	Longitude
Exloo	The Netherlands	52.8° N	6.4° E
Garching	Germany	48.1° N	12.6° E
Chilbolton	United Kingdom	51.1° N	1.4° W

region as the instrument is based in this region. For comparison day and night results will be presented. The day was chosen because it was a geomagnetically quiet day as indicated by Kp and Dst indices shown in Figure 7.3, and will therefore illustrate normal day to day variability of the ionosphere.

Electron density maps over the European region and surroundings, latitudinal range of 34° - 70° N and longitudinal range of 12° W - 30° E, on 24 March 2004 at 12H20 and 21H00 UT, representing ionospheric conditions during day and at night respectively, are presented in Figure 7.4. The comparison of the plots show the diurnal trend, where the electron densities during the day are greater than the electron densities at night. A South-East to North-West electron density gradient is observed in Figure 7.4(a).

Figure 7.5 presents results of 10 MHz ordinary "—" and extra-ordinary "---" ray paths with elevations angles of 25° (black), 45° (magenta), and 80° (white). The waves are traveling through the day time and night time ionosphere at some of the LOFAR stations; station information is provided in Table 7.1. Figure 7.5 (a) to (d) present rays propagating in from 90° West of North, while Figure 7.5(e) and (f) present rays propagating from 90°

(a) Day time: 12H20 (b) Night time: 21H00

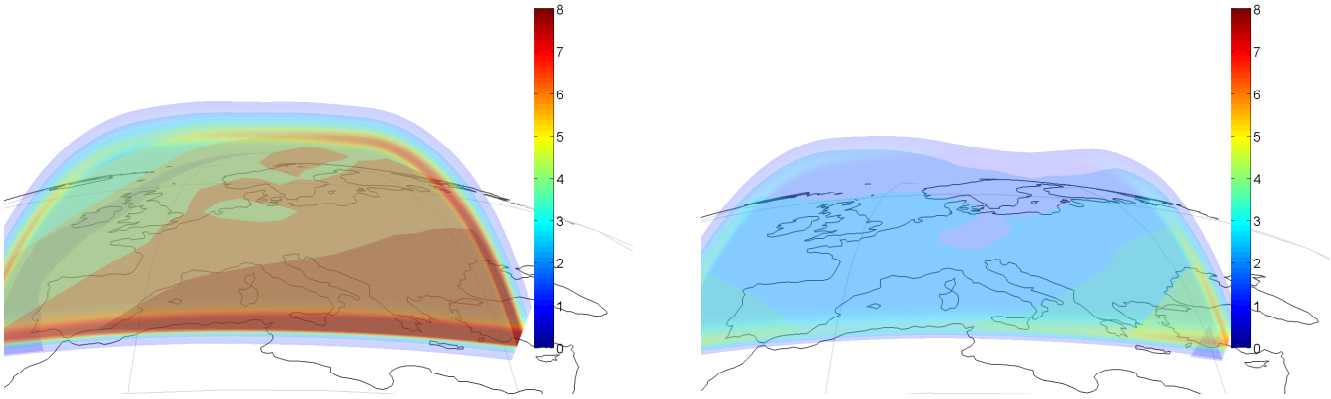

Figure 7.4: 3D Electron density maps on 24 March 2004 at 12H20 and 21H00 UT in the European region, which covers latitudes of 34° N to 70° N and longitudes of 12° W to 30° E. Electron density in units of 10^{11} electrons per cubic metre. Note colour bar values varies from 0 to 8 electrons per m^3.

East of North. The refraction is severe during the day in all the stations such that the low and mid elevation rays do not reach the stations as they are sent back into space; only the near-zenith elevation rays reach the stations. However during the night the refraction is only at low elevation angels; mid and near-zenith elevation rays reach the stations.

Figure 7.6 presents propagation curves for (a) 20 MHz and (b) 50 MHz waves traveling through the day time ionosphere from 90° West of North at elevation angles of 25° (black), 45° (magenta), and 80° (white) and received in Exloo station. The plots illustrate that the degree of bending of the ray paths decreases as the frequency increases. This is due to the inverse relationship between the refractive index and the frequency, which can be seen for example from Equation 3.22 in Chapter 3.

Figure 7.7 presents the deviation of a 10 MHz ray landing points for the ray traveling in the absence of the ionosphere to the ray traveling through (a) day time and (b) night time ionosphere. From both plots in Fig 7.7 it can be seen that there is significant deviation in the landing points when the ray has traversed the ionosphere than in the absence of the ionosphere. This deviation is more severe for the day time ionosphere than the night time ionosphere, because of the higher electron density during the day. Also the extra-ordinary wave mode (represented by blue "×") experiences different deviations from the ordinary wave mode (represented by red "o") because the wave modes take slightly different paths in the ionosphere.

(a) Exloo Day

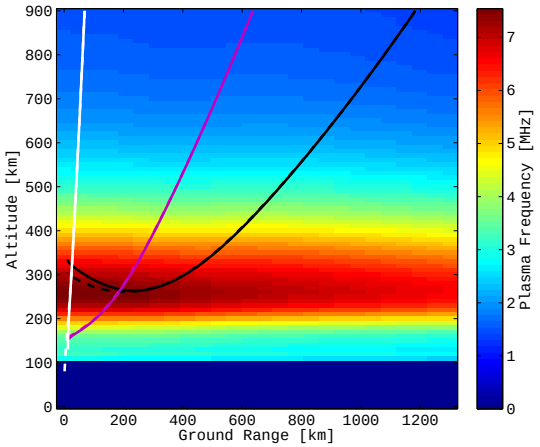

(b) Exloo Night

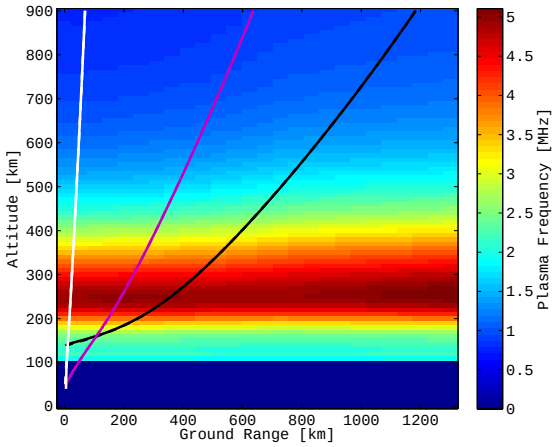

(c) Garching Day

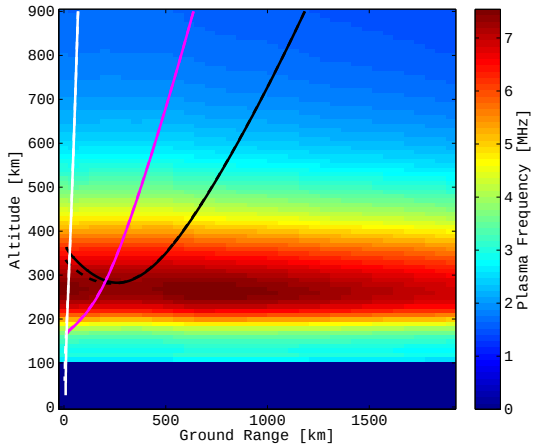

(d) Garching Night

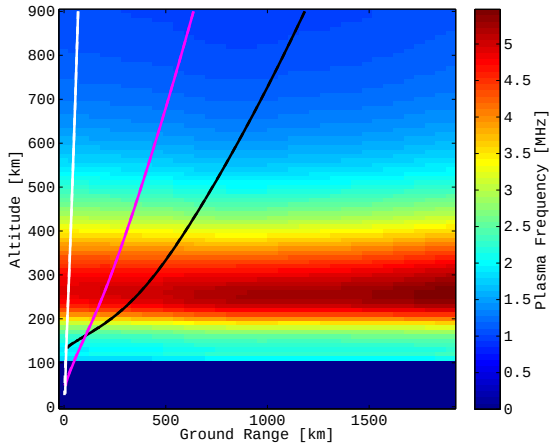

(e) Chilbolton Day

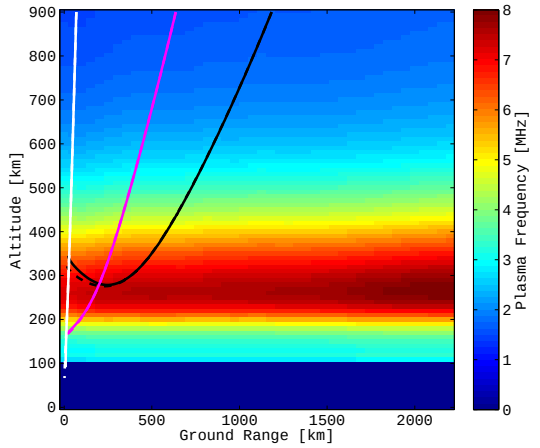

(f) Chilbolton Night

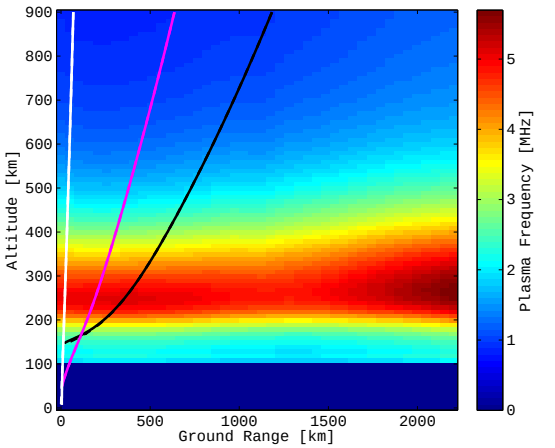

Figure 7.5: Ordinary "—" and extra-ordinary "---" ray propagations of 10MHz wave at elevation angels of 25° (black), 45° (magenta), and 80° (white) through day and night time ionospheres.

(a) 20 MHz

(b) 50 MHz

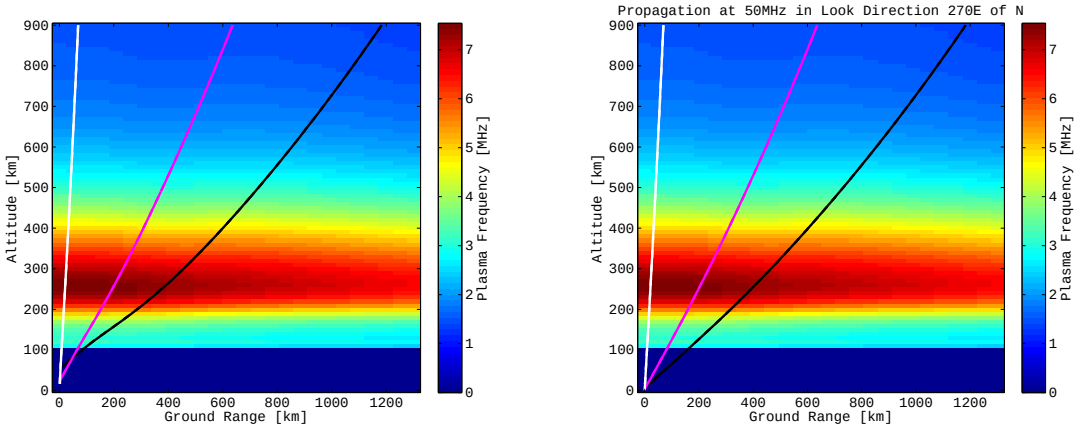

Figure 7.6: Ordinary "—" and extra-ordinary "- - -" ray propagations of (a) 20 and (b) 50 MHz waves at elevation angles of 25° (black), 45° (magenta), and 80° (white) through the day time ionosphere at Exloo.

Figure 7.8 presents phase path deviations experienced by a 10MHz extra-ordinary mode ray propagating through the ionosphere (a) during the day (i.e. 12:20 UT) and (b) at night (i.e. 21:00 UT). The ray has an elevation of 80° and bearing of LOFAR array is 0° East of North. The negative sign in the phase path difference means that the phase path has decreased and that the geometric distortions are insufficient to reverse the effect of a reduction in phase refractive index, (*Coleman, 2011; private communication*). It is noted that the variation in the phase deviations scale roughly with variation in electron density across the map and time in Figure 7.8; the higher electron density areas have greater phase path deviations and phase path deviations are greater during the day than at night. It is worth mentioning that although the magnitude of the phase path deviations are quite large (over 3 cycles during the day and over 1 cycle at night), the variation of phase path deviations across the map is not that large; difference is roughly 180° during the day and 140° at night. It is expected that the biggest difference across the map will be when the solar terminator falls within the map, as there are instabilities and turbulence in the ionosphere associated with the passing of the solar terminator.

(a) Day time

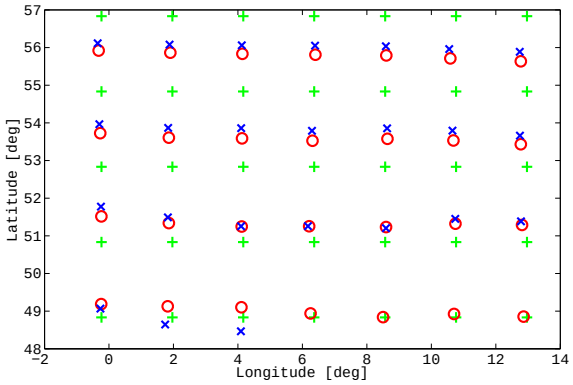

(b) Night time

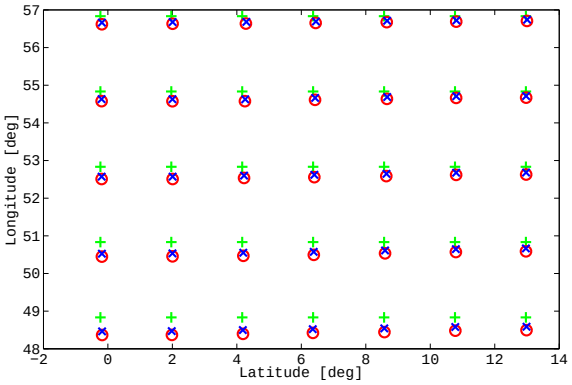

Figure 7.7: 10MHz ordinary (represented by red "o") and extra-ordinary (represented by blue "×") ray landing coordinates when the ray traversed the ionosphere, and in the absence of the ionosphere (represented by green "+"). The elevation of the ray is 50° and the bearing of the ray is 0° East of North.

7.6 Statistical analysis of TEC changes over different timescales

Having demonstrated the effect of the ionosphere on radio signals, during quiet magnetic conditions, it is useful to investigate the change in TEC over different time scales. This investigation will give an indication of the TEC perturbations under different conditions. The analysis for the difference in TEC over 5, 10, 30 and 60 minutes was performed. TEC changes were calculated as follows:

$$\text{TEC change} = X(t + \Delta t) - X(t), \tag{7.6}$$

where X denotes (filtered) TEC, t is time in minutes, Δt is time window length. This is similar to the rate of change of TEC index (ROTI) and derivative of rate of change of TEC index (DROTI), however these indices are used for scintillation studies over the equatorial region, see for example *Basu et al.* (1999) and *Bhattacharyya et al.* (2000), and therefore ROTI/DROTI studies will not be used for comparisons with TEC changes results obtained in this section. The results presented in this section were obtained from processing all the TEC data available between 1975 and 1991.

Histograms showing the change in TEC either side of a 5, 10, 30 and 60 minute time

(a) Phase Deviations at 12:20 UT

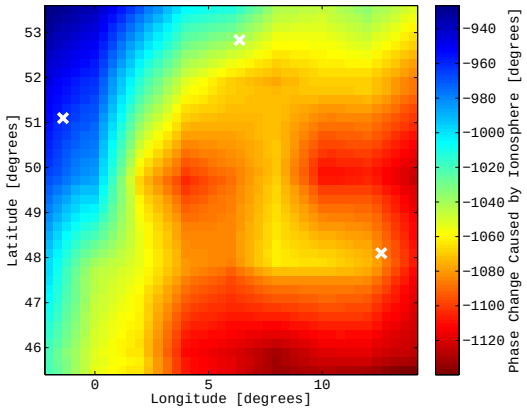

(b) Phase Deviations at 21:00 UT

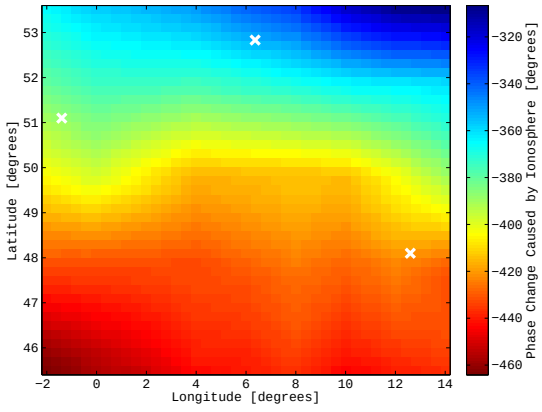

(c) Maximum Electron Density at 12:20 UT

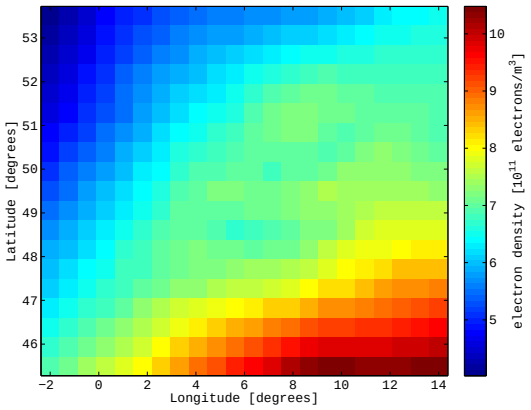

(d) Maximum Electron Density at 21:00 UT

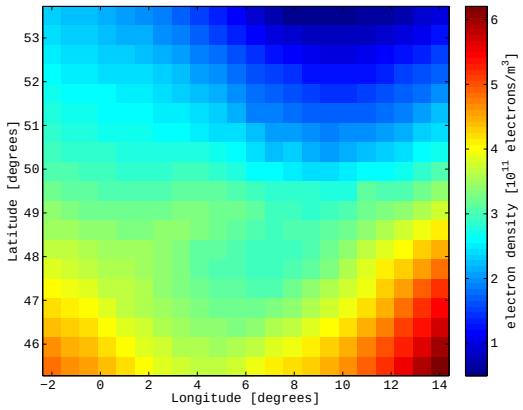

Figure 7.8: Phase path deviations caused by the ionosphere for a 10MHz extra-ordinary mode ray having an elevation of 80° and bearing of 0° East of North at (a) 12:20 UT and (b) 21:00 UT; white "×" symbols mark the positions of the Exloo, Garchin and Chilbolton LOFAR stations. Maximum electron density maps at the corresponing times are also shown in (c) and (d).

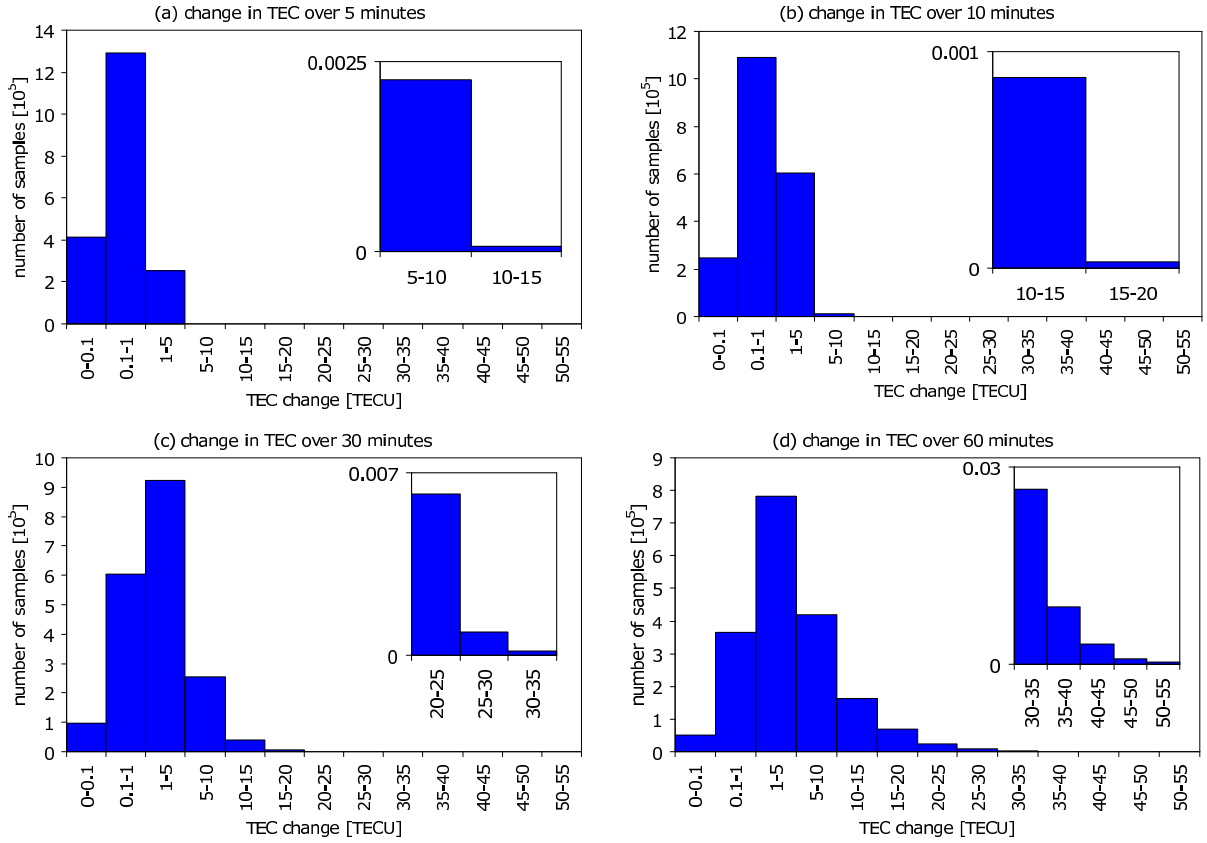

Figure 7.9: Histograms of changes in TEC over different time windows. The inserts accompanying the figures are the rescaled bins that are too small to be seen clearly in the original sized figures.

window are presented in Figure 7.9(a) - (d) respectively. The most dominant bin is the bin with the most samples. Figure 7.9 shows that for the shorter time windows, i.e 5 and 10 minutes, the most dominant change in TEC has values between 0.1-1 TECU, while for the longer time windows, i.e 30 and 60 minutes, the most dominant change in TEC has values between 1-5 TECU. Also over 80% of the change in TEC values in the 5 minute window fall below 1 TECU, over 68% TEC change in the 10 minute window are less than 1 TECU, over 63% are greater than 1 TECU in the 30 minute window, and over 77% are greater than 1 TECU in the 60 minute window. In short, as the window grows longer, the change in TEC gets higher. This makes sense since as the window grows larger, larger TEC changes are expected as the diurnal trend will be included in the results.

Figure 7.10 (a) - (d) presents histograms of changes in TEC for the filtered profiles. The filtered profiles are obtained from applying a Savitzky-Golay filter with a cut-off period of 3 hours as used in the TID analysis, and explained in Chapter 4 Section 4.2.1. It can

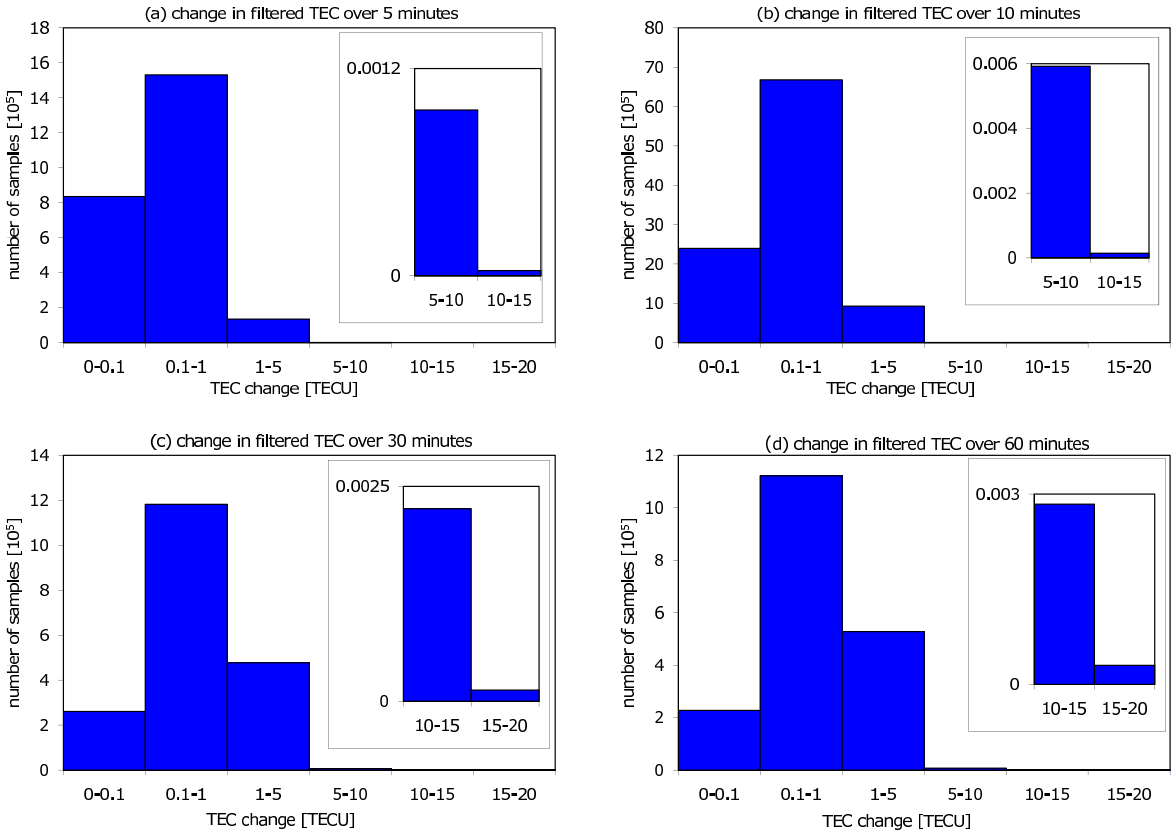

Figure 7.10: Histograms of changes in filtered TEC over different time windows. The inserts accompanying figures are the rescaled bins that are too small to be seen clearly in the original sized figures.

be seen that throughout the different time windows, most dominant change in TEC lies between 0.1-1 TECU. Also, Figure 7.10 shows that for the shorter time windows, i.e 5 and 10 minutes, most of the TEC changes (i.e over 90%) fall below 1 TECU while for the longer time windows, i.e 30 and 60 minutes, most of the TEC changes (i.e over 84%) are greater than 0.1 TECU. It is interesting that again as the window grows larger, larger TEC changes are observed in the filtered profile. It is interesting because this trend cannot be associated with the diurnal (or semi-diurnal) trend since this trend has been removed.

Seasonal analysis of all the data (i.e 1975-1991) is presented in Figures 7.11 and 7.12 for both TEC and filtered TEC. Furthermore a comparison of seasonal trends between TEC and filtered TEC during solar minimum (i.e 1975-1976) and solar maximum (i.e 1989-1990) is presented in Figures 7.13 and 7.14. The probability of getting a TEC change of a certain size in each time window is seasonally adjusted so that the probabilities are for a day randomly sampled from the year where each season is given an equal weight. This

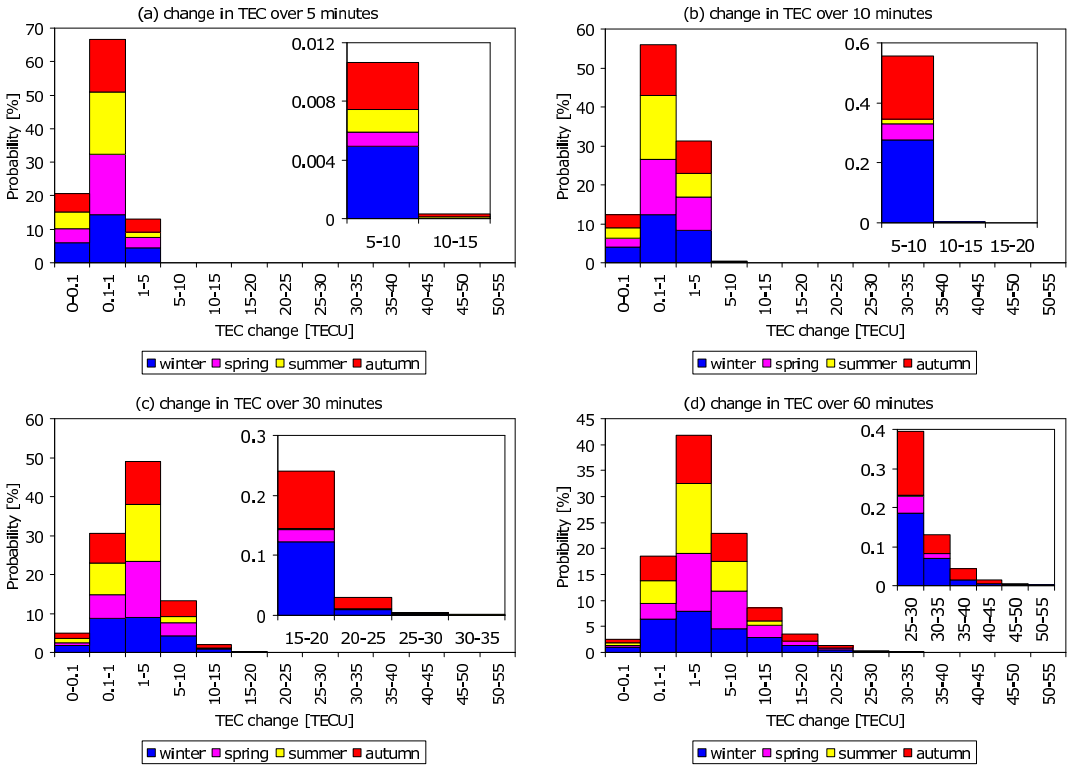

Figure 7.11: Histograms of probabilities for changes in TEC over different time windows by season. The inserted accompanying figures are the rescaled bins that are too small to be seen clearly in the original sized figures.

adjustment ensures that the results obtained from the seasonal analysis are not biased on the number of samples per season. The probability of each size in each time window during each season is calculated as follows:

$$P_{i,j,k} = \frac{N_{i,j,k}}{N_{j,k}} \times P_k \times 100 = \frac{N_{i,j,k}}{N_{j,k}} \times 0.25 \times 100 \tag{7.7}$$

where i denotes size of TEC change, j denotes the time window and k denotes the season, $N_{i,j,k}$ is the number of samples with size of TEC change i in time window j during season k, $N_{j,k}$ is the total number of samples in time window j during season k and P_k is the prior probability of getting a season k. Note that the probability of getting each season is assumed to be the same, i.e 0.25. The histograms in Figure 7.11 - Figure 7.14 are effectively a mixture of seasonal probability mass functions.

Study of Figure 7.11 shows no clear dominant season throughout each time window. For example, winter has the least probability of having a 1-5 TECU TEC change for the 5

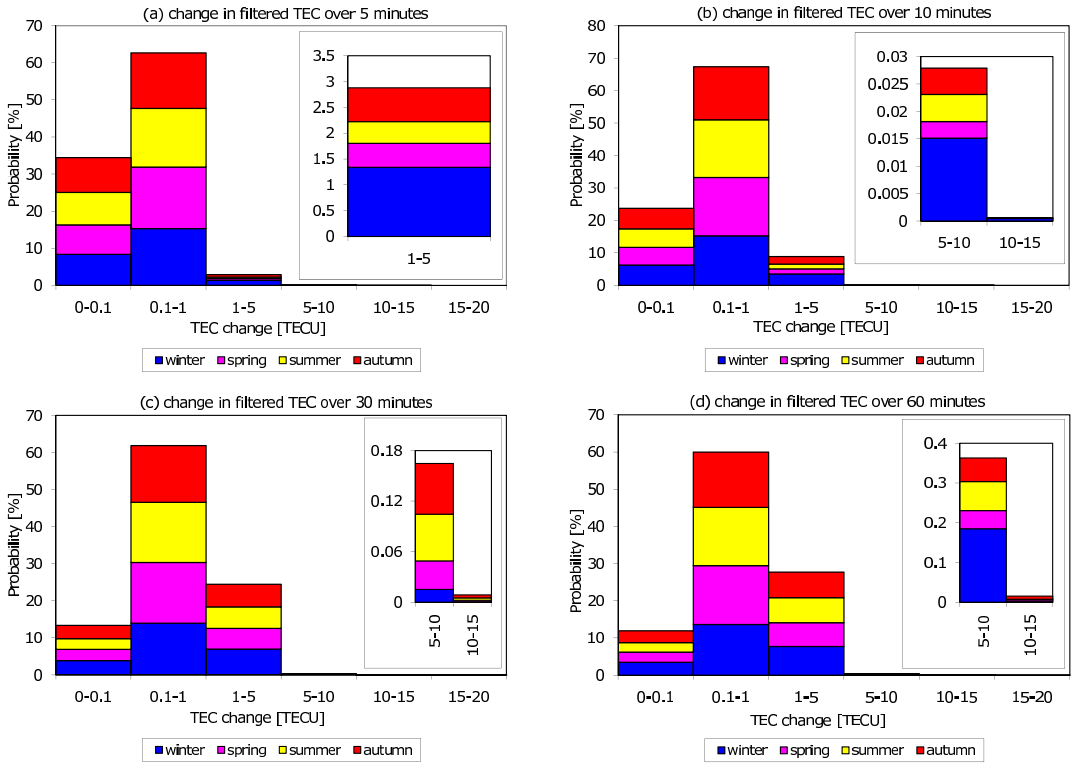

Figure 7.12: Histograms of probabilities for changes in filtered TEC over different time windows by season. The inserts accompanying figures are the rescaled bins that are too small to be seen clearly in the original sized figures.

and 10 minute windows, while summer has the least probability of having a 1-5 TECU TEC change. Even within one time window the season variation for the different TEC gradients is not consistent. For example for the 30 minute window, spring has the least probability in TEC change of 0-0.1 TECU, while winter has the least probability in TEC change of 1-5 TECU but has greatest probability in TEC change of 10-15 TECU. Similar observations are seen in the season analysis of the filtered TEC profiles presented in Figure 7.12; there is no consistent seasonal trend. The absence of a consistent seasonal trend is also observed in the analysis of TEC and filtered TEC gradients during solar minimum and solar maximum, as can be seen from Figures 7.13 and 7.14.

The results presented in Table 7.2 are calculations of the average and maximum change in TEC (absolute and filtered, where the filtered TEC is denoted TEC_{SG}) over the different time windows during the entire period of the data coverage, at each season and solar cycle phase. Data for solar minimum was taken from October 1975 to September 1976 and from December 1989 to December 1990 for solar maximum. It is worth noting that the highest mean and maximum change in TEC (for absolute TEC measurements) is obtained from

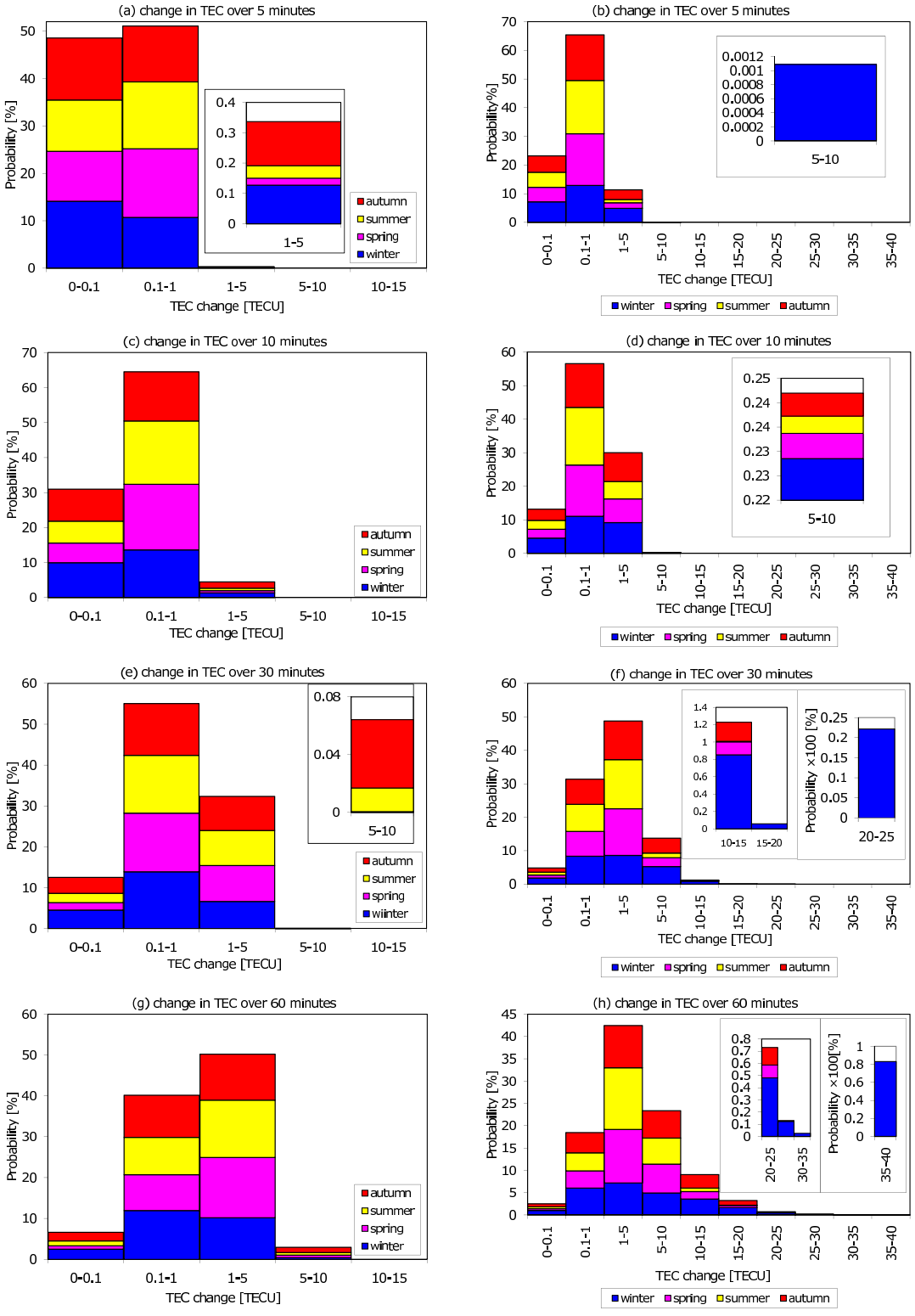

Figure 7.13: Histograms of probabilities for changes in TEC during solar minimum (left column) and solar maximum (right column) over different time windows by season. The inserts accompanying figures are the rescaled bins that are too small to be seen clearly in the original sized figures.

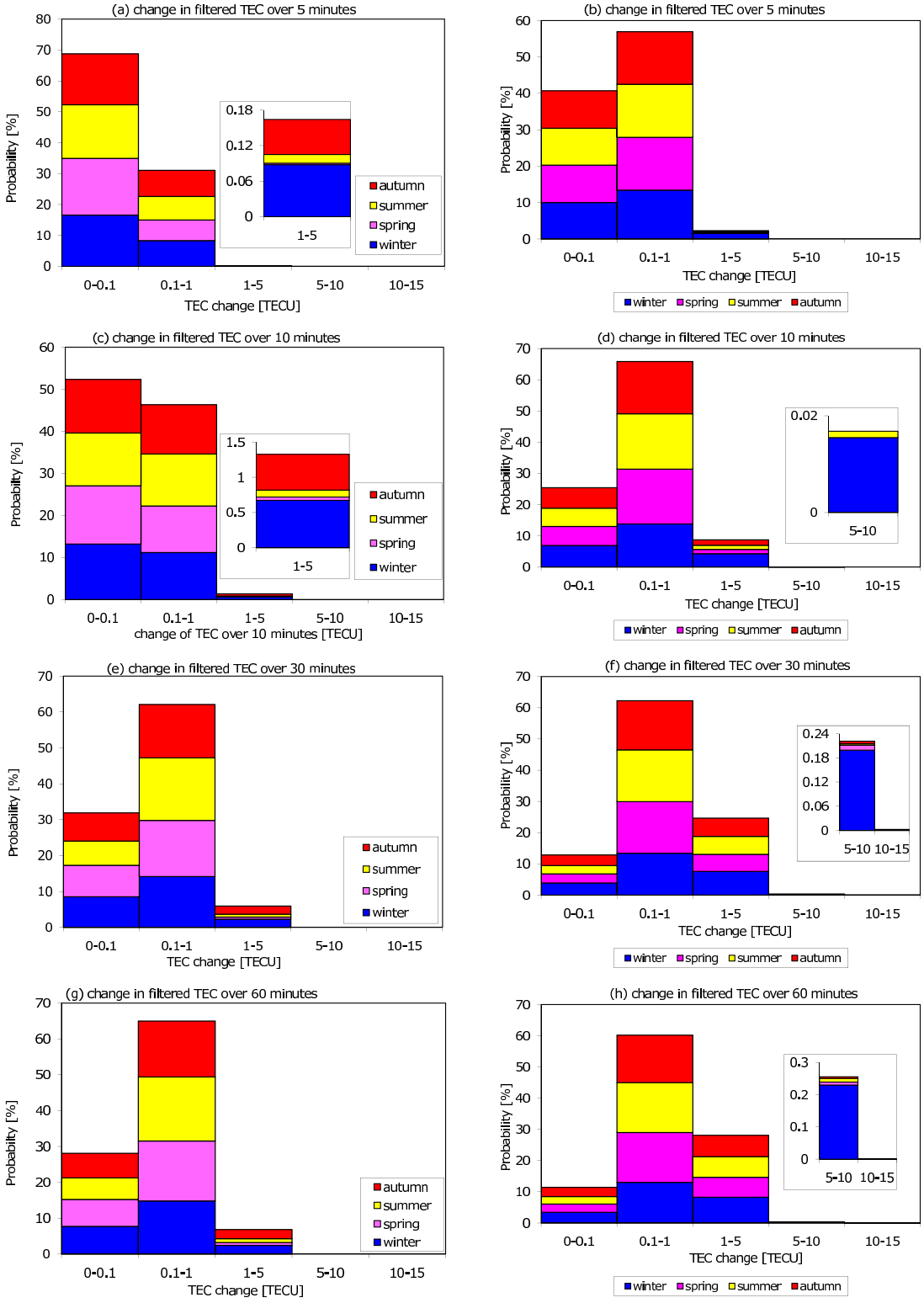

Figure 7.14: Histograms of probabilities for changes in filtered TEC during solar minimum (left column) and solar maximum (right column) over different time windows by season. The inserts accompanying figures are the rescaled bins that are too small to be seen clearly in the original sized figures.

Table 7.2: Total, seasonal and solar cycle average and maximum change in TEC over 5, 10, 30 and 60 minute windows.

	5 minute		10 minute		30 minute		60 minute	
	TEC	TEC_{SG}	TEC	TEC_{SG}	TEC	TEC_{SG}	TEC	TEC_{SG}
Total mean	0.5	0.3	0.9	0.4	2.5	0.7	4.9	0.8
Total max	12.8	12.4	15.5	12.6	31.6	18.9	54.1	18.5
Winter mean	0.5	0.3	1.0	0.5	2.8	0.8	5.4	1.0
Winter max	9.9	8.7	15.2	12.8	31.6	14.8	54.1	11.8
Spring mean	0.5	0.3	0.9	0.4	2.7	0.7	5.3	0.7
Spring max	8.3	6.6	9.7	8.7	18.9	14.9	35.0	13.9
Summer mean	0.4	0.2	0.7	0.4	1.9	0.7	3.6	0.8
Summer max	12.5	12.4	12.8	12.6	30.0	13.1	49.2	10.9
Autumn mean	0.5	0.2	1.0	0.4	2.9	0.7	5.6	0.8
Autumn max	12.8	9.8	15.5	9.8	28.4	18.9	48.2	18.5
Solar min mean	0.2	0.1	0.3	0.2	0.8	0.3	1.5	0.4
Solar min max	3.3	3.4	3.2	3.4	6.4	4.5	11.3	4.5
Solar max mean	0.5	0.2	0.9	0.4	2.5	0.7	4.9	0.8
Solar max max	5.6	4.2	8.3	8.3	20.7	12.0	38.2	10.5

the 60 minute window. The highest average change in TEC for the filtered TEC measurements is obtained from the 60 minute window, while the highest maximum change in TEC is obtained from the 30 minute window, showing that the maximum change in TEC is not necessarily obtained from the longest time window. Also, average and maximum TEC changes are greater during higher solar activity than during lower solar activity.

It should be noted that the resulted presented in this section are from Faraday rotation derived slant TEC, where only the first order term and the geomagnetic field term were used in the approximation of the refractive index. Studies have shown that at lower frequencies the higher order terms are not negligible, for example see *Lay et al.* (2011) and *Petit and Luzum* (2010). Although not all these studies show the ionospheric errors estimated from the higher order terms in TECU, they all give an indication about the impact of the higher order terms in relation to the first order term, at lower frequencies. However the first order term contributes the most therefore this study is very useful in terms of range of expected TEC fluctuations over short time scales during different seasons and solar cycle.

7.7 Summary

Through a ray tracing technique with the use of measured ionospheric electron density maps, results have been presented that can help to show the impact of the ionosphere on two different radio systems. The results showed that the low elevation, low frequency signals are strongly refracted by the ionosphere such that they do not reach the receiving LOFAR stations. The level of refraction was shown to vary geographically. Also, the severity of refraction varied temporally where signals traversing the day time ionosphere were affected more than those traversing the night time ionosphere. Phase shifts, caused by ray bending, experienced by the rays were found to vary across the European regions, but were comparable during both day and night time. These results indicate that frequency management will be vital for the full use of the array, especially at low frequencies and for rays propagating at low elevations. It is worth noting that the results for this case study were for a quiet ionosphere. During disturbed conditions the ionosphere changes dramatically and very quickly. Therefore under such conditions, it is expected that the ionosphere will have more severe impacts on the ray propagations.

EGNOS uses a single layer ionospheric model to produce ionospheric corrections to the GPS signals which are provided as part of the service. Therefore a statistical analysis on the change in TEC will be useful to the EGNOS community in bounding TEC errors produces by this model. The statistical study was done by calculating change in TEC over different time windows, i.e 5, 10, 30 and 60 minutes windows. In terms of short-term gradients in TEC during 1975-1982 and 1989-1991, the maximum changes in absolute TEC were 12.8 TECU, 15.5 TECU, 31.6 TECU and 54.1 TECU per 5 minutes, 10 minutes, 30 minutes and 60 minutes respectively. For the filtered TEC data the maximum changes were 12.4 TECU, 12.6, 18.9 and 18.5 per 5, 10, 30 and 60 minutes respectively. However during the solar minimum period of 1975-1976, the maximum changes in absolute TEC measurements were 3.3, 3.2, 6.4 and 11.3 TECU per 5, 10, 30 and 60 minutes respectively, while for the filtered TEC measurements the maximum changes were 3.4, 3.4, 4.5 and 4.5 TECU per 5, 10, 30 and 60 minutes windows respectively. Also, during the solar maximum period of 1989-1990, the maximum changes in absolute TEC measurements were 5.6, 8.3, 20.7, and 38.2 TECU per 5, 10, 30 and 60 minutes respectively, while for the filtered TEC measurements the maximum changes were 4.2, 8.3, 12.0 and 10.5 per 5, 10, 30 and 50 minutes respectively.

The largest change in absolute TEC was observed in autumn for both the 5 and 10 minute windows and in winter for both the 30 and 60 minute windows. On the other hand, for the filtered TEC profiles the greatest change in TEC was observed in summer for the 5 and 10 minute windows and in autumn for the 30 and 60 minute windows. Also, average and maximum change in TEC was higher during solar maximum than during solar minimum. The information obtained from this study is intended to be used as a guide for perturbations that can be observed in TEC measurements during different seasons and geomagnetic conditions. This information should be useful to LOFAR and EGNOS users, as well as planners of future radio instruments.

Chapter 8

Conclusions and Future Work

8.1 Summary and Conclusions

The availability of radio measurements from global navigation and communication systems has made possible local and global studies of the ionosphere using TEC measurements. For example, TEC measurements from different missions have been used to probe the response of the ionosphere to storms; reviewed by *Mendillo* (2006). New radio systems are planned or under development in order to improve the accuracy and resolution of the existing systems. In order to make these improvements viable, measurements from existing instruments can be used to study the effects of the ionosphere on ray propagation. In this project, TEC measurements calculated from Faraday rotation measurements have been used to study changes in TEC from different seasons, geomagnetic and solar activities. Also the data was used to produce a statistical study of the tides, TIDs, and DDMs. These studies were carried out in order to quantify reasonable measurements and identify errors introduced by the ionosphere on radio measurements. Chapter 1 presented the thesis objectives and overview, while Chapter 2 presented material on the theory of the ionosphere, TIDs, DDMs and tides. The instruments and measurements used to study the ionosphere and the three wave structure (i.e TIDs, DDMs and tides) were presented in Chapter 3.

Accurate extraction of tides and TID components in the measurements rely on the methods used. In Chapter 4 case studies were then done to determine the accuracy of chosen methods that analyse TEC measurements for tides, and TID signatures. In the case of tides, see Section 4.1, a delay filter adopted from *Bernhardt et al.* (1976) was used because

the filter was designed from similar data and had shown success in determining different components of the tides. Results from tidal case studies showed that the filter was not sufficient to show conclusive results with our measurements. This conclusion was drawn based on the fact that even though the filter was successful in pulling out the lunar tides, these were observed in the spectrum of post filtered signal, but not observed in the spectrum of pre-filtered data (i.e the original signal). Furthermore, the amplitude of the observed lunar tide was comparable to noise level in the lunar tide amplitude spectrum. Therefore it was impossible to verify if the filter was extracting real lunar tides from the measurements.

In the case of TIDs, three time-series analysis methods were investigated, namely Savitzky-Golay filter, Fourier analysis and wavelet analysis, see Section 4.2. In order to obtain amplitude and period information of TIDs, Fourier analysis was applied to TEC measurements. The diurnal component, and slow varying components, swamped the spectrum such that it was impossible to recognise a TID signature from the spectrum. It became necessary to detrend the data in order to reveal the high frequency structures. The Savitzky-Golay filter with a cut-off frequency of 0.3 cycles per hour was used to remove low frequency structures. Also it was useful to determine during which part of the day had the most TID activity. To determine this, discrete wavelet analysis was used because the method allowed for frequency and time decomposition of the non-stationary signal. The wavelet analysis employed a discrete Meyer wavelet which had an orthonormal basis, thus facilitating the decomposition of the measurements into TEC variations in different parts of the day by using the ANOVA method. This then made it possible to determine which part of the day had the most TID activity. The advantages and disadvantages of the Savitzky-Golay filter, and discrete Fourier and wavelet analyses were evaluated through a case study of two TEC profiles; one varying fairly smoothly and another with prominent wave structures. It was realised that each method provided complementary information about TIDs and concluded that all three methods should be used to get the most information.

Also discussed in Chapter 4 is the method used to extract information on DDM structures, see Section 4.3. This included the methods used to calculate the duration of the structure, the relative magnitudes of each peak of the DDM structure, and probabilities of observing the DDM structures during different seasons and geomagnetic condition. These were used to produce statistics on occurrences and amplitudes of the DDM structures, and to determine whether there is a single mechanism responsible for the DDM.

Chapter 5 presented results on the wave amplitudes, periods and variability of the TIDs. The plan was to use Fourier analysis to extract periods and amplitudes of the TID structures. However due to the non-stationarity of the observable it was found that the method produced unrealistic amplitudes. Therefore TID amplitudes were extracted directly from detrended data. Seasonal as well as solar activity comparisons were done for this study. Solar minimum was represented by 1975-1976 and solar maximum by 1989-1990. The results from direct inspection of the detrended data showed that daily absolute maximum amplitudes range from 0.65 to 4.8 TECU during solar minimum and from 1.7 to 12.9 TECU during solar maximum. The observed maximum amplitudes of the waves are largest at solar maximum. The mean amplitudes are largest in autumn and winter with both seasons having a mean of 2.5 TECU during solar minimum. At solar maximum the mean amplitudes are largest in winter, where the mean wave amplitude is 5.8 TECU. In comparison to the maximum diurnal TEC, the maximum TID amplitude was 17%, and the maximum of the mean amplitude was 4.1% during both solar cycle phases. From Fourier analysis it was observed that the periods of the waves vary between 0.44 and 3.0 hours during solar maximum and between 0.37 and 3.0 hours during solar minimum. The most commonly occurring period lie between approximately 1.7-1.8 hours during solar minimum and between approximately 1.7-2.0 hours during solar maximum. It was observed that during solar minimum the periods of the most dominant components were longer in autumn and summer than in winter and spring, while during solar maximum the longest periods of such components occurred in summer. Results from the discrete wavelet analysis show that the TIDs contributed more significantly to the TEC variability during mid-day than during the morning and evening. Results from discrete wavelet analysis suggest that the mid-day TIDs, with periods between 48 minutes and 1.6 hours, were predominantly larger in terms of energy than early morning or evening TIDs during both solar minimum and maximum. The morning waves were larger than the evening TIDs during solar minimum but a similar trend was not observed during solar maximum. No seasonal trend was observed for the large scale TIDs, i.e period of 1.6 hours. However for the medium scale TIDs, i.e period of 48 minutes, comparatively little activity was observed during summer during both phases of the solar cycle. It is important to note that due to the nature of our data there is some limitation regarding the accuracy of the amplitudes and the variation analyses. It was recognised that the medium scale TIDs with shorter periods and shorter wavelengths will have had a smaller amplitude measured because of the effects described in Section 4.2.5.

Chapter 6 presented results of the study of DDM structures. Out of 1,366 TEC profiles there were 302 TEC profiles observed to have a DDM structure. The DDM structures could be classified into two groups; enhancement structures where the peaks of the structure are greater than their corresponding calculated monthly mean profile, and the depletion structures where peaks of the structure are similar to the monthly mean profile and the depletion was lower than the monthly mean. The probability of getting a DDM was found to be greater during moderate geomagnetic than quiet and disturbed geomagnetic conditions, and greater during winter and summer than during spring or autumn. The analysis showed that the second peak occurred later during summer than during the other seasons, while the time of the first peak did not vary much with season. The magnitude of the peaks were found not to significantly vary with season or geomagnetic condition. The times of occurrence of the peaks of the DDM structures were also not found to significantly vary with geomagnetic condition. Of the 302 DDM structures observed, only 119 could be verified with $foF2$ measurements from an ionosonde in Rome, due to either no corresponding $foF2$ measurements for that day or a DDM structure not clearly visible in $foF2$ measurements. There was not enough supporting evidence to link DDM structures to plasma vertical displacement as only a few cases were found where $hmF2$ had the same double peak structure. A study of the relationship between the occurrence of a DDM structure and substorm activity was inconclusive as the results were subjective depending on the threshold one used in defining substorm activity based on the AE index and/or the X component of the magnetic field. Therefore while other authors have suggested that the DDM structures are linked to thermospheric winds or vertical $\mathbf{E}\times\mathbf{B}$ drift driven by geomagnetic storm and/or substorm activities, the results presented in Chapter 6 show that there is no sufficient evidence to confirm that the storms or substorms are the main sources of DDM structures; the structures were observed in the absence of the disturbed geomagnetic or auroral conditions. This observations suggests that there are multiple drivers producing the DDM structures.

Resulting from the study on the size (i.e amplitude and period), variation and origin of the different wave structures in the ionosphere, an effort was made to understand how modern ionospheric measurements could be used to determine how operations of the new radio astronomy LOFAR would be affected by the ionosphere. This telescope will operate at lower frequencies than existing telescopes (10-250 MHz) and over a very wide area (longest baseline about 1,500 km). This study, presented in Chapter 7, involved using TEC measurements from GPS to determine ionospheric electron density maps over the European region where LOAR is located. Propagation simulations of low frequency rays

were performed using the ray tracing technique of *Coleman* (1993) through an ionosphere during a quiet day of 24 March 2004. The simulations were ran for day time and night time ionosphere to compare the results. The results from this case study demonstrated that low elevation rays, below at least 40° during day time and below at least 30° during night time, do not reach the observing stations. This means that on a quiet day during mid-solar cycle celestial objects at these and lower elevations will not be observable at 10 MHz. The refraction of ray paths was observed to be less severe at higher frequencies, although the paths still deviated from straight lines. Coordinates of the ray points that have travelled through the ionosphere and phase shift measurements across the array varied widely but were found to be comparable during both day and night time. These results indicated that careful attention has to paid to individual antennas during phase corrections as the errors associated with refraction are expected to vary across the array. The degree of refraction and phase deviations were found to vary with time. Therefore continuous monitoring of the telescope will also be important.

After the results showing that even a quiet time ionosphere had major effects on ray propagation, especially at low elevation and frequencies, it was deemed useful to investigate how much the ionosphere varied from TEC measurements over about 11 years. The results from this study are presented in Chapter 7. In order to carry out the investigation, TEC measurements from 1975 to 1991 were used to calculate TEC changes in different time windows, i.e 5, 10, 30 and 60 minute windows. It was determined that at most TEC changed by 12.8 TECU over 5 minutes, 15.5 TECU over 10 minutes, 31.6 TECU over 30 minutes and 54.1 TECU over 60 minutes. The largest TEC changes were seen in autumn for the 5 and 10 minute windows and in winter for the longer windows. Removing the diurnal trend, it was seen that the largest TEC changes were seen in summer for the 5 and 10 minute windows and in autumn for the 30 and 60 minute windows. These large TEC gradients will probably introduce more dramatic errors during LOFAR operations, which will again need careful monitoring and handling during post processing.

The statistical analysis of the changes in TEC during short-term time scales might also be useful to the users and managers of the EGNOS system. The results presented in Chapter 7 can be used as a guide on TEC gradients observed in the ionosphere over many solar cycles. The EGNOS system is meant to improve the accuracy of existing navigation systems therefore the TEC gradients results can be used to assess the level of accuracy of the new system and also to gauge the performance of the system in the next maximum

solar cycle.

In summary, wave structures of various scales have been observed from TEC measurements across different seasons and solar activities. These structures have been shown to be of considerable magnitudes. This means that the error introduced by the ionosphere in single frequency satellite navigational systems would be greatly affected by the presence and magnitude of these structures. Therefore adequate modelling of TIDs should be included in ionospheric models to reduce ionospheric effects and improve measurement accuracy. It is also important to tell astronomers when best to calibrate telescopes that are sensitive to ionospheric conditions, such as LOFAR, or what are the likely bounds on their errors.

It is important to note that many of the results presented in this thesis were limited to measurements from a single location. For instance, in order to trace the source(s) of the observed TIDs, data from other locations would be needed and then correlated to our observations to calculate TIDs' speed and direction. *Pi et al.* (1995) have found that DDM structures are observed from more than one location with time delays of a few hours. This suggests that the DDM structures are not localised. The results from the comparison of our measurements with ionosonde data seem to validate the observation in *Pi et al.* (1995). The study presented here as well as previous studies have not been successful in finding the driving forces of the DDM structures. However the statistical analysis in this study is intended to supplement and stimulate further research into the physical mechanisms responsible for TIDs and DDM structures, and thereby encourage the development of more accurate ionospheric models. Such models will be important for systems such as EGNOS, which are designed to correct GPS signals allowing greater navigational and positional accuracy.

8.2 Future Work

This work has looked into studying ionospheric perturbations using TEC measurements calculated from Faraday rotation measurements, which were collected from a single location at mid-latitudes in Italy. Structures such as TIDs and DDM have been analysed, but sources and driving forces of these structures have not be identified. With data from multiple stations, one could study TIDs' speed and direction, thus pinpoint their sources.

It was shown how wavelet analysis could give both frequency and time information. However the discrete Meyer wavelet used in our study was shown to have limited frequency resolution, but can a better wavelet be used or designed?

The extraction of semi-diurnal lunar tide component from our measurements was unsuccessful. Another method of extracting this component could be investigated, such as the method used by *Bhuyan and Tyagi* (1986). Because of the limitation of the available continuous data, any filtering method implemented must accommodate this limitation.

A possible signature of an 18-day wave was observed in TEC measurements post tidal component filtering. Lomb-Scargle periodogram could be used to study planetary wave-type oscillations in the ionosphere.

Modelling the conditions required to produce the DDM structures was not be investigated. Can we use instruments such as EISCAT (European Incoherent SCATter[1]) radars, for the electric field drift measurements, and TIMED (Thermosphere Ionosphere Mesosphere Energetics and Dynamics[2]), for wind measurements, together with existing thermospheric wind models to explain the dynamics of the DDM structures? Also, one can use multi-location observations to study the direction of movements of the structures and give a better understanding of the driving forces of these structures.

In this study the use of ray propagation theory with ionospheric maps illustrated the potential of the monitoring system for monitoring the effects of the ionosphere during LOFAR operations. This could be extended into real time monitoring. Grid resolution of the reconstruction was 2×2 degree, can this grid resolution be improved and thus improve the accuracy of the ray-tracing method? The study could also be used for future instruments such as the SKA (Square Kilometer Array[3]).

The statistical results on TEC changes should prove useful to planners of improved navigation augmentation systems who need to know the bounds of TEC changes in the mid-latitude ionosphere.

[1]http://www.eiscat.se/
[2]http://sd-www.jhuapl.edu/TIMED/WWW/index.php
[3]http://www.skatelescope.org/

Appendix A

ANOVA Error Analysis

The discrete wavelet basis functions and the time series are both finite in length. To fit the wavelet at the beginning and end of the time signal, padding the time signal with zeros at the edges was necessary to conserve the total variation of the signal and thus implement ANOVA at different scales. However, this padding introduces edge effects. At larger scales the edge effects are worse as more errors creep further into the centre of the time series and fewer coefficients are deemed reliable. There are other ways to pad the time signal to reduce edge effects, e.g. symmetric padding, but the total variation is not in general preserved. The cone of influence is the region of the wavelet scalogram in which edge effects become important, *Torrence and Compo* (1998). For each scale, it can be defined as the half length of a wavelet filter at that scale. However rather than using the half length, i.e. 51 coefficients, of the full filter, which has 102 coefficients, an effective half length with 10 coefficients is used here. This new effective half length was introduced because the remaining coefficients are very small and seemingly negligible. This definition of the cone of influence can be justified because the sum square of the 20 central coefficients make up 99.98% of the sum square coefficients of the total filter, meaning that this effective filter encompasses almost all of the total variation of the filter. Figure A.1 gives an illustration of the coefficients that lie inside the cones of influence of the edges, defined on the effective half length. It is clearly seen that the edge effects are more influential at higher scales.

To assess the sort of errors the edge effect will introduce to the wavelet analysis, the diurnal variation of TEC was modeled by a sinusoidal function of 1 day period. The scalogram of this function was expected to be zero at scales of less than 1024, and therefore if the coefficients differ from zero, these coefficients indicate the errors one associates with the

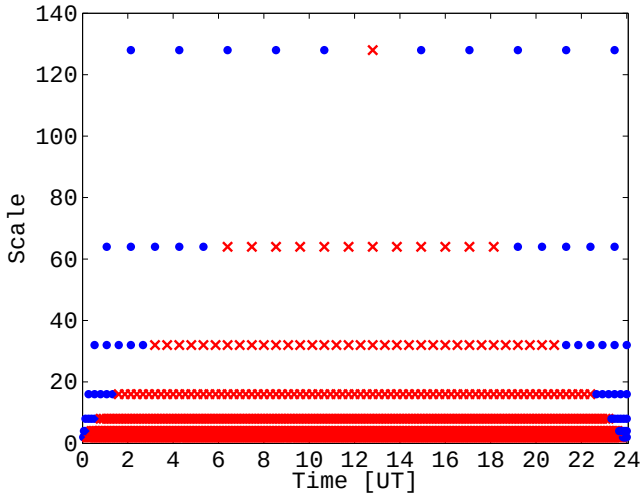

Figure A.1: Dyadic scaling of the discrete wavelet coefficients; the blue dots show the coefficients that lie inside the cones of influence of the edges.

transform at those scales. This allows us to then produce approximate error bounds on the coefficients of the wavelet transform obtained from our data.

Let the total variation of the TEC data within a day be:

$$N\sigma_S^2 = \sum_{i=1}^{N} |c_i|^2, \tag{A.1}$$

where the summation is only over wavelet coefficients at all scales and times. Also, let the total variation within a window W be:

$$V_W = \sum_{i \in W} |c_i|^2, \tag{A.2}$$

where c_i refers to the wavelet coefficients at all scales and times within W.

Expressing the total variation within a window as a percentage of the total variation in a day, the following equation is obtained:

$$P_W = \frac{V_W}{N\sigma_S^2} \times 100. \tag{A.3}$$

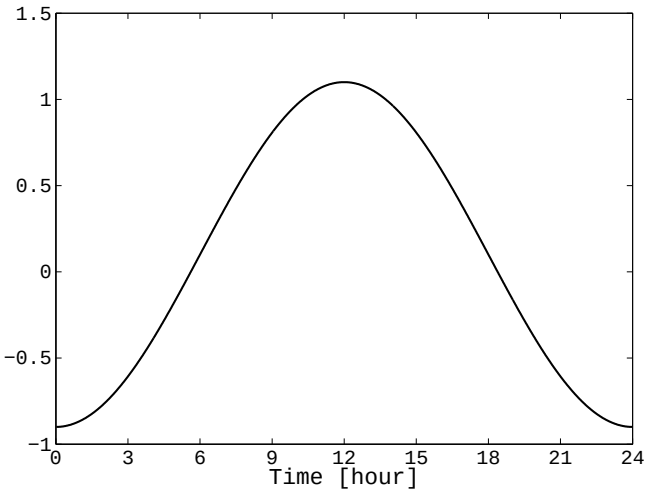

Figure A.2: Sinusoidal function, with a period of 1 day, simulating the diurnal TEC.

Next, let

$$N\sigma'^2 = \sum_{i=1}^{N} |c_i'|^2, \tag{A.4}$$

denote the total variation of the sinusoidal function, see Figure A.2, where c_i' are the relevant discrete wavelet transform coefficients. Next, the coefficients of the sinusoidal function are scaled so that the total variations of the sinusoidal function and of the time signal are identical. Hence the scaled coefficients are:

$$c_i'' = c_i' \sqrt{\frac{\sigma_S^2}{\sigma'^2}}. \tag{A.5}$$

The upper and lower bounds of the variation of TEC within a time window (denoted by W) are:

$$V_{W,L} = \sum_{i \in W} (|c_i| - |c_i''|)^2 \text{ and } V_{W,U} = \sum_{i \in W} (|c_i| + |c_i''|)^2, \tag{A.6}$$

where i ranges across all times and scales within W. We have been overly cautious and have assumed that coefficients from edge effects may be added or subtracted in magnitude from those of the signal (and hence are respectively in phase or antiphase).

Table A.1: Estimated error bound

SCALE	BOUND LEVEL	MAX [%]
32	LOWER	0.0237
32	UPPER	0.0237
64	LOWER	1.2438
64	UPPER	1.2534

Then the variation of TEC within W may be estimated to lie between $V_W - \varepsilon_{W,L}$ % and $V_W + \varepsilon_{W,U}$ %, where the error bounds are approximated as:

$$\varepsilon_{W,L} = \frac{(V_W - V_{W,L})}{V_W} \times 100 \text{ and } \varepsilon_{W,U} = \frac{(V_{W,U} - V_W)}{V_W} \times 100. \tag{A.7}$$

This analysis has been done for a simple case where the function used to represent diurnal TEC is fairly smooth near both the edges of the function, refer to Figure A.2, thus simplifying and giving an optimistic rough error analysis. We expect that if there are shorter period (higher frequency) waves intersecting the edges of the function, then the errors induced by the edge effects will be worse. However the analysis seems reasonable for a first pass approximation because inspection of our data suggests there are less TIDs at night time.

The results of this error analysis are presented in Table A.1 for each day in both the solar minimum and the solar maximum phases, where the W denotes the morning, mid-day and evening time windows, i.e Time $\in$ [05H00, 08H00], Time $\in$ [08H01, 15H59], and Time $\in$ [16H00, 21H00] respectively. The errors in Table A.1 give the worst case i.e. maximum error calculated. Note that it is expected that the errors would be smaller during the mid-day window than during the morning or evening windows.

Appendix B

Confidence Level Analysis

A confidence level is defined here as the probability of the relative magnitude or time of occurrence of a peak in one season or geomagnetic condition being greater than in a different season or geomagnetic condition. The probabilities are calculated as follows:

$$P(B > A) \approx \sum_{i=1}^{N} \left[P(A = x_i) \times \sum_{j=i+1}^{N} P(B = x_j) \right] \times 100, \tag{B.1}$$

where A is a relative magnitude or time of occurrence of a peak in season or geomagnetic condition being tested, B is a relative magnitude or time of occurrence of a peak in another season or geomagnetic condition, and $\{x_1, x_2, ..., x_N\}$ relates to relative magnitude $\in$ [6, 58] % or discretised time $\in$ [5, 20] UT hours. The confidence level is therefore $P(B > A)$. The probabilities are presented in Figures B.1 - B.6. Note that the approximation in Equation (B.1) is due to the discretisation errors in the probability mass function calculated on the data, and these probability mass functions are themselves estimates of the true underlying probability mass functions.

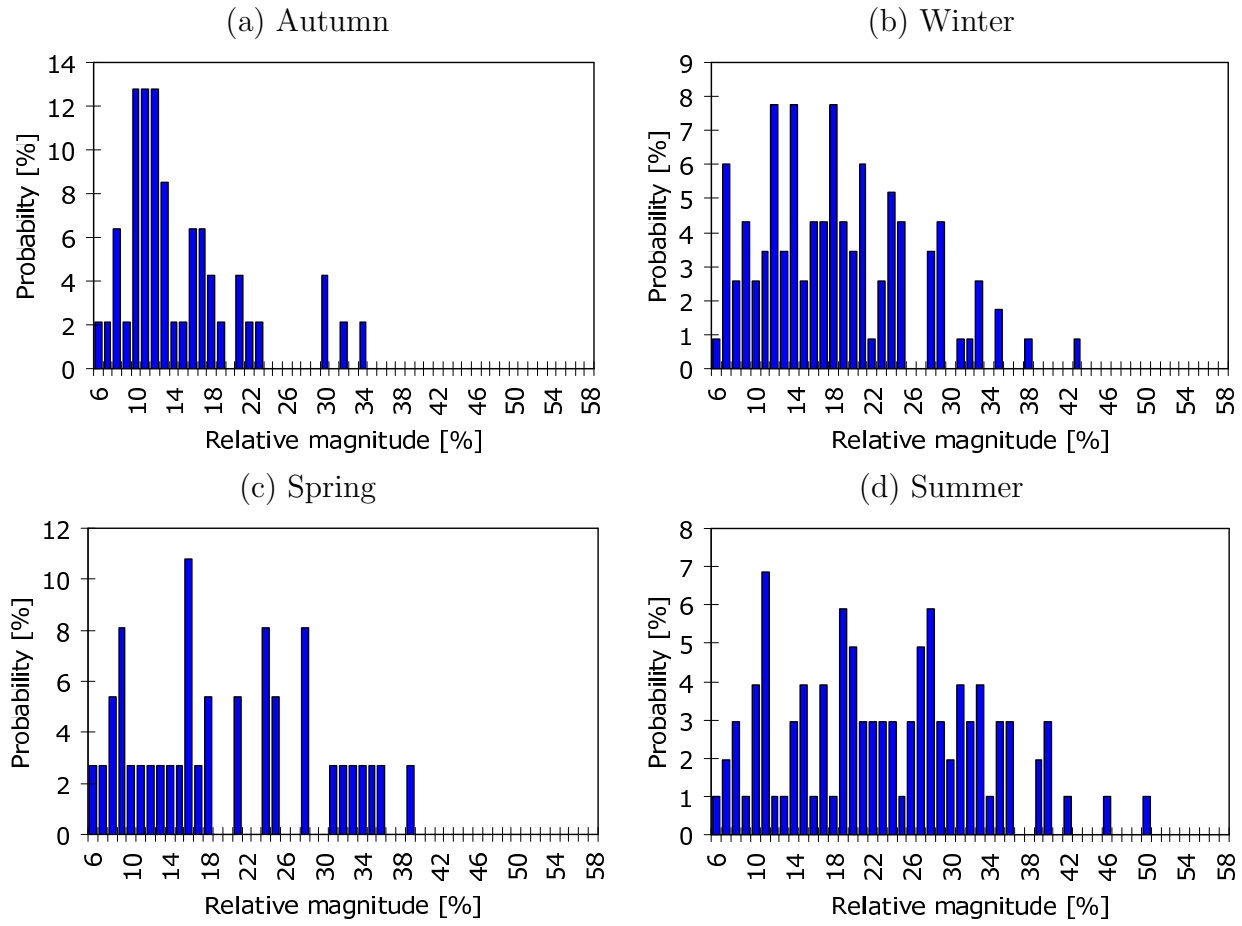

Figure B.1: Seasonal histograms of the relative magnitude of the first peak.

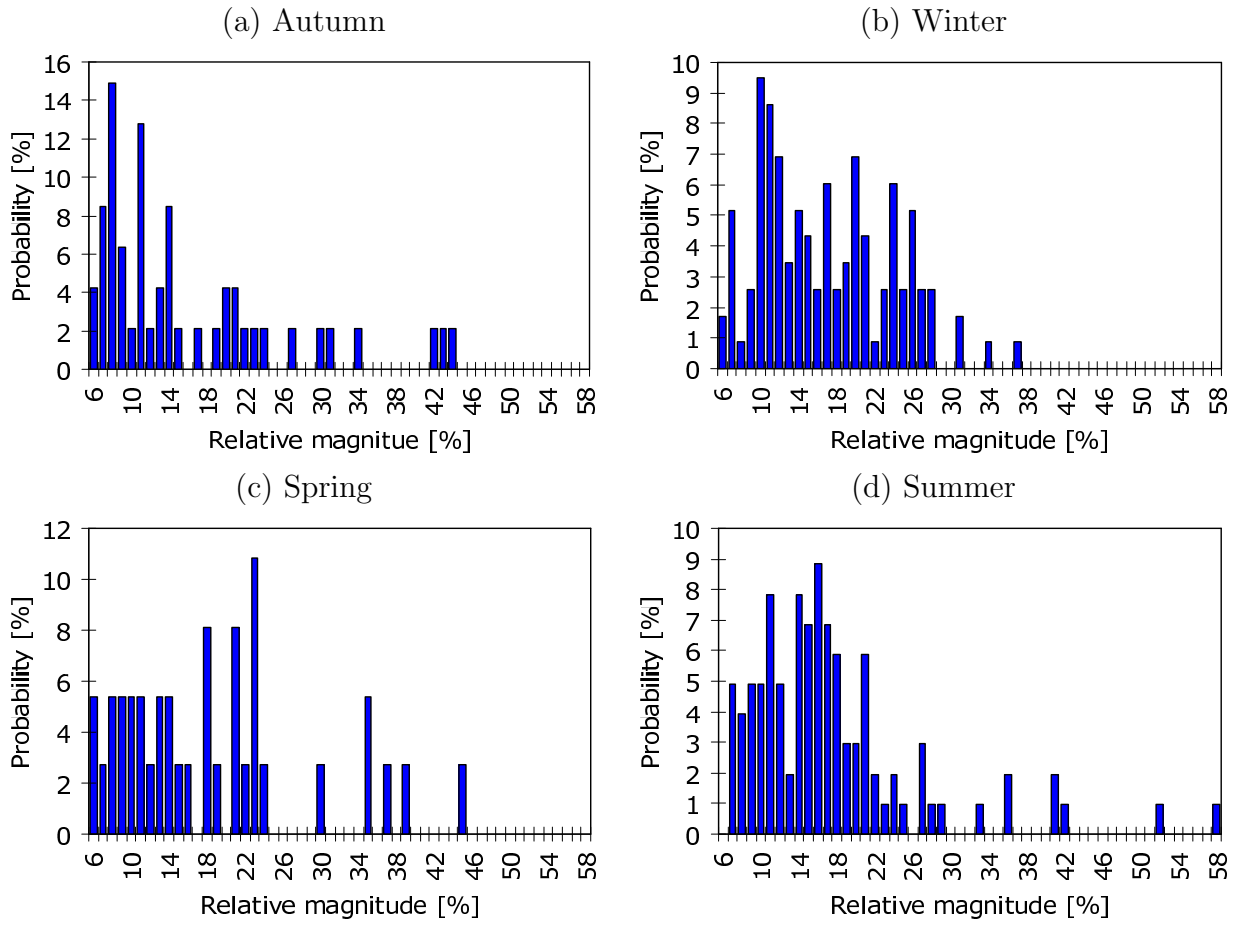

Figure B.2: Seasonal histograms of the relative magnitude of the second peak.

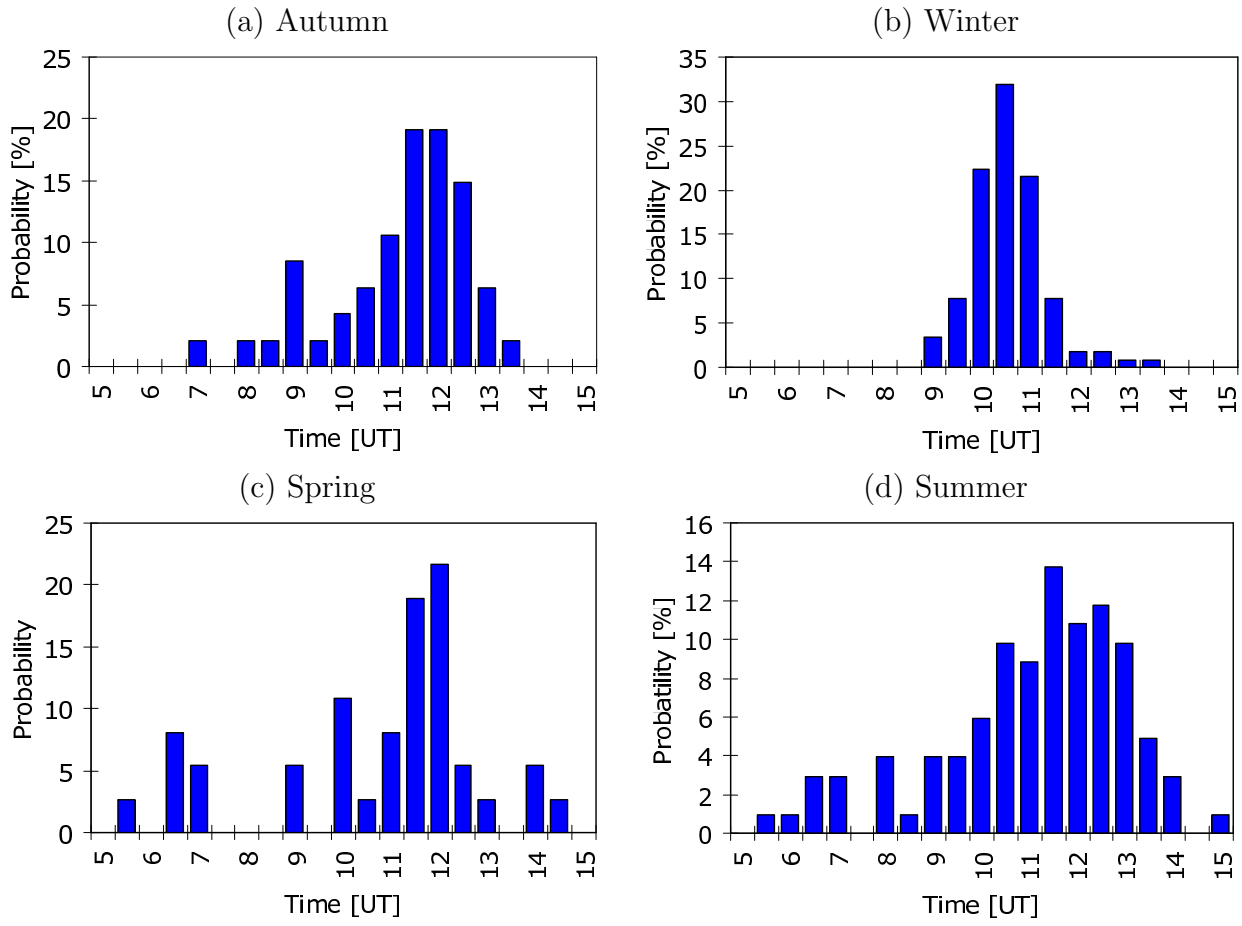

Figure B.3: Seasonal histograms of the time of occurrence of the second peak.

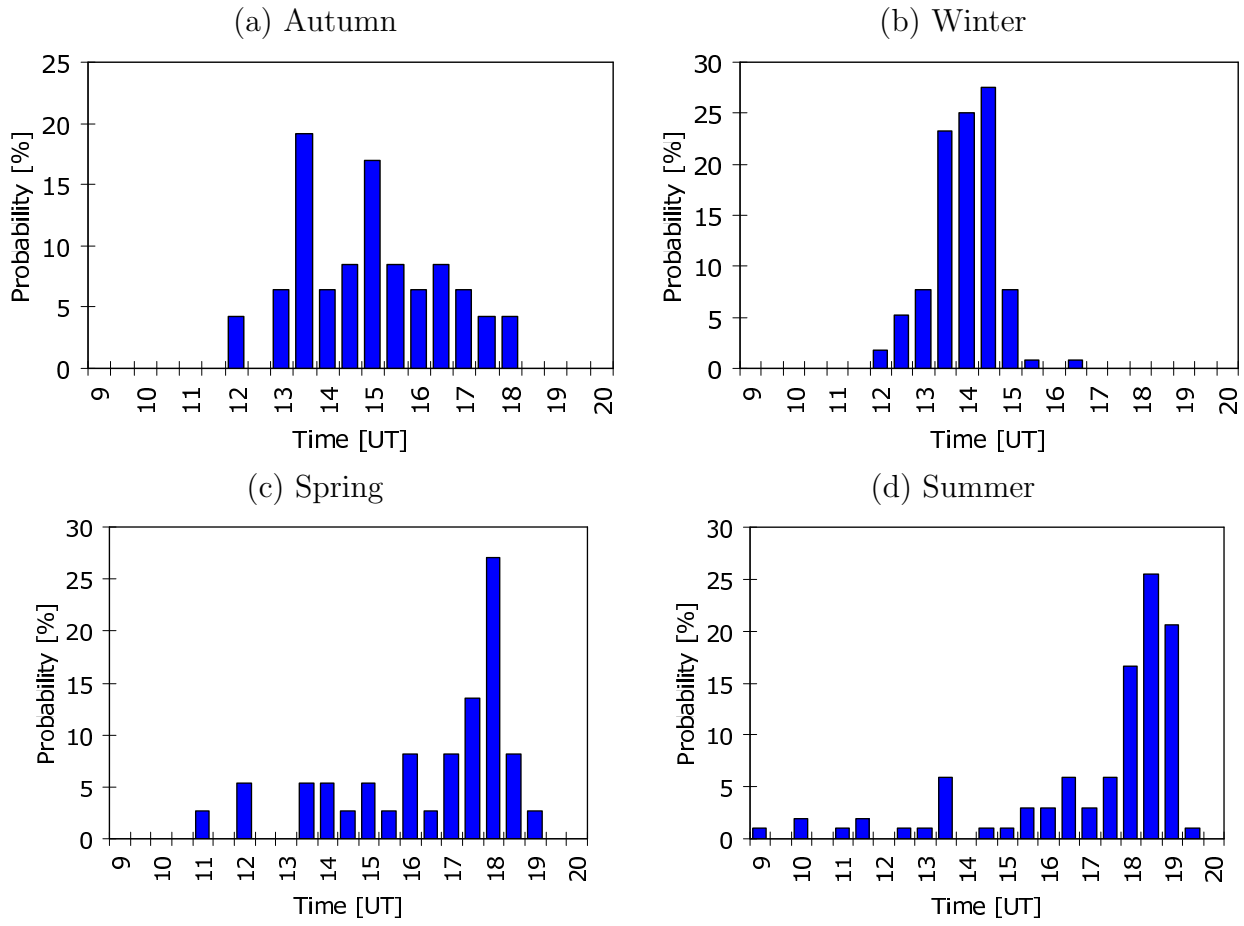

Figure B.4: Seasonal histograms of the time of occurrence of the second peak.

(a) Relative magnitude of first peak during quiet geomagnetic conditions

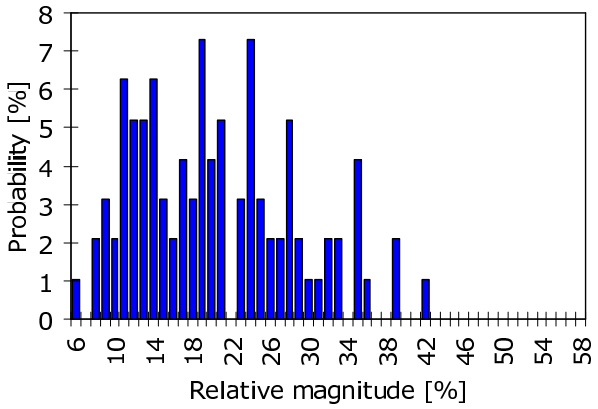

(b) Relative magnitude of first peak during moderate geomagnetic conditions

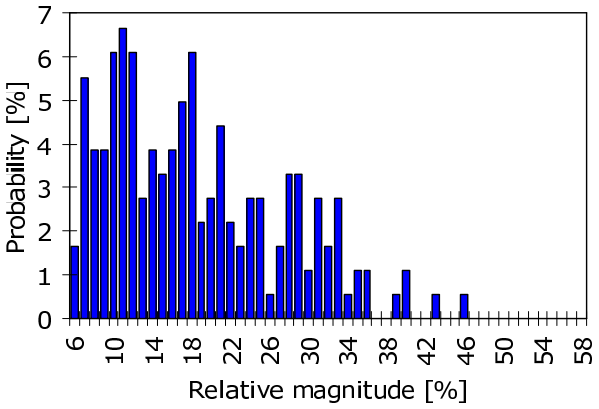

(c) Relative magnitude of first peak during disturbed geomagnetic conditions

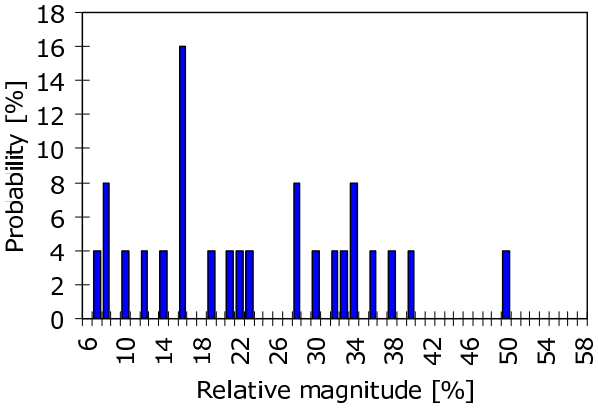

(d) Relative magnitude of first peak during quiet geomagnetic conditions

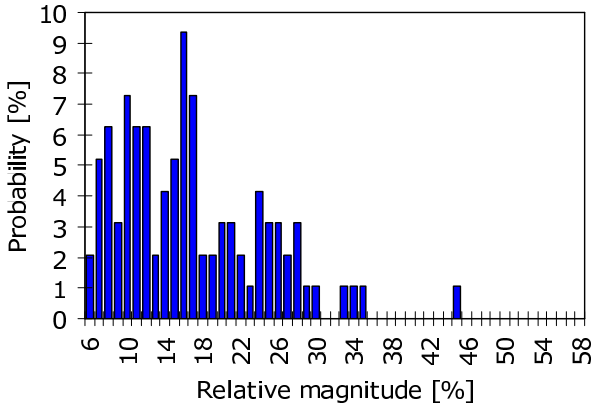

(e) Relative magnitude of first peak during moderate geomagnetic conditions

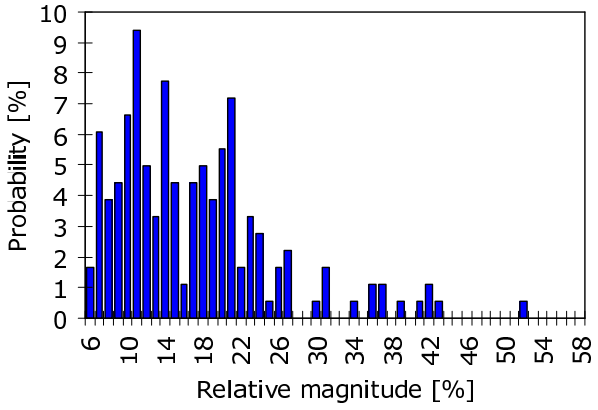

(f) Relative magnitude of first peak during disturbed geomagnetic conditions

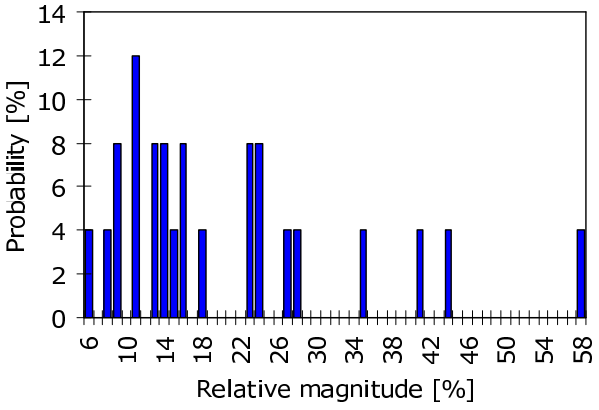

Figure B.5: Geomagnetic condition histograms of the relative magnitude of the first and second peaks.

(a) Time of occurrence of first peak during quiet geomagnetic conditions

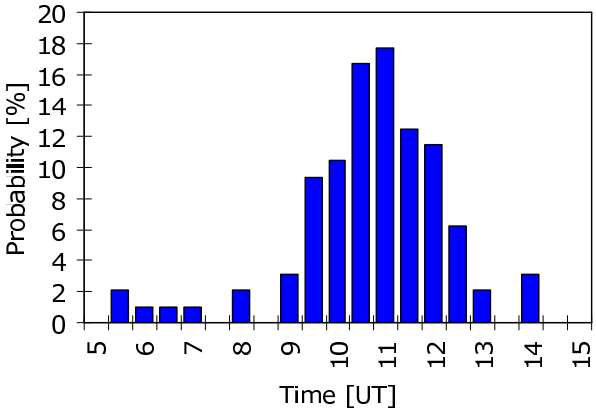

(b) Time of occurrence of first peak during moderate geomagnetic conditions

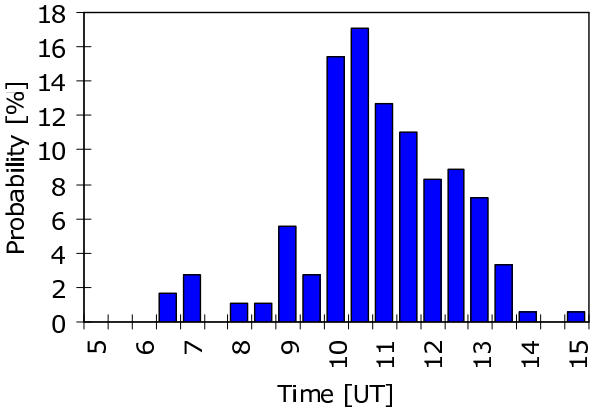

(c) Time of occurrence of first peak during disturbed geomagnetic conditions

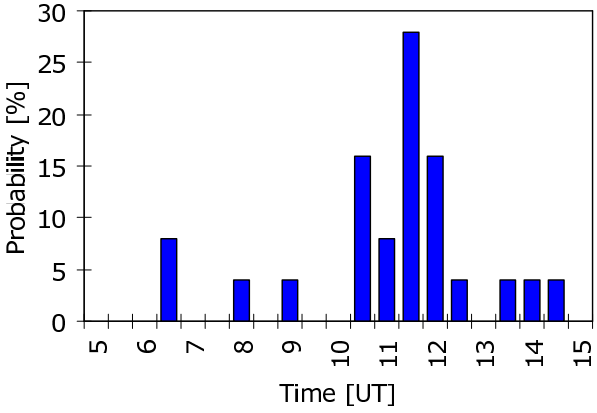

(d) Time of occurrence of first peak during quiet geomagnetic conditions

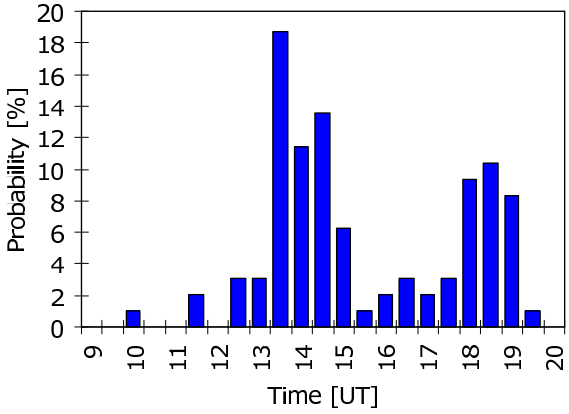

(e) Time of occurrence of first peak during moderate geomagnetic conditions

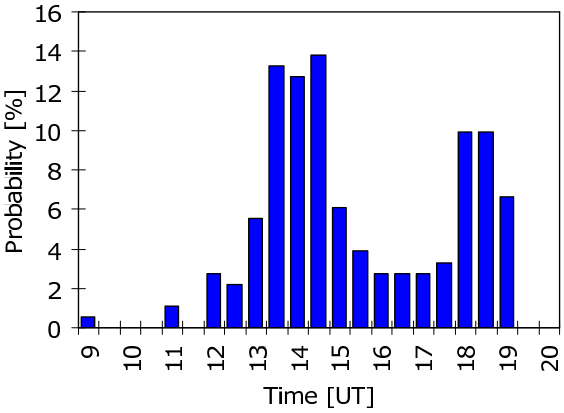

(f) Time of occurrence of first peak during disturbed geomagnetic conditions

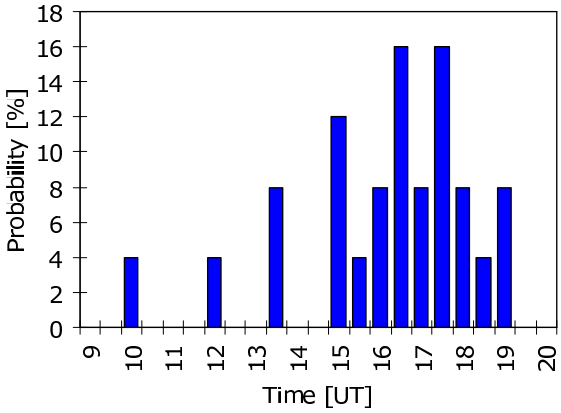

Figure B.6: Histograms of time of occurrence of first and second peaks during different geomagnetic conditions.

Appendix C

Examples of TEC Profiles, filtered TEC Profiles and Scalograms

Presented in this chapter are TEC profiles, Savitzky-Golay filtered TEC profiles and scalograms from discrete wavelet analysis during the solar minimum phase of 1975-1976 and the solar maximum phase of 1989-1990. Two profiles from each month during each solar cycle phase were randomly selected to as examples of the results obtained from the TID analysis. In each figure, the top plots are the TEC versus time profiles, the middle plots are the filtered TEC versus time profiles and the bottom plots are the scalograms with the coefficients measured in $TECU^2$. TEC is measured in TECU and time is measured in UT hour.

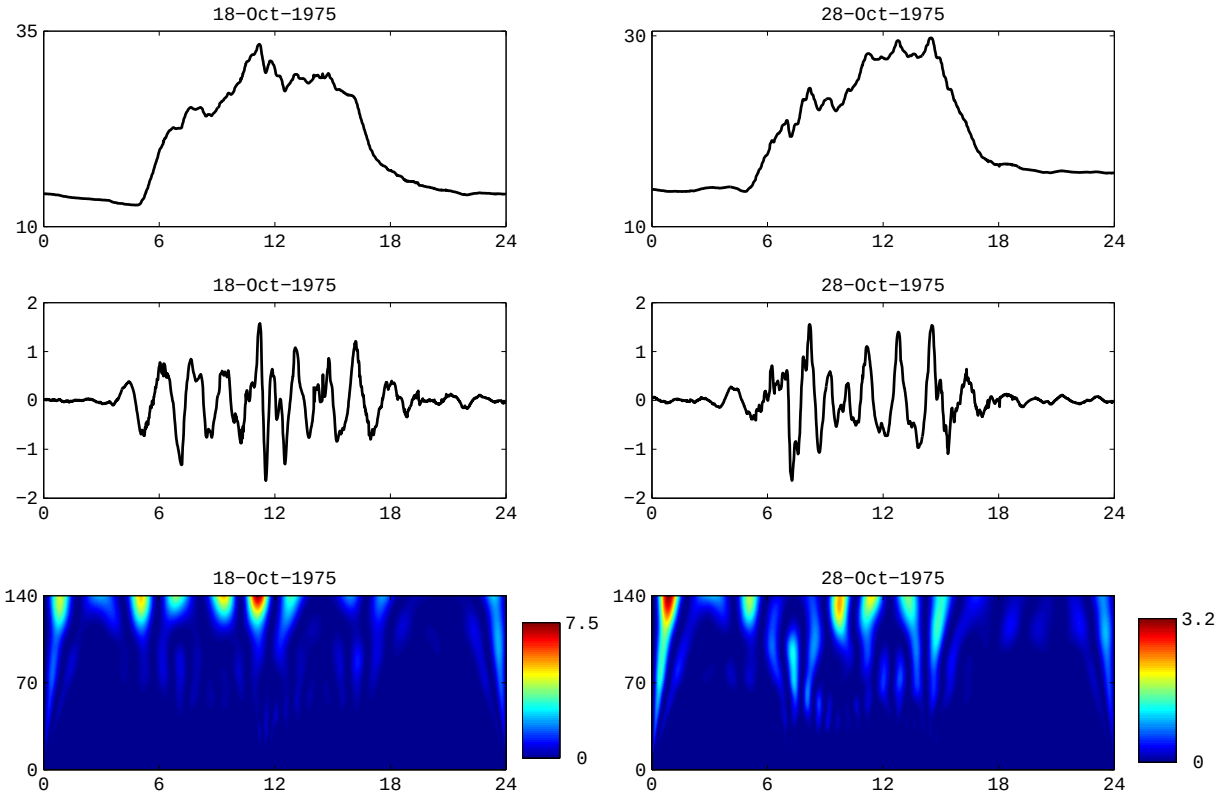
18-Oct-1975
28-Oct-1975
18-Oct-1975
28-Oct-1975
18-Oct-1975
28-Oct-1975
7.5
0
3.2
0

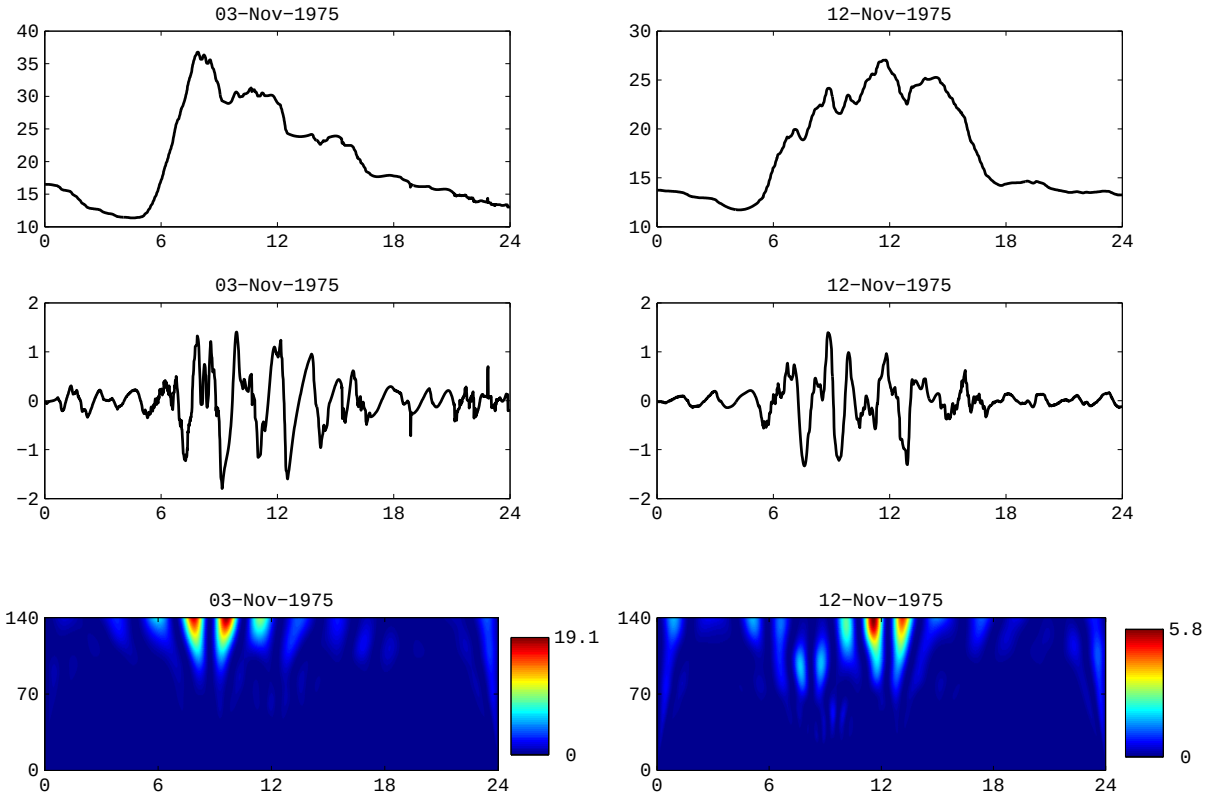
03-Nov-1975
12-Nov-1975
03-Nov-1975
12-Nov-1975
03-Nov-1975
12-Nov-1975
19.1
0
5.8
0

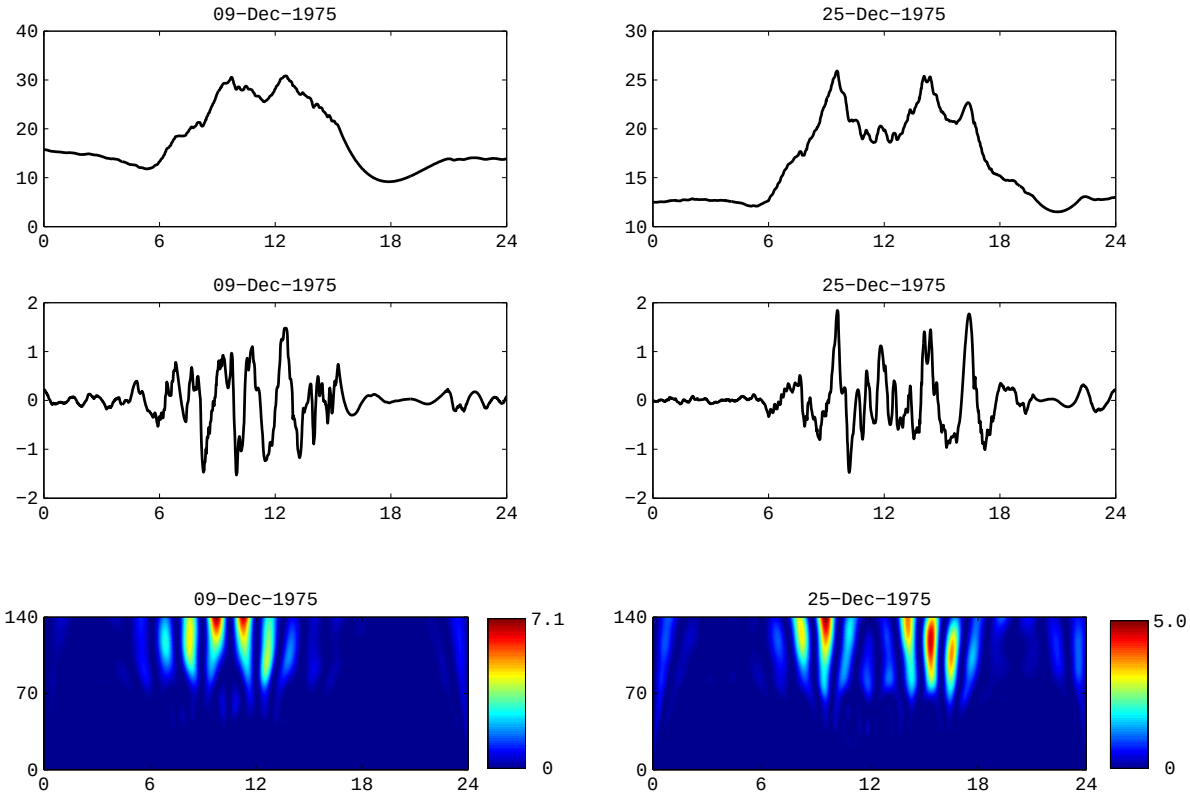
09-Dec-1975
25-Dec-1975
09-Dec-1975
25-Dec-1975
09-Dec-1975
25-Dec-1975
7.1
0
5.0
0

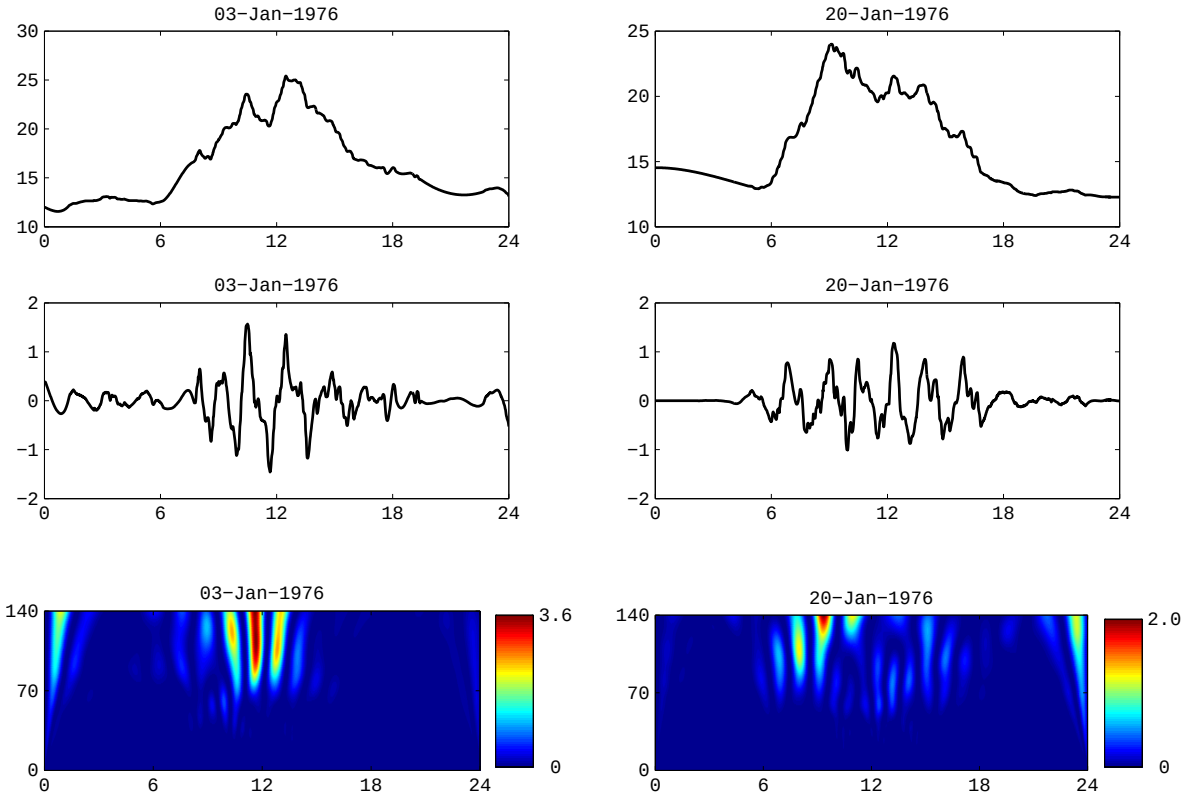
03-Jan-1976
20-Jan-1976
03-Jan-1976
20-Jan-1976
03-Jan-1976
20-Jan-1976
3.6
2.0

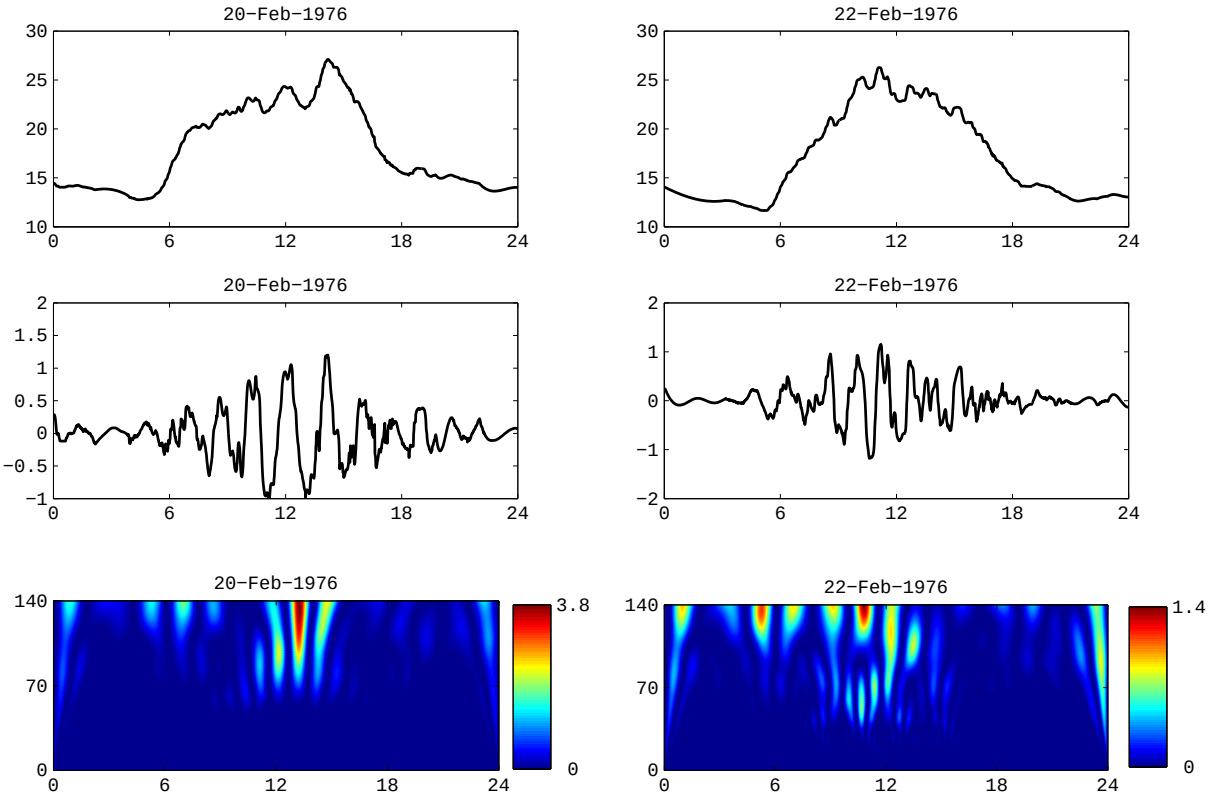
20−Feb−1976
22−Feb−1976
20−Feb−1976
22−Feb−1976
20−Feb−1976
22−Feb−1976
3.8
1.4

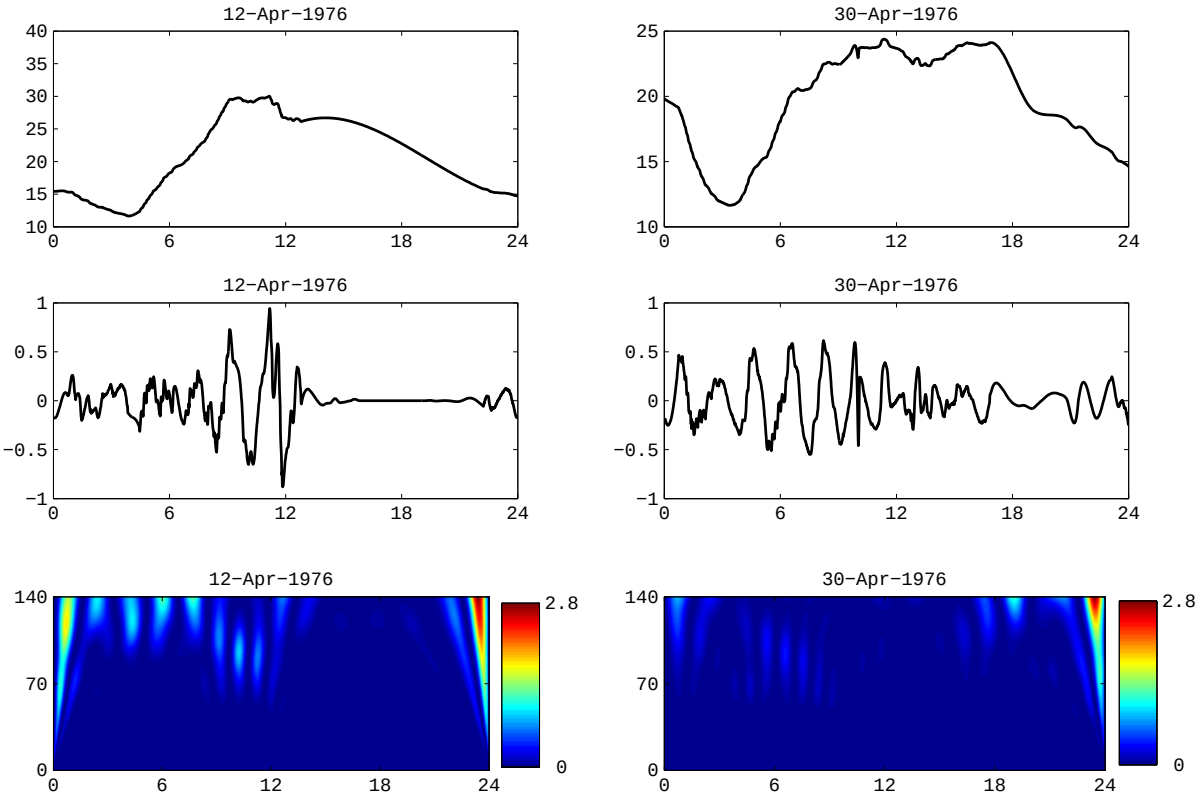
12−Apr−1976
30−Apr−1976
12−Apr−1976
30−Apr−1976
12−Apr−1976
30−Apr−1976
2.8
0
2.8
0

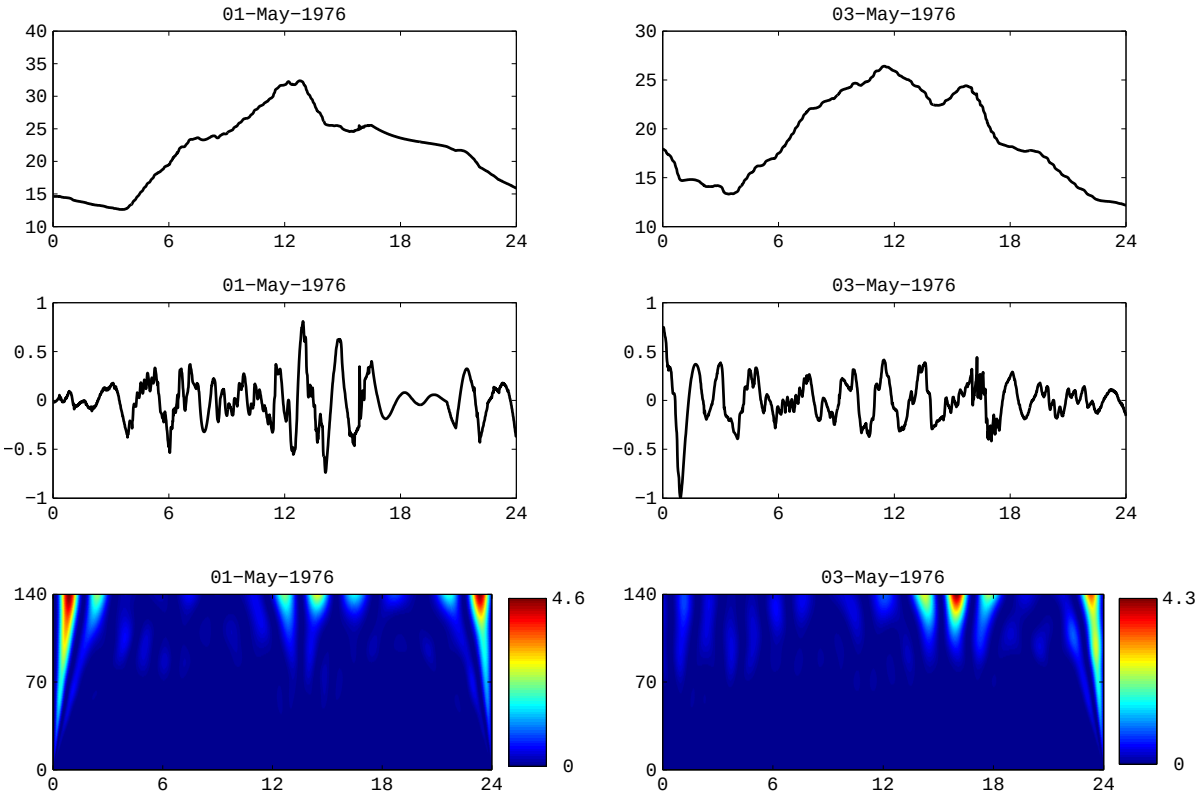
01−May−1976
03−May−1976
01−May−1976
03−May−1976
01−May−1976
03−May−1976
4.6
0
4.3
0

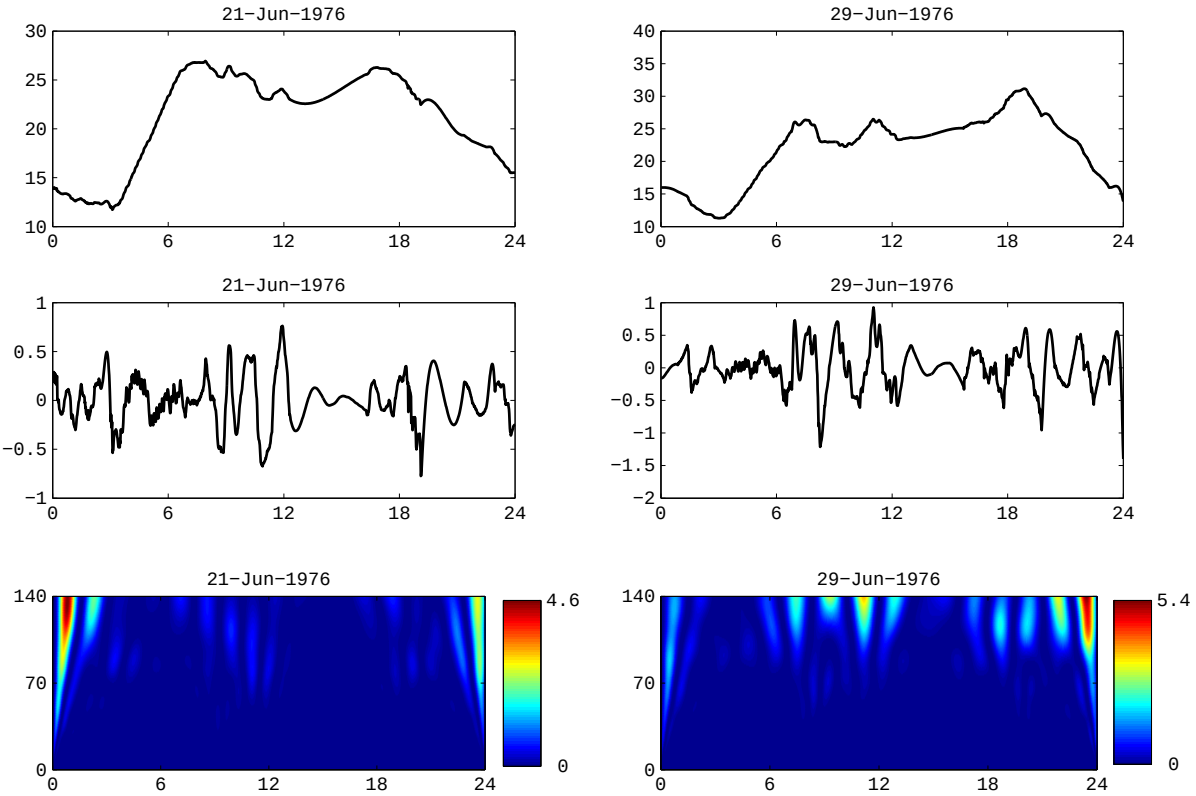
21−Jun−1976
29−Jun−1976
21−Jun−1976
29−Jun−1976
21−Jun−1976
4.6
0
29−Jun−1976
5.4
0

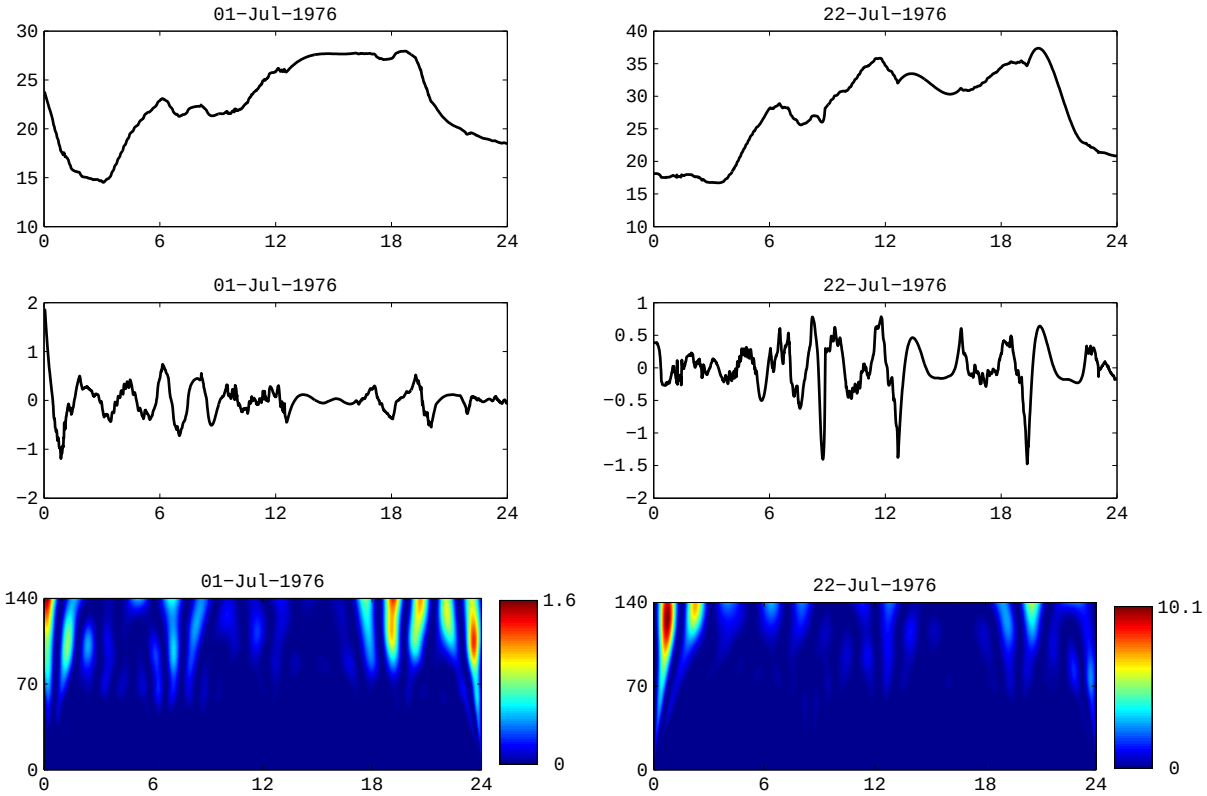
01-Jul-1976
22-Jul-1976
01-Jul-1976
22-Jul-1976
01-Jul-1976
22-Jul-1976
1.6
10.1

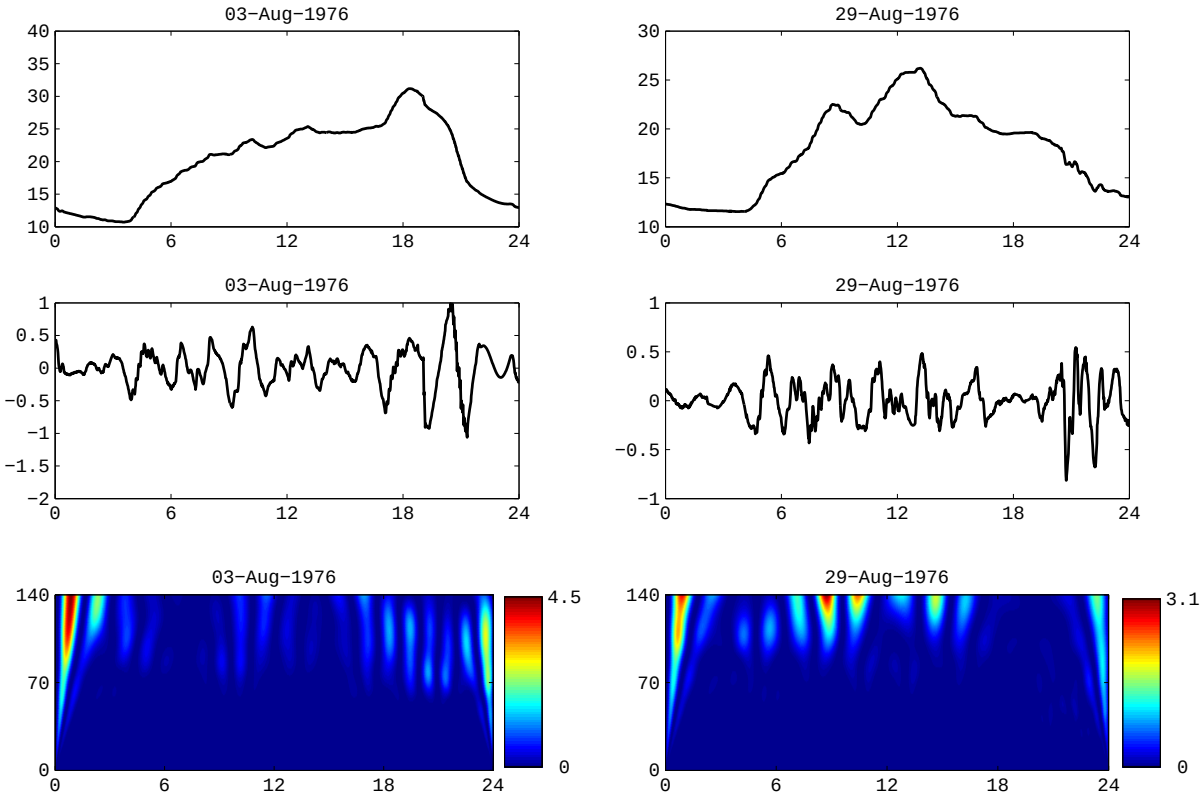
03−Aug−1976
29−Aug−1976
03−Aug−1976
29−Aug−1976
03−Aug−1976
29−Aug−1976
4.5
0
3.1
0

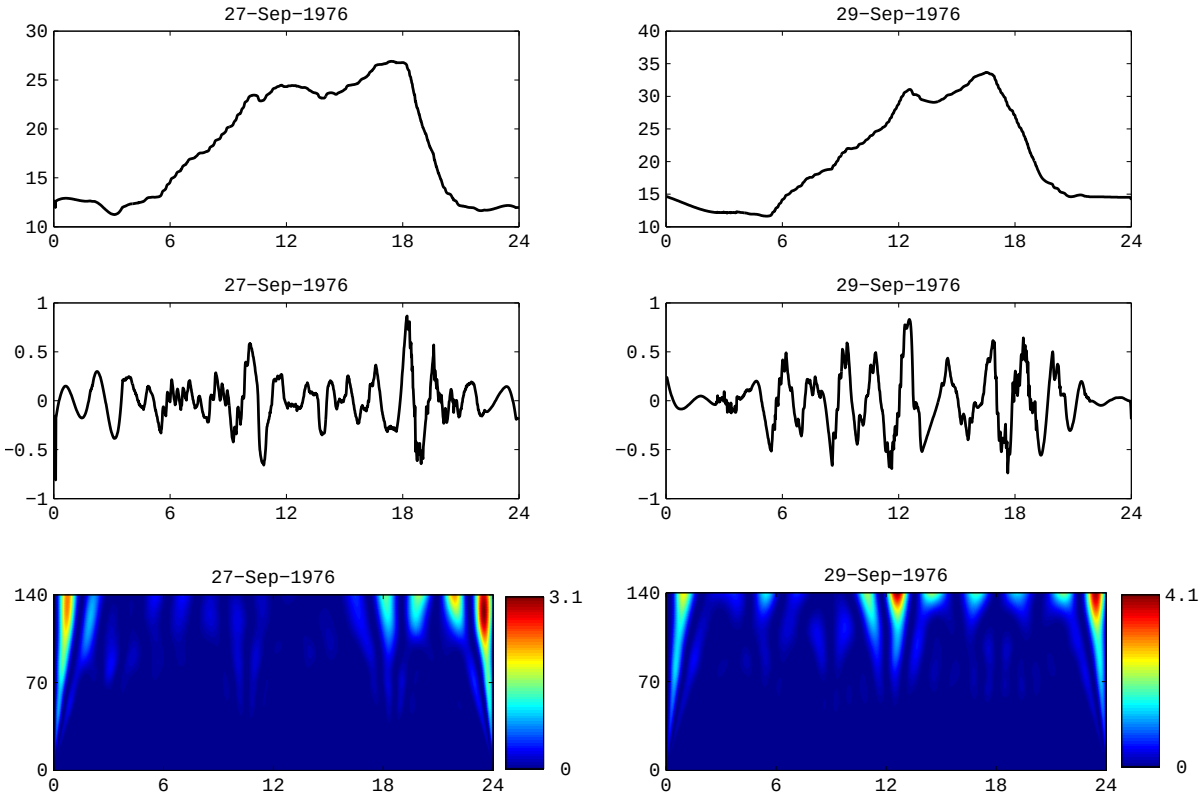
27−Sep−1976
29−Sep−1976
27−Sep−1976
29−Sep−1976
27−Sep−1976
29−Sep−1976
3.1
4.1

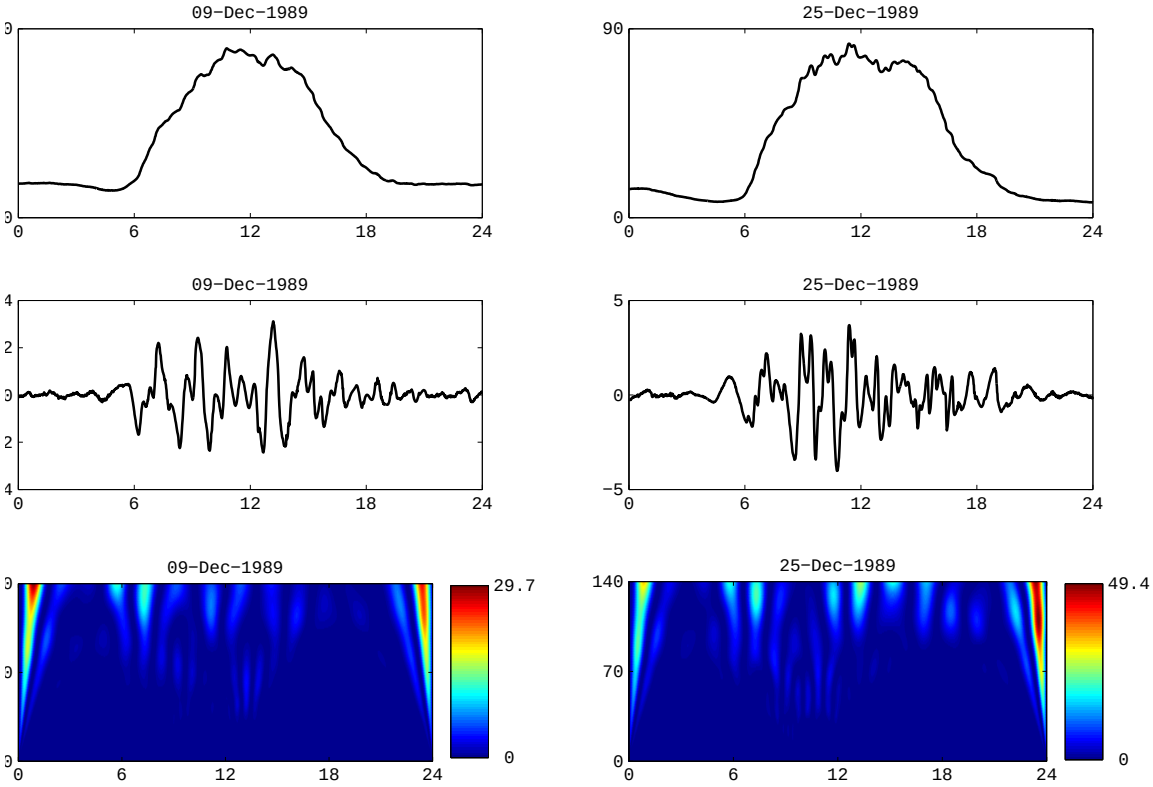
09−Dec−1989
25−Dec−1989
09−Dec−1989
25−Dec−1989
09−Dec−1989
29.7
0
25−Dec−1989
49.4
0

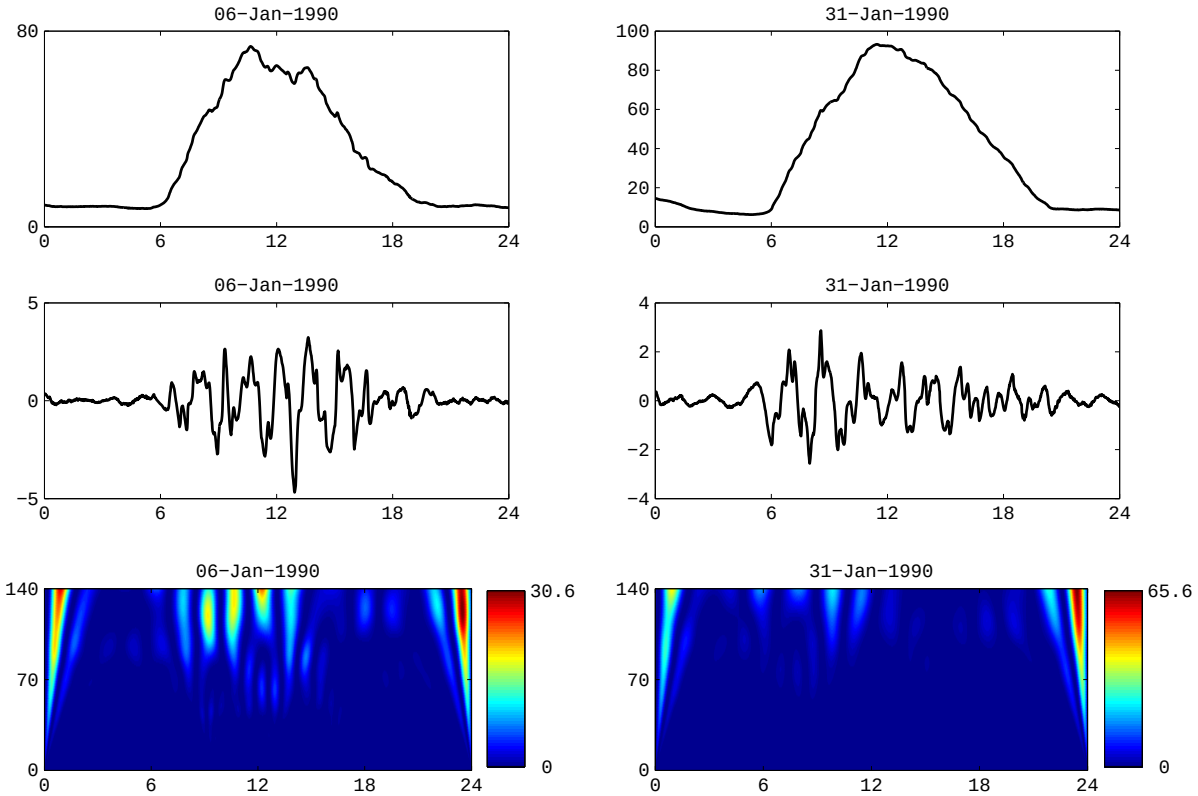
06-Jan-1990
80
0
0
6
12
18
24
31-Jan-1990
100
80
60
40
20
0
0
6
12
18
24
06-Jan-1990
5
0
−5
0
6
12
18
24
31-Jan-1990
4
2
0
−2
−4
0
6
12
18
24
06-Jan-1990
140
70
0
0
6
12
18
24
30.6
0
31-Jan-1990
140
70
0
0
6
12
18
24
65.6
0

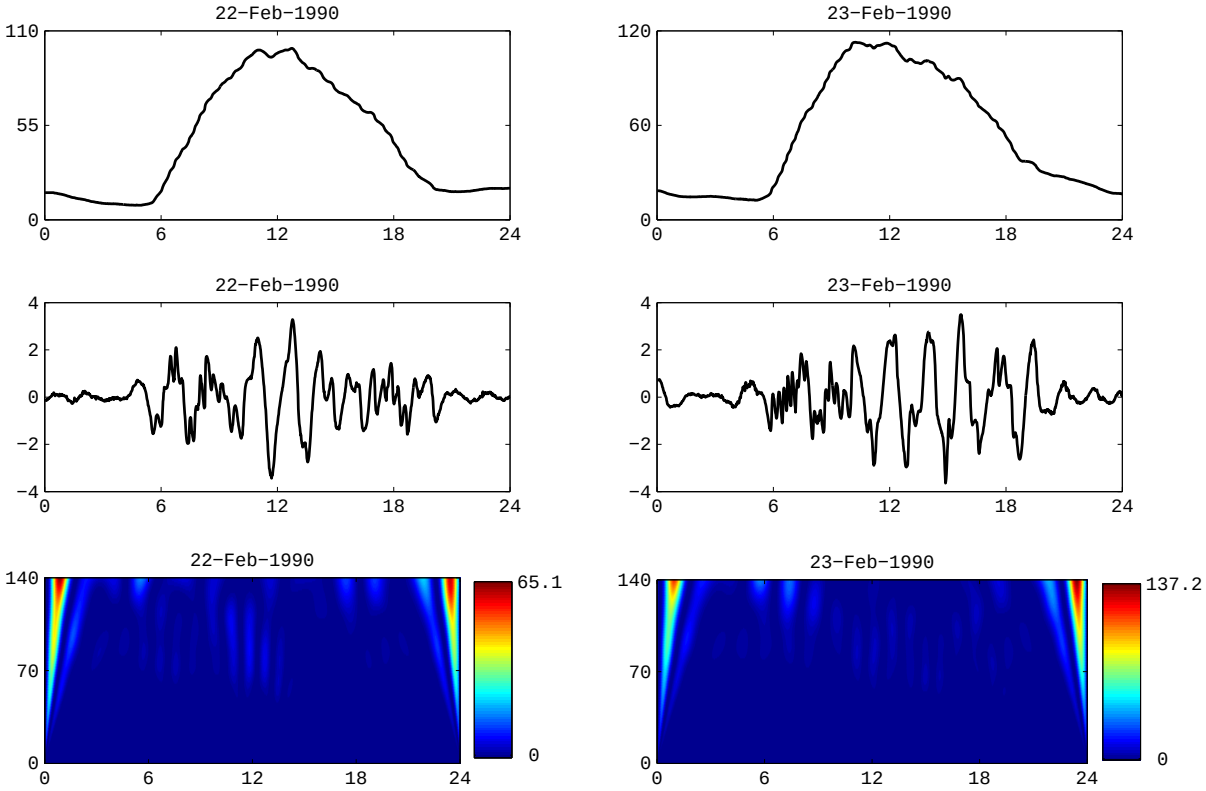
22−Feb−1990
110
55
0
0
6
12
18
24
23−Feb−1990
120
60
0
0
6
12
18
24
22−Feb−1990
4
2
0
−2
−4
0
6
12
18
24
23−Feb−1990
4
2
0
−2
−4
0
6
12
18
24
22−Feb−1990
140
70
0
0
6
12
18
24
65.1
0
23−Feb−1990
140
70
0
0
6
12
18
24
137.2
0

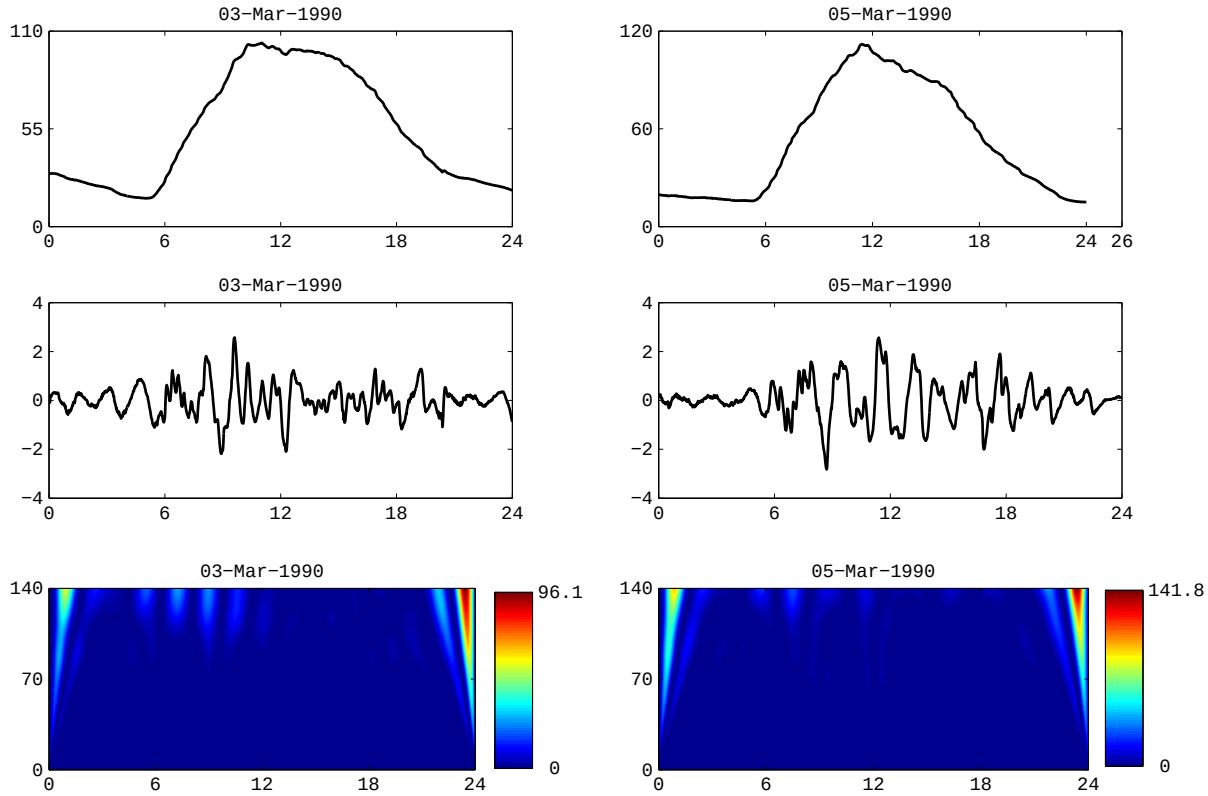
03−Mar−1990
110
55
0
0
6
12
18
24
05−Mar−1990
120
60
0
0
6
12
18
24
26
03−Mar−1990
4
2
0
−2
−4
0
6
12
18
24
05−Mar−1990
4
2
0
−2
−4
0
6
12
18
24
03−Mar−1990
140
70
0
0
6
12
18
24
96.1
0
05−Mar−1990
140
70
0
0
6
12
18
24
141.8
0

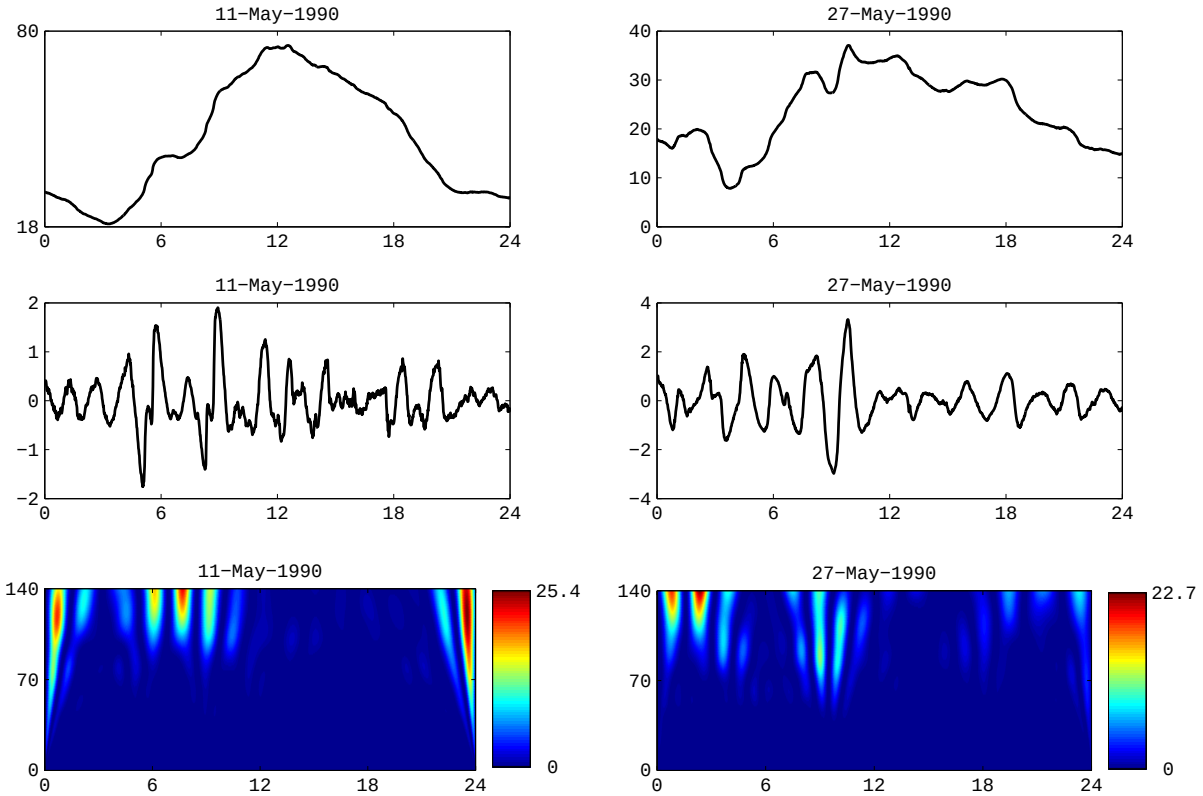
11−May−1990
80
18
0
6
12
18
24
27−May−1990
40
30
20
10
0
11−May−1990
2
1
0
−1
−2
27−May−1990
4
2
0
−2
−4
11−May−1990
140
70
0
25.4
0
27−May−1990
22.7

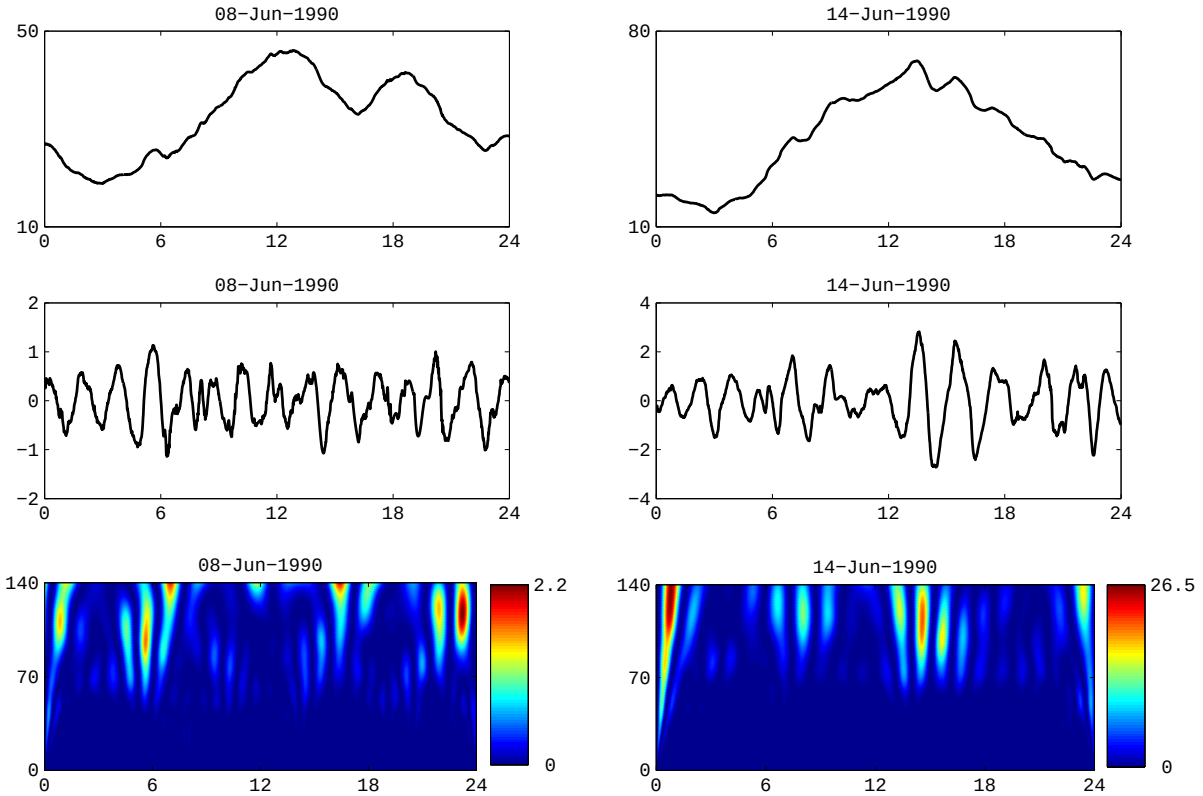
08-Jun-1990
50
10
0
6
12
18
24
14-Jun-1990
80
10
0
6
12
18
24
08-Jun-1990
2
1
0
−1
−2
0
6
12
18
24
14-Jun-1990
4
2
0
−2
−4
0
6
12
18
24
08-Jun-1990
140
70
0
0
6
12
18
24
2.2
0
14-Jun-1990
140
70
0
0
6
12
18
24
26.5
0

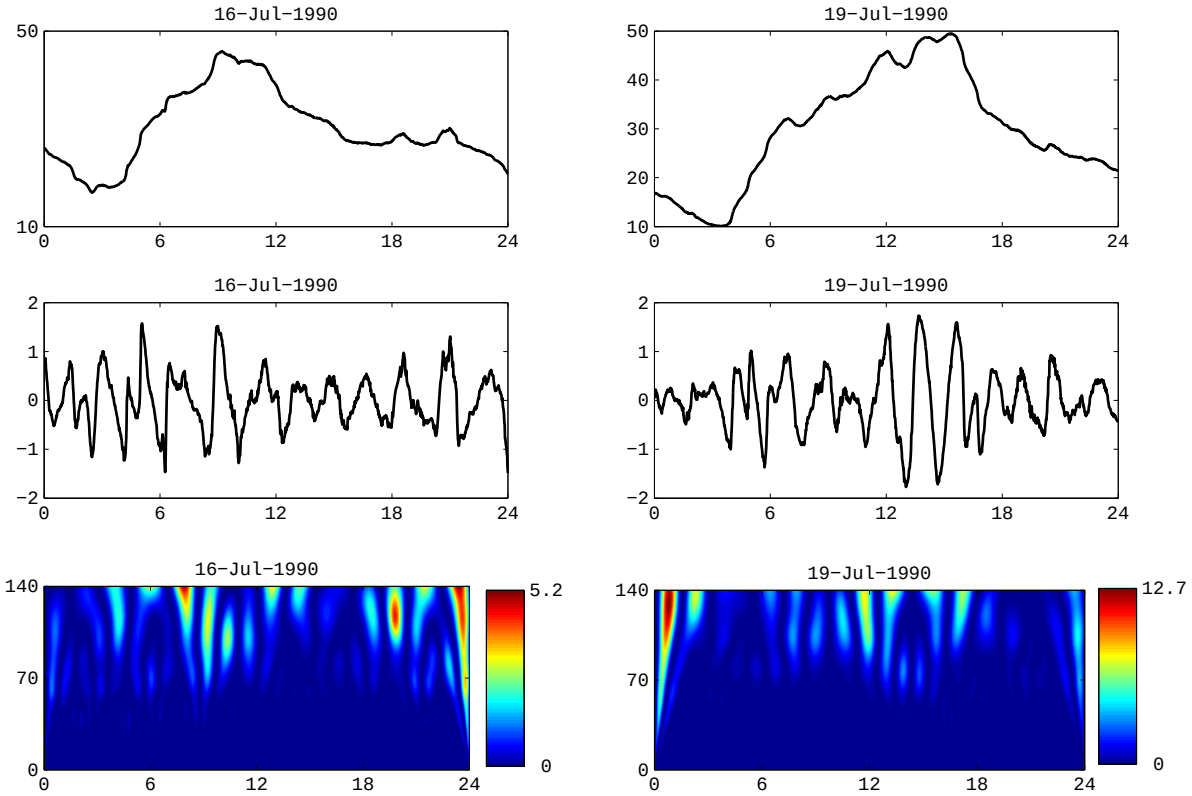
16-Jul-1990
19-Jul-1990
16-Jul-1990
19-Jul-1990
16-Jul-1990
19-Jul-1990
5.2
12.7

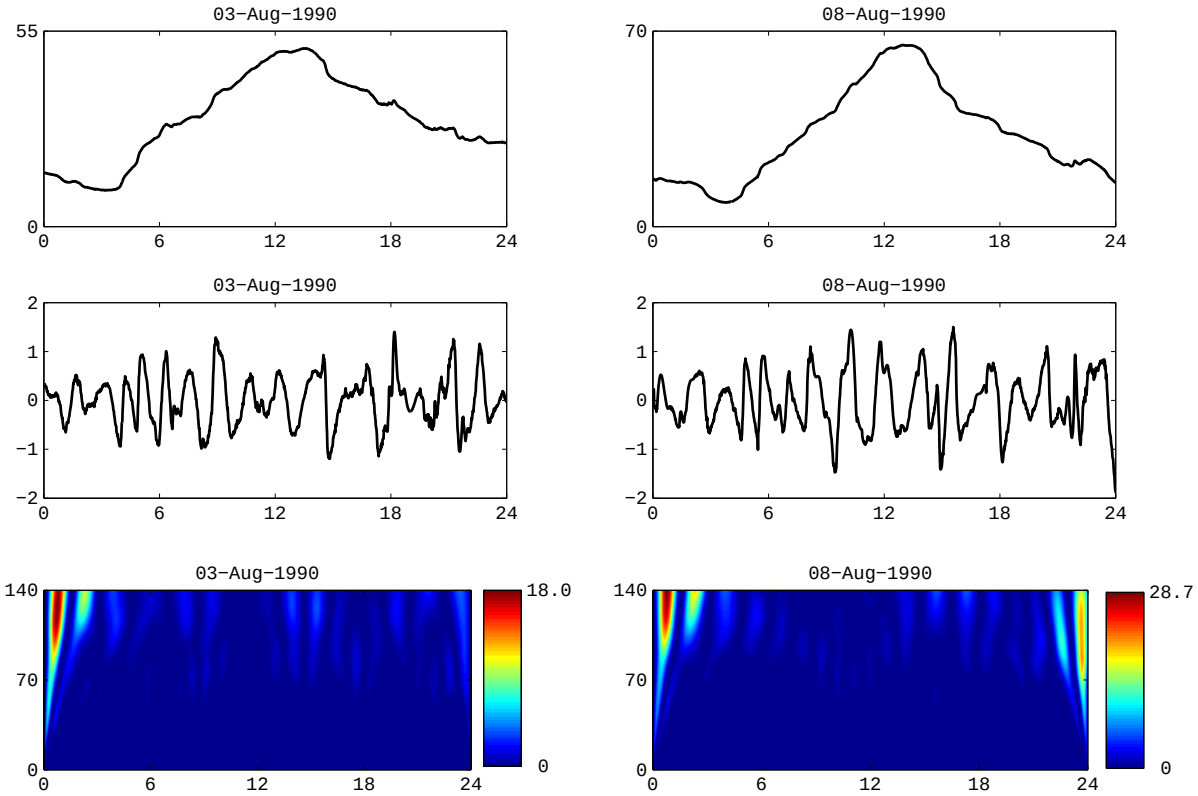
03-Aug-1990
55
0
0
6
12
18
24
08-Aug-1990
70
0
0
6
12
18
24
03-Aug-1990
2
1
0
−1
−2
0
6
12
18
24
08-Aug-1990
2
1
0
−1
−2
0
6
12
18
24
03-Aug-1990
140
70
0
0
6
12
18
24
18.0
0
08-Aug-1990
140
70
0
0
6
12
18
24
28.7
0

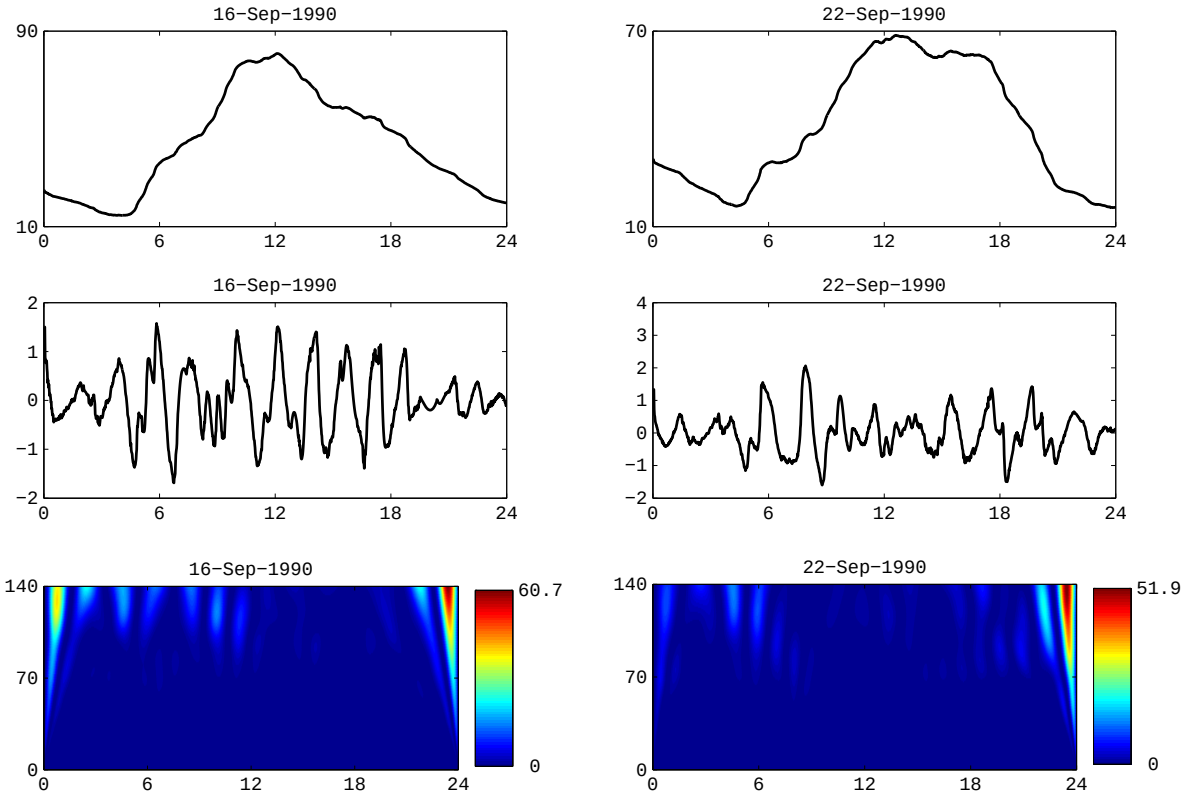
16-Sep-1990
90
10
0
6
12
18
24
22-Sep-1990
70
10
0
6
12
18
24
16-Sep-1990
2
1
0
−1
−2
0
6
12
18
24
22-Sep-1990
4
3
2
1
0
−1
−2
0
6
12
18
24
16-Sep-1990
140
70
0
0
6
12
18
24
60.7
0
22-Sep-1990
140
70
0
0
6
12
18
24
51.9
0

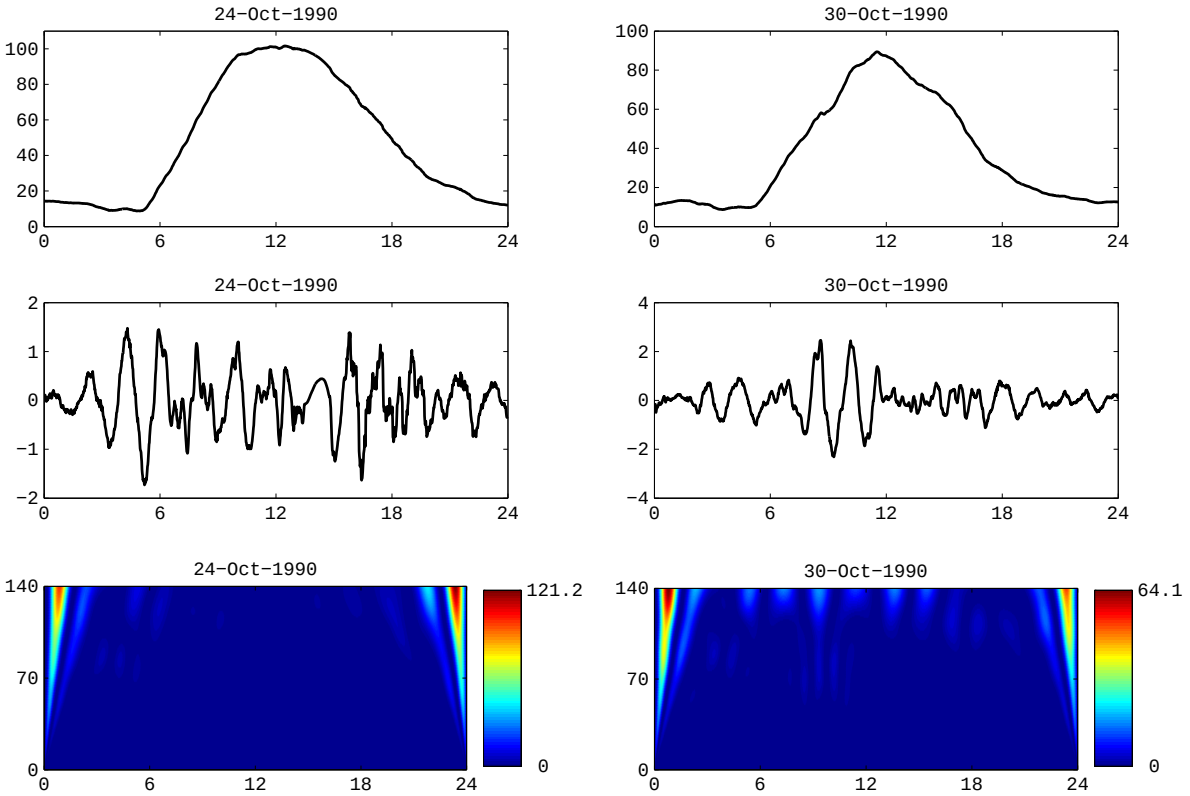
24-Oct-1990
30-Oct-1990
24-Oct-1990
30-Oct-1990
24-Oct-1990
121.2
0
30-Oct-1990
64.1
0

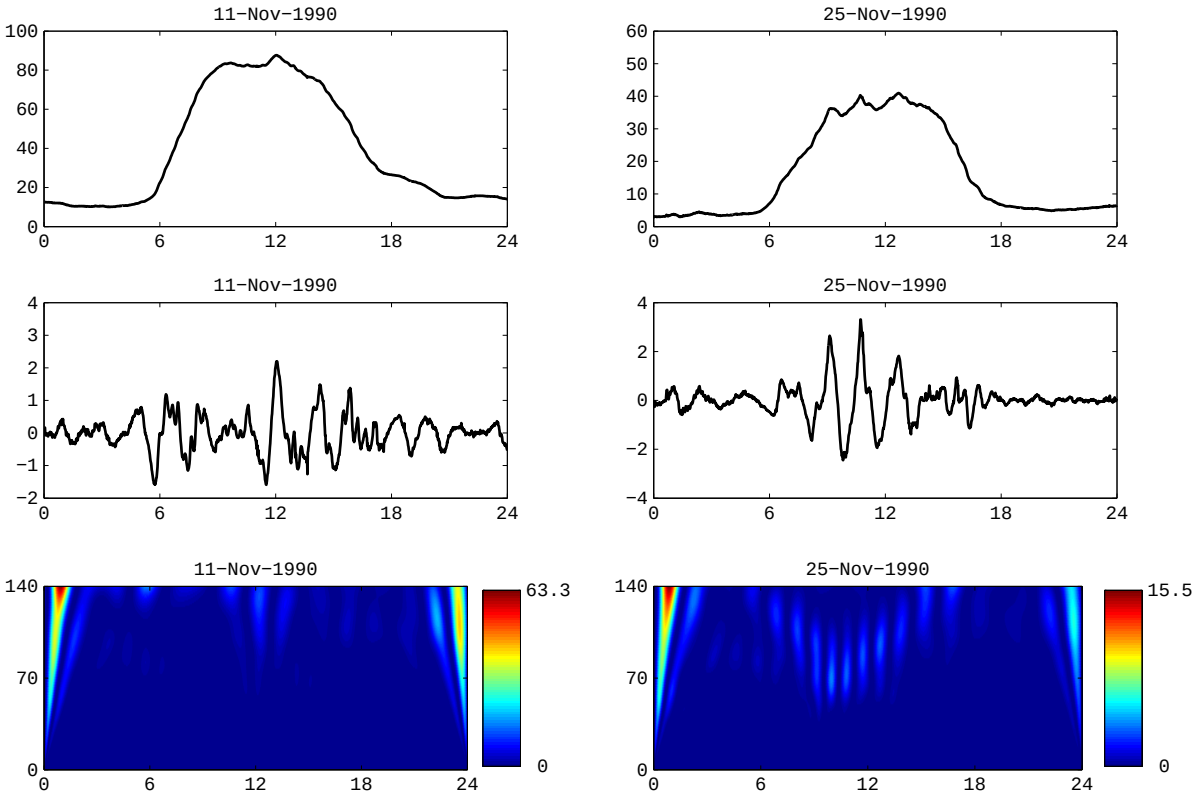
11−Nov−1990
25−Nov−1990
11−Nov−1990
25−Nov−1990
11−Nov−1990
25−Nov−1990
63.3
0
15.5
0

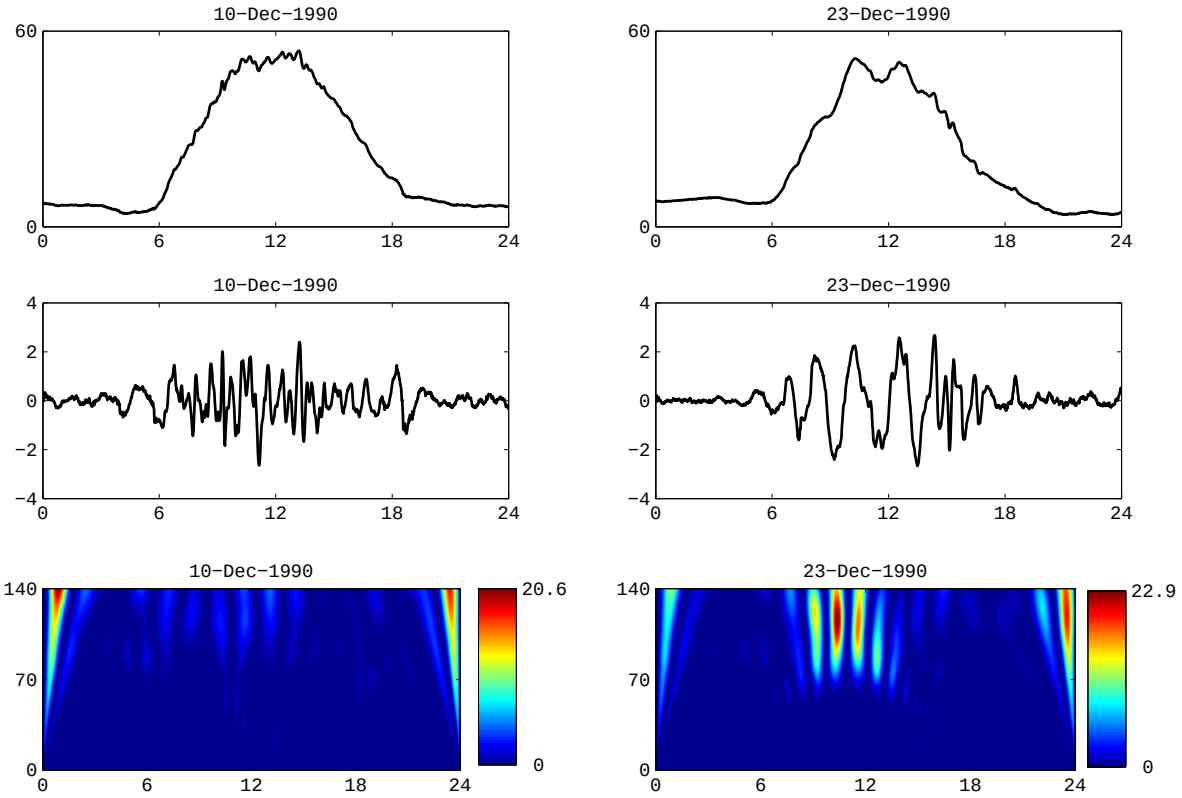
10-Dec-1990
23-Dec-1990
60
0
0
6
12
18
24
10-Dec-1990
23-Dec-1990
4
2
0
−2
−4
10-Dec-1990
23-Dec-1990
140
70
0
20.6
22.9

Appendix D

Profiles with Diurnal Double Maxima (DDM) Structures

TEC, measured in TECU, versus time, measured in UT hour, profiles with a DDM structure are presented here. The vertical lines in each figure mark the local sunrise, noon and sunset times respectively.

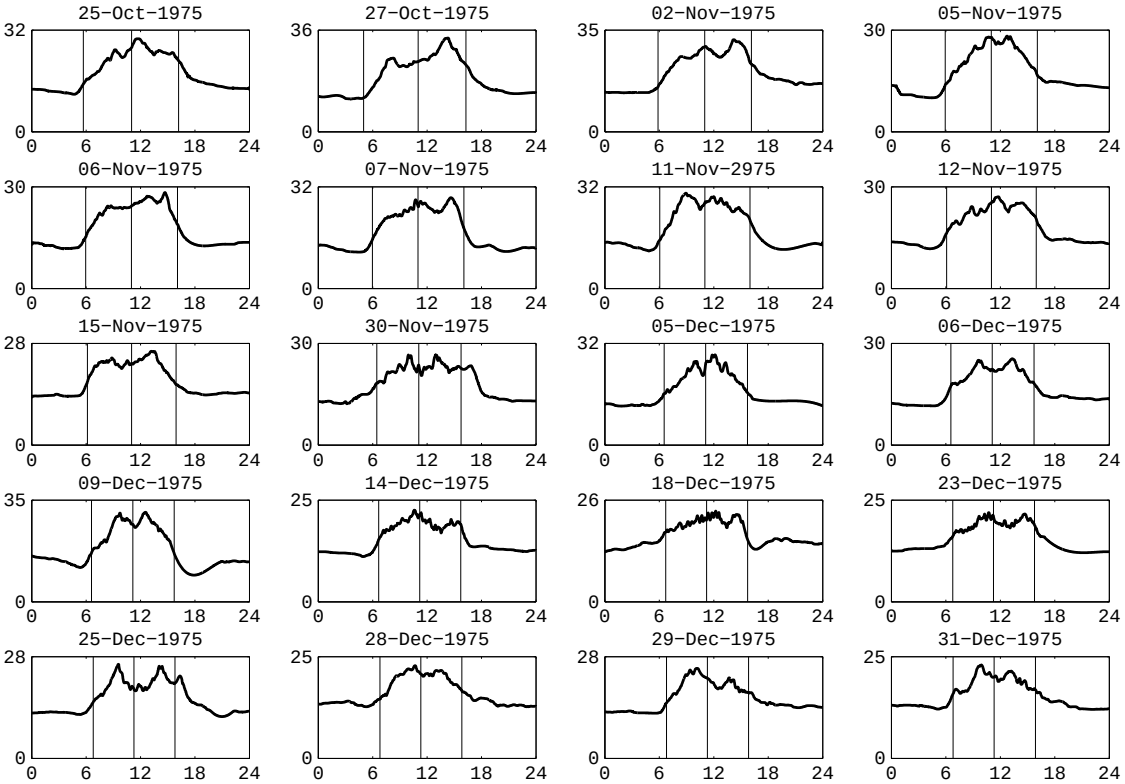
25-Oct-1975
27-Oct-1975
02-Nov-1975
05-Nov-1975
06-Nov-1975
07-Nov-1975
11-Nov-2975
12-Nov-1975
15-Nov-1975
30-Nov-1975
05-Dec-1975
06-Dec-1975
09-Dec-1975
14-Dec-1975
18-Dec-1975
23-Dec-1975
25-Dec-1975
28-Dec-1975
29-Dec-1975
31-Dec-1975

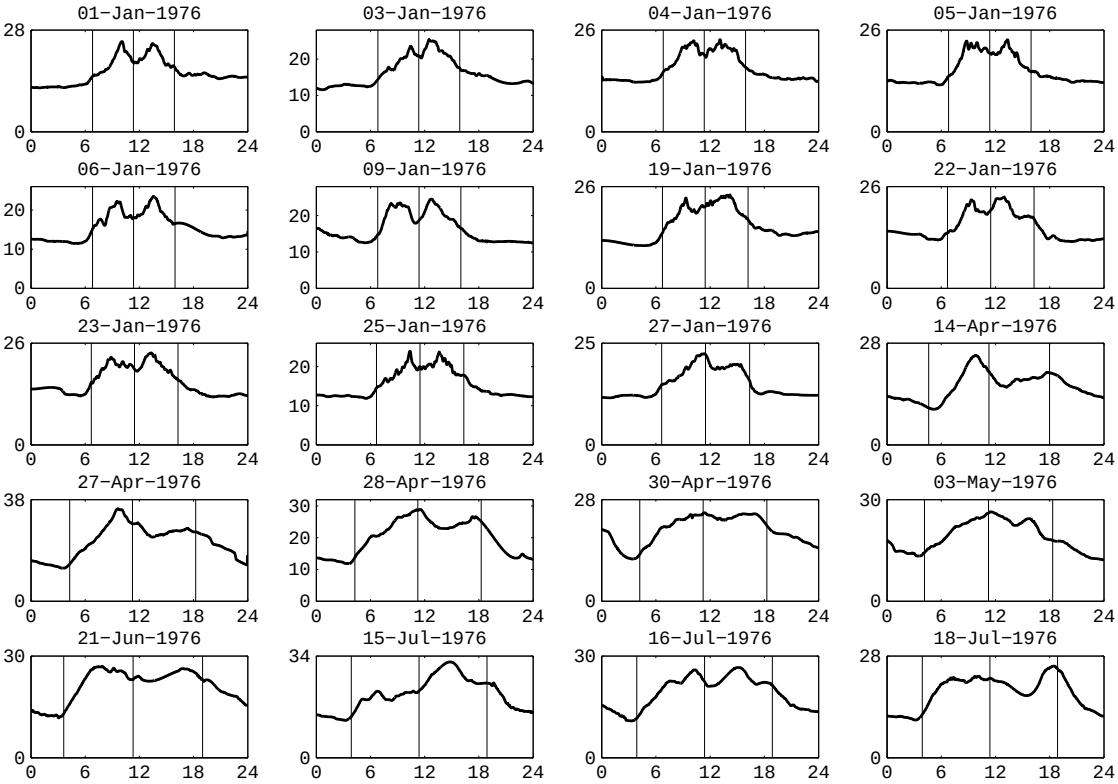
01-Jan-1976
03-Jan-1976
04-Jan-1976
05-Jan-1976
06-Jan-1976
09-Jan-1976
19-Jan-1976
22-Jan-1976
23-Jan-1976
25-Jan-1976
27-Jan-1976
14-Apr-1976
27-Apr-1976
28-Apr-1976
30-Apr-1976
03-May-1976
21-Jun-1976
15-Jul-1976
16-Jul-1976
18-Jul-1976

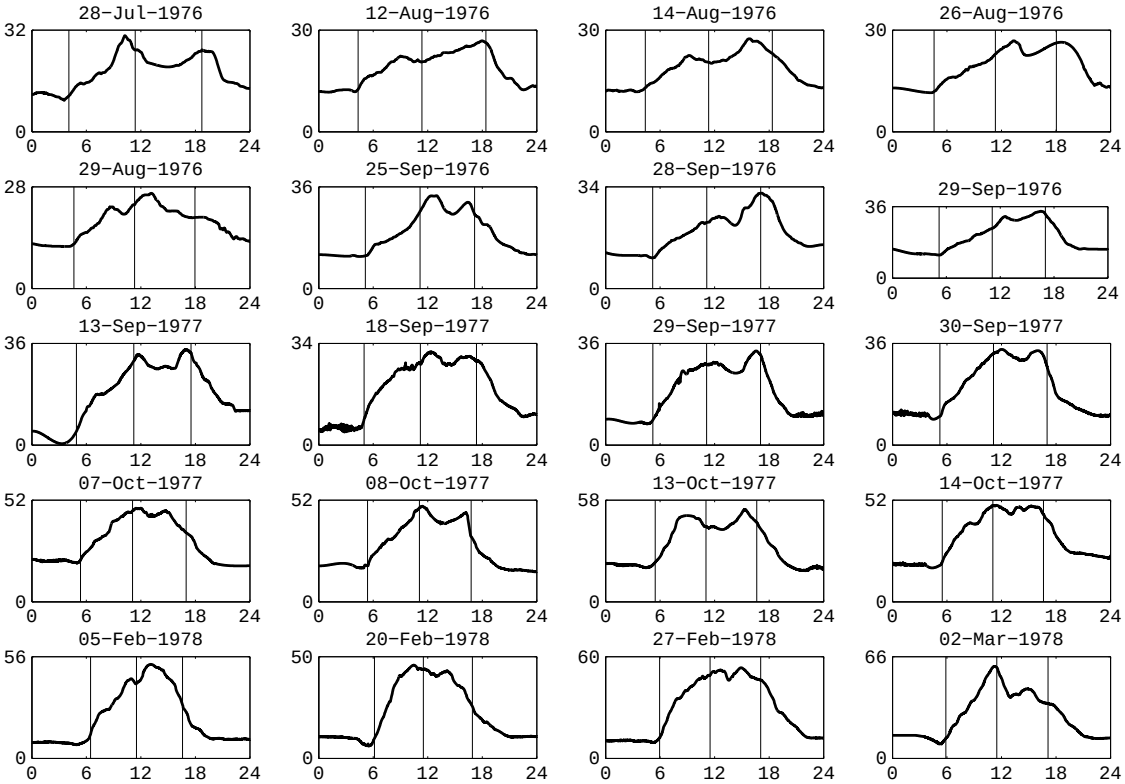
28–Jul–1976
12–Aug–1976
14–Aug–1976
26–Aug–1976
29–Aug–1976
25–Sep–1976
28–Sep–1976
29–Sep–1976
13–Sep–1977
18–Sep–1977
29–Sep–1977
30–Sep–1977
07–Oct–1977
08–Oct–1977
13–Oct–1977
14–Oct–1977
05–Feb–1978
20–Feb–1978
27–Feb–1978
02–Mar–1978

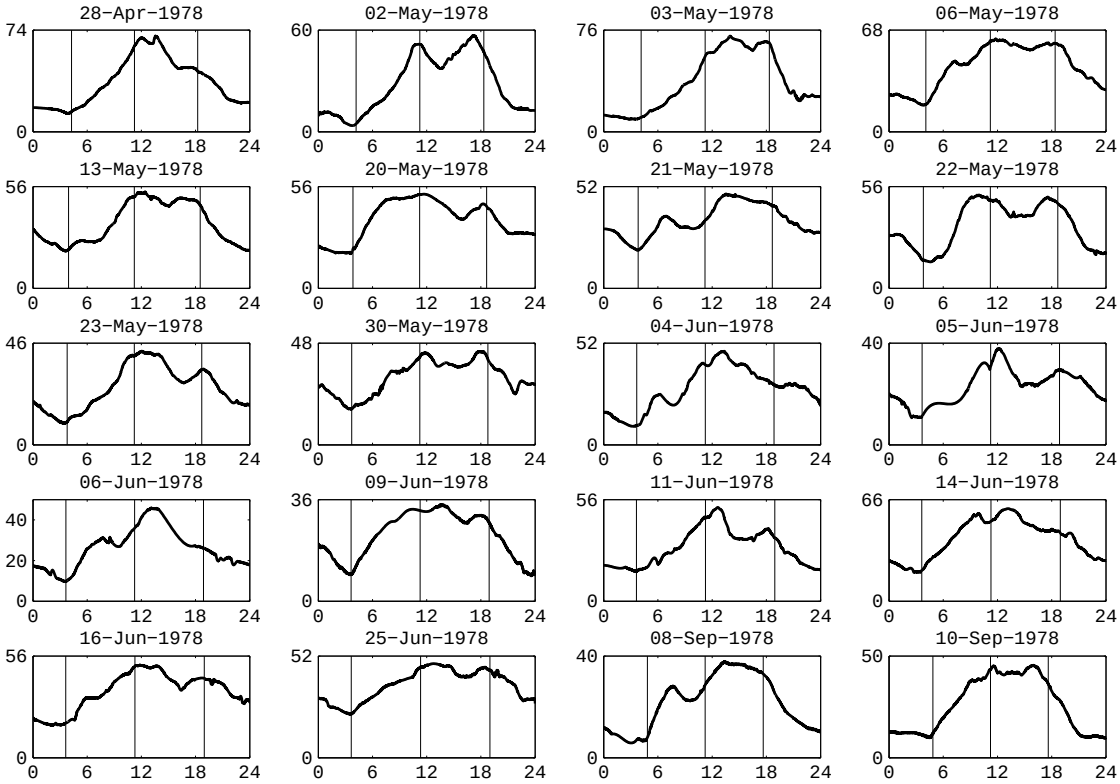
28-Apr-1978
74
0
0 6 12 18 24
02-May-1978
60
0
0 6 12 18 24
03-May-1978
76
0
0 6 12 18 24
06-May-1978
68
0
0 6 12 18 24
13-May-1978
56
0
0 6 12 18 24
20-May-1978
56
0
0 6 12 18 24
21-May-1978
52
0
0 6 12 18 24
22-May-1978
56
0
0 6 12 18 24
23-May-1978
46
0
0 6 12 18 24
30-May-1978
48
0
0 6 12 18 24
04-Jun-1978
52
0
0 6 12 18 24
05-Jun-1978
40
0
0 6 12 18 24
06-Jun-1978
40
20
0
0 6 12 18 24
09-Jun-1978
36
0
0 6 12 18 24
11-Jun-1978
56
0
0 6 12 18 24
14-Jun-1978
66
0
0 6 12 18 24
16-Jun-1978
56
0
0 6 12 18 24
25-Jun-1978
52
0
0 6 12 18 24
08-Sep-1978
40
0
0 6 12 18 24
10-Sep-1978
50
0
0 6 12 18 24

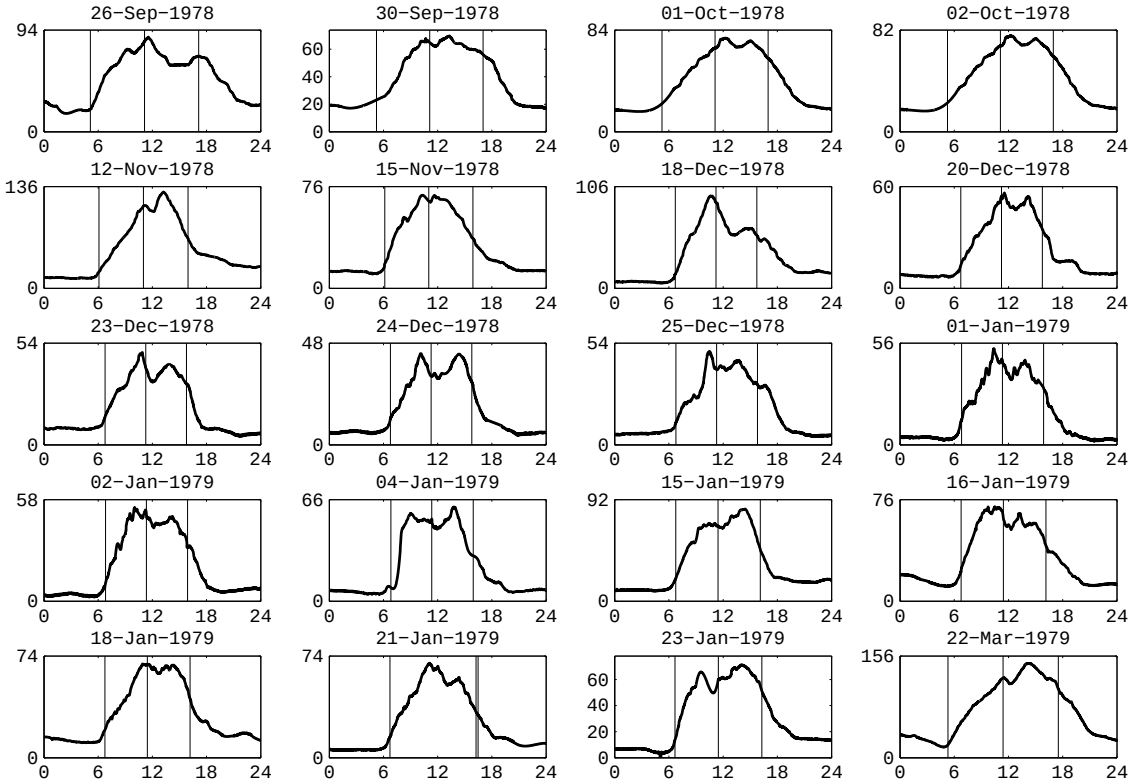
26-Sep-1978
30-Sep-1978
01-Oct-1978
02-Oct-1978
12-Nov-1978
15-Nov-1978
18-Dec-1978
20-Dec-1978
23-Dec-1978
24-Dec-1978
25-Dec-1978
01-Jan-1979
02-Jan-1979
04-Jan-1979
15-Jan-1979
16-Jan-1979
18-Jan-1979
21-Jan-1979
23-Jan-1979
22-Mar-1979

Appendix E

Publications

Journal Papers

1. Z. T. Katamzi, N. D. Smith, C. N. Mitchell, P. Spalla and M. Materassi, Statistical analysis of traveling ionospheric disturbances using TEC observations from geostationary satellites, *Journal of Atmospheric and Solar-Terrestrial Physics*, *in press*, doi:10.1016/j.jastp.2011.10.06, 2011

Conference Papers

1. Z. T. Katamzi, N. D. Smith, C. N. Mitchell and P. Spalla, Ionospheric Waves Detected from Geostationary Satellites TEC Measurements, *Proceedings of ESA 2^{nd} International Colloquium - Scientific and Fundamental Aspects of the Galileo Programme*, Padua, Italy, October 2009

2. C. Coleman, Z. T. Katamzi and C. N. Mitchell, Monitoring the Ionospheric Effects on LOFAR Operations, *Proceedings of 13^{th} International Ionospheric Effects Symposium*, Virginia, USA, May 2011

Bibliography

Afraimovich, E. L., E. A. Kosogorov, O. S. Lesyata, I. I. Ushakov, and A. F. Yakovets, Geomagnetic control of the spectrum of traveling ionospheric disturbances based on data from a global GPS network, *Annales of Geophysicae*, *19*, 723–731, 2001.

Afraimovich, E. L., E. I. Astafieva, S. V. Voeykov, B. Tsegmed, A. P. Potekhin, and J. L. Rasson, An investigation of the correlation between ionospheric and geomagnetic variations using data from the GPS and INTERMAGNET networks, *Advances in Space Research*, *38*, 2332–2336, 2006.

Afraimovich, E. L., I. K. Edemskiy, S. V. Voeykov, Y. V. Yasyukevich, and I. V. Zhivetiev, Spatio-temporal structure of the wave packets generated by the solar terminator, *Advances in Space Research*, *44*, 824–835, 2009.

Allain, D. J., and C. N. Mitchell, Ionospheric delay corrections for single-frequency GPS receivers over Europe using tomographic mapping, *GPS Solution*, *13*(2), 141–151, doi: 10.1007/s10291-008-0107-y, 2009.

Amm, O., R. Nakamura, H. U. Frey, Y. Ogawa, M. Kubyshkina, A. Balogh, and H. Reme, Substorm topology in the ionosphere and magnetosphere during a flux rope event in the magnetotail, *Annales of Geophysicae*, *24*, 735–750, 2006.

Austen, J. R., S. J. Franke, and C. H. Liu, Ionospheric imaging using computerized tomography, *Radio Science*, *23*(3), 299–307, 1988.

Basu, S., K. M. Groves, J. M. Quinn, and P. Doherty, A comparison of TEC fluctuations and scintillations at Ascensio Island, *Journal of Atmospheric and Solar-Terrestrial Physics*, *61*(16), 1219–1226, doi:Doi:10.1016/S1364-6826(99)00052-8, 1999.

Belcher, D. P., and H. J. Strangeways, Ionosphere-induced first and higher order errors for space based SAR, in *Proceedings of the 11th International Conference on Ionospheric Radio Systems and Techniques*, pp. 122–126, IET, Edinburgh, 2009.

Bernhardt, P., D. Antoniadis, and A. da Rosa, Lunar perturbations in columnar elec-

tron content and their interpretation in terms of dynamo electrostatic fields, *Journal of Geophysical Research*, *81*(34), 5957–5963, 1976.

Bhattacharyya, A., T. L. Beach, and P. M. Kintner, Nighttime equatorial ionosphere: GPS scintillations and differential carrier pahse fluctuations, *Radio Science*, *35*(1), 209–224, 2000.

Bhuyan, K., S. B. Singh, and P. Bhuyan, Application of generalized singular value decomposition to ionospheric tomography, *Annales of Geophysicae*, *22*, 3437–3444, 2004.

Bhuyan, P., and T. Tyagi, Lunar and solar diurnal variations of ionospheric electron content at Dehli, *Journal of Atmospheric and Terrestrial Physics*, *48*(3), 301–310, 1986.

Blagoveshchensky, D., A. Kalishin, and J. MacDougall, Effects of a "day-time" substorm on the ionosphere and radio propagation, *Advances in Space Research*, *44*, 1008–1012, doi:10.1016/j.asr.2009.06.019, 2009.

Boonstra, A., S. Wijnholds, S. van der Tol, and B. Jeffs, Calibration, sensitivity and RFI mitigation requirements for LOFAR, in *30th IEEE International Conference on Acoustics, Speech and Signal Processing*, pp. 869–872, Philadelphia, PA, 2005.

Boska, J., P. Sauli, J. Geman Sole, and L. F. Alberca, Diurnal variation of gravity wave activity at midlatitudes in the ionospheric F region, *Studia Geophysica et Geodaetica*, *47*(3), 579–586, 2003.

Boskova, J., and J. Lastovicka, Seasonal variation of gravity wave activity in the lower ionosphere in central europe, *Studia Geophysica et Geodaetica*, *45*(1), 85–92, 2001.

Bracewell, R. N., *The Fourier transform and its applications*, Circuits and Systems, third ed., McGraw Hill Book Co., Singapore, 2000.

Budden, K., *The propagation of radio waves: The theory of radio waves of lower power in the ionosphere and magnetosphere*, Cambridge University Press, Cambridge, U.K., 1988.

Bust, G. S., and C. N. Mitchell, History, current state, and future directions of ionospheric imaging, *Reviews of Geophysics*, *46*(RG1003), 2008.

Carlson, H. C., Jr, and A. Egeland, *Introduction to Space Physics*, chap. The aurora and the auroral ionosphere, Cambridge University Press, Cambridge, U.K., 1995.

Chapman, S., and R. Lindzen, *Atmospheric tides: Thermal and gravitational*, D. Reidel Publishing Company, Dordrecht, Holland, 1970.

Checcacci, P. F., E. Capannini, and P. Spalla, I.R.O.E. ground equipment for ATS-6, in *The geophysical use of satellite beacon observations symposium*, pp. 726–735, Boston University, Boston, U.S.A., 1976.

Checcacci, P. F., E. Capannini, and P. Spalla, Results on the operational test of the I.R.O.E. ATS-6 measuring equipment, in *Symposium of the COSPAR satellite beacon group*, Firenze, Italy, 1978.

Chimonas, G., and C. Hines, Atmospheric gravity waves induced by a solar eclipse, 2, *Journal of Geophysical Research*, *76*(28), 7003–7005, 1971.

Ciraolo, L., and P. Spalla, Ionospheric instrumentation: A new approach, in *International Beacon Satellite Symposium on the investigation of the ionosphere by means of beacon satellite measurements*, pp. 1–7, Beijing, China, 1988.

Clemesha, B. R., P. P. Batista, R. A. Buriti da Costa, and N. Schuch, Seasonal variation in gravity wave activity at three locations in Brazil, *Annales of Geophysicae*, *27*, 1059–1065, 2009.

Coleman, C. J., A general purpose ionospheric ray tracing procedure, *Tech. rep.*, Defence Science and Technology Organisation, Australia, 1993.

Coleman, C. J., Ionospheric ray-tracing equations and their solution, *Radio Science Bulletin*, *325*, 17–23, 2008.

Cot, C., and H. Teitelbaum, Generation of gravity waves by inhomogeneous heating of the atmosphere, *Journal of Atmospheric and Terrestrial Physics*, *42*, 877–833, 1980.

Daubechies, I., *Ten lectures on wavelets*, Capital City Press, Montpelier, Vermont, U.S.A, 1992.

Davies, K., *Ionospheric radio*, *IEE Electromagnetic waves series*, vol. 31, Peter Peregrinus Ltd, Exeter, 1990.

de Souza, A. M., and J. F. G. Monico, The wavelet method as an alternative for reducing ionospheric effects from single-frequency GPS receivers, *Journal of Geodesy*, *81*(12), 799–804, doi:10.1007/s00190-007-0150-4, 2007.

Dieminger, W., J. P. Schodel, G. Schmidt, and G. K. Hartmann, Recording gravity waves by means of geostationary beacon-satellites, *Journal of Atmospheric and Terrestrial Physics*, *32*, 1615–1617, 1970.

Evans, J., A note on lunar tides in the ionosphere, *Journal of Geophysical Research*, *83*(A4), 1647–1652, 1978.

Evans, J., J. Holt, and R. Wand, A differential-Doppler study of traveling ionospheric disturbances from Millstone Hill, *Radio Science*, *18*(3), 435–451, 1983.

Fremouw, E. J., J. A. Secan, and B. M. Howe, Application of stochastic inverse theoty to ionospheric tomography, *Radio Science*, *27*(5), 721–732, 1992.

Galushko, V. G., V. V. Paznukhov, Y. M. Yampolski, and F. J. C., Incoherent scatter rada observation of AGW/TID events generated by the moving solar terminator, *Annales of Geophysicae*, *16*, 821–827, 1998.

Gaussiran II, T. L., G. S. Bust, and T. W. Garner, LOFAR as an ionospheric probe, *Planetary and Space Science*, *52*, 1375–1380, doi:10.1016/j.pss.2004.2004.09.007, 2004.

Gonzalez, W. D., J. A. Joselyn, Y. Kamide, H. W. Kroehl, G. Rostoker, B. T. Tsurutani, and V. M. Vasyliunas, What is a geomagnetic storm?, *Journal of Geophysical Research*, *99*(A4), 5771–5792, 1994.

Hagan, M., J. Forbes, and A. Richmond, *Encyclopedia of Atmospheric Sciences*, vol. 1, chap. Atmospheric Tides, pp. 159–165, Academic Press, 2003.

Hajj, G. A., R. Ibanez-Meier, E. R. Kursinski, and L. J. Romans, Imaging the ionosphere with the Global Positioning Systems, *International Journal of Imaging Systems and Technology*, *5*(2), 174–184, 1994.

Hargreaves, J., *The Solar-Terrestrial Environment: An Introduction to Geospace*, Cambridge Atmospheric and Space Science Series, Cambridge University Press, Cambridge, 1992.

Haselgrove, J., Ray theory and a new method for ray tracing, in *The physics of the ionosphere: Report of conference*, pp. 355–364, Physical Society, Cambridge, U.K., 1954.

Hines, C., Internal atmospheric gravity waves at ionospheric heights, *Canadian Journal of Physics*, pp. 1441–1481, 1960.

Hofmann-Wellenhof, B., H. Lichtenegger, and J. Collins, *Global Positioning System: Theory and practice*, vol. 5th revised edition, Springer-Verlag, New York, U.S.A., 2001.

Hooke, W. H., Ionospheric irregularites produced by internal atmospheric gravity waves, *Journal of Atmospheric and Terrestrial Physics*, *30*(5), 795–823, doi:Doi:10.1016/S0021-9169(68)80033-9, 1968.

Huang, Y., and B. Jeng, On the forenoon bite-out in the critical frequency of the F2-Layer, *Journal of Atmospheric and Terrestrial Physics*, *40*, 581–582, 1978.

Jakowski, N., R. Leitinger, and L. Ciraolo, Behaviour of large scale structures of the electron content as a key paremeter for range errors in GNSS applications, *Annals of Geophysics*, *47*(2/3), 1031–1047, 2004.

Jonsson, P., and L. Eklundh, TIMESAT - a program for analyzing time-series of satellite sensor data, *Computers and Geosciences*, *30*, 833–845, doi:10.1016/j.cageo.2004.05.006, 2004.

Kamide, Y., and S. I. Akasofu, Notes on the auroral electrojet indices, *Reviews of Geophysics and Space Physics*, *21*(7), 1647–1656, 1983.

Kelley, M. C., In situ ionospheric observations of severe weather-related gravity waves and associated small-scale plasma structure, *Journal of Geophysical Research*, *102*(A1), 329–335, 1997.

Klausner, V., P. R. Fagunde, Y. Sahai, C. M. Wrasse, V. G. Pillat, and F. Becker-Guedes, Observation of GW/TID oscillations in the F2 layer at low latitude during high and low solar activity, geomagnetic quiet and disturbed periods, *Journal of Geophysical Research*, *114*, A02,313, 2009.

Kohl, H., J. King, and D. Eccles, Some effects of neutral winds on the ionospheric F-layer, *Journal of Atmospheric and Terrestrial Physics*, *30*(10), 1733–1744, 1968.

Lastovicka, J., Forcing of the ionosphere by waves from below, *Journal of Atmospheric and Solar-Terrestrial Physics*, *68*, 479–497, 2006.

Lay, E. H., S. Close, P. Colestock, and G. S. Bust, Development and error analysis of nonlinear ionospheric removal algorithm for ionospheric electron density determination using broadband RF data, *Journal of Geophysical Research*, *116*, A02,316, doi:Doi:10.1029/2010JA015862, 2011.

Lee, M., R. Pradipta, A. Labno, L. Burton, J. Cohen, S. Dofma, A. Coster, M. Sulzer, and S. Kuo, Did tsunami-launched gravity waves trigger ionospheric turbulence over Arecibo?, *Journal of Geophysical Research*, *113*, A01,302, 2008.

Leitinger, R., Ionospheric tomography, in *Review of Radio Science: 1996-1999*, pp. 581–623, Wiley -IEEE Press, 1999.

Liu, J. H., C. C. Hsiao, L. C. Tsai, C. H. Liu, F. S. Kuo, H. Y. Lue, and C. M. Huang, Vertical phase and group velocities of internal gravity waves derived from ionograms

during the solar eclipse of 24 October 1995, *Journal of Atmospheric and Solar-Terrestrial Physics*, *60*, 1679–1686, 1998.

Mannucci, A. J., B. A. Iijima, U. J. Lindqwister, X. Pi, L. Sparks, and W. B. D., GPS and Ionosphere, in *Review of Radio Science: 1996-1999*, pp. 625–665, Wiley -IEEE Press, New York, U.S.A., 1999.

Materassi, M., and C. N. Mitchell, Wavelets analysis of GPS amplitude scintillation: A case study, *Radio Science*, *42*(1), RS1004, 2007.

McNamara, L., *The Ionosphere: Communications, Surveillance, and Direction Finding*, Orbit: A Foundation Series, Kreiger Publishing Company, Malabar, Florida, 1991.

McPherron, R. L., *Magnetic Storms*, chap. The Role of Substorms in the Generation of Magnetic Storms, pp. 131–147, Geophysical Monograph 98, American Geophysical Union, Washington DC, USA, 1997.

Mendillo, M., Storms in the ionosphere: Patterns and processes for total electron content, *Reviews of Geophysics*, *44*, RG4001, doi:10.1029/2005RG000193, 2006.

Misiti, M., Y. Misiti, G. Oppenheim, and J.-M. Poggi, *Wavelet toolbox user's guide (Version 3)*, Natick, U.S.A, 2006.

Mitchell, C. N., and P. S. Spencer, A three-dimensional time dependent algorithm for ionospheric imaging using GPS, *Annales of Geophysicae*, *44*(4), 687–697, 2003.

Mitchell, C. N., L. Kersley, J. A. T. Heaton, and S. E. Pryse, Determination of the vertical electron-density profile in ionospheric tomography: Experimental results, *Annales of Geophysicae*, *15*(6), 747–752, 1997.

Pedatella, N., and J. Forbes, Global structure of the lunar tide in ionospheric total electron content, *Geophysical Research Letters*, *37*, L06,103, 2010.

Percival, D., and A. Walden, *Wavelet methods for time series analysis*, Cambridge University Press, Cambridge, 2000.

Perrin, O., EGNOS Training Course (Demonstration in China), http://www.icao.int/icao/en/ro/nacc/meetings/2004/gnss/, 2003.

Petit, G., and B. Luzum, Iers conventions (2010), *Tech. Rep. 36*, International Earth Rotation and Reference Systems Service (IERS), 2010.

Pi, X., M. Mendillo, and M. Fox, Diurnal double maxima patterns in the F region iono-

sphere: Substorm-related aspects, *Journal of Geophysical Research*, *98*(A8), 13,677 – 13,691, 1993.

Pi, X., M. Mendillo, P. Spalla, and D. Anderson, Longitudinal effects of ionospheric responses to substorms at middle and low latitudes: A case study, *Annales of Geophysicae*, *13*, 863–870, 1995.

Press, W. H., S. A. Teukolisky, W. T. Vetterling, and B. P. Flannery, *Numerical Recipes in C: The art of scientific computing*, Cambridge University Press, Cambridge, U.K., 1992.

Rastogi, R. G., and S. Sanatani, Forenoon bite-out of F2 layer ionisations at tropical latitudes, *Annales of Geophysicae*, *24*, 75–80, 1968.

Raymund, T., J. R. Austen, S. J. Franke, C. H. Liu, J. A. Klobuchar, and J. Stalker, Application of computerized tomography to the investigation of ionospheric structures, *Radio Science*, *25*(5), 771–789, 1990.

Raymund, T., Y. Bresler, D. N. Anderson, and R. E. Daniell, Model-assisted ionospheric tomography: A new algorithm, *Radio Science*, *29*(6), 1493–1512, 1994.

Reiger, M., R. Leitinger, and S. J. Bauer, Mesoscale ionospheric anomalies not associated with space weather, *Radio Science*, *41*(6), RS6S10, 2006.

Rishbeth, H., and O. Garriott, *Introduction to ionospheric physics*, *International Geophysics Series*, vol. 14, Academic Press, INC, New York, 1969.

Rishbeth, H., K. J. F. Sedgemore-Schulthess, and T. Ulich, Semiannual and annual variations in the height of the ionospheric F2-peak, *Annales of Geophysicae*, *18*, 285–299, 2000.

Romano, V., S. Pau, M. Pezzopane, Z. E., B. Zolesi, G. De Franceschi, and S. Locatelli, The electronic space weather upper atmosphere (eswua) project at INGV: advancements and state of art, *Annales of Geophysicae*, *26*, 345–351, 2008.

Rose, J. A. R., D. J. Allain, and C. N. Mitchell, Reduction in the ionospheric error for a single-frequency GPS timing solution using tomography, *Annals of Geophysics*, *52*(5), 469–486, 2009.

Rostoker, G., S. I. Akasofu, J. Foster, R. A. Greenwald, Y. Kamide, K. Kawasaki, A. T. Y. Liu, R. L. McPherron, and C. T. Russell, Magnetospheric Substorms - Definition and Signatures, *Journal of Geophysical Research*, *85*(A4), 1663–1668, 1980.

Saryo, T., M. Takeda, T. Araki, T. Sato, T. Tsuda, S. Fukao, and S. Kato, A midday bite-out event of the F2-layer observed by MU radar, *Journal of Geomagnetism and Geoelectricity*, *41*, 727–734, 1989.

Sauli, P., S. G. Roux, P. Abry, and J. Boska, Acoustic-gravity waves during solar eclipses: Detection and characterization using wavelet transforms, *Journal of Atmospheric and Solar-Terrestrial Physics*, *69*, 2465–2484, 2007.

Skone, S., R. Yousuf, and A. Coster, Performance evaluation of the Wide Area Augmentation System for ionospheric storm events, *Journal of Global Positioning Systems*, *3*(1-2), 251–258, 2004.

Soicher, H., Traveling ionospheric disturbances (TIDs) at mid-latitudes: Solar cycle phase dependence, *Radio Science*, *23*(3), 283–291, 1988.

Somsikov, V. M., A spherical model of wave generation in the atmosphere by the solar terminator, *Journal of Atmospheric and Terrestrial Physics*, *49*(5), 433–438, 1987.

Somsikov, V. M., On mechanisms for the formation of atmospheric irregularities in the solar terminator region, *Journal of Atmospheric and Terrestrial Physics*, *57*(1), 75–83, 1995.

Somsikov, V. M., and B. Gangulay, On the formation of atmospheric inhomogeneities in the solar terminator region, *Journal of Atmospheric and Terrestrial Physics*, *57*(12), 1513–1523, 1995.

Strangeways, H. J., V. Gherm, and N. N. Zernov, Fast determination of phase advance, path delay and ray path curvature between satellites through a 3d ionosphere for l-band transmissions, *IET Seminar Digests (2007)*, *2007*(11961), 365, doi:DOI:10.1049/ic.2007.1488, 2007.

Tanskanen, E. I., A comprehensive high-throughput analysis of substorms observed by IMAGE magnetometer network: Years 1993-2003 examined, *Journal of Geophysical Research*, *114*, A05,204, doi:10.1029/2008JA013682, 2009.

Titheridge, J. E., and M. J. Buonsanto, A comparison of northern and southern hemisphere TEC storm behaviour, *Journal of Atmospheric and Solar-Terrestrial Physics*, *50*(9), 763–780, 1988.

Torrence, C., and G. P. Compo, A practical guide to wavelet analysis, *Bulleting of the Amerian Meteorological Society*, *79*(1), 61–78, 1998.

Tsugawa, T., N. Kotake, and Y. Otsuka, Medium-scale traveling ionospheric disturbances

observed by GPS receiver network in Japan: A short review, *GPS Solution*, *11*, 139–144, 2007.

van der Tol, S., and A. van der Veen, Ionospheric calibration for the LOFAR radio telescope, in *International Symposium on Signals, Circuits and Systems*, pp. 457–460, Iasi, Romania, 2007.

Yin, P., and C. N. Mitchell, Use of radio-occultation data for ionospheric imaging during the April 2002 disturbances, *GPS Solution*, *9*, 156–163, 2005.

Yousuf, R., and S. Skone, WAAS Performance Evaluation under Increased Ionospheric Activity, in *ION GNSS 18th International Technical Meeting of the Satellite Division*, pp. 2316–2327, Long Beach, CA, 2005.

Zhang, H., W. Zhu, J. Peng, and H. C., Analysis of the ionosphere wave-motion with GPS, *Chinese Science Bulleting*, *50*(13), 1373–1381, 2005.

Zhang, L. Q., Z. H. Liu, Z. W. Ma, W. Baumhohann, J. Wu, M. Dunlop, J. K. Shi, L. Lu, and J. Y. Wang, A new processing method for the AE index, *Science in China Series E: Technological Sciences*, *51*(10), 1713–1720, 2008.

Zhao, Y., and A. C. Reynolds, Estimation and removal of tidal effects from pressure data, *SPE journal*, *14*(1), 144–152, 2009.